



UNIVERSITY OF

LIVERPOOL

The Development of Superhydrophobic Materials for Real-World Applications

Yasmin Ahmed Mehanna

Department of Chemistry
University of Liverpool

'This Thesis is submitted in accordance with the requirements of the University of
Liverpool for the degree of Doctor of Philosophy in Chemistry.'

April 2022

Declaration

I, Yasmin A. Mehanna, confirm that the work presented in this PhD thesis is my own. Where information has been derived from other sources, or work has been carried out by/in collaboration with others, I confirm that this has been clearly indicated.

Acknowledgements

Firstly, I would like to thank my supervisor, Dr Colin Crick, for giving me the opportunity to work in his group, for all the support he has generously and continuously provided, and for everything he has taught me through the last four years. I also thank all the Crick group members, past and present, for the great time I spent with them; especially Becky, for her tremendous help from the very first day I joined the group. In addition, I would like to thank my secondary supervisor, Dr Anna Slater, for her great support and valuable advice.

I would like to thank everyone who has contributed to this research and helped me advance throughout my study, without whom this thesis would not have come to its current form; Dr Alex Ciupa and Dr Keith Arnold for their continuous help and support in measurement and imaging, Dr Troy Manning and Dr Luke Daniels for their assistance with the MOF-related work, Dr Marco Marcello and Dr Marie Held for their great efforts in 3D imaging and post-analysis, Dr Tom Hasell and Veronica Hanna for valuable guidance and help with mechanical testing. In addition, I am very grateful to my friends, Walaa, Alaa and Mostafa, for all the writing sessions without which I cannot imagine finishing this thesis.

Finally, I would like to thank my family and friends, who without none of this would have been possible, and to whom I dedicate this thesis. To my parents, sisters and brother for their endless support. To my friends, Aya, Hager and Ghada, for the countless support they always provided, and to Esraa, who I cannot thank enough for always being there through the ups and downs regardless of the distances. To all the friends I met in Liverpool who made this place feel like home. Last but foremost, I am forever grateful to my husband, Osama, who has been there supporting and encouraging me even when times were challenging, and who without, this journey would have been much harder.

Abstract

Inspired by many natural systems, superhydrophobic materials have been widely reported throughout the scientific literature. Their distinguished properties, owing to their inherent hydrophobicity and rough morphology, allowed their development for several application fields. In spite of their promising functionalities, the commercial availability of these materials is still limited. This is attributed to several factors, including material compatibility, inadequate deposition routes, physical resilience, and scaling-up complications. While the reported methods to fabricate novel surfaces are abundant, the consideration of these limiting factors is crucial for the wider applicability of superhydrophobic surfaces.

The aim of this thesis is to promote the applicability of superhydrophobic surfaces in real-life applications. This is achieved by investigating the limitations of these surfaces and attempting to address them. The inclusion of heat-sensitive substrates was attempted for a heat-dependant deposition method, which was achieved by re-designing the technical setup and re-adjusting the deposition parameters accordingly (Chapter 2). Following this, the signified influence of coatings resilience on their applicability motivated the introduction of a simple analysis methodology for resilience assessment, combining image analysis and mass-loss tracking (Chapter 3). In addition, the investigation of resilience-enhancement of polymer/particle composite coatings was conducted, aiming to relate the properties of coating components to the observed robustness (Chapter 4). After that, the inclusion of recycled waste polymers was attempted to fabricate a superhydrophobic filter for oil/water separation, through the utilisation of micronized polymer powder and investigation of the optimum treatment conditions (Chapter 5). Finally, the applicability of superhydrophobic coatings in protecting water-sensitive materials was examined as an example of an important application of superhydrophobic coatings (Chapter 6).

Contents

Declaration	3
Acknowledgements	5
Abstract	7
Abbreviations	16
Publications	18
1. Introduction	20
1.1. Superhydrophobicity: Definition and Requirements	20
1.1.1. The Lotus Effect and Requirements for Superhydrophobicity	20
1.1.2. Characterisation of Superhydrophobicity	22
1.2. Wetting Models	24
1.2.1. Young's Equation	24
1.2.2. Wenzel Model	26
1.2.3. Cassie-Baxter Model	28
1.3. Fabrication of Superhydrophobic Surfaces	30
1.3.1. Top-Down Approaches	31
1.3.1.1. <i>Etching</i>	31
1.3.1.2. <i>Lithography</i>	34
1.3.1.3. <i>Template Imprinting</i>	35
1.3.2. Bottom-Up Approaches	36
1.3.2.1. <i>Rough deposition of hydrophobic material</i>	36
1.3.2.1.1. <i>3D printing</i>	37
1.3.2.1.2. <i>Electrospinning</i>	37
1.3.2.1.3. <i>Chemical vapour deposition</i>	38
1.3.2.2. <i>Deposition of the treated materials</i>	40
1.3.2.2.1. <i>Covalent functionalization</i>	40
1.3.2.2.2. <i>Physical treatment</i>	43

1.4.	Applications of Superhydrophobic Surfaces.....	44
1.4.1.	Self-Cleaning Surfaces	44
1.4.2.	Surface Protection	45
1.4.3.	Drag Reduction.....	46
1.4.4.	Oil-water Separation	47
1.5.	Factors Limiting Wider Applicability of Superhydrophobic Surface	47
1.5.1.	Fabrication Approaches and Scaling-Up Restrictions.....	48
1.5.2.	Durability Concerns against Real-life Challenges.....	49
1.6.	Thesis Outline.....	51
1.7.	References	52
2.	The Room-Temperature Deposition of Thermally-Activated Polymers.....	62
2.1.	Introduction.....	62
2.1.1.	Aerosol-Assisted Chemical Vapour Deposition	62
2.1.1.1.	<i>Mechanism of producing rough polymeric coatings.....</i>	<i>62</i>
2.1.1.2.	<i>Deposition of thermosetting polymers for superhydrophobic applications</i>	<i>64</i>
2.1.2.	Chapter Aim.....	66
2.2.	Experimental Methods	67
2.2.1.	Materials.....	67
2.2.2.	Polymer Solution Preparation	68
2.2.3.	Deposition Conditions	68
2.2.4.	Characterisation.....	69
2.3.	Results and Discussion.....	70
2.3.1.	Deposition of PDMS Elastomer.....	70
2.3.1.1.	<i>Developing the ta-AACVD procedure.....</i>	<i>70</i>
2.3.1.2.	<i>Activation and Deposition Temperature</i>	<i>73</i>
2.3.1.3.	<i>Physical Robustness.....</i>	<i>74</i>
2.3.1.4.	<i>Physical Appearance</i>	<i>74</i>
2.3.1.5.	<i>Coating Hydrophobicity.....</i>	<i>75</i>

2.3.1.6.	<i>Surface Imaging</i>	76
2.3.1.7.	<i>Other Factors Examined</i>	78
2.3.1.8.	<i>Temperature-Sensitive Substrates</i>	79
2.3.2.	Deposition of Thermoplastic Polymers.....	80
2.3.2.1.	<i>Chemical compatibility</i>	80
2.3.2.2.	<i>Surface roughness</i>	83
2.4.	Conclusions.....	84
2.5.	References.....	85
3.	Quantitative Imaging Analysis of Coating Abrasion	88
3.1.	Introduction.....	88
3.1.1.	Current Methods for Assessment of Coating Resilience	88
3.1.1.1.	<i>Abrasion techniques</i>	88
3.1.1.2.	<i>Post-abrasion assessment</i>	90
3.1.2.	Chapter Aim	91
3.2.	Experimental Methods.....	92
3.2.1.	Materials.....	92
3.2.2.	Silica Hydrophobization	92
3.2.3.	Coating Preparation.....	92
3.2.4.	Coating Deposition	93
3.2.5.	Resilience Assessment.....	94
3.3.	Results and Discussion	95
3.3.1.	Establishing the Technique.....	95
3.3.1.1.	<i>Abrasion conditions</i>	95
3.3.1.2.	<i>Selecting imaging method</i>	96
3.3.1.3.	<i>Mass detection</i>	97
3.3.2.	Developing the Code for Image Processing.....	97
3.3.2.1.	<i>Influence of threshold on the generated binary images</i>	97
3.3.2.2.	<i>Threshold-selection code conceptualization</i>	98
3.3.2.3.	<i>Threshold-selection code description</i>	99

3.3.2.4.	<i>Evaluating the dependence on other variables.....</i>	104
3.3.3.	Mass-loss Trend	105
3.3.3.1.	<i>Mass-tracking in comparison with image processing.....</i>	106
3.3.3.2.	<i>Mass difference</i>	108
3.3.4.	Advantages, Limitations and Possible Adjustments to Different Sample Requirements	109
3.4.	Conclusions	111
3.5.	References	111
4.	Investigation of the Resilience of Polymer/Particle Composite Coatings	116
4.1.	Introduction	116
4.1.1.	Approaches for Resilience	116
4.1.2.	Challenges Facing the Fabrication of Superhydrophobic coatings ..	117
4.1.3.	Superhydrophobic Polymer/Particle Composites (SPPCs).....	118
4.1.4.	Chapter Aim.....	119
4.2.	Experimental Methods	119
4.2.1.	Materials	119
4.2.2.	Silica Hydrophobization	120
4.2.3.	Coating Preparation	120
4.2.4.	Coating Deposition	120
4.2.5.	Resilience Assessment.....	121
4.2.6.	Mechanical Testing	122
4.2.6.1.	<i>Films Preparation.....</i>	122
4.2.6.2.	<i>Testing conditions.....</i>	123
4.2.7.	Characterisation.....	124
4.2.7.1.	<i>Confocal imaging conditions</i>	124
4.2.7.2.	<i>Preparation of fluorescent coatings.....</i>	124
4.2.7.3.	<i>Other Characterisation.....</i>	124
4.3.	Results and Discussion.....	124
4.3.1.	Mechanical Properties of Polymers.....	124

4.3.1.1.	<i>PVC polymers</i>	125
4.3.1.2.	<i>PDMS polymers</i>	126
4.3.2.	<i>Influence of Polymer</i>	126
4.3.2.1.	<i>PVC polymers</i>	127
4.3.2.1.1.	<i>Coating performance</i>	127
4.3.2.1.2.	<i>Adhesion/cohesion failure</i>	129
4.3.2.2.	<i>PDMS polymers</i>	132
4.3.2.2.1.	<i>Correction for noise</i>	132
4.3.2.2.2.	<i>Coating performance</i>	133
4.3.2.2.3.	<i>Relating coating performance to polymer properties</i>	135
4.3.2.2.4.	<i>Adhesion/cohesion failure</i>	137
4.3.3.	<i>Influence of Particles</i>	138
4.3.3.1.	<i>Determining optimum mass ratio for μSiO_2</i>	138
4.3.3.2.	<i>Changing particle size</i>	139
4.3.3.3.	<i>Combining different particle sizes</i>	141
4.4.	<i>Conclusions</i>	143
4.5.	<i>References</i>	143
5.	<i>Micronized Polyethylene Filters for Oil/Water Separation</i>	146
5.1.	<i>Introduction</i>	146
5.1.1.	<i>Polymer Recycling and Micronization</i>	146
5.1.2.	<i>Sintering</i>	147
5.1.3.	<i>Chapter Aim</i>	148
5.2.	<i>Experimental Methods</i>	149
5.2.1.	<i>Materials</i>	149
5.2.2.	<i>Filter Preparation</i>	149
5.2.3.	<i>Separation Efficiency Assessment</i>	150
5.2.4.	<i>Characterisation</i>	151
5.3.	<i>Results and Discussion</i>	152
5.3.1.	<i>Powder Properties</i>	152

5.3.2.	Treatment of Powder and Effect of Hydrophobicity	152
5.3.2.1.	<i>Use of Solvent</i>	153
5.3.2.2.	<i>Heat Treatment</i>	154
5.3.2.3.	<i>Hydrophobicity of the filters</i>	155
5.3.2.4.	<i>Structure of the filter</i>	157
5.3.3.	Separation Efficiency	158
5.4.	Conclusions	160
5.5.	References	160
6.	Water Protective Coatings for Metal-Organic Frameworks.....	164
6.1.	Introduction	164
6.1.1.	Metal-Organic Frameworks.....	164
6.1.1.1.	<i>Issues with water stability</i>	165
6.1.1.2.	<i>Methods for protection against water</i>	165
6.1.2.	Chapter Aim.....	166
6.2.	Experimental Methods	167
6.2.1.	Materials	167
6.2.2.	MOFs Synthesis	167
6.2.2.1.	<i>Thin-film deposition of ZIF-8</i>	167
6.2.2.2.	<i>Synthesis of ZIF-8 powder</i>	167
6.2.2.3.	<i>Synthesis of ZIF-67 powder</i>	168
6.2.2.4.	<i>Synthesis of MOF-5 powder</i>	168
6.2.2.5.	<i>Synthesis of HKUST-1 powder</i>	168
6.2.3.	Compression into pellets.....	168
6.2.4.	Hydrophobic Treatment	168
6.2.5.	Water-Stability Testing.....	169
6.2.6.	Characterisation.....	169
6.3.	Results and Discussion.....	170
6.3.1.	ZIF-8 thin-films.....	170
6.3.2.	MOFs pellets.....	171

6.3.3. Water stability	173
6.4. Conclusions	178
6.5. References	179
7. Conclusions	182
7.1. Discussion Outline	182
7.2. Conclusions and Future Work	182
7.2.1. Chapter 2: Room-Temperature Deposition of Rough Coatings	182
7.2.2. Chapter 3: Quantifiable Resilience Assessment	184
7.2.3. Chapter 4: Resilience Enhancement of Composite Coatings	185
7.2.4. Chapter 5: Oil-water Separation Filters	186
7.2.5. Chapter 6: Protecting MOFs	187
7.3. References	188
Appendix	189
Appendix 1: Threshold selection code	190
Appendix 2: Full image sets for scanning experiments	192

Abbreviations

AACVD	Aerosol-Assisted Chemical Vapour Deposition
AFM	Atomic Force Microscopy
CNT	Carbon Nanotube
CVD	Chemical Vapour Deposition
DCM	Dichloromethane
DMF	N,N-dimethylformamide
FAS	Fluoroalkylsilane
HF	Hydrogen Fluoride
HKUST-1	Hong Kong University of Science and Technology
HMDS	Hexamethyldisilazane
MeIM	Methylimidazole
MeOH	Methanol
MOF	Metal-Organic Framework
M_{ratio}	Mass Ratio
M_w	Molecular Weight
MWPECVD	Microwave Plasma-Enhanced Chemical Vapour Deposition
PDMS	Polydimethylsiloxane
PECVD	Plasma-Enhanced Chemical Vapour Deposition
PEG	Polyethylene Glycol
PMMA	Polymethyl methacrylate
PScMS	Poly(styrene-co- α -methylstyrene)
PLA	Polylactic Acid
PTFE	Polytetrafluoroethylene
PVC	Polyvinyl Chloride
PVDF	Polyvinylidene difluoride
PXRD	Powder X-ray Diffraction
RGB	Red, Green, Blue
SEM	Scanning Electron Microscope
SPNC	Superhydrophobic Polymer/Nanoparticle Composite
TA	Tilt Angle

ta-AACVD	Thermally-Activated AACVD
TEOS	Tetraethylorthosilicate
T _g	Glass Transition Temperature
TGA	Thermogravimetric Analysis
THF	Tetrahydrofuran
TS	Tensile Strength
UV	Ultraviolet Radiation
WCA	Water Contact Angle
ZIF	Zeolitic Imidazolate Framework

Publications

1. Surface tension and viscosity dependence of slip-length over random-structured superhydrophobic surfaces. L. Zhang, Y. A. Mehanna, C. R. Crick and R. J. Poole. *Langmuir*, 2022, (manuscript under peer review).
2. Study on the Influence of Polymer/Particle Properties on the Resilience of Superhydrophobic Coatings. Y. A. Mehanna and C. R. Crick. *ACS Omega*, 2022, **7**, 18052–18062.
3. Image analysis methodology for a quantitative evaluation of coating abrasion resistance. Y. A. Mehanna and C. R. Crick. *Applied Materials Today*, 2021, **25**, 101203(1-6).
4. The challenges, achievements and applications of submersible superhydrophobic materials. Y. A. Mehanna, E. Sadler, R. L. Upton, A. G. Kempchinsky, Y. Lu and C. R. Crick. *Chem. Soc. Rev.*, 2021, **50**, 6569-6612.
5. Heat-Treated Micronized Polyethylene Powder for Efficient Oil/Water Separating Filters. Y. A. Mehanna and C. R. Crick. *Materials*, 2020, **13**, 3160(1-12).
6. Highly rough surface coatings via the ambient temperature deposition of thermosetting polymers. Y.A. Mehanna, R. L. Upton and C. R. Crick. *J. Mater. Chem. A*, 2019, **7**, 7333-7337.

Chapter 1:

Introduction

1. Introduction

1.1. Superhydrophobicity: Definition and Requirements

The interaction of water with surfaces has been a subject of interest for many decades. Nature is replete with fascinating surface designs that are structured to interact with water in a specific way that promotes functionality and facilitates adaptation to the surrounding environment. These designs, although demonstrating a high level of sophistication that makes accurate replication way too complex, provide a source for basic structural principles that have been widely studied and adopted for the fabrication of surfaces with specific water affinity. Surfaces with both high and low affinity to water are relevant to many applications, which signifies the importance of studying surface wettability and developing methods to control it depending on the desired outcome.¹⁻³ Superhydrophobic surfaces are characterised by their high water repellence and have been reported for a variety of applications. These applications include self-cleaning surfaces,^{4,5} anti-fouling,^{6,7} anti-icing,^{8,9} drag reduction,^{10,11} oil/water separation,^{12,13} in addition to others. Superhydrophobic surfaces are also widely seen in nature, from the water spider (*Gerris remigis*) which can stand on the water surface,^{14,15} to the *Salvinia molesta* leaves that can resist wetting for several weeks of underwater submersion.^{16,17} One of the most known examples of natural-existing water repellent surfaces is the Lotus leaves, after which the famous 'Lotus effect' has been named.¹⁸

1.1.1. The Lotus Effect and Requirements for Superhydrophobicity

The Lotus effect describes the self-cleaning mechanism observed on the Lotus plant leaf surface (*Nelumbo nucifera*).¹⁹ While a water droplet would usually slide along a tilted hydrophobic surface, a surface with a high enough hydrophobicity would cause the near-spherical droplet to roll across the surface instead (**Figure 1.1**). This rolling action improves the chances of picking up surface-bound contaminants (dirt particles, bacteria, etc.).²⁰

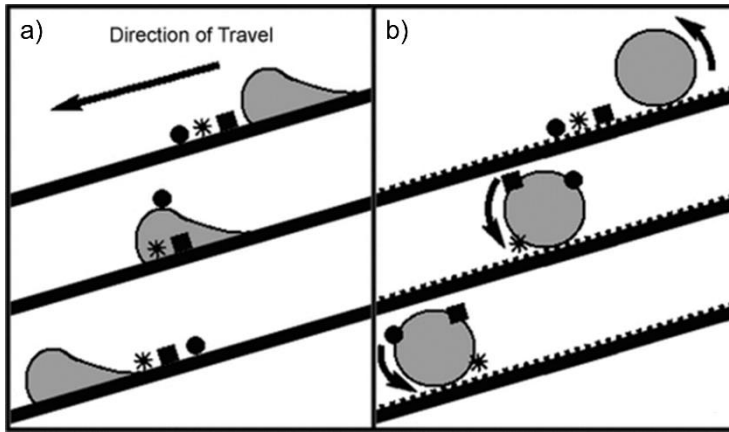


Figure 1.1: Schematic illustrating a) water sliding over the contaminants on a hydrophobic surface vs. the self-cleaning action caused by droplet rolling on a superhydrophobic surface. Figure retrieved from ref.²¹

Examining the structure of the Lotus leaves demonstrating this mechanism, it was found that they have a waxy surface coating that repels water. In addition, scanning electron microscope (SEM) imaging of the leaves showed complex 3D microstructure textures, with an additional layer of smaller-scale hair-like features covering both the surface protrusions and the flat regions (**Figure 1.2a**). These microstructures were shown to cause air to be trapped underneath the water upon wetting the surface, which enables the rolling motion.²⁰

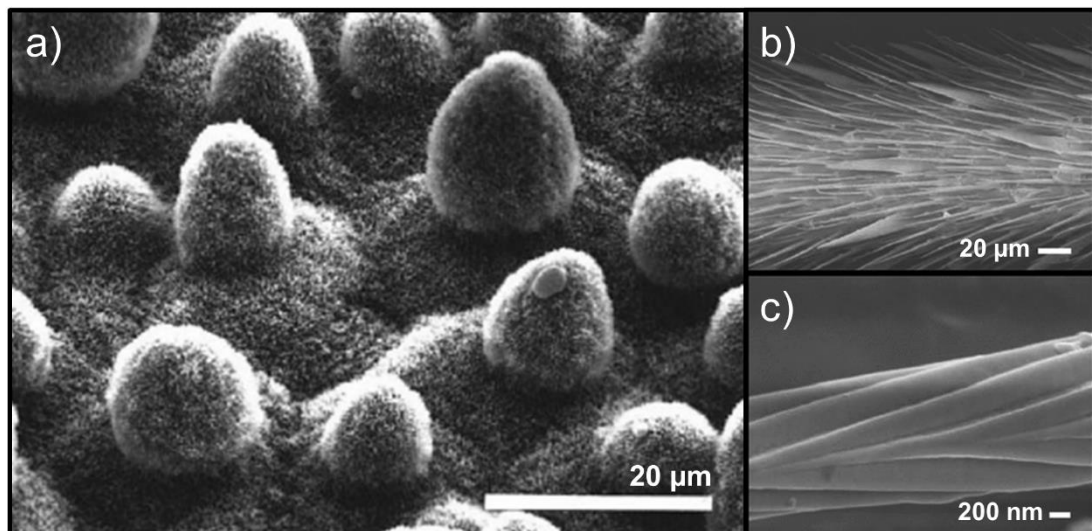


Figure 1.2: SEM images for a) a Lotus leaf, showing the highly rough surface morphology, and b-c) a water-spider leg, showing the leg covered with spindle-like structures (b), while these structures contain nano grooves (c) to add a smaller-scale roughness. Scale bars are shown for each image. Figure retrieved from a) ref.²² b-c) ref.¹⁴

Another fascinating natural superhydrophobic surface is found in the water spider (*Gerris remigis*), which is an example of many insects that are known for their ability to 'walk on water'. This ability is primarily attributed to the high surface tension of the

water, but also to the hydrophobic waxy leg coating found on the spider's legs that hinders the possibility of breaking the surface tension and dipping inside the water.^{14,15} However, a closer examination of the legs (*via* SEM) reveals a surface structure consisting of micron-sized filaments that have a nano-grooved nature (**Figure 1.2b-c**), resulting in a dual-scale roughness.¹⁴ These surfaces are 'a drop in the ocean' of the natural existing creatures with distinctive water repellence emerging from their exceptional structural complexity.

While many reports attempted direct replication of natural surfaces,^{23,24} these examples formed the basis for the vast majority of synthetic superhydrophobic surfaces, as studying these examples and deducing the main structural/compositional factors that are key for high hydrophobicity was intensely reported and widely utilised. It is currently well-established that there are two main requirements for superhydrophobicity: the inherent hydrophobicity of the surface composition and the surface roughness. Materials with low surface energy (i.e. small energy difference between the bulk material and the surface, hence, forming a new solid-liquid interface with water is energetically unfavourable) are known for their water-repellent behaviour. However, the maximum water contact angle (WCA, Section 1.1.2) that can be achieved by a flat, low surface-energy material is $\sim 120^\circ$.^{25,26} This can be increased above $> 175^\circ$ in some cases utilizing the same chemical composition, just by roughening the surface.²⁷ In addition, building a structure with hierarchical roughness, i.e. combining dual-scale texture, is reported to improve hydrophobicity and also enhance surface durability.^{28,29} This was observed in nature (both *Salvinia* leaves and water spider legs featured this) and also in synthetic coatings where micro/nanoscale roughness is applied.

1.1.2. Characterisation of Superhydrophobicity

Several methods have been used to measure surface wettability and differentiate between hydrophilic and hydrophobic surfaces. The most commonly utilised is WCA measurement. The WCA of a surface is measured from the surface-water contact plane to the tangent line of water-air contact. A surface is defined as hydrophilic when $\theta < 90^\circ$, and as superhydrophilic when $\theta < 5^\circ$. These surfaces favour the interaction with water which results in extended wetting and low contact angles. In contrast, hydrophobic and superhydrophobic surfaces resist water spreading and are defined by contact angles $\theta > 90^\circ$ and $\theta > 150^\circ$, respectively (**Figure 1.3**).³⁰ A maximum contact angle is achieved when the droplet is completely spherical, and a minimum

contact angle is obtained for super-hydrophilic surfaces where the droplet spreads to completely wet the surface.^{21,31}

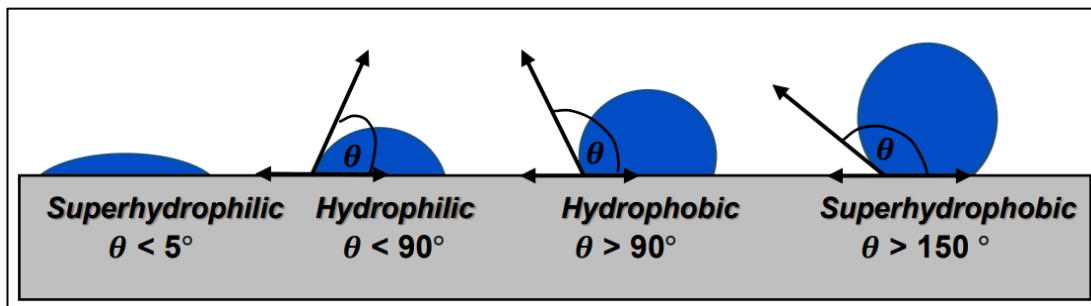


Figure 1.3: Illustration of how the WCA is measured and categories of surfaces based on their WCA values. Figure retrieved from ref.³²

Measuring WCAs is widely reported and accepted as a reliable method to assess surface-water interaction. However, the shape of the water droplet is not reproducible, hence the repeated readings of contact angle can significantly vary (by 20° for some surfaces). This is due to the heterogeneity of the surface, both in topography and chemical composition. In addition, WCAs are generally high for superhydrophobic surfaces irrespective of the surface wetting mechanism (Section 1.2). While some surfaces are found to be ‘slippery’ where the water droplet can hardly remain still on the surface, other surfaces exhibit a ‘pinning effect’, where the droplet sticks to the surface underneath and can be hard to completely remove.³³ Therefore, other methods have been developed to complement WCA measurements.

The measurements of advancing and receding angles have been introduced to differentiate between ‘slippery’ and ‘sticky’ surfaces. When a water droplet is placed on a surface, a range of contact angles could be observed, with maximum (advancing, θ_A) and minimum (receding, θ_R) angles are recorded. There are two different methods to measure θ_A and θ_R ; either by substrate tilting or droplet-volume changing. Advancing and receding angles could be measured by placing a droplet on the surface and tilting the surface gradually. At the point just before the droplet starts to move, θ_A is measured at the front of the droplet (the higher angle) while θ_R is measured at the back of the droplet (**Figure 1.4a**). Alternatively, the droplet could be placed on the surface with a needle/syringe touching the top of the droplet. The needle then is used to inject (or withdraw) water into the droplet. The contact angle of the droplet will increase as a result of volume expansion until reaching a point where the water/air tangent starts to shift while maintaining the same angle (water/air baseline is expanding), which is taken to be θ_A . The receding angle is taken while the

volume is detracted when, again, the water/air baseline is shrinking while the angle remains constant (**Figure 1.4b**).³⁴ The difference between the advancing and the receding angles is defined as contact angle hysteresis (CAH). For highly superhydrophobic surfaces with minimal water pinning, CAH is usually $< 10^\circ$.³⁴

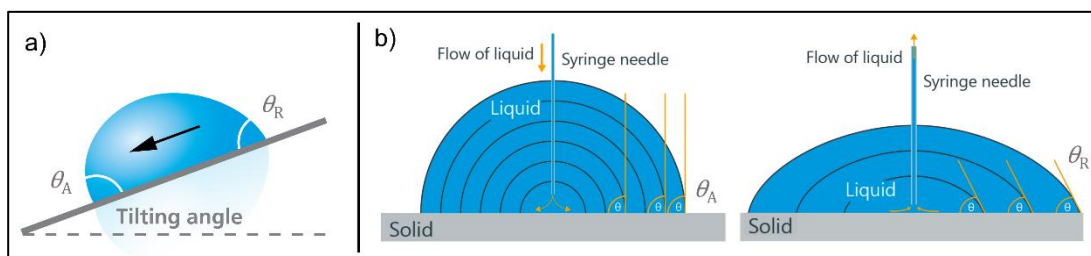


Figure 1.4: Measuring the advancing and receding angles by a) substrate tilting or b) droplet-volume changing. Figure retrieved from a) ref.³⁵ b) ref.³⁶

Alternative methods have been reported for the same purpose. The tilting angle is measured by gradually tilting the substrate and recording the angle at which the droplet starts to move off the surface. Surfaces with high hydrophobicity usually have tilting angles $< 10^\circ$.^{37,38} Water bouncing has been reported, where the number of water bounces on the surface can be linked to the extent of its hydrophobicity.^{39,40} Both methods examine the degree of water-surface adhesion, as a droplet would hardly move off a surface with high water pinning even if the surface is being flipped,⁴¹ and is not expected to bounce off the surface as well.³⁹

1.2. Wetting Models

Due to the relevance of the wettability behaviour of surfaces to their applicability in several fields, it is important to understand and predict the interaction between these surfaces and water. For these purposes, surface wetting models were developed to study the solid/water/air interaction and to predict the wettability mechanism. As demonstrated earlier, the degree of surface hydrophobicity is determined by its WCA. The models discussed here utilise the surface properties to predict the measured contact angle and indicate how the hydrophobicity can be maximised.

1.2.1. Young's Equation

Young's Equation is considered to be the simplest wetting model. It visualises an "ideal surface" that is perfectly flat and chemically homogenous. The model uses interfacial surface tensions/energies (per unit area) to indicate the resultant equilibrium contact angle (**Equation 1.1, Figure 1.5**).⁴²

$$\gamma_{SA} = \gamma_{SL} + \gamma_{LA} \cos \theta_e \quad (1.1)$$

The contact between the droplet and the surface forms a dynamic three-phase contact line. The contact angle (θ_e) is determined when the three interfacial tensions [solid-air (γ_{SA}), solid-liquid (γ_{SL}), liquid-air (γ_{LA})] balance and reach thermodynamic equilibrium. For a surface to show a hydrophobic wetting behaviour, the solid-liquid interfacial energy (γ_{SL}) should exceed the solid-air interfacial energy (γ_{SA}). In this case, the water droplet changes shape to minimise the solid-liquid interfacial area, until the lowest possible energy state of the system is reached. Therefore, large contact angles are observed, reflecting the hydrophobic nature of the solid surface. The reverse is true for hydrophilic wetting behaviour, where contact angles of $\theta < 90^\circ$ and $\theta < 5^\circ$ are seen for hydrophilic and superhydrophilic wetting behaviours, respectively. This is due to the solid-liquid interfacial energy (γ_{SL}) being minimised, favouring surface-droplet contact.

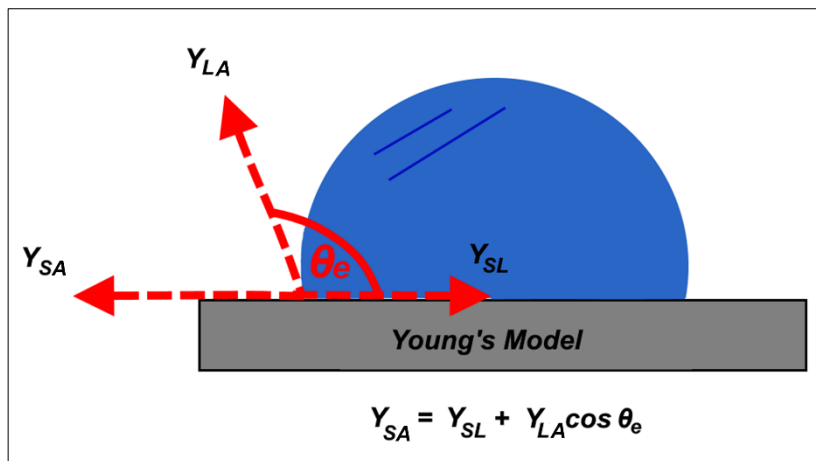


Figure 1.5: Schematic illustrating Young's Model, highlighting the equilibrium contact angle (θ_e) and interfacial surface tensions [solid-air (γ_{SA}),

solid-liquid (γ_{SL}), liquid-air (γ_{LA})] of a static water droplet on a flat surface. Figure retrieved from ref.⁴³

While this model explains the hydrophobic nature of low surface energy surfaces, the idealised presentation of the surface hardly exists, as chemical homogeneity and surface flatness are not commonly achieved. Surfaces generally vary in composition and properties, and therefore, usually contain surface defects, impurities and/or some extent of surface roughness.⁴⁴ In addition, this equation does not explain how the observed contact angle of a surface can be increased solely by introducing a degree of roughness, without changing the chemical composition (Section 1.1.1). This is due to Young's equation not accounting for any heterogeneous contact beneath the

droplet. Alternative wetting models have been proposed to elucidate the wetting behaviours of real-life solid surfaces.^{45,46}

1.2.2. Wenzel Model^{46,47}

A correction factor has been introduced to account for surface roughness, which is referred to as the roughness factor. This factor differentiates between the projected surface area, which is the area of solid-liquid contact assuming surface flatness, and the actual surface area, which accounts for the additional contact areas caused by protrusions/surface structuring (**Figure 1.6**). This factor (r) is defined by **Equation 1.2**:

$$r = \frac{\text{Actual surface}}{\text{Geometric projected surface}} \quad (1.2)$$

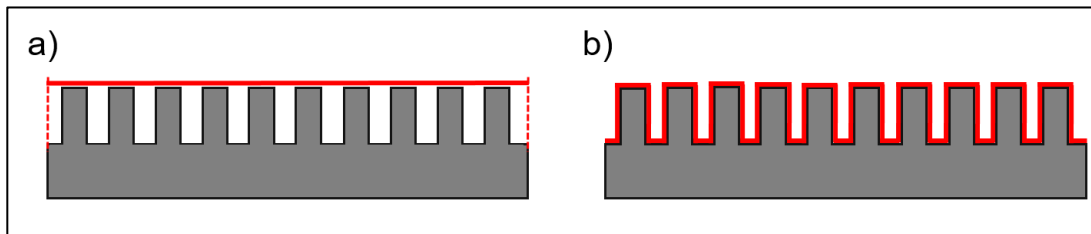


Figure 1.6: A 2D Illustration of the difference between a) the geometric projected surface area and b) the actual surface area. The red line represents how the area is measured in both cases.

The Wenzel model assumes a complete wetting of the rough surface, meaning that no air is trapped underneath the droplet (**Figure 1.7**). Wenzel model has been used to relate surface wettability to both the surface interfacial tensions and the surface roughness through the direct inclusion of a roughness factor (**Equation 1.3**):

$$\cos \theta_w = r \cos \theta_e = \frac{r (\gamma_{SA} - \gamma_{SL})}{\gamma_{LA}} \quad (1.3)$$

Where θ_w is the Wenzel contact angle, and θ_e is Young's contact angle. As the factor (r) is always > 1 for any rough surface, this equation mathematically suggests the surface properties being magnified as it gets roughened, in comparison to its flat analogous. This means that, while the contact angle of a hydrophobic surface will increase when roughened, roughening of a hydrophilic surface will result in a reduction in the contact angle (hydrophobic gets more hydrophobic, hydrophilic gets more hydrophilic). To explain this from a chemistry point of view, the change in the

net free energy of the surface should be considered. It should be noted that the surface tension of the solid does not change by roughening, as this solely depends on the chemistry of the surface material. However, the formation of new interfaces caused by the roughening intensifies the change in the net energy per unit area of the surface.

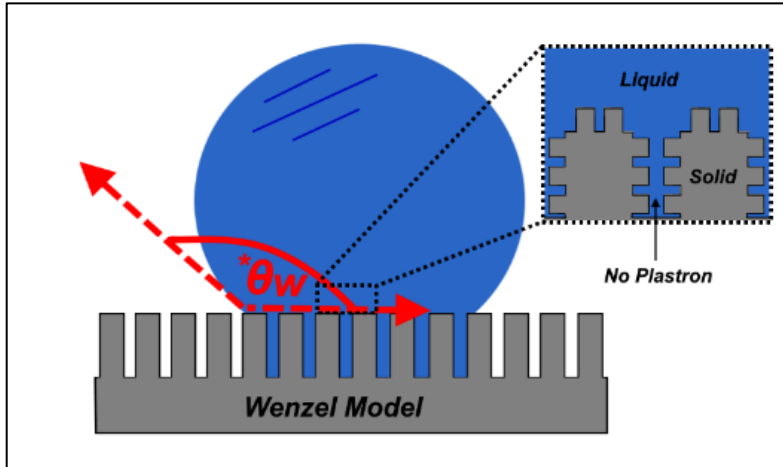


Figure 1.7: Schematic illustrating the wetting of a roughened surface according to the Wenzel model. Figure retrieved from ref.⁴³

Force vectors are used to indicate the change in the surface wetting characteristics upon roughening. These vectors are represented by S_1 (for the solid-vapour interface) and S_{12} (for the solid-liquid interface). The adhesion tension (A) is defined as the difference between these force vectors (**Equation 1.4**):

$$A = S_1 - S_{12} \quad (1.4)$$

For a hydrophobic surface, the solid-liquid interfacial area will be minimised. This requires S_{12} to increase to oppose the wetting, which will result in A having a negative value. The adhesion tension (A) is related to the liquid surface tension (S_2) and the contact angle (θ_e) by **Equation 1.5**:

$$A = S_2 \cos \theta_e \quad (1.5)$$

For a smooth surface, combining these equations gives:

$$A = S_1 - S_{12} = S_2 \cos \theta_e \quad (1.6)$$

Accounting for surface roughness is achieved by multiplying the adhesion tension (A) by the roughness factor (r):

$$rA = r(S_1 - S_{12}) = S_2 \cos \theta_e \quad (1.7)$$

Figure 1.8 demonstrates the force vectors and the adhesion tension. It also illustrates how the net energy change signifies by roughening, as for a smooth surface, a certain surface free energy value is associated with a larger area compared to a rough surface.

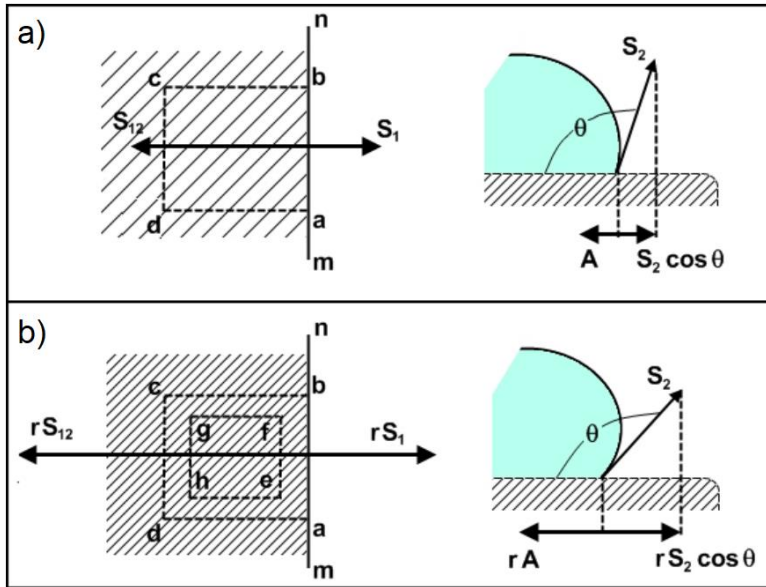


Figure 1.8: Illustration of the force vectors acting on a wetted surface for a certain area (a-b-c-d) in a) a smooth and b) a rough surface. As the change in the net energy is higher in the rough surface (indicated by multiplication by the roughness factor), a smaller area (e-f-g-h) in the rough surface has the same surface free energy as the larger (a-b-c-d) area in the smooth surface. Figure retrieved from ref.⁴⁸

a smaller area (e-f-g-h) in the rough surface has the same surface free energy as the larger (a-b-c-d) area in the smooth surface. Figure retrieved from ref.⁴⁸

1.2.3. Cassie-Baxter Model ^{45,49}

This model also accounts for the surface roughness. Contrary to the Wenzel model where complete wetting is assumed, the Cassie-Baxter model suggests the formation of air pockets underneath the droplet as a result of trapped air not being displaced by wetting. In this model, the solid/air interface in a dry surface is replaced with solid/liquid and liquid/air interfaces when wetted. The areas of these interfaces and the energy associated with them are used to describe the surface wetting behaviour.

For a rough, porous (air retained after wetting) surface, f_1 is the total area of the solid/liquid interface and f_2 represents the same for the liquid/air interface. Upon wetting, an area f_1 of the solid/air interface is removed (an energy $f_1\gamma_{SA}$ is gained), while a new solid/liquid interface is formed in that area (an energy $f_1\gamma_{SL}$ is expended). In addition, a liquid/air interface is formed in an area f_2 (an energy $f_2\gamma_{LA}$ is expended). The net energy E_D expended upon wetting could be expressed using **Equation 1.8**:

$$E_D = f_1(\gamma_{SL} - \gamma_{SA}) + f_2\gamma_{LA} \quad (1.8)$$

To relate the previous equation to Young's model, Young's equation can be rearranged such that the net energy could be related to the contact angle θ_e :

$$\cos \theta_e = \frac{(\gamma_{SA} - \gamma_{SL})}{\gamma_{LA}} = \frac{-E}{\gamma_{LA}} \quad (1.9)$$

Where E is the energy required to form a unit area of the solid/liquid interface. The previous two equations could be used to express the apparent contact angle θ_D in terms of the solid/liquid contact angle and the areas of the solid/liquid and the liquid/air interfaces (**Equation 1.10**):

$$\cos \theta_D = \frac{-E_D}{\gamma_{LA}} = f_1 \cos \theta_e - f_2 \quad (1.10)$$

For a rough but not porous surface (i.e. the surface is completely wetted), the previous equation is reduced to the Wenzel equation ($f_2 = 0$, $f_1 = r$). A water droplet placed on a surface in a Wenzel wetting state exhibits strong pinning, while the trapped air in the Cassie-Baxter wetting state makes the surface 'slippery'.⁵⁰

The Cassie-Baxter model can be used to produce exceptionally accurate results, as it describes a wetted interface in detail. However, a comprehensive understanding of how water interacts with any given surface is hard to achieve, as the exact position of the different interfaces cannot be accurately characterised or predicted, particularly for surfaces that do not have repeating structures. As a result, a simplification to the Cassie-Baxter model was made by assuming that the solid/liquid and the liquid/air interfaces formed upon wetting are flat (i.e. water only wetting the top of any surface protrusions).⁵⁰ This leads to (for a unit area) $f_1 + f_2 = 1$, which could be expressed as fractions of the total planar contact of solid/liquid ($f_1 = \Phi_s$ and $f_2 = 1 - \Phi_s$). The simplified equation is expressed by **Equation 1.11**:

$$\cos \theta_D = \Phi_s \cos \theta_e + \Phi_s - 1 \quad (1.11)$$

The difference between the original and the simplified Cassie-Baxter models in terms of the position of the interface plane is demonstrated in **Figure 1.9**.

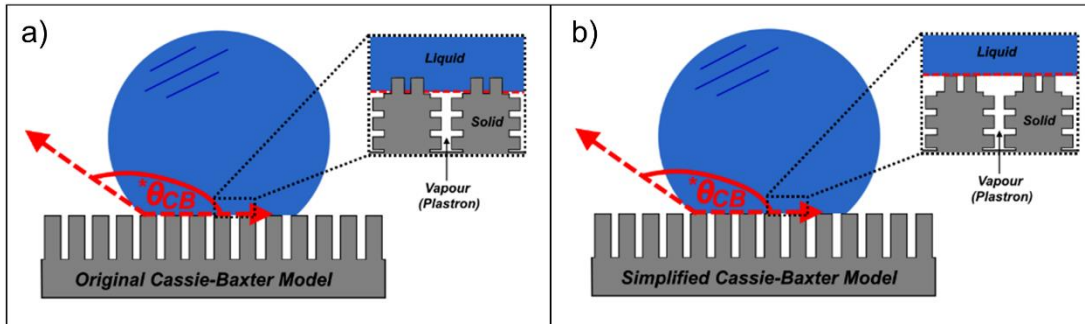


Figure 1.9: Schematic illustrating the wetting of a roughened surface according to a) the original Cassie-Baxter model, where the exact areas of both the solid/liquid and liquid/air interfaces are accounted for, and b) the simplified Cassie-Baxter model, where the interfaces are assumed to be flat. Figure retrieved from ref.⁴³

1.3. Fabrication of Superhydrophobic Surfaces

Methods for generating superhydrophobic surfaces are numerous and follow different fabrication routes. This originated from the wide selection of materials with low surface energy, as well as the variety of approaches for the introduction of surface roughness.^{21,48} A categorisation of these methods can be made based on the approach of constructing surface roughness, which falls into two main categories: i) top-down approaches; in which structuring of the surface of bulk material is attempted to introduce roughness, and ii) bottom-up approaches; where constructing roughness from small-scale material addition is followed.^{32,51} Furthermore, another categorisation can be made by looking into the required treatment of precursor material or the deposited surface. This is noticed for bottom-up approaches, where some coating techniques do not guarantee a rough deposition by the sole act of coating deposition. Hence, careful selection and processing investigation of the coating material is required.^{21,48} **Figure 1.10** presents the two main categories for fabrication approaches. The discussion in this section will follow the same order as illustrated in the figure, starting by mentioning some ‘top-down’ techniques and then moving to ‘bottom-up’ methods where the deposition is intended to roughen the surface. Following this, deposition techniques that do not necessitate the production of rough morphology will be briefly mentioned, while focusing on general methods for material treatment that were reported and combined with these deposition techniques. It is worth noting that this is a simplified description of the reported methods, although many more-complicated fabrication techniques can involve more than one of these routes, depending on the designed surface and the targeted application.

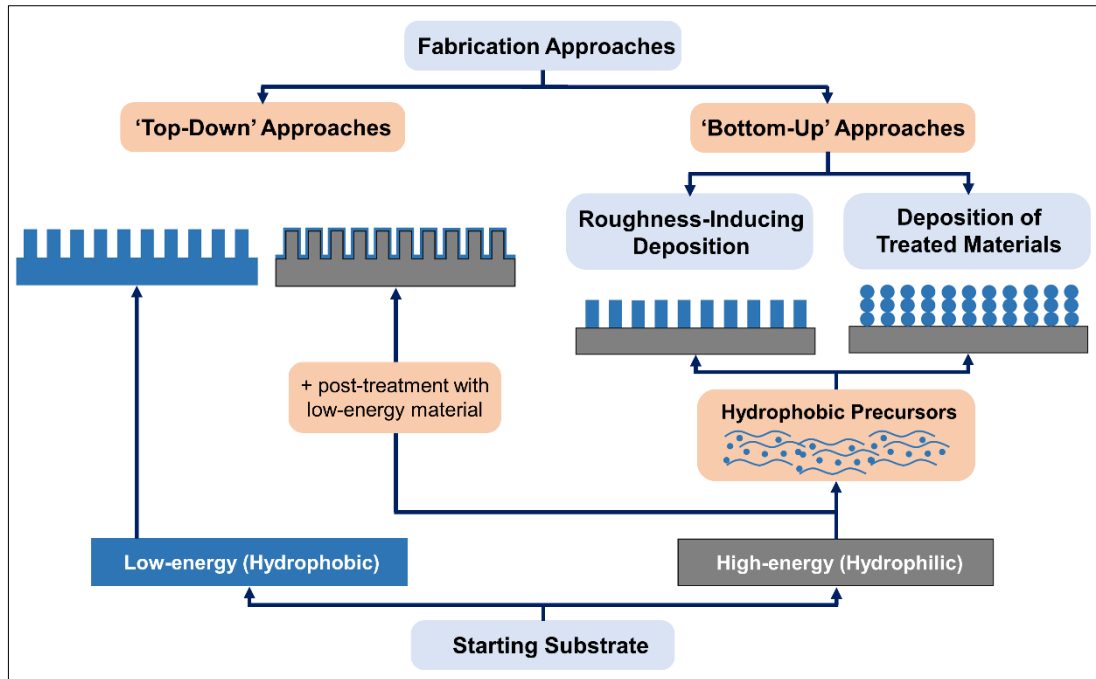


Figure 1.10: Schematic illustrating the approaches for fabrication of superhydrophobic surfaces, and how this can be related to the choice of the starting materials.

1.3.1. Top-Down Approaches

For the approaches discussed in this section, bulk substrates (or material laying on a substrate) are structured to produce rough morphology. This can be done by the selective removal of a hard material, or by imprinting of soft material using a mould. Examples of common 'top-down' techniques applied for the synthesis of superhydrophobic surfaces are presented here.

1.3.1.1. Etching

Etching methods provide a simple approach to increasing the surface roughness of the substrates. In general, etching results in the removal of surface material, either isotopically (i.e. uniform in all directions) or anisotropically (i.e. uniform in a specific direction).⁵² Several variations of etching techniques exist, which can be implemented independently or in combination with other fabrication approaches to generate hierarchical surface texturing. In many cases, the etched substrate is then modified using a low surface energy material to obtain superhydrophobicity.^{32,53}

Etching can be done through chemical routes, which are generally facile and not costly. These involve the removal of substrate material by exposure to harsh (acidic

or basic) solutions. Kim *et al.* reported the synthesis of superhydrophobic stainless steel surfaces by hydrogen fluoride (HF) etching and dipping in a hot 0.1% NaCl solution, followed by fluorination treatment (**Figure 1.11a**). The effect of the HF etching time was studied, and it was found that 20-min etching led to the highest WCA (164°) and lowest sliding angle (5°). The treatment with 0.1% NaCl solution was found to further enhance the hydrophobicity (WCA = 168° , sliding angle = 2°). This was due to the petal-like structures formed on the etched surface, which provided hierarchical texturing. The NaCl dipping time was not found to influence the hydrophobicity or the surface structure, which was attributed to the low solution concentration not causing further interaction after initial corrosion of high energy areas. The surfaces showed retention of superhydrophobicity after 30 days of placing in water.⁵⁴ Several other reports utilised chemical etching while sharing the main two-step procedure. Examples include the etching of stainless steel substrates with sulfuric acid⁵⁵ and ferric chloride,⁵⁶ followed by the modification using octadecyltrichlorosilane⁵⁵ and dodecyltrimethoxysilane,⁵⁶ respectively.

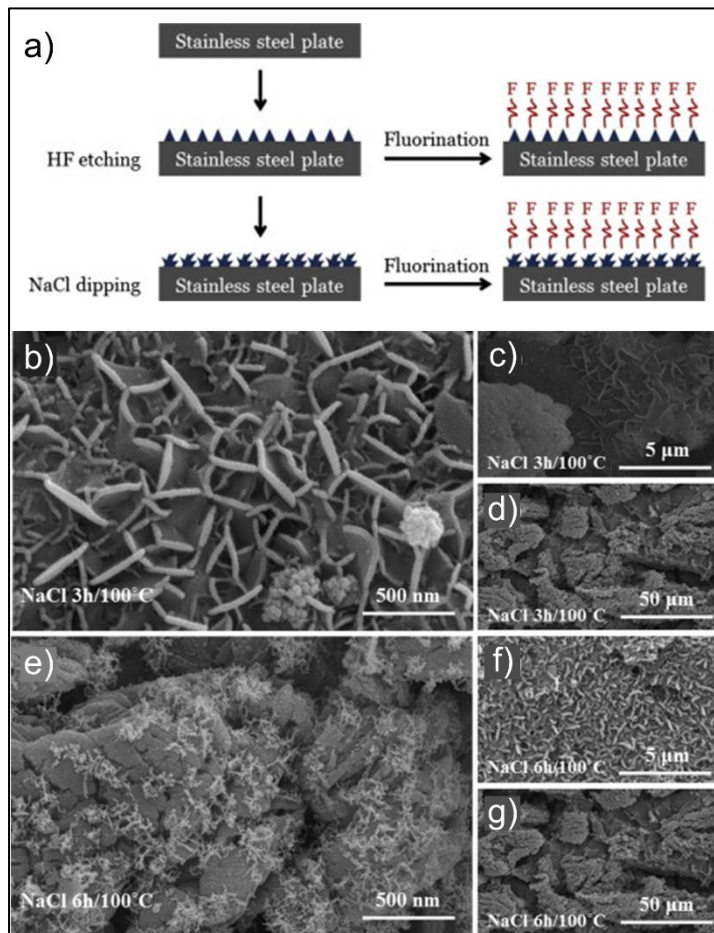


Figure 1.11: a) Schematic illustrating the procedure for etching and treatment of stainless steel substrates. b-g) SEM images of substrates after dipping in 0.1% NaCl solution at 100°C for b-d) 3 hrs and e-g) 6 hrs, showing the petal-like microstructures. Scale bars are shown for each image. Figure retrieved from ref.⁵⁴

While chemical etching is usually straightforward and convenient, it is not considered an environmentally-friendly method due to the large volume of chemicals that are

required to maintain consistent etching. In addition, this method provides limited control over the specifications of the resulting surfaces. Plasma etching is among other techniques that have been established as alternative dry etching technologies of higher precision. Plasma is defined as an ionised gas produced when sufficient energy is provided to a neutral gas, resulting in electrons and charged ions. Plasma etching is based on the removal of material by reactive species that can selectively attack surface material. In some cases, optical masks are applied to facilitate micro/nanopatterning.^{32,57} Takahashi *et al.* investigated the effect of changing the plasma sources on the hydrophobicity and surface morphology of polytetrafluoroethylene (PTFE) surfaces. Ar and N₂ plasma were incapable of generating superhydrophobic surfaces, as the WCAs did not exceed 130° for N₂ plasma-treated surfaces even with increasing the exposure time, while Ar plasma-treated surfaces did not show much improvement compared to the untreated PTFE. Meanwhile, etching with O₂ and CF₄ plasma generated highly nano-scale structured surfaces (porous holes after 1.5 hrs and fibre-like features after 2 hrs exposure to O₂ and CF₄ plasma, respectively). This was reflected in the measured WCAs, which reached ~154° and ~171° for O₂ and CF₄ plasma, respectively.⁵⁸

Barshilia *et al.* reported the utilization of Ar/O₂ plasma for PTFE surface treatment. Combining both Ar and O₂ for plasma generation was found to be beneficial for achieving superhydrophobicity without altering the chemical nature of the surface, which was challenging to maintain using Ar plasma solely. Plasma-treatment time was investigated, and it was noticed that increasing the time resulted in the increased formation of 'leaf-like protrusions' (**Figure 1.12**). This was reversed by reaching 5-hr exposure, which could be caused by re-sputtering that was allowed during the extended reaction period.⁵⁸

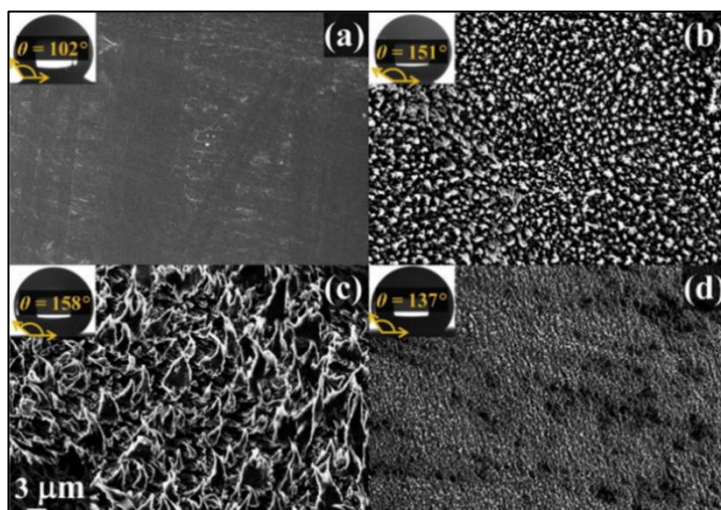


Figure 1.12: SEM images of a) untreated PTFE substrates as well as treated with Ar/O₂ plasma for b) 2 hrs, c) 4 hrs and d) 5 hrs. Insets show WCA measured from the respective PTFE surfaces. Scale bar is indicated. Figure retrieved from ref.⁵⁴

1.3.1.2. Lithography

Lithography is a widely recognised technique for the production of small-scale surface patterning on substrates and thin films. While different types of lithography have been established, the most common is photolithography. The general procedure for this technique involves the coating of the substrate (or the material attached to it) with a thin layer of a light-sensitive photoresist, which is irradiated (by UV, X-ray, electron beam, etc.) through an optical mask prepared with a specific geometric pattern, allowing the transfer of this pattern into the surface. A developing stage is needed to remove the exposed (or the unexposed) material, generating a positive (or a negative) replicate. In many cases, this can be followed by post-treatment with a hydrophobic material (**Figure 1.10**).⁵⁹

Öner and McCarthy reported the fabrication of a series of silicon surfaces with a large range of feature sizes and shapes. This included square posts, varying in size (2-128 μm) and height (20-140 μm), in addition to staggered rhombus-shaped and star-shaped posts (**Figure 1.13**). Post-treatment with different silanization reagents was carried out. The degree of superhydrophobicity of the fabricated surfaces, indicated by measurements of receding angles, was found to be independent of either the post height or the treatment reagent utilised. However, it was affected by the x-y dimensions of the posts as well as the spacing between them, as increasing either of them was found to increase the receding angle and maximise the pinning of the water droplet.⁶⁰

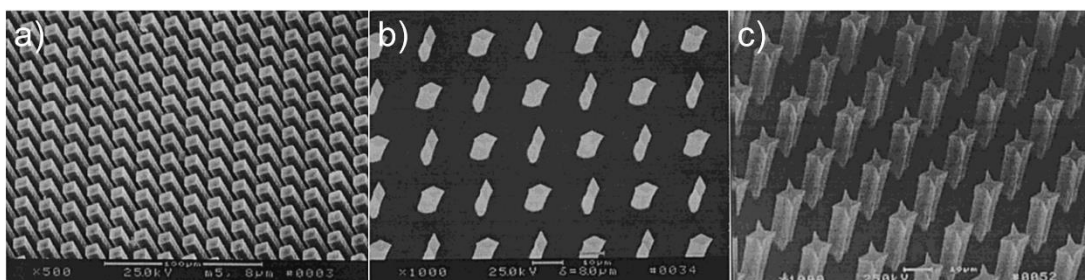


Figure 1.13: SEM images of a) square, b) staggered rhombus and c) four-armed star-shaped silicon arrays fabricated by photolithography. Scale bars are shown for each image. Figure retrieved from ref.⁶⁰

Kim *et al.* reported the utilization of a printed metal mask to produce a structured superhydrophobic surface. This was done by coating a polymer mould with metal using thermal evaporation, which was brought into contact with the photoresist to transfer the metal pattern into the photoresist. The metal photomask, along with

combining resist lens for light focusing, allowed for the generation of smaller-scale patterns (reaching 160 nm-wide pillars) with larger depths ($\sim 1 \mu$).⁶⁰

1.3.1.3. Template Imprinting

Also termed ‘soft lithography’, and shares the main theory with photolithography in terms of creating a replica of a previously-prepared pattern. This technique enables the direct transfer of natural (or synthetic) surface designs by mould-imprinting against a soft material. Inspired by the rough surfaces present in nature, there have been many reports of fabricating patterned rough surfaces utilizing the actual surfaces of superhydrophobic plants *via* moulding (**Figure 1.14a**).^{23,61–63} Nano-casting of polydimethylsiloxane (PDMS) on a lotus leaf was used to generate a negative template (when the PDMS layer is lift-off). The negative template could be cast again with PDMS to make a positive replicate of the leaf microstructures (**Figure 1.14b**).⁶¹ Another report used the negative PDMS template to press against an ‘ink’ of epoxy-based polymer, which, after lift to dry, showed a structure similar to lotus leaf under SEM (**Figure 1.14c**).⁶² Using polyethylene was reported as well, involving pressing against the PDMS template and melting using a vacuum oven (**Figure 1.14d**).⁶³ As a way to make this method scalable for mass-production, a Bamboo leaf was coated with a thin layer of gold, followed by electroforming of a nickel negative template, which could be used multiple times to make a positive replica.²³

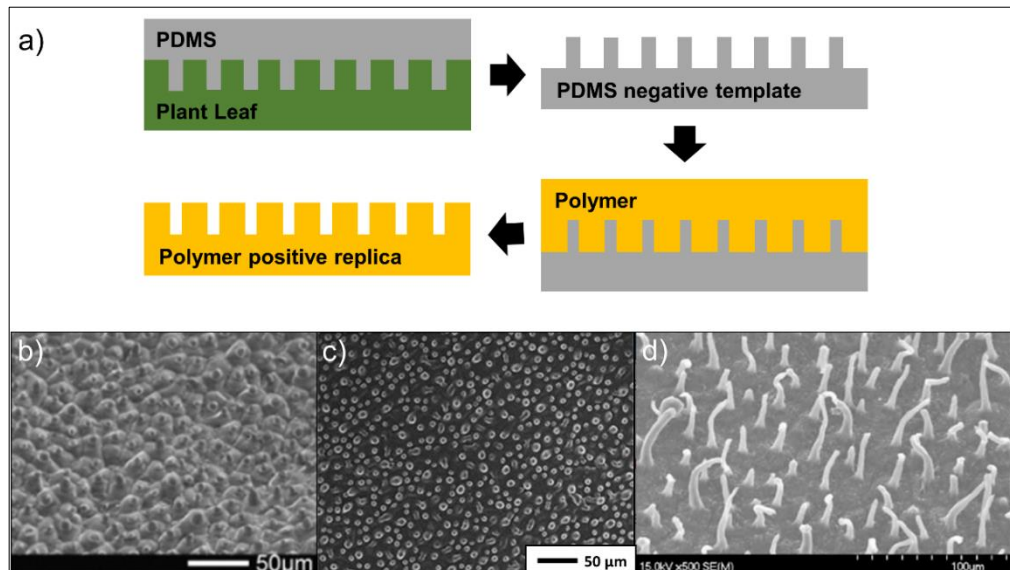


Figure 14: a) A schematic illustrating the procedure of using plant leaf as a template for the generation of rough polymer replicates. SEM of b) PDMS, c) epoxy-based polymer, and d) polyethylene surfaces that were fabricated using lotus leaf as a template. Scale bars are included. Figure retrieved from b) ref.⁶¹ c) ref.⁶² and d) ref.⁶³

Led by the 'leaf mould' approach, the attempts to fabricate a mould without using plants' leaves were investigated. Marzolin *et al.* have fabricated a mould by the micro-printing of hexadecanethiolate on top of a gold-coated silicon wafer, with printed features of $2\ \mu\text{m}$ (**Figure 1.15a**). This mould was used to fabricate a patterned surface of silica by casting silica precursors on the mould and annealing the resulting film after removing the mould at 1100°C . SEM imaging of the silica film has confirmed the formation of patterned micro-features (**Figure 1.15b**).⁶⁴

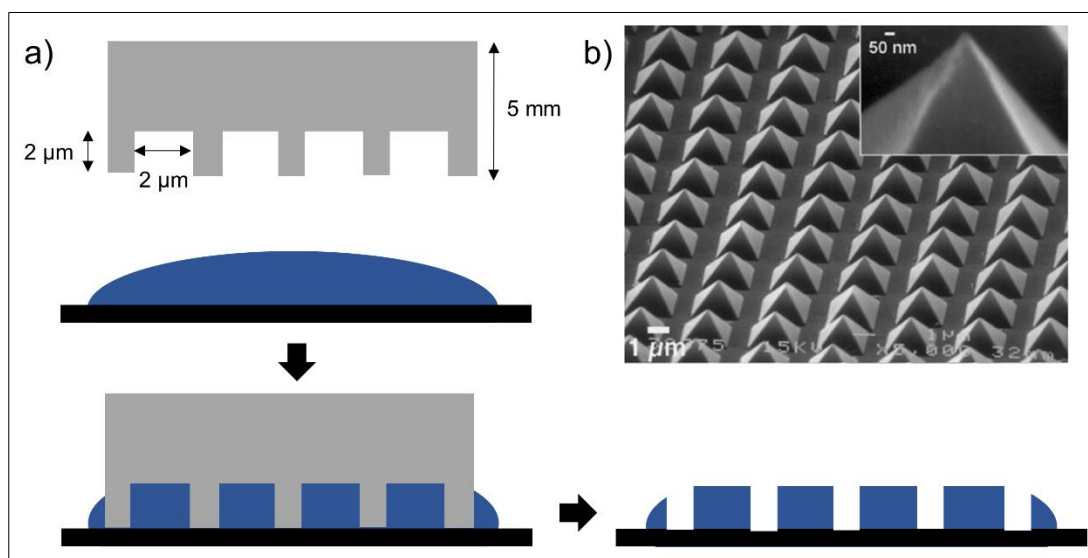


Figure 15: a) A schematic for the mould and the patterned surface fabricated, and b) an SEM image for the obtained silica film. Figure retrieved from b) ref.⁶⁴

1.3.2. Bottom-Up Approaches

In contrast to the previous methods, 'bottom-up' approaches involve the assembly of small hydrophobic blocks to construct a superhydrophobic rough surface. These methods can provide wide flexibility over the chosen starting materials and their processing procedure, depending on the application requirements. This section will give an overview of common examples of these techniques.

1.3.2.1. Rough deposition of hydrophobic material

While the 'bottom-up' categorisation implies the utilization of small-scale hydrophobic building units, the deposition processes can vary in terms of roughness introduction. Some of these techniques ensure a rough surface formation just by the act of deposition, with no further processing required for the starting materials. Common examples of these methods include 3D printing, electrospinning and chemical vapour deposition, which will be discussed here.

1.3.2.1.1. 3D printing

3D printing is a deposition technique that involves a layer-by-layer surface construction and has been reported for superhydrophobic surfaces fabrication. Due to the great control over the construction parameters provided by this technique, it was reported for the replication of the *Salvinia* leaf ‘eggbeater’ structure (**Figure 1.16a**). Multi-walled CNTs were added to the liquid photo-curable resin utilised to increase surface roughness. The number of arms of the eggbeater shape (N), as well as their spacing (d), was investigated for their effect on the superhydrophobic properties (**Figure 1.16b-f**). It was found that the hydrophobicity is maximised when the spacing is kept at $d=0.5$. Moreover, applying $N=2$ resulted in a highly superhydrophobic surface ($WCA = 170^\circ$), although the reduced number of arms made the structures fragile. Applying $N=4$ was found to be a good compromise between both strength and superhydrophobicity ($WCA = 152^\circ$).²⁴

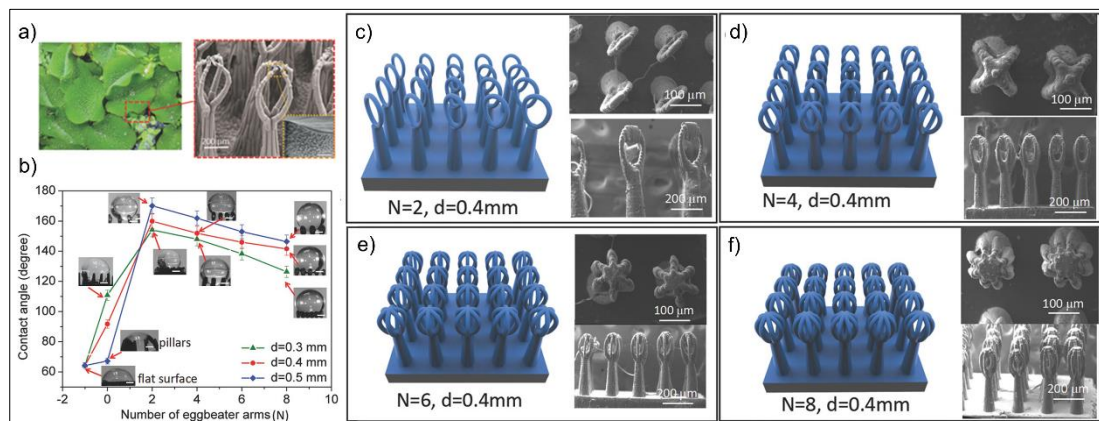


Figure 16: a) the *Salvinia* leaf and an SEM image of the eggbeater hair structure. b) Plot for WCAs of the 3D-printed eggbeater arrays with different numbers of eggbeater arms (N) and spacing (d). c-f) Schematic and SEM images for the prepared surfaces at $d=0.4$ and c) $N=2$, d) $N=4$, e) $N=6$ and) $N=8$. Scare bars are shown for each SEM image. Figure retrieved from a) ref,⁶⁵ and b-f) ref.²⁴

1.3.2.1.2. Electrospinning

Electrospinning involves the application of a strong electric field on a polymer solution (or a polymer melt) to transform it into filaments. These filaments can then be collected to form a nonwoven web. Due to the nano-scale of the electrospun filaments, as well as the simple fabrication produce, electrospinning was reported for the synthesis of superhydrophobic filters and membranes.⁶⁶

Ren *et al.* reported the electrospinning of superhydrophobic PDMS/polymethyl methacrylate (PMMA) membranes for water desalination. The effect of electrospinning parameters, like the applied voltage, injection rate, polymer solution concentration and PDMS/PMMA mass ratio, on the membrane morphology and hydrophobicity, was investigated. The membrane demonstrated an excellent salt rejection efficiency of 99.96%.⁶⁷ Cho *et al.* demonstrated the electrospinning of isotactic polypropylene from both a melted polymer and a heated polymer solution.⁶⁸ Lee *et al.* prepared a superhydrophobic oil/water separation filter by electrospinning of polystyrene onto a stainless steel mesh.⁶⁹ Moreover, the introduction of zinc oxide (ZnO) nanoparticles as an additive to the electrospinning polyvinylidene difluoride (PVDF) solution was reported by Liu *et al.* The effect of ZnO addition was observed in the increased average diameter of the electrospun fibres (from 127 nm for pure PVDF membrane to 1.8 μm for PVDF/10 wt.% ZnO), which is attributed to the increased viscosity of the polymer solution. In addition, this introduced hierarchical roughness which resulted in a recorded WCA of 171° (**Figure 1.17**).⁷⁰

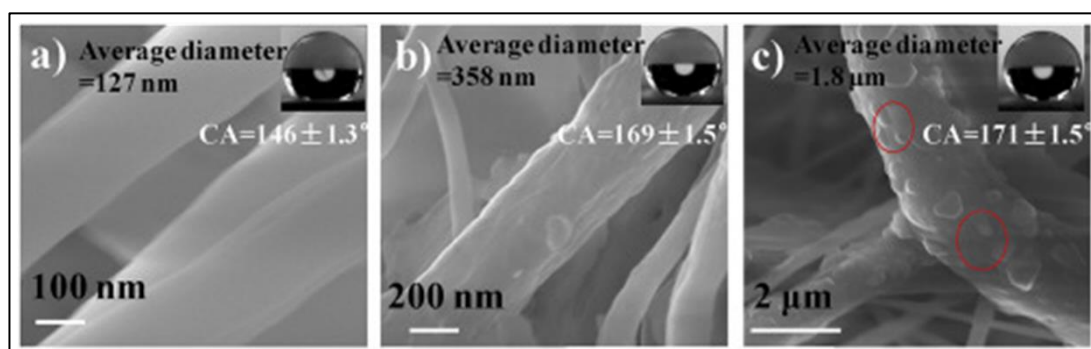


Figure 17: SEM images of a) pure PVDF membrane, b) PVDF/5 wt.% ZnO membrane and c) PVDF/10 wt.% ZnO membrane. Insets show WCA measured from the respective membrane. Scale bars are shown for each image. Figure retrieved from ref.⁷⁰

1.3.2.1.3. Chemical vapour deposition

Chemical vapour deposition (CVD) involves the deposition of gaseous-phase precursors to form a solid product.⁷¹ The reactants should be supplied in the vapour state, which requires a vaporization step for non-gaseous reactants. The reactants then get transported, generally by a pressure gradient or a carrier gas, into the substrate where the reaction takes place and solid-film formation happens. Heating is generally used to initiate the reaction, and any unreacted material gets extracted from the system.⁷²

In general, the standard mechanism for CVD tends to produce flat, chemically homogenous coatings.⁷² Therefore, the roughness development for surfaces prepared using this technique is usually introduced by two approaches: i) introducing a modified method of CVD that allows rough deposition or ii) pre- (or post-) treatment of the precursor, substrate and/or the generated coating. The second approach would fit more the description of the 'Deposition of the treated materials' discussed in the following section, but the technique has been mentioned here as the generation of rough surfaces without utilizing treated materials is still achievable.

Several CVD techniques were developed to control the morphology of the deposited coatings. For example, pulsed plasma-enhanced CVD (PECVD) was reported by Yang *et al.* for the deposition of rough PTFE using hexafluorobenzene as a precursor. Films prepared at a decreased plasma pulse duration were found to be highly superhydrophobic (WCA over 160°), which was attributed to the longer plasma-off period allowing more time for radicals to collide and form more particles leading to rough PTFE films (**Figure 1.18**).⁷³

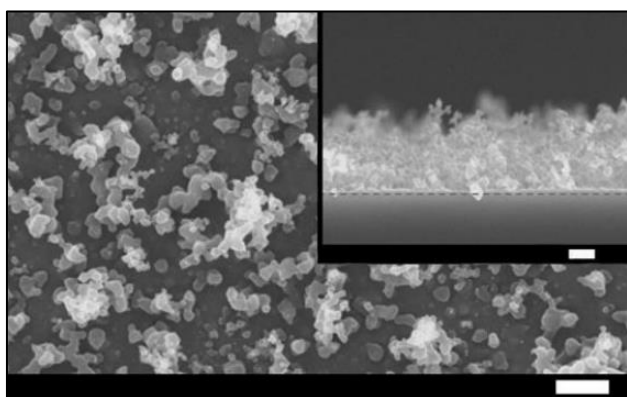


Figure 1.18: SEM of a superhydrophobic PTFE surface deposited using pulsed PECVD. The pulses of plasma were required for the material to agglomerate during the deposition of the film (scale bars = 1 μm). Figure retrieved from ref.⁷³

Nanostructured films using trimethylmethoxysilane precursor were deposited using another version of PECVD which involves microwave utilization (MWPECVD). The films were characterised by their superhydrophobic nature, rough structure as well as transparency.⁷⁴ These films were also reported for the synthesis of hydrophobic-hydrophilic templates, where MWPECVD was used to fabricate the superhydrophobic films and the masked exposure to vacuum ultraviolet irradiation created the heterogeneity in surface-water interaction.⁷⁴

Atmospheric pressure CVD was used for the deposition of tungsten diselenide (WSe_2) onto glass substrates. A structure of perpendicularly-oriented thin needles was observed, which led to recorded WCAs up to 145° and a Wenzel wetting behaviour (with no sliding even at a tilt angle of 90°).⁷⁴ Furthermore, aerosol-assisted

CVD was reported for the deposition of rough thermosetting polymer coatings, which is discussed in more detail in Section 2.1.

Alternatively, other reports combined CVD deposition with the choice of a rough mesh,⁷⁵ a plasma-etched copper substrate,⁷⁶ as well as growing over carbon fibres⁷⁷ to add a micro-roughness level. Controlled deposition of CNT films was achieved by depositing over silicon templates with a well-defined quadrate micro-pillar array,⁷⁸ as well as by chemical functionalization of CNTs with perfluoroarylazide groups to force patterns deposition.⁷⁹

1.3.2.2. *Deposition of the treated materials*

While the previous methods led to the generation of rough surfaces, other 'bottom-up' techniques were reported for superhydrophobic surface fabrication. These include some basic and conventional methods, like spray coating, dip coating and spin coating. However, a simple utilization of hydrophobic material (e.g. polymer) with any of these techniques will not make a superhydrophobic surface, as these methods generally make smooth coatings. Therefore, materials should be carefully chosen/combined so that the roughness formation is facilitated. This can be achieved by starting with micro/nanoscale hydrophilic particles and adding a hydrophobic component (either by chemical functionalization or physical mixing), or by choosing the hydrophobic material and finding a suitable roughening agent for it.

While the discussion in this section so far was focused more on the techniques themselves, here, the focus will deviate to looking over general approaches for material selection and processing that have been reported for coatings deposited *via* the basic deposition methods. This is to shed light on an important area in superhydrophobic surfaces research that is widely reported and involved in real-life applications. The processing methods discussed here will be categorised under two sections: i) covalent functionalization, and ii) physical treatment.

1.3.2.2.1. *Covalent functionalization*

The treatment of roughening particles has been heavily reported, which led to expanding the selection of coating materials to include some naturally hydrophilic precursors. SiO₂ and TiO₂ particles are commonly used for superhydrophobic coating fabrication, which are frequently prepared, along with other metal oxides, *via* the sol-gel method. Sol-gel involves the conversion of metal alkoxides precursors into a colloidal solution through a series of hydrolysis and condensation reactions, followed

by progression into making integrated networks (**Figure 1.18**).^{80,81} The particles generated *via* this method, although highly homogenous and easily controlled through the reaction conditions, do not show hydrophobicity due to the hydroxyl groups covering the particle's surface. While some reports utilised a co-precursor with one or more hydrophobic groups to reduce the number of the hydroxyl groups,⁸² the hydrophobicity was found to be dependent on the ratio of hydrophobic/hydrophilic groups present on the particle surface, which may be insufficient to demonstrate water repellence.⁸³ Post functionalization, both for particles prepared by one or more precursors, has been reported to enhance the hydrophobicity (**Figure 1.18**).⁸²

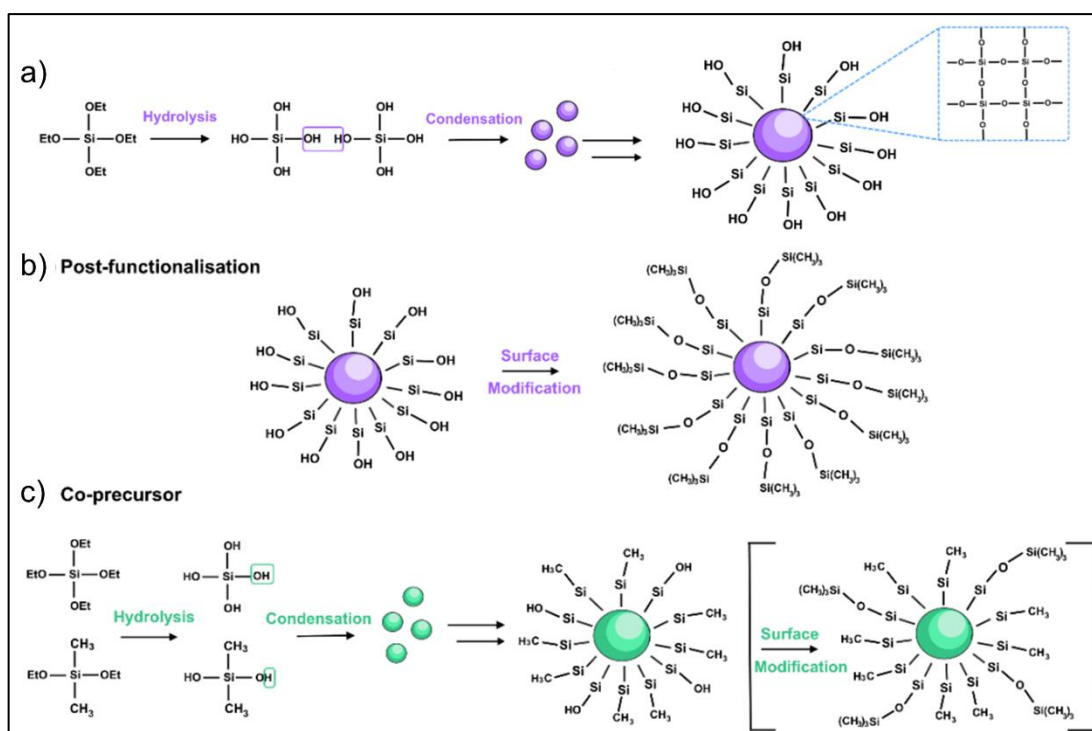


Figure 1.18: Illustration of SiO₂ nanoparticles synthesis using the sol-gel method involving a) tetraethylorthosilicate (TEOS) precursor and b) showing possible post-treatment with hexamethyldisilazane (HMDS). Another route for the synthesis is shown c) by combining dimethyldiethoxysilane with TEOS as a co-precursor with two hydrophobic groups, which can also be followed by further surface modification for the remaining hydroxyl group. Figure retrieved from ref.³²

Different functionalization routes have been reported, including the utilization of fluorinated compounds due to their great water repellence. Fluoroalkylsilane (FAS) molecules are commonly used for particle modification, which consists of a long fluorinated alkyl chain attached to a functional group that can undergo hydrolysis (like Si(EtOH)₃ and Si(Cl)₃). Activated by hydrolysis, the FAS molecules can replace the hydroxyl group covering the particle's surface through a condensation reaction, and

render the surface hydrophobic (**Figure 1.19**).⁸⁴ FAS-functionalization of TiO₂ nanoparticles was reported by Lu *et al.* for the formation of a spray-painting suspension, where the coated surfaces demonstrated a self-cleaning effect even after being contaminated with oil.⁵ Coating of SiO₂, Al₂O₃ and SiO₂/TiO₂-hybrid nanoparticles with FAS was also reported and proven capable of generating highly superhydrophobic surfaces.^{85–87}

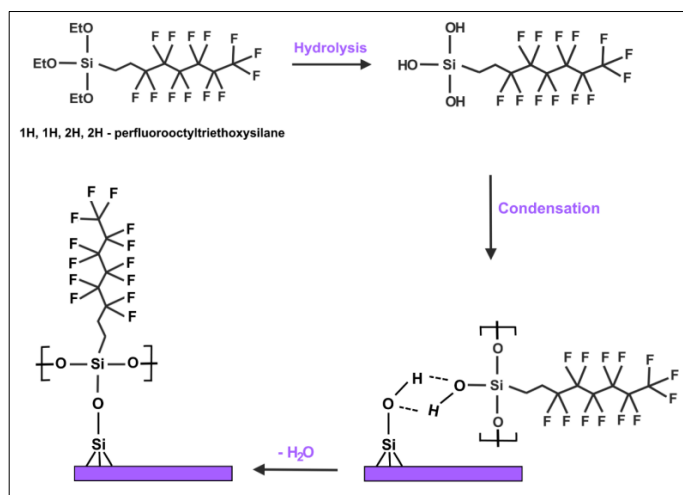


Figure 1.19: Illustration of the functionalization mechanism of SiO₂ nanoparticles with FAS (typically the figure shows 1H, 1H, 2H, 2H-perfluorooctyltriethoxysilane). The surface with the silanol groups represents the surface of the SiO₂ nanoparticles. Figure retrieved from ref.³²

Despite the excellent performance of FAS-modified coatings, attempts to find alternatives for fluorinated compounds are encouraged, due to their environmental incompatibility.⁸⁸ A common example that is widely reported for SiO₂ functionalization is HMDS (**Figure 1.20**).^{89–91}

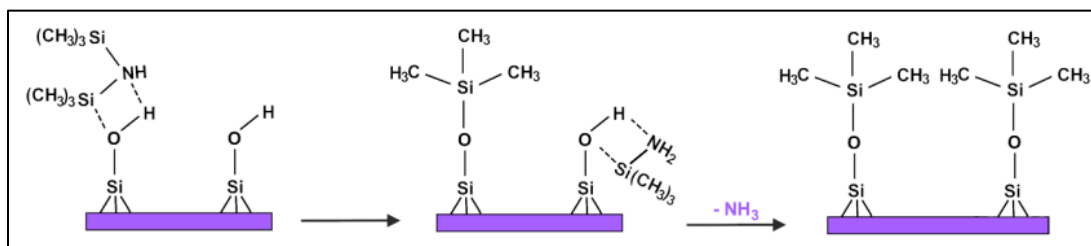


Figure 1.20: Illustration of the proposed functionalization mechanism of SiO₂ nanoparticles with HMDS. Figure retrieved from ref.³²

Due to the triple-branched CH₃ groups that replace the hydroxyl groups during functionalization, the surface of the nanoparticles becomes covered with a dense layer of hydrophobic groups.⁹² This surface coverage can be also achieved by utilizing long linear hydrocarbon chains, although the length of the chain should be carefully considered. Wang *et al.* demonstrated this by using smooth and roughened copper surfaces with self-assembled monolayers of *n*-alkanoic acids [CH₃(CH₂)_{*n*}COOH, *n* = 1-16] with varying chain lengths, and investigated the effect this had on the

hydrophobicity of the surfaces. For the roughened surfaces, a WCA of $\sim 0^\circ$ was observed for $n = 1$, while it was sharply enhanced with increasing the chain length until reaching $\sim 160^\circ$ for $n \geq 9$. Meanwhile, the smooth surface showed a similar trend, although the WCA changed less dramatically (from $\sim 70^\circ$ to 113°), as eliminating the surface structuring reduces the extent of both hydrophilic and hydrophobic properties (in agreement with the Wenzel model, Section 1.2.2).⁹³

The previous discussion presented approaches for altering the surface chemistry of rough precursors. Meanwhile, there were other approaches reported for roughening hydrophobic materials by covalent linking. Examples include in-situ growing nanoparticles into porous polymer membranes,⁹⁴ and utilizing polymers with specific building blocks that can undergo hydrolysis/condensation reactions to chemically bond with silicates.⁹⁵

1.3.2.2.2. Physical treatment

In contrast to the examples demonstrated in the previous section, other fabrication methods rely on intermolecular interactions, rather than covalent bonding, to generate roughened hydrophobic coatings. The advantage of this approach is its extended applicability to a wider range of polymers/particles that can be incorporated, as the requirements for the presence of specific functional groups become unnecessary.

A common example of the physical treatment for introducing roughening/hydrophobicity is through incorporating polymers/nanoparticles composites. Upton *et al.* developed an array of Superhydrophobic polymer/nanoparticle composites (SPNCs) formulations that can be deposited through both solution-based (i.e. spray/dip-coating) and solvent-free (i.e. heat pressing) techniques. The general principles for designing SPNC systems were outlined, like the optimum polymer/nanoparticle mass ratio (**Figure 1.21**), the effect this has on the hydrophobicity, self-cleaning properties and UV stability, and how this differs for thermosetting and thermoplastic polymers. A range of polymers (PDMS, polyethylene, polyvinyl chloride and polypropylene) and nanoparticles (SiO_2 , TiO_2 and CeO_2) were incorporated, which was done by simple stirring using a compatible solvent.⁹⁶ In another report, it was shown that $\text{TiO}_2/\text{CeO}_2/\text{PDMS}$ coatings demonstrated an improved UV stability compared to $\text{TiO}_2\text{-FAS}$ and $\text{CeO}_2\text{-FAS}$ coatings.⁹⁷ The resilience of these coatings can be improved by incorporating reinforcement additives. This was demonstrated for heat-pressed HMDS-modified- SiO_2 /polyethylene where carbon nanofibers were utilised and the SPPC formulation

was adjusted accordingly. The coatings survived over 100 abrasion cycles, as well as retained hydrophobicity after 28 days of underwater submersion.⁹⁸

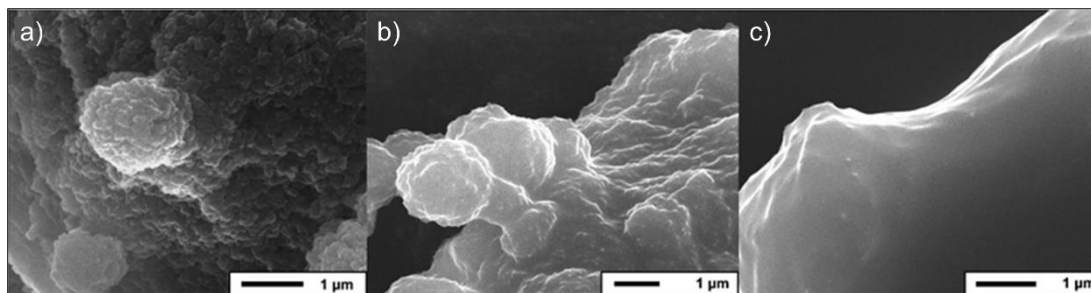


Figure 1.21: SEM images of SiO₂-PDMS SPNCs deposited *via* spray coating from a hexane solution. The images illustrate how the surface roughness changes with changing the polymer thickness (polymer/SiO₂ ratio). Typical polymer thicknesses for these images are a) 6 nm, b) 8 nm and c) 10 nm. Scale bars are shown for each image. Figure retrieved from ref.⁹⁶

Moreover, the incorporation of silica nanoparticles with PDMS has been reported intensively. This can take various forms, examples include: silica nanoparticles forming a sphere-core and coated with a hydrophobic polymer layer to improve their adhesion to the PDMS layer⁹⁹, added with different sizes to increase the degree of roughness¹⁰⁰, or incorporated with the polymer in a layer-by-layer manner¹⁰¹. All these methods have been proven to add to the surface hydrophobicity by increasing surface roughness.

1.4. Applications of Superhydrophobic Surfaces

Owing to the distinguished water interaction that is demonstrated by superhydrophobic surfaces, they have been involved in many application fields. This section discusses a few of the main applications of these surfaces.

1.4.1. Self-Cleaning Surfaces

Driven by the first natural inspiration for superhydrophobicity, the Lotus leaf and its self-cleaning mechanism, attempts for replicating this mechanism for synthetic surfaces have been widely investigated. Factors affecting the self-cleaning efficiency have been studied by Bhushan *et al.* including the surface hierarchy, size of dirt particles, tilting of the substrate and the pressure of the falling water. It was found that larger dirt particles are easier to be removed, while the surface generally needs to be tilted above its water sliding angle for the self-cleaning action to take place. Hierarchical surfaces showed the best performance. Moreover, the impact pressure of the water droplets was found to affect the dirt removal efficiency, as droplets hitting

the surface with higher impact pressure allowed removal of dirt particles laying both on the top surface and inside the air pockets, while only superficial removal can be achieved using low-pressure impact (**Figure 1.22**).¹⁰²

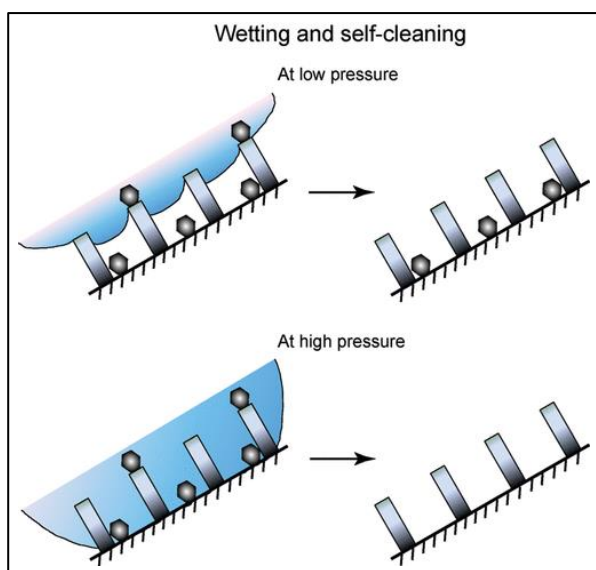


Figure 1.22: Schematic illustrating the dirt-removing mechanism by water droplets hitting the surface with different impact pressures. While the low pressure resulted in picking up dirt articles on top of the surface, high-pressure impact allowed droplets to pick up additional dirt particles laying inside the air pockets. Figure retrieved from ref.¹⁰²

Self-cleaning coatings have been widely studied, and currently, many coating formulations are commercially available and can be applied to a wide range of surfaces, including glass windows, outdoor glass surfaces, fabrics, shoes, etc.). Examples of these commercial products include Lotus-Effect®, Aeroxide® LE, NeverWet and Ultra-Ever Dry.³²

1.4.2. Surface Protection

The high water-repellence demonstrated by superhydrophobic coatings can be applied to surfaces/applications where water exposure needs to be avoided. This can be a result of the material's sensitivity to water (i.e. promotes degradation or corrosion), or if the water presence causes functionality blocking/reduction (i.e. fouling, bacterial adhesion, fog condensation or ice formation).^{103–105} Many reports have attempted to address these needs. Pan *et al.* developed a PMMA/hydrophobic SiO₂ nanoparticles mixture that was sprayed on steel surfaces. The surfaces showed excellent anti-corrosion behaviour, as well as anti-icing as the surfaces resisted ice-layer formation while placed in humid conditions at - 20°C.¹⁰³ While the reported examples are too numerous to cover here, examples for superhydrophobic coating of a class of water-sensitive materials, metal-organic frameworks (MOFs), will be discussed in Chapter 6.

1.4.3. Drag Reduction

Around 12% of the world's transportation energy consumption is spent on marine transportation, meanwhile, 60% of this energy is used to overcome frictional drag. Frictional drag takes place as a result of materials travelling through fluid phases. This leads to larger fuel consumption to overcome drag forces and, hence, costly transport and more CO₂ emissions. Reducing these forces would greatly benefit both the environment and economy, which can be achieved through the involvement of a superhydrophobic surface.^{106–108} This is not solely caused by their low surface energy, but mainly due to the trapped air in surfaces demonstrating the Cassie-Baxter state which reduces solid-water contact.^{43,53}

Wang *et al.* conducted a sailing test to demonstrate the effect of superhydrophobic coating on reducing drag forces. A steel ship model was spray-coated with a suspension of PMMA/nano-SiO₂, and compared its average speed in water to an uncoated ship, which was found to be significantly higher (**Figure 1.23**).¹⁰⁹ Zhang *et al.* applied chemical etching to produce superhydrophobic materials for drag reduction studies. The produced surface consisted of ZnO nanowires on steel substrates and exhibited drag reduction between 40-50% compared to untreated surfaces.¹¹⁰ Since the drag reduction effect is directly related to the trapped air, many reports investigated different structural factors that can influence the longevity of the air layer, like the random/ordered topography,^{111,112} single-scale/hierarchical texturing,¹¹³ as well as the size of the air pockets (i.e. spacing between features).¹¹⁴

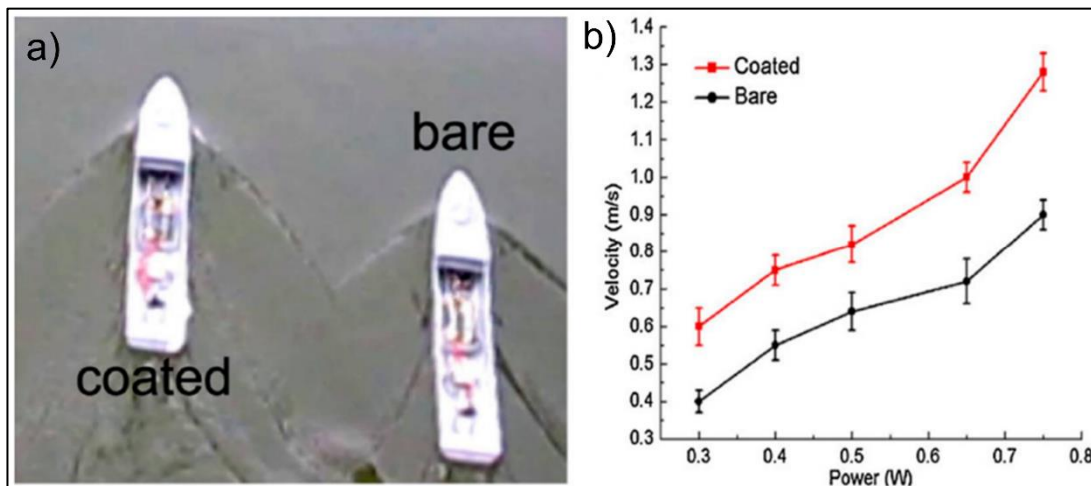


Figure 1.23: a) Sailing experiment for coating/uncoated ship models at a powder supply of 0.5 W. b) Plot for the velocity vs. power supply for both ship models. Figure retrieved from ref.¹⁰⁹

1.4.4. Oil-water Separation

Oil contaminated water is a significant environmental hazard that has a huge effect on the marine ecosystem and can cause an additional threat to many biological species.^{115,116} The release of oil into the environment can result from waste produced by many industries, as well as leakage during oil drilling/transportation.¹¹⁵ Many designs have been reported for the synthesis of superhydrophobic materials to separate oil from water, these include oil skimmers,¹¹⁷ sponges,^{118–120} meshes,^{121,122} foams^{123,124} and selective filters.^{125,126} The common feature in all these designs is the ability for materials/devices to interact differently with oil and water. This leads to oil being absorbed and separated, while water is unselected.¹²⁷

High oil/water separation efficiencies have been widely achieved for various materials, with many exceeding a 97% efficiency value.^{128–130} A common approach utilises metallic meshes, as they provide mechanically strong porous structures and can be treated to control their wetting properties.¹³¹ This includes the controlled growth of ZnO on stainless steel meshes to create superhydrophobic and superoleophilic filters, where both high WCA ($\geq 152^\circ$) and high separation (above 99%) were achieved.^{132–134} Textiles have been investigated due to their desirable low-cost, light-weight, and inherently rough microstructure, where polymer coating of fibres is reported as a surface-modification approach.^{135,136} Selective absorbent materials with a high proportion of oil intake have also been developed in many forms and utilizing different materials, this includes; CNT aerogels,¹³¹ graphene oxide nanosheets,¹³⁷ and polymer sponges.¹³⁸ In addition, films fabricated by heat-treating hydrophobic polymer powder have been reported to efficiently separate oil from water in harsh conditions.¹³⁹

1.5. Factors Limiting Wider Applicability of Superhydrophobic Surface

As demonstrated in the previous section, the unique interaction of superhydrophobic surfaces with water results in many desirable properties that are beneficial in several applications. While a considerable amount of research has been conducted to produce superhydrophobic surfaces using a broad spectrum of materials, fabrication methods, resultant properties, and wide-ranging targeted applications, the impact of these surfaces on everyday materials is currently limited. This is attributed to many factors, which can be divided into two main categories: issues concerning the fabrication of the superhydrophobic surfaces, and problems with their efficiency/durability while utilised in the targeted applications. This section outlines a

brief overview of the current challenges standing against the wider applicability of superhydrophobic coatings.

1.5.1. Fabrication Approaches and Scaling-Up Restrictions

Many synthetic routes have been developed and reported for the fabrication of superhydrophobic surfaces that were successful on the laboratory scale. However, this does not necessitate suitability at the industrial scale, as many issues can arise when scaling-up is attempted. This is related to most of the synthesis main components/steps (i.e. materials, fabrication method, conditions, post-processing, etc.), which makes scaling up even more challenging.

The chosen materials, while potentially providing good hydrophobicity and acceptable performance, can be cost-ineffective and/or cause environmental concerns. Meanwhile, several applications involve additional restrictions on the utilised materials, especially those that involve direct contact with food (food packaging, coating of carton drinks bottles, paper straws, etc.). This hinders the extension of many of the reported coatings into these fields due to the unsuitability of their chemical composition.¹⁴⁰ As an example, fluorinated alkyls are known for their low surface energy and are widely reported for the fabrication of superhydrophobic coatings,^{141–143} although long-chain fluorocarbons are potentially toxic to humans.¹⁴⁴ Another factor is that, while the hydrophobic components themselves can be safe, they may require dissolving to facilitate the processing, which could necessitate the utilization of toxic solvents and, hence, inconvenient disposing precautions.¹⁴⁵

The fabrication procedure can also involve many problems, despite the variations in the reported methods that allow some degree of flexibility. Surfaces that are constituted from a patterned roughness or *via* deposition of ordered textures usually involve the utilization of complex and high-tech equipment. This can be difficult, expensive and time-consuming if the surfaces are enlarged. This issue is intensified when dual micro-nano scale roughness is considered, as this requires higher resolution equipment, adding another layer of complexity and leading to higher cost and longer time needed. In addition, these synthesis techniques may have restrictions on the utilised materials, which adds another burden and reduced the materials choices even more.¹⁴⁶ On the other hand, random deposition of roughness features, while is generally simpler and involve more basic techniques, can maximise chemical heterogeneity in the fabricated surfaces. This is due to the reduced control over the coating process, and can lead to inconsistency in the coating behaviour and creates defective regions that facilitate surface degradation.

For both synthesis approaches (patterned and random deposition), other factors originate from the deposition conditions. Multi-step fabrication routes are common in literature. However, some of them involve too complex steps that hinder wider applicability.^{147,148} In addition, heating the substrate to 'bake' the deposited coating is essential for many procedures, although it adds a costly step as well as limits the choices of applicable substrates depending on the applied temperature.¹⁴⁹

The realization of these issues is growing and has led to new research scopes that aim at generating superhydrophobic surfaces *via* more 'industry-friendly' routes. Some reports attempted to reduce the quantity of the utilised solvent,¹⁵⁰ replace it with another more suitable alternative¹⁴⁵ or by selecting a coating method where the need for a solvent is eliminated.¹⁵¹ Other reports succeeded in using water-based solutions,¹⁴² of which were also combined with incorporating fluorine-free polymers,^{88,152} plant-based materials¹⁵³ and even edible polymers.^{140,154} Regarding the fabrication methods/conditions, eliminating the need for heating has also been introduced to facilitate a wider-scale application.¹⁴⁹ In addition, a few studies combined both patterned and random deposition techniques to achieve improved coating properties. Photolithography/3D printing was used to form the main micro-scale textures, while nanoparticles were added to account for the additional nano-scale roughness level to avoid using more complex approaches.^{155,156}

1.5.2. Durability Concerns against Real-life Challenges

Passing the fabrication stage, several new challenges face the surfaces once integrated into the application environment. These can affect the surface behaviour and, potentially, lead to a partial or a complete loss of superhydrophobic properties and, hence, inadequate functionality. The hydrophobicity loss can take place through three main pathways: **i)** chemical degradation, **ii)** physical degradation and **iii)** changing of the wetting mechanism (**Figure 1.24**).

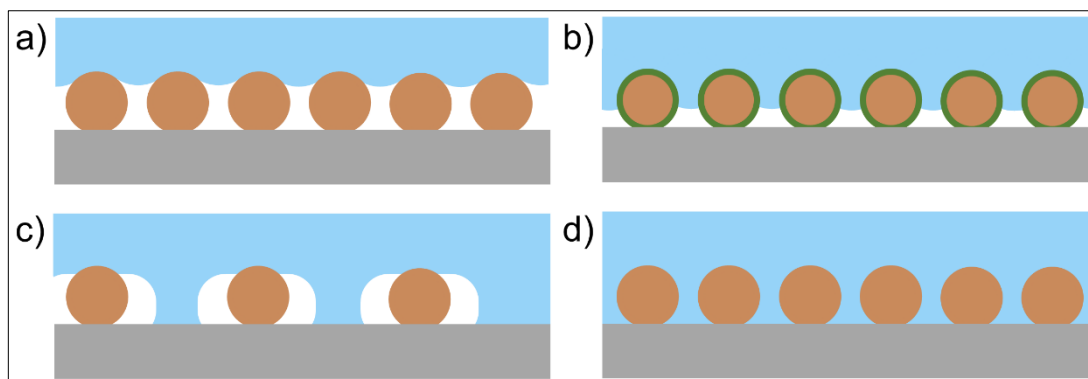


Figure 1.24: Schematic illustrating possible degradation mechanisms that a superhydrophobic surface (a) can undergo. This includes b) chemical degradation (the green rings represent a less hydrophobic material), c) physical degradation and d) changing of the wetting mechanism.¹⁵⁷

Surface chemistry can be altered by several surrounding factors. Guided by Young's equation (1.1), increasing the surface energy of the coating material leads to a decrease in the observed WCA. This can be achieved by damaging the surface, either by the removal of covalently-bound hydrophobic surface groups (through exposure to harsh conditions, examples include strong acid/alkali solutions, placement of photocatalytic particles or extreme heat treatment) or by introducing chemical contamination into the surface (e.g. surface fouling, hard-water staining).^{32,157–159}

Physical damage to the surface structure is considered a major limitation for many superhydrophobic surfaces. This is due to the surface architecture consisting of micro/nanoscale features. Although this is known to be fundamental for superhydrophobicity (Section 1.1.1), these features are inherently weak and are susceptible to breaking with a minimal physical load (as little as a finger wipe for some surfaces).^{5,147,157} This makes many surfaces unsuitable for applications where challenges like scratching or abrasion are expected.

Another mechanism leading to a loss/reduction of superhydrophobicity is the alteration of the water-surface wetting, by moving from a Cassie-Baxter to a Wenzel wetting state (i.e. loss of trapped air). As shown in Section 1.2.3, complete displacement of trapped air during wetting increases the adhesion between water and the surface and reduces the contact angle. This can be initiated using different stimuli, like the increased hydrostatic pressure (as a result of increased water depth -for submerged surfaces- or the fluid shear forces), the diffusion of air into water (caused by the exchange of gases between air and water driven by the concentration gradient

across the air-water interface) or the condensation of water droplets inside air pockets (initiated by the presence of hydrophilic impurities).⁴³

Chemical and physical damages are more difficult to address, as surfaces need to be pre-designed with self-healing mechanisms for the functionality to be restored.¹⁵⁷ Surfaces with regenerative abilities after plasma etching treatment^{160,161} as well as repeated cycles of abrasion^{162,163} have been reported. On the other hand, the removal of trapped air is considered to be recoverable, as it can be achieved by re-installation of the surface after drying. Meanwhile, the development of surface designs with maximised tolerance against wetting has been investigated,^{164–166} along with mechanisms for an air-layer restoration –while maintained in the application setup– through the incorporation of physical/chemical air-supplying routes.^{167–169}

1.6. Thesis Outline

As demonstrated in the previous discussion, and while the fabrication and development of new surfaces with superhydrophobic properties are still required, the investigation of the mentioned concerns is crucial in regards to the surface applicability. The main aim of the research outlined in this thesis was to promote the applicability of superhydrophobic surfaces, which took different pathways in each chapter:

- The inclusion of heat-sensitive substrates was the main aim in Chapter 2, where the deposition of superhydrophobic coatings *via* the pre-established aerosol-assisted CVD (AACVD) was further developed to achieve room-temperature coating deposition, dispensing the necessity of substrate exposure to elevated temperatures.
- Chapter 3 is aimed to address the resilience assessment of the coatings against abrasion, through the introduction of a straightforward image analysis/mass-loss tracking technique.
- This technique is heavily applied in Chapter 4, where the main aim was to investigate the relation between the coating components and the observed robustness and utilize this for the fabrication of coatings with improved resilience.
- Chapter 5 aimed at facilitating the incorporation of recycled polymers into the fabrication of oil/water separation filters, by designing a fabrication method utilizing micronized polymer powder.

- In Chapter 6, the investigation of the applicability of superhydrophobic coatings in the protection of water-sensitive materials is discussed, where MOFs were chosen for this purpose.

1.7. References

- 1 K. Gerasopoulos, W. L. Luedeman, E. Ölçeroglu, M. McCarthy and J. J. Benkoski, *ACS Appl. Mater. Interfaces*, 2018, **10**, 4066–4076.
- 2 B. Mondal, M. M. G. Eain, Q. Xu, V. M. Egan, J. Punch and A. M. Lyons, *ACS Appl. Mater. Interfaces*, 2015, **7**, 23575–23588.
- 3 M. Camaiti, L. Brizi, V. Bortolotti, A. Salvini, P. Antonella and P. Fantazzini, *ACS Appl. Mater. Interfaces*, 2017, **9**, 37279–37288.
- 4 R. Fürstner, W. Barthlott, C. Neinhuis and P. Walzel, *Langmuir*, 2005, **21**, 956–961.
- 5 Y. Lu, S. Sathasivam, J. Song, C. R. Crick, C. J. Carmalt and I. P. Parkin, *Science (80-.)*, 2015, **347**, 1132–1135.
- 6 X. He, P. Cao, F. Tian, X. Bai and C. Yuan, *Surf. Coatings Technol.*, 2019, **357**, 180–188.
- 7 C. H. Xue, X. J. Guo, J. Z. Ma and S. T. Jia, *ACS Appl. Mater. Interfaces*, 2015, **7**, 8251–8259.
- 8 L. Cao, A. K. Jones, V. K. Sikka, J. Wu and D. Gao, *Langmuir*, 2009, **25**, 12444–12448.
- 9 H. Wang, L. Tang, X. Wu, W. Dai and Y. Qiu, *Appl. Surf. Sci.*, 2007, **253**, 8818–8824.
- 10 C. Lee and C. J. Kim, *Phys. Rev. Lett.*, 2011, **106**, 014502.
- 11 J. W. Gose, K. Golovin, M. Boban, J. M. Mabry, A. Tuteja, M. Perlin and S. L. Ceccio, *J. Fluid Mech.*, 2018, **845**, 560–580.
- 12 E. Sadler and C. R. Crick, *Sustain. Mater. Technol.*, 2021, **29**, e00321.
- 13 Y. A. Mehanna and C. R. Crick, *Mater. 2020, Vol. 13, Page 3160*, 2020, **13**, 3160.
- 14 X. Gao and L. Jiang, *Nature*, 2004, **432**, 36.
- 15 X. Feng and L. Jiang, *Adv. Mater.*, 2006, **18**, 3063–3078.
- 16 W. Barthlott, T. Schimmel, S. Wiersch, K. Koch, M. Brede, M. Barczewski, S. Walheim, A. Weis, A. Kaltenmaier, A. Leder and H. F. Bohn, *Adv. Mater.*, 2010, **22**, 2325–2328.
- 17 M. Amabili, A. Giacomello, S. Meloni and C. M. Casciola, *Adv. Mater. Interfaces*, 2015, **2**, 1500248.
- 18 C. Neinhuis and W. Barthlott, *Ann. Bot.*, 1997, **79**, 667–677.
- 19 G. Carbone and L. Mangialardi, *Eur. Phys. J. E*, 2005, **16**, 67–76.

- 20 M. Zhang, S. Feng, L. Wang and Y. Zheng, *Biotribology*, 2016, **5**, 31–43.
- 21 C. R. Crick and I. P. Parkin, *A Eur. J.*, 2010, **16**, 3568–3588.
- 22 W. Barthlott and C. Neinhuis, *Planta*, 1997, **202**, 1–8.
- 23 S.-M. Lee and T. Hun Kwon, *Nanotechnology*, 2006, **17**, 3189–3196.
- 24 Y. Yang, X. Li, X. Zheng, Z. Chen, Q. Zhou and Y. Chen, *Adv. Mater.*, 2018, **30**, 1704912(1–11).
- 25 M. Miwa, A. Nakajima, A. Fujishima, K. Hashimoto and T. Watanabe, *Langmuir*, 2000, **16**, 5754–5760.
- 26 J. Bico, U. Thiele and D. Quéré, *Colloids Surfaces A Physicochem. Eng. Asp.*, 2002, **206**, 41–46.
- 27 Van Honschoten J W, E. M. T. N. R and E. M, *J. Colloid Interface Sci.*, 2009, **329**, 133–139.
- 28 N. Gao, Y. Y. Yan, X. Y. Chen and D. J. Mee, *Mater. Lett.*, 2011, **65**, 2902–2905.
- 29 W. Li and A. Amirfazli, *Soft Matter*, 2008, **4**, 462–466.
- 30 N. Verplanck, Y. Coffinier, V. Thomy and R. Boukherroub, *Nanoscale Res. Lett.*, 2007, **2**, 577.
- 31 E. Ueda and Pavel A. Levkin, *Adv. Mater.*, 2013, **25**, 1234–1247.
- 32 R. L. Upton, University of Liverpool, 2021.
- 33 D. Quéré, A. Lafuma and J. Bico, *Nanotechnology*, 2003, **14**, 1109.
- 34 L. Gao and T. J. McCarthy, *Langmuir*, 2006, **22**, 6234–6237.
- 35 S. Lauren, How to measure contact angle hysteresis?, <https://www.biolinscientific.com/blog/how-to-measure-contact-angle-hysteresis>, (accessed 20 February 2022).
- 36 KRUSS, Hysteresis, <https://www.kruss-scientific.com/en/know-how/glossary/hysteresis>, (accessed 20 February 2022).
- 37 R. Taurino, E. Fabbri, D. Pospiech, A. Synytska and M. Messori, *Prog. Org. Coatings*, 2014, **77**, 1635–1641.
- 38 K. Koch, B. Bhushan, Y. C. Jung and W. Barthlott, *Soft Matter*, 2009, **5**, 1386–1393.
- 39 C. R. Crick and I. P. Parkin, *Chem. Commun.*, 2011, **47**, 12059–12061.
- 40 C. R. Crick and I. P. Parkin, *J. Mater. Chem. A*, 2013, **1**, 799–804.
- 41 D. Zheng, Y. Jiang, W. Yu, X. Jiang, X. Zhao, C. H. Choi and G. Sun, *Langmuir*, 2017, **33**, 13640–13648.
- 42 M. Callies and D. Quere, *Soft Matter*, 2005, **1**, 55–61.
- 43 Y. A. Mehanna, E. Sadler, R. L. Upton, A. G. Kempchinsky, Y. Lu and C. R. Crick, *Chem. Soc. Rev.*, 2021, **50**, 6612.
- 44 C. Dorrer and J. Ruhe, *Soft Matter*, 2009, **5**, 51–61.
- 45 A. B. D. Cassie and S. Baxter, *Trans. Faraday Soc.*, 1944, **40**, 546–551.

- 46 Robert N. Wenzel, *Ind. Eng. Chem.*, 1936, **28**, 988–994.
- 47 R. N. Wenzel, *J. Phys. Chem.*, 1949, **53**, 1466–1467.
- 48 C. R. Crick, University College London, 2011.
- 49 A. B. D. Cassie, *Discuss. Faraday Soc.*, 1948, **3**, 11.
- 50 D. Quéré, A. Lafuma and J. Bico, *Nanotechnology*, 2003, **14**, 1109–1112.
- 51 G. Ozin, A. Arsenault and L. Cademartiri, *Nanochemistry: A Chemical Approach to Nanomaterials*, RSC Publishing, 2nd edn., 2008.
- 52 A. M. Manasa, B. R. Deepu and P. Savitha, *Mater. Today Proc.*, 2021, **42**, 1270–1273.
- 53 Y. Zhang, Z. Zhang, J. Yang, Y. Yue and H. Zhang, *Nanomaterials*, 2022, **12**, 44(1–22).
- 54 J. H. Kim, A. Mirzaei, H. W. Kim and S. S. Kim, *Appl. Surf. Sci.*, 2018, **439**, 598–604.
- 55 T. A. Saleh and N. Baig, *Prog. Org. Coatings*, 2019, **133**, 27–32.
- 56 Y. Liu, Y. Bai, J. Jin, L. Tian, Z. Han and L. Ren, *Appl. Surf. Sci.*, 2015, **355**, 1238–1244.
- 57 R. Jafari, S. Asadollahi and M. Farzaneh, *Plasma Chem. Plasma Process.*, 2012, **33**, 177–200.
- 58 H. C. Barshilia and N. Gupta, *Vacuum*, 2014, **99**, 42–48.
- 59 P. Roach, N. J. Shirtcliffe and M. I. Newton, *Soft Matter*, 2008, **4**, 224–240.
- 60 D. Öner and T. J. McCarthy, *Langmuir*, 2000, **16**, 7777–7782.
- 61 M. Sun, C. Luo, L. Xu, H. Ji, Q. Ouyang, D. Yu and Y. Chen, *Langmuir*, 2005, **21**, 8979–8981.
- 62 B. Liu, Y. He, Y. Fan and X. Wang, *Macromol. Rapid Commun.*, 2006, **27**, 1859–1864.
- 63 J. Feng, M. Huang and X. Qian, *Macromol. Mater. Eng.*, 2009, **294**, 295–300.
- 64 C. Marzolin, S. P. Smith, M. Prentiss and G. M. Whitesides, *Adv. Mater.*, 1998, **10**, 571–574.
- 65 C. Zeiger, I. C. Rodrigues Da Silva, M. Mail, M. N. Kavalenka, W. Barthlott and H. Hölscher, *Bioinspir. Biomim.*, 2016, **11**, 056003(1–9).
- 66 I. Sas, R. E. Gorga, J. A. Joines and K. A. Thoney, *J. Polym. Sci. Part B Polym. Phys.*, 2012, **50**, 824–845.
- 67 L. F. Ren, F. Xia, J. Shao, X. Zhang and J. Li, *Desalination*, 2017, **404**, 155–166.
- 68 D. Cho, H. Zhou, Y. Cho, D. Audus and Y. L. Joo, *Polymer (Guildf.)*, 2010, **51**, 6005–6012.
- 69 M. W. Lee, S. An, S. S. Latthe, C. Lee, S. Hong and S. S. Yoon, *ACS Appl. Mater. Interfaces*, 2013, **5**, 10597–10604.
- 70 Z. Liu, H. Wang, E. Wang, X. Zhang, R. Yuan and Y. Zhu, *Polymer (Guildf.)*,

- 2016, **82**, 105–113.
- 71 H. O. Pierson, *Handbook of chemical vapor deposition (CVD): principles, technology, and applications*, Noyes Publications, 1992.
- 72 W. A. Bryant, *J. Mater. Sci.*, 1977, **12**, 1285–1306.
- 73 S. H. Yang, C. H. Liu, W. T. Hsu and H. Chen, *Surf. Coatings Technol.*, 2009, **203**, 1379–1383.
- 74 Y. Wu, H. Sugimura, Y. Inoue and O. Takai, *Chem. Vap. Depos.*, 2002, **8**, 47–50.
- 75 F. Bayram, E. S. Mercan and M. Karaman, *Colloid Polym. Sci.*, 2021, **299**, 1469–1477.
- 76 I. Vilaró, J. L. Yagüe and S. Borrós, *ACS Appl. Mater. Interfaces*, 2017, **9**, 1057–1065.
- 77 H. O. Seo, K. D. Kim, M. G. Jeong, Y. D. Kim, K. H. Choi, E. M. Hong, K. H. Lee and D. C. Lim, *Macromol. Res.*, 2012, **20**, 216–219.
- 78 T. Sun, G. Wang, H. Liu, L. Feng, L. Jiang and D. Zhu, *J. Am. Chem. Soc.*, 2003, **125**, 14996–14997.
- 79 S. J. Pastine, D. Okawa, B. Kessler, M. Rolandi, M. Llorente, A. Zettl and J. M. J. Fréchet, *J. Am. Chem. Soc.*, 2008, **130**, 4238–4239.
- 80 Y. Y. Yan, N. Gao and W. Barthlott, *Adv. Colloid Interface Sci.*, 2011, **169**, 80–105.
- 81 A. Hooda, M. S. Goyat, J. K. Pandey, A. Kumar and R. Gupta, *Prog. Org. Coatings*, 2020, **142**, 105557(1–21).
- 82 X. Zhang, F. Zheng, L. Ye, P. Xiong, L. Yan, W. Yang and B. Jiang, *RSC Adv.*, 2014, **4**, 9838–9841.
- 83 X. Zhang, W. Su, M. Lin, X. Miao, L. Ye, W. Yang and B. Jiang, *J. Sol-Gel Sci. Technol.*, 2015, **74**, 594–602.
- 84 D. Schondelmaier, S. Cramm, R. Klingeler, J. Morenzin, C. Zilkens and W. Eberhardt, *Langmuir*, 2002, **18**, 6242–6245.
- 85 S. Liu, X. Liu, S. S. Latthe, L. Gao, S. An, S. S. Yoon, B. Liu and R. Xing, *Appl. Surf. Sci.*, 2015, **351**, 897–903.
- 86 X. Wang, J. Zeng, X. Yu, C. Liang and Y. Zhang, *Appl. Surf. Sci.*, 2019, **465**, 986–994.
- 87 X. Ke, S. Guo, B. Gou, N. Wang, X. Zhou, L. Xiao, G. Hao and W. Jiang, *Adv. Mater. Interfaces*, 2019, **6**, 190102(15–11).
- 88 J. E. Mates, R. Ibrahim, A. Vera, S. Guggenheim, J. Qin, D. Calewatts, D. E. Waldroup and C. M. Megaridis, *Green Chem.*, 2016, **18**, 2185–2192.
- 89 D. Lai, G. Kong and C. Che, *Surf. Coatings Technol.*, 2017, **315**, 509–518.
- 90 C. C. Chang, Y. T. Wu and L. P. Cheng, *J. Coatings Technol. Res.*, 2016, **13**, 999–1007.
- 91 R. Zhu, M. Liu, Y. Hou, L. Zhang, M. Li, D. Wang and S. Fu, *ACS Appl. Mater. Interfaces*, 2020, **12**, 17004–17017.

- 92 D. Goswami, S. K. Medda and G. De, *ACS Appl. Mater. Interfaces*, 2011, **3**, 3440–3447.
- 93 S. Wang, L. Feng, H. Liu, T. Sun, X. Zhang, L. Jiang and D. Zhu, *ChemPhysChem*, 2005, **6**, 1475–1478.
- 94 X. Zhang, Z. Liu, X. Zhang, Y. Li, H. Wang, J. Wang and Y. Zhu, *Chem. Eng. J.*, 2018, **343**, 699–707.
- 95 F. Farbod, B. Pourabbas and M. Sharif, *J. Polym. Sci. Part B Polym. Phys.*, 2013, **51**, 441–451.
- 96 R. L. Upton, Z. Davies-Manifold, M. Marcello, K. Arnold and C. R. Crick, *Mol. Syst. Des. Eng.*, 2020, **5**, 477–483.
- 97 R. L. Upton and C. R. Crick, *Mol. Syst. Des. Eng.*, 2020, **5**, 876–881.
- 98 R. L. Upton, A. Fedosyuk, J. B. Edel and C. R. Crick, *ACS Appl. Nano Mater.*, 2021, **4**, 10090–10102.
- 99 M. Zahid, J. A. Heredia-guerrero, A. Athanassiou and I. S. Bayer, *Chem. Eng. J.*, 2017, **319**, 321–332.
- 100 Q. Ke, W. Fu, H. Jin, L. Zhang, T. Tang and J. Zhang, *Surf. Coat. Technol.*, 2011, **205**, 4910–4914.
- 101 L. Zhang, Y. Li, J. Sun and J. Shen, *J. Colloid Interface Sci.*, 2008, **319**, 302–308.
- 102 B. Bhushan, Y. C. Jung and K. Koch, *Langmuir*, 2009, **25**, 3240–3248.
- 103 S. Pan, N. Wang, D. Xiong, Y. Deng and Y. Shi, *Appl. Surf. Sci.*, 2016, **389**, 547–553.
- 104 S. Mukherjee, A. M. Kansara, D. Saha, R. Gonnade, D. Mullangi, B. Manna, A. V. Desai, S. H. Thorat, P. S. Singh, A. Mukherjee and S. K. Ghosh, *Chem. – A Eur. J.*, 2016, **22**, 10937–10943.
- 105 J. B. Decoste, G. W. Peterson, M. W. Smith, C. A. Stone and C. R. Willis, *J. Am. Chem. Soc.*, 2012, **134**, 1486–1489.
- 106 M. Lynes, *International energy outlook 2016, Transportation Sector*, 2016.
- 107 M. Xu, A. Grabowski, N. Yu, G. Kerezyte, J. W. Lee, B. R. Pfeifer and C. J. Kim, *Phys. Rev. Appl.*, 2020, **13**, 1.
- 108 S. A. Mäkiharju, M. Perlin and S. L. Ceccio, *Int. J. Nav. Archit. Ocean Eng.*, 2012, **4**, 412–422.
- 109 N. Wang, L. Tang, Y. Cai, W. Tong and D. Xiong, *Colloids Surfaces A Physicochem. Eng. Asp.*, 2018, **555**, 290–295.
- 110 H. Zhang, Y. Tuo, Q. Wang, B. Jin, L. Yin and X. Liu, *Surf. Eng.*, 2018, **34**, 596–602.
- 111 M. A. Samaha, H. Vahedi Tafreshi and M. Gad-el-Hak, *Phys. Fluids*, 2011, **23**, 012001-1-012001–8.
- 112 H. Aziz and H. V. Tafreshi, *Int. J. Multiph. Flow*, 2018, **98**, 128–138.
- 113 E. Taghvaei, A. Moosavi, A. Nouri-Borujerdi, M. A. Daeian and S. Vafaeinejad, *Energy*, 2017, **125**, 1–10.

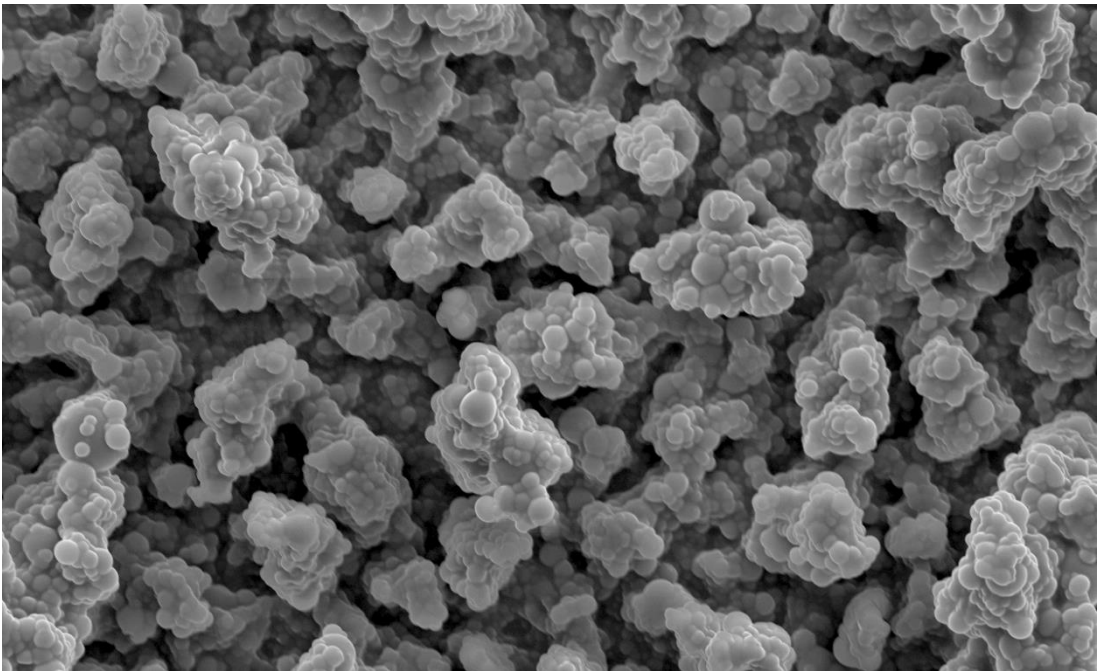
- 114 M. Xu, N. Yu, J. Kim and C. J. C. Kim, *J. Fluid Mech.*, 2020, **908**, 6.
- 115 R. K. Gupta, G. J. Dunderdale, M. W. England and A. Hozumi, *J. Mater. Chem. A*, 2017, **5**, 16025–16058.
- 116 J. S. van Eenennaam, M. Rohal, P. A. Montagna, J. R. Radović, T. B. P. Oldenburg, I. C. Romero, A. T. J. Murk and E. M. Foekema, *Mar. Pollut. Bull.*, 2019, **141**, 164–175.
- 117 N. P. Ventikos, E. Vergetis, H. N. Psarافتis and G. Triantafyllou, *J. Hazard. Mater.*, 2004, **107**, 51–58.
- 118 Q. Zhu, Y. Chu, Z. Wang, N. Chen, L. Lin, F. Liu and Q. Pan, *J. Mater. Chem. A*, 2013, **1**, 5386–5393.
- 119 D. D. Nguyen, N. H. Tai, S. B. Lee and W. S. Kuo, *Energy Environ. Sci.*, 2012, **5**, 7908–7912.
- 120 C. R. Crick, D. S. Bhachu and I. P. Parkin, *Sci. Technol. Adv. Mater.*, 2014, **15**, 065003.
- 121 C. R. Crick, J. A. Gibbins and I. P. Parkin, *J. Mater. Chem. A*, 2013, **1**, 5943–5948.
- 122 C. R. Crick, F. T. Ozkan and I. P. Parkin, *Sci. Technol. Adv. Mater.*, 2015, **16**, 055006.
- 123 X. Dong, J. Chen, Y. Ma, J. Wang, M. B. Chan-Park, X. Liu, L. Wang, W. Huang and P. Chen, *Chem. Commun.*, 2012, **48**, 10660–10662.
- 124 P. Calcagnile, D. Fragouli, I. S. Bayer, G. C. Anyfantis, L. Martiradonna, P. D. Cozzoli, R. Cingolani and A. Athanassiou, *ACS Nano*, 2012, **6**, 5413–5419.
- 125 J. Bong, T. Lim, K. Seo, C. A. Kwon, J. H. Park, S. K. Kwak and S. Ju, *Sci. Rep.*, 2015, **5**, 1–6.
- 126 K. Rohrbach, Y. Li, H. Zhu, Z. Liu, J. Dai, J. Andreasen and L. Hu, *Chem. Commun.*, 2014, **50**, 13296–13299.
- 127 Z. Xu, Y. Zhao, H. Wang, H. Zhou, C. Qin, X. Wang and T. Lin, *ACS Appl. Mater. Interfaces*, 2016, **8**, 5661–5667.
- 128 J. Gu, P. Xiao, J. Chen, F. Liu, Y. Huang, G. Li, J. Zhang and T. Chen, *J. Mater. Chem. A*, 2014, **2**, 15268–15272.
- 129 J. Li, L. Yan, W. Hu, D. Li, F. Zha and Z. Lei, *Colloids Surfaces A Physicochem. Eng. Asp.*, 2016, **489**, 441–446.
- 130 N. Liu, Y. Chen, F. Lu, Y. Cao, Z. Xue, K. Li, L. Feng and Y. Wei, *ChemPhysChem*, 2013, **14**, 3489–3494.
- 131 Q. Ma, H. Cheng, A. G. Fane, R. Wang and H. Zhang, *Small*, 2016, **12**, 2186–2202.
- 132 D. Tian, X. Zhang, X. Wang, J. Zhai and L. Jiang, *Phys. Chem. Chem. Phys.*, 2011, **13**, 14606–14610.
- 133 C. F. Wang, F. S. Tzeng, H. G. Chen and C. J. Chang, *Langmuir*, 2012, **28**, 10015–10019.
- 134 H. Li, M. Zheng, L. Ma, C. Zhu and S. Lu, *Mater. Res. Bull.*, 2013, **48**, 25–29.

- 135 X. Zhou, Z. Zhang, X. Xu, F. Guo, X. Zhu, X. Men and B. Ge, *ACS Appl. Mater. Interfaces*, 2013, **5**, 7208–7214.
- 136 Y. Shang, Y. Si, A. Raza, L. Yang, X. Mao, B. Ding and J. Yu, *Nanoscale*, 2012, **4**, 7847–7854.
- 137 J. Zou and F. Kim, *Nat. Commun.*, 2014, **5**, 1–9.
- 138 Q. Shuai, X. Yang, Y. Luo, H. Tang, X. Luo, Y. Tan and M. Ma, *Mater. Chem. Phys.*, 2015, **162**, 94–99.
- 139 T. Zhao, D. Zhang, C. Yu and L. Jiang, *ACS Appl. Mater. Interfaces*, 2016, **8**, 24186–24191.
- 140 W. Wang, K. Lockwood, L. M. Boyd, M. D. Davidson, S. Movafaghi, H. Vahabi, S. R. Khetani and A. K. Kota, *ACS Appl. Mater. Interfaces*, 2016, **8**, 18664–18668.
- 141 J. D. Kim, H. Sugimura and O. Takai, *Vacuum*, 2002, **66**, 379–383.
- 142 A. Millionis, K. Dang, M. Prato, E. Loth and I. S. Bayer, *J. Mater. Chem. A*, 2015, **3**, 12880–12889.
- 143 Z. Yoshimitsu, A. Nakajima, T. Watanabe and K. Hashimoto, *Langmuir*, 2002, **18**, 5818–5822.
- 144 F. Suja, B. K. Pramanik and S. M. Zain, *Water Sci. Technol.*, 2009, **60**, 1533–1544.
- 145 S. Kim, J. W. Lee and W. Hwang, *ACS Appl. Mater. Interfaces*, 2020, **12**, 28869–28875.
- 146 R. Jafari, C. Cloutier, A. Allahdini and G. Momen, *Int. J. Adv. Manuf. Technol.*, 2019, **103**, 1225–1238.
- 147 J. Zhang, J. Zhao, W. Qu, X. Li and Z. Wang, *J. Colloid Interface Sci.*, 2020, **580**, 211–222.
- 148 L. A. M. Carrascosa, D. S. Facio and M. J. Mosquera, *Nanotechnology*, 2016, **27**, 095604(1–13).
- 149 D. S. Facio and M. J. Mosquera, *ACS Appl. Mater. Interfaces*, 2013, **5**, 7517–7526.
- 150 R. Iqbal, B. Majhy and A. K. Sen, *ACS Appl. Mater. Interfaces*, 2017, **9**, 31170–31180.
- 151 J. W. Krumpfer and T. J. McCarthy, *Langmuir*, 2011, **27**, 11514–11519.
- 152 R. Cai, K. Glinel, D. De Smet, M. Vanneste, N. Mannu, B. Kartheuser, B. Nysten and A. M. Jonas, *ACS Appl. Mater. Interfaces*, 2018, **10**, 15346–15351.
- 153 J. M. Morrissette, P. J. Carroll, I. S. Bayer, J. Qin, D. Waldroup and C. M. Megaridis, *Green Chem.*, 2018, **20**, 5169–5178.
- 154 P. Hao, X. Lou, L. Tang, F. Wang, Z. Chong and L. Guo, *Prog. Org. Coatings*, 2022, **162**, 106590(1–8).
- 155 C. V. Ngo and D. M. Chun, *Sci. Reports 2016 61*, 2016, **6**, 36735(1–9).
- 156 T. Li, M. Paliy, X. Wang, B. Kobe, W. M. Lau and J. Yang, *ACS Appl. Mater. Interfaces*, 2015, **7**, 10988–10992.

- 157 C. R. Crick, in *Superhydrophobic Surfaces-Fabrications to Practical Applications*, IntechOpen, 2018, pp. 11–38.
- 158 L. K. Ista, M. E. Callow, J. A. Finlay, S. E. Coleman, A. C. Nolasco, R. H. Simons, J. A. Callow and G. P. Lopez, *Appl. Environ. Microbiol.*, 2004, **70**, 4151–4157.
- 159 M. Gryta, *Desalination*, 2007, **216**, 88–102.
- 160 Y. Li, B. Ge, X. Men, Z. Zhang and Q. Xue, *Compos. Sci. Technol.*, 2016, **125**, 55–61.
- 161 H. Wang, Y. Xue, J. Ding, L. Feng, X. Wang and T. Lin, *Angew. Chemie*, 2011, **123**, 11635–11638.
- 162 S. Ramakrishna, K. S. S. Kumar, D. Mathew and C. P. Reghunadhan Nair, *Sci. Rep.*, 2015, **5**, 18510(1–11).
- 163 M. Wu, B. Ma, T. Pan, S. Chen and J. Sun, *Adv. Funct. Mater.*, 2016, **26**, 569–576.
- 164 L. Chen, Z. Guo and W. Liu, *J. Mater. Chem. A*, 2017, **5**, 14480–14507.
- 165 E. M. Domingues, S. Arunachalam and H. Mishra, *ACS Appl. Mater. Interfaces*, 2017, **9**, 21532–21538.
- 166 E. J. Lee, B. J. Deka, J. Guo, Y. C. Woo, H. K. Shon and A. K. An, *Environ. Sci. Technol.*, 2017, **51**, 10117–10126.
- 167 B. J. Lee, Z. Zhang, S. Baek, S. Kim, D. Kim and K. Yong, *Sci. Rep.*, 2016, **6**, 1–11.
- 168 Z. Li, J. Marlina, D. Pranantyo, B. L. Nguyen and C. H. Yap, *J. Mater. Chem. A*, 2019, **7**, 16387–16396.
- 169 C. Lee and C. J. Kim, *Phys. Rev. Lett.*, 2011, **106**, 1–4.

Chapter 2:

The Room-Temperature Deposition of Thermally- Activated Polymers



Publications:

Highly rough surface coatings via the ambient temperature deposition of thermosetting polymers. [Y.A. Mehanna](#), R. L. Upton and C. R. Crick. *J. Mater. Chem. A*, 2019, 7, 7333-7337.

Contributions:

Scanning Electron Microscopy: Preparation and Imaging of PDMS coatings was conducted by Rebekah Upton (University of Liverpool)

2. The Room-Temperature Deposition of Thermally-Activated Polymers

2.1. Introduction

Chemical vapour deposition (CVD) has been widely reported for the fabrication and deposition of superhydrophobic coatings, as demonstrated in Section 1.3.2.1.2. Although this technique proved compatible with various types of precursors, the requirement of these precursors to be in a gaseous state is considered one of the major limitations of CVD. As many precursors do not naturally exist in this state, a vaporisation step is needed to be carried out, either by heating or by reducing pressure, limiting the applicability of this technique only to volatile liquid materials.^{1,2}

Aerosol-assisted CVD (AACVD) is a modification of the conventional CVD technique. In AACVD, an aerosol is generated from the liquid/solution precursor, eliminating the need for vaporisation. This modification also allows extending the selection of precursors to involve polymers, which are practically difficult to evaporate before undergoing thermal degradation due to their huge molecular weight (M_w) and extremely low vapour pressure.³

This section discusses the theory of AACVD and presents previous reports utilizing it for the fabrication of superhydrophobic coatings. In addition, it highlights the main limitation of this technique, which will be addressed in this chapter.

2.1.1. Aerosol-Assisted Chemical Vapour Deposition

2.1.1.1. Mechanism of producing rough polymeric coatings

Similar to CVD, AACVD usually operates at elevated temperatures. As the involvement of polymers is considered in AACVD, it is important to understand the interaction of polymers to heat. Polymers are classified into two main categories depending on how they physically respond when heated; thermoplastic and thermosetting polymers (**Figure 2.1**). In thermoplastic polymers, polymeric chains are connected by weak intermolecular forces. When heated, the chains overcome these forces and the polymer starts to soften. During this state, the polymer can be easily reshaped into alternative structures. These polymers solidify again when the heat is removed, meaning that the melting process is reversible.⁴ On the other hand, thermosetting polymers consist of polymeric chains that usually exist in a soft solid or a viscous liquid state, and when the reaction is initiated (by heat or possible other stimuli, like irradiation or adding a catalyst) these chains undergo cross-linking. Unlike

thermoplastic polymers, the formed covalent bonds are stronger, making a rigid network of polymers that is difficult to process. This means the change that occurs in thermosetting polymers when heated is irreversible. Further heating of the cured thermosetting polymer would lead to thermal degradation of the polymer.⁵

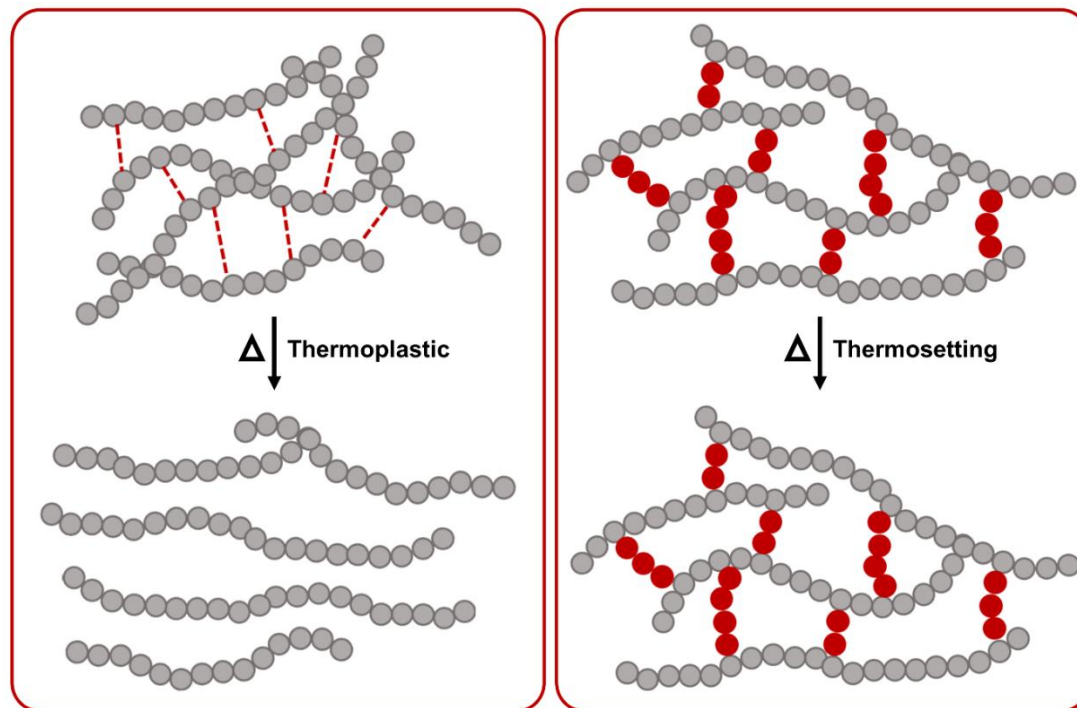


Figure 2.1: Schematic showing the structural differences between thermoplastic vs thermosetting polymers upon heating. While the weak intermolecular interactions between thermoplastic polymer chains allow polymer melting, the strong, covalent crosslinking bonds in thermosetting polymers form a rigid network that remains structurally intact.⁴

A wide range of coatings for various applications can be deposited using AACVD.⁶⁻⁸ For superhydrophobic coatings, the two requirements for high water repellence must be satisfied; low surface energy and high surface roughness (Section 1.1.1).⁹ While the former requirement can be controlled by the choice of the coating material, the latter should be achieved by tailoring the deposition conditions (Section 2.3.1.1). **Figure 2.2** illustrates the mechanism for the deposition of a rough coating using a thermosetting polymer. This is due to the ability of thermosetting polymers to harden and preserve structure when heated. The generated aerosol droplets (consisting of polymer and solvent) enter the hot reactor, where the solvent gets evaporated and the polymer crosslinking occurs. This allows the deposition of cured/partially cured polymer spheres, forming coatings with a micro-structured surface.^{10,11}

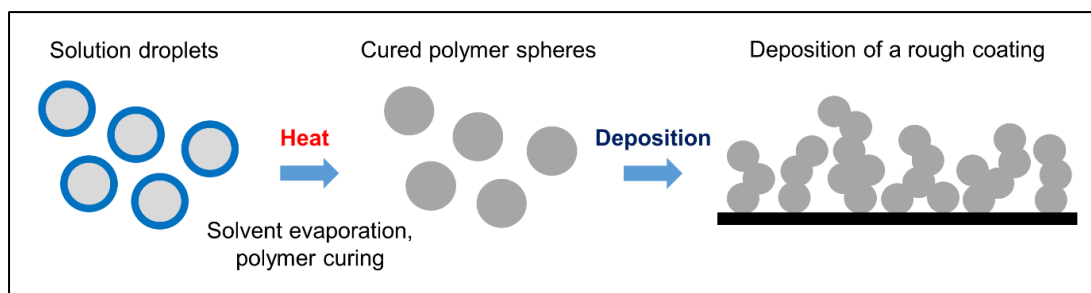


Figure 2.2: Schematic illustrating the mechanism for generating a rough morphology using AACVD. The droplets generated by the aerosol are heated to evaporate the solvent and cure the polymer, which allows the deposition of rough coating textures.^{10,11}

The typical setup for the AACVD is illustrated in **Figure 2.3**. A solution of the precursor material in a suitable solvent is incorporated, from which an aerosol is generated. The aerosol generator (an ultrasonic humidifier) is placed under a glass vessel that contains the precursor solution, with a small amount of water filling the gap between the ultrasonic-vibrating plate and the glass vessel, so vibrations can be carried through it. When the aerosol generator is turned on, a mist is generated from the solution, transforming it from bulk liquid to small droplets. This mist is carried by gas flow into the heater. Inside the heater, the elevated temperature allows solvent evaporation and polymer curing. The substrate is kept inside where the cured polymer droplets start to deposit on top of it, forming a thin coating of polymer with rough morphology.

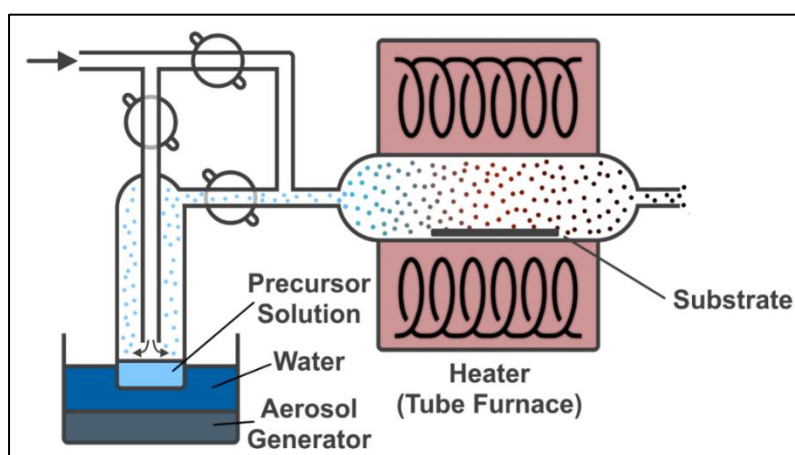


Figure 2.3: AACVD setup. The aerosol generated from the precursor solution is carried by nitrogen flow into the furnace, where the substrate is placed and the deposition occurs.

2.1.1.2. Deposition of thermosetting polymers for superhydrophobic applications

The involvement of polymer precursors for the deposition of superhydrophobic coatings via AACVD has been reported first by Crick et al.^{10–14} where a thermosetting polymer, typically PDMS was used to fabricate highly rough surface coatings. A range

of temperatures has been tested to reach the optimum temperature that would result in both solvent evaporation and polymer curing. It was found that a temperature above 300°C resulted in high hydrophobicity (WCAs of 160°) and rough microstructure formation (indicated using SEM, **Figure 2.4a**).¹⁰ To demonstrate the applicability of this technique with various types of thermosetting polymers, melamine-formaldehyde resin, a polymer with a hydrophilic nature, was used to fabricate rough films (**Figure 2.4b**).¹⁵ The films were shown to possess a hydrophobic nature when the film thickness reaches a certain level, at which the air trapped inside the rough features gaps would be enough for a water droplet to remain on the surface and not wet it, despite the water/polymer interaction that might be favoured in thinner films.¹⁵

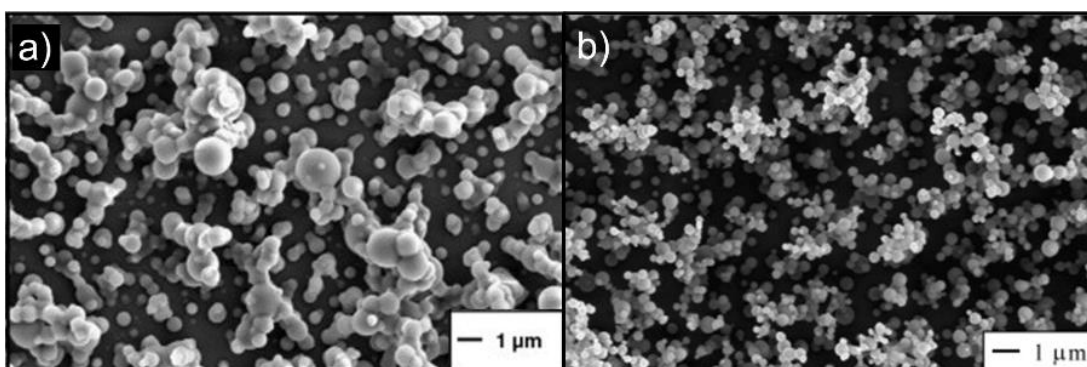


Figure 2.4: SEM images for a) PDMS and b) melamine-formaldehyde resin coatings deposited via AACVD. Figure retrieved from a) ref.¹⁰ b) ref.¹⁵

Due to their excellent superhydrophobic properties, AACVD-generated PDMS coatings were utilised in several applications. PDMS-coated copper-mesh membranes were used to make effective oil-water separation membranes.¹² In addition, the functionality of these coatings was proven to be feasible by the direct incorporation of different nanoparticle solutions into the main polymer solution, which would widen the applicability of the generated coatings in photo-catalysis, high surface area catalysis and antibacterial coatings.^{13,14,16} Nanoparticles like iron oxide, nickel, TiO₂, CoO and silica-coated gold nanoparticles were successfully added in a one-pot process to the polymer surface, while the particles maintained their properties with no detected interference with the polymer.¹⁴ The photocatalytic activity of incorporated TiO₂ nanoparticles in PDMS coating using AACVD was investigated, and it was found that the photo-degradation of contaminants occurred without affecting the films themselves.¹⁶ In another report, copper nanoparticles were added by a separate CVD step on a prepared PDMS surface, in which the bacterial cell adhesion was decreased significantly compared to un-functionalised PDMS surfaces.¹³

2.1.2. Chapter Aim

AACVD is an effective method for the deposition of thermosetting polymer solutions into micro-scale features to construct rough surfaces. Using materials with a hydrophobic nature, along with the rough morphology produced, the water repellence of the generated coatings would increase dramatically (Section 2.1.1.2). However, some limitations stand against broadening the applicability of this technique. One of them is the elevated temperatures required for solvent evaporation/polymer curing, which the substrates would be kept under for the whole deposition time.¹¹ This puts restrictions on the choice of the substrate, as many of them would undergo thermal decomposition (paper, fabric, plastics, *etc.*) or oxidation (metallic substrates) under such temperatures. Typically, in all of the previously mentioned reports, glass substrates were the only type of substrates tested,^{10,11} due to the ability of glass to withstand high temperatures. To enhance the applicability of this technique, the deposition must be scaled up to different substrates to meet the requirements for the targeted end product.

The first part of this chapter aims to solve this limitation. The importance of this is not limited to the ability to coat any surface, but it is even crucial to the functionality of many materials. The literature has numerous reports on functional materials that could be promising in different applications, but they suffer from their instability in water or even moisture, which sometimes it is impossible to completely get rid of in a typical reaction medium. For these materials, having a hydrophobic coating would be of great value in enhancing their performance. However, not all of them can withstand the high temperatures required for AACVD coating.

To accomplish this aim, a variation of the AACVD, named thermally-activated AACVD (ta-AACVD), has been designed and tested for this purpose.¹⁷ The technique utilises a similar setup to that in **Figure 2.3**, while keeping the substrate outside the reactor (**Figure 2.5**). As described previously, the aerosol generator is used to produce a mist that is carried by nitrogen flow into the furnace. The heater is set to a high temperature (necessary for polymer curing), which could be thought of as an 'activation' of the polymer to be in a state that is suitable for deposition of a rough coating. The substrate is kept outside where the ambient temperature is around 25°C. The gas flow, carrying the 'thermally-activated' polymer, continues to exit the furnace through the gas outlet and then hit the substrate where the deposition occurs. The chapter discusses the adjustment of the deposition parameters, such as the temperature, gas flow and substrate position, to obtain a room-temperature deposition of rough coatings.

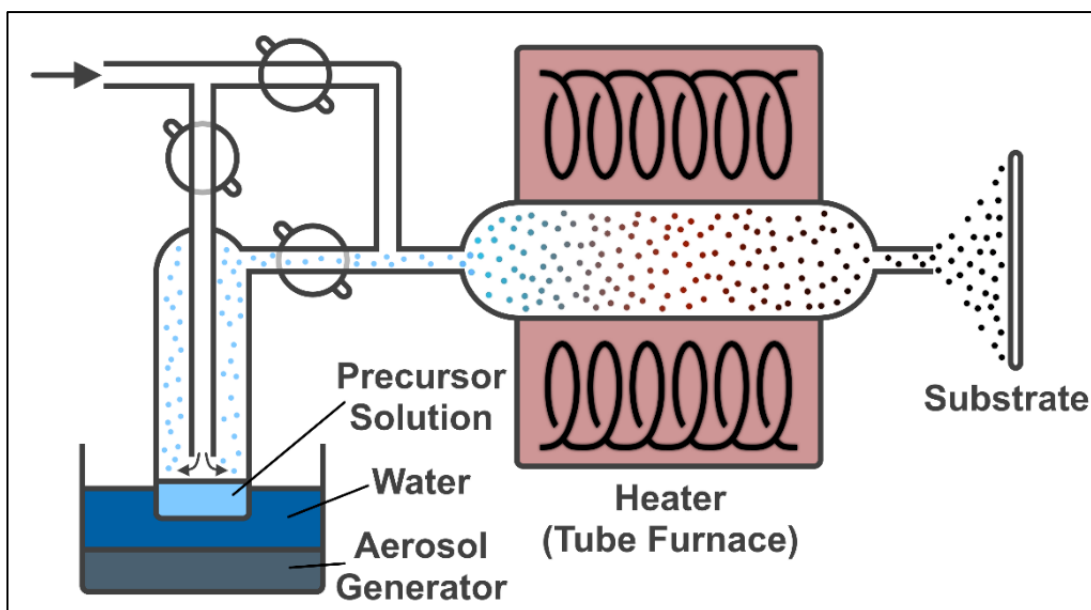


Figure 2.5: ta-AACVD setup. The main setup components are shared with the traditional AACVD, the only difference is the substrate position that is kept outside.

The second part of this chapter investigates the possibility of applying this technique using thermoplastic polymers and highlights how the deposited coating can vary by changing the curing mechanism of the polymer utilised.

2.2. Experimental Methods

2.2.1. Materials

SYLGARD® 184 was purchased from Dow Chemical. High M_w poly(vinyl chloride) (PVC, product number 81387) and poly(styrene-co- α -methylstyrene) (PScMS, product number 457205) were purchased from Sigma Aldrich. Polyethylene glycol 8,000 Powder (PEG, product number 43443) was purchased from Alfa Aesar. Chloroform (analytical grade, $\geq 99.8\%$) was purchased from Fisher scientific. Glass microscope slides (brought from Thermoscientific) were used as substrates for most of this research. However, subsequent experiments were conducted on temperature-sensitive substrates, this included; paper, cardboard, and aluminium (all acquired from RS Components).

Sylgard 184 is a Silicone Elastomer consists of two parts: the base polymer (PDMS), and a siloxane-based curing agent. **Figure 2.6** shows the structure of both the base and the crosslinking oligomers, as well as the crosslinking mechanism which is platinum-catalysed.

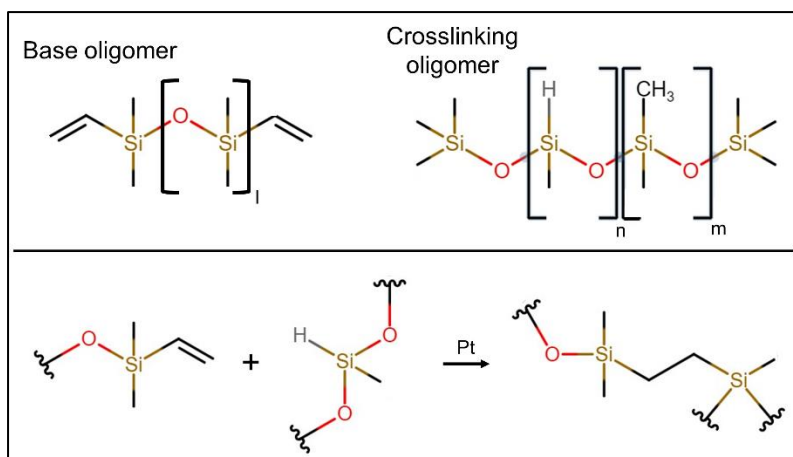


Figure 2.6: Base and crosslinking oligomers for Sylgard 184, and the curing mechanism of PDMS.

2.2.2. Polymer Solution Preparation

For PDMS (SYLGARD), both polymer parts, with a ratio (10:1, polymer: curing agent) were dissolved in chloroform (0.7 g of polymer in 100 mL). The mixture was allowed to stir for 15 minutes which enabled the polymer to fully dissolve. This solution was used immediately after stirring was stopped to avoid premature curing of the polymer before being incorporated in the AACVD process.

For this work, glass substrates were mostly used. To increase the glass-coating adhesion, these substrates were pre-coated with a thin layer of flat PDMS. To form this initial layer, typically, both polymer parts were used with the previous ratio, with 2.0 g of polymer being dissolved in 10 mL of chloroform. After stirring for 10 minutes, a portion of the solution was used to completely cover a microscope slide. Spin-coating was then used to cast a thin layer of the polymer solution. A speed of 4000 rpm was applied for 25 seconds. The coated glass was subjected to heat for ~1 minute using a heat gun, this was maintained until all the solvent was observed to evaporate. For the rest of the substrates (paper, cardboard and aluminium), no pre-treatment was done and they were used as received.

For PVC, PScMS, and PEG polymers, the polymer was dissolved in chloroform with the same ratio (0.7 g of polymer in 100 mL of chloroform). The solution was stirred for about 15 minutes. No pre-treatment of glass substrates was applied.

2.2.3. Deposition Conditions

An ultrasonic humidifier (PIFCO HEALTH, operating frequency: 40 kHz, power: 25 W) was used to generate an aerosol from the prepared solution. This aerosol was then carried by a flow of nitrogen gas and allowed to cure in a tube furnace, where the activation temperature (temperature inside the tube furnace) was varied from 200-

450°C (for PDMS, and from 60°C to a maximum of 300°C for other thermoplastic polymers, more details could be found in section 2.3.8). The typical temperatures applied for PDMS were: 200, 280, 360, 400 and 450°C. The thermal degradation, light interaction, rough-morphology formation and WCAs were all performed for PDMS samples and the analysis could be found with more details in the results section. The deposition temperature (the temperature at the substrate) was measured by placing a thermometer at the substrate position while the deposition took place.

The substrate was placed outside the furnace, ~1 cm from the furnace outlet (refer to **Figure 2.5**). The carrier gas flow was adjusted to 1.0 L/min and varied later on to examine the effect of changing the flow rate on the properties of the generated films. The deposition process continued for approximately 60 minutes, and it was terminated when the precursor solution was depleted and no more mist was being produced.

2.2.4. Characterisation

IR spectroscopy was carried out using Bruker (Vertex 70) FT-IR (over a wavenumber range of 400 to 4000 cm^{-1} , resolution: 2 cm^{-1}). Light-interaction with samples was examined using Agilent Technologies (Cary 5000) UV-vis-NIR spectrometer (over a wavelength range of 350-800 nm, resolution: 1 nm), by measuring visible-light transmission through the prepared surfaces (the surfaces prepared using AACVD at different curing temperatures and a smooth surface prepared by spin-coating for comparison).

Materials robustness testing was carried out using the application/removal of adhesive tape (Scotch Tape - 600), whereby a portion of the tape was applied to the coating, secured by manually pressing down, and then arbitrarily removed from the surface. A scalpel blade was also used to assess resilience, using a range of pressures to scrap the surface coating.

Kruss (DSA100E) Drop Shape Analyser was used to measure WCAs, using a water droplet volume of 5 μL . This was repeated five times across each sample and the average was calculated. Water bouncing experiments were carried out, whereby water droplets were dropped from a height of 20 mm (tip to the surface) using a micro-syringe fitted with a 27 gauge dispensing tip (unless otherwise stated). The water droplets from this tip were ~8 μL in size and were left to detach under their weight. Methylene blue was added to the water to aid visualisation, this dye addition was not

observed to change the behaviour of the water droplets on the surface. The bouncing was filmed at 1000 frames per second using a SONY RX10-III camera.

SEM imaging was performed using a field emission microscope (JEOL, JSM-7001F) using an acceleration voltage of 10 kV for samples deposited on glass substrates, and 5 kV for the remaining samples (a lower voltage was used as charge accumulation was noticed to be higher on these substrates).

Thermogravimetric analysis (TGA) was conducted for PVC using (TA 209 F1 Libra) under nitrogen flow, with a temperature range of 25°C-950°C and a heating rate of 20°C.min⁻¹. A sample mass of around 4 mg was used for testing.

2.3. Results and Discussion

The experiments conducted in this chapter were designed to fulfil two main aims: i) establishing a room-temperature AACVD deposition of thermosetting polymers and ii) investigating the applicability of extension into incorporating thermoplastic polymers. The results presentation and the related discussion in this section will follow the above sequence.

2.3.1. Deposition of PDMS Elastomer

2.3.1.1. Developing the ta-AACVD procedure

Several factors can affect the deposition process in the AACVD setup. Examples include operating temperature, gas flow rate, solvent properties and others. As the aim is to generate superhydrophobic materials deposited on a substrate, these factors should be adjusted such that the polymer curing is optimum to build a rough structure. While many of these factors have been investigated previously in other reports,^{10,11,15,18-20} moving the deposition process to room temperature necessitates re-optimisation. This section will detail the main factors affecting AACVD deposition and describe the development of the ta-AACVD protocol.

i) Aerosol generator: The type of aerosol generator used can control the size of the generated solution droplets, and hence, the dimension of the rough features formed. An alternative to an ultrasonic humidifier, an atomiser delivery system, has been developed and reported.²¹ Using this system, the average droplet size generated was 0.35 µm, while it is around 45 µm for the aerosol generated by an ultrasonic humidifier. This led to a decrease in the size of surface features (from

~ 1 μm to ~ 100 nm).²¹ In this work, an ultrasonic humidifier was used as indicated in the majority of the previous reports.

ii) The solvent used: Choosing a 'good' solvent is vital for the deposition process, and many requirements should be taken into consideration in this process:

- It should be a solvent in which the polymer is completely soluble, without undergoing unwanted degradation or chain shortening.
- The possibility of generating a mist out of it is important to consider. Some solvents (e.g. water) can be hard to generate an aerosol from due to their high surface tension.²²
- The boiling point of the selected solvent should be lower than the temperature under which the deposition occurs. Otherwise, complete evaporation of solvent would not be ensured, and solvent residuals can affect the deposited polymer particles, leading to softening/reshaping of the formed features. However, it should be noted that solvents with very low boiling points, e.g. acetone, can evaporate before reaching the reactor, resulting in ineffective transfer.
- The solvent should have a high flash point and self-ignition temperature for a safe operation of the experiment. Even though an inert carrier gas is used, the exhaust port opens into an oxygenated atmosphere (air).

Informed by previous reports, chloroform was used. It is a good solvent for PDMS (Sylgard 184), with a boiling point of 61°C (much lower than the temperature range tested) and is considered to be a non-flammable solvent.^{23,24}

iii) Carrier gas: The type of gas carrying the aerosol generated needs to be considered, as well as the flow rate:

- Gas type: gases like oxygen could cause substrate/solvent/polymer oxidation at elevated temperatures, and may even raise safety concerns when the solvent has a flashpoint lower or comparable to the operating temperature. In all deposition experiments reported here, nitrogen gas has been used.
- Gas flow rate: this rate directly affects the residence time of the precursors in the reactor, in turn determining the deposition process. It was observed (when the gas flow rate was tested in this work) that if the flow rate is too fast, the time that precursor droplets spend inside the heated region may be limited, and this may lead to the deposition of a molten layer of polymer that would not preserve any microstructure formed, as both solvent removal and curing were limited. Conversely, too slow gas flow can lead to increased condensation of the aerosol limiting its transfer to the reactor, in addition to promoting the complete

curing of the polymer before reaching the substrate (especially if the distance between the substrate and the gas inlet is considerably large) leading to deposition on the reactor walls instead. The flow rate was subjected to extensive optimisation (see section 2.3.1.7).

iv) Deposition temperature: It is very important to run the experiment at a suitable temperature. Since the heating region is dedicated to solvent evaporation and polymer curing, the temperature should be sufficient to achieve both. However, elevated temperatures could lead to the thermal decomposition of the polymer or precursors. This again highlights the importance of using a low-boiling-point solvent so that when the polymer-curing temperature is reached, the solvent would be evaporated. In this work (*ta*-AACVD experiments), the deposition occurs outside the heater. The term 'deposition temperature' would be used to refer to the temperature at the substrate, which is not exceeding 30°C for the highest temperature tried (400°C). The temperature inside the heater that is used to cure the polymer would be referred to as 'activation temperature'. A range of activation temperatures was tried, starting from 200°C to 400°C. The effect of changing the activation temperature on the coating properties is discussed in detail in the following sections.

v) Substrate position and type: The substrate needs to be placed where polymer curing is expected (d_0 refers to the optimum distance between the substrate and the furnace outlet). Placing the substrate too close or too far from the furnace outlet may lead to having an uncoated substrate (**Figure 2.7**). A too-close positioning ($d_1 < d_0$) would not allow time for the fast gas to slow down, and hence will drive away from the substrate. Placing it too far ($d_2 > d_0$) would increase the loss and minimise substrate coverage. In all the experiments reported here, the substrates were kept outside the heater, 1 cm apart from the gas outlet, which was determined by repeated trialling of different distances.

In addition, since high temperatures are required, the selected substrate should be stable at the operating temperatures. In this work, and since the *ta*-AACVD technique does not require the substrate to be exposed to high temperatures, examples of temperature-sensitive substrates were tried. More information is found in section 2.3.1.8.

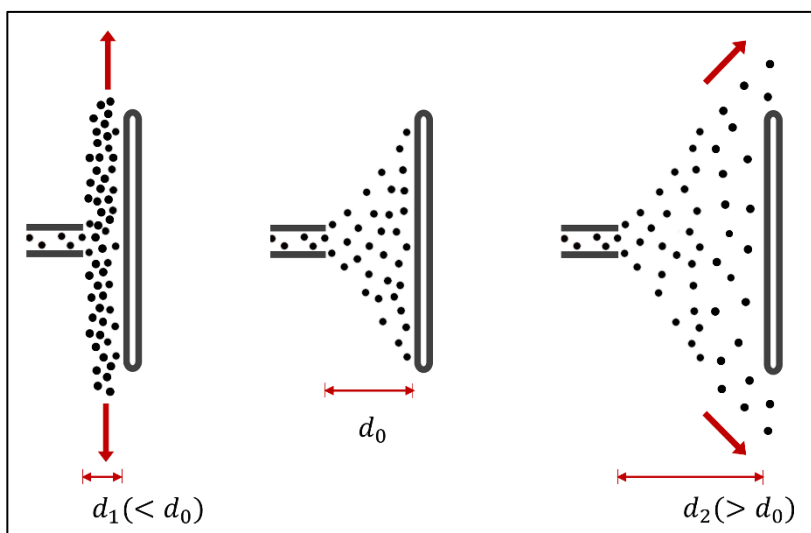


Figure 2.7: Schematic illustrating how the substrate position affects the amount of polymer deposited on its surface. d_0 represents the optimum spacing distance, with d_1

and d_2 are two other distances closer to and further away from the furnace outlet, respectively.

2.3.1.2. Activation and Deposition Temperature

The effect of changing the activation temperature has been investigated in different ways. While the activation temperature varied from 200°C to 400°C, the deposition temperature (measured at the substrate position) did not change significantly. The deposition temperature was found to be around 25°C and did not exceed 30°C when using an activation temperature of 400°C, which means that the deposition occurred at a temperature close to room temperature. Although the deposition temperature was similar for all the samples for different activation temperatures, it was found that activation temperature dramatically affected the deposited films and their properties (Sections 2.3.1.5 and 2.3.1.6).

To ensure that the PDMS polymer is stable at these temperatures and does not undergo thermal decomposition, FT-IR was used. This also allowed confirmation of polymer deposition took place, particularly relevant to transparent samples (the relationship between activation temperature and film transparency would be explained in section 2.3.1.4). **Figure 2.8** shows the IR spectra of a PDMS scratched from a coated glass slide at an activation temperature of 400°C. The main PDMS peaks could be identified: Si-CH₃ stretching and bending peaks at 780, 1257 cm⁻¹, Si-O-Si at 1000 cm⁻¹ and C-H stretching at 2962 cm⁻¹. The spectrum is similar to that obtained from a PDMS sample cured at room temperature.

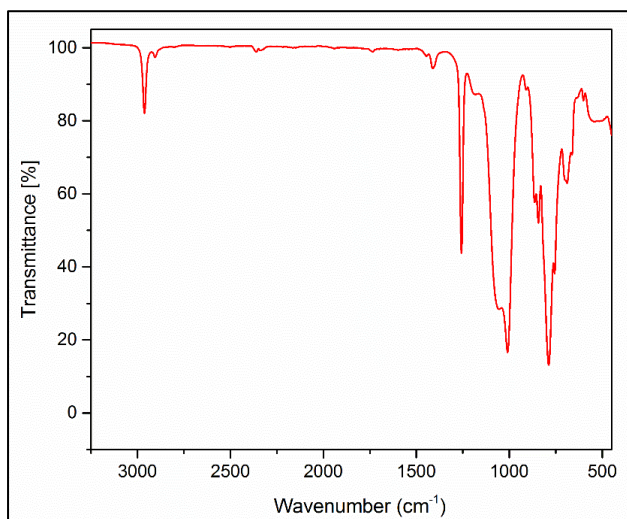


Figure 2.8: IR spectrum of PDMS coating removed from a coated glass slide. The coatings were deposited by AACVD using an activation temperature of 400°C.

2.3.1.3. Physical Robustness

The films prepared at an activation temperature of 400°C (with the highest WCA – Section 2.3.1.5) were tested for physical robustness by applying and removing an adhesive tape^{25–27}, and by a scalpel blade scratching. The films showed resilience to the adhesive tape test, with the coating being largely unaffected. This was comparable to the resilience of the films prepared by traditional AACVD (i.e. where the activation/deposition temperatures were the same). When scratching by a scalpel blade (with a moderate force), the films were largely removed from the substrate.

2.3.1.4. Physical Appearance

The difference in the light interaction behaviour of the PDMS coatings deposited at different activation temperatures is shown in **Figure 2.9**. Starting from the lowest temperature applied (200°C), the deposited film was transparent. Moving to higher temperatures, film transparency decreased gradually, until a completely opaque/white film was achieved at an activation temperature of 400°C. The IR spectra were not observed to change for these different temperatures, which suggests thermal degradation is minimal, and not the cause of the difference in light interaction. As the chemical structure of the polymer is assumed to be consistent, this suggests a change at the micro-level in the polymer structure that made the polymer interact differently with light (allowing for more diffuse reflection and less transparency).²⁸ The transmittance in the visible light region (from 350 to 800 nm) was performed on these substrates to confirm the observation made with the naked eye. The sample deposited at 200°C allowed more than 95% of light to be transmitted, while the sample

done at 400°C allowed less than 2% (**Figure 2.10**). The changes in the polymer microstructure were further investigated by WCA measurements and SEM imaging.



Figure 2.9: PDMS coating on glass substrates deposited using ta-AACVD at activation temperatures of (from left to right) 200, 280, 360 and 400°C. Note; the glass slide shown are microscope slides of typical dimensions (75 x 25 mm).

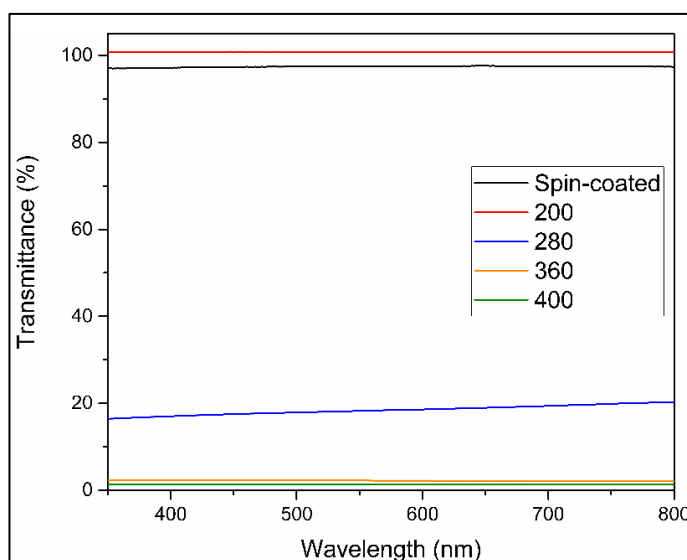


Figure 2.10: UV-vis transmittance spectra of visible light region deposited through ta-AACVD, with samples prepared at activation temperatures of 200, 280, 360, and 400°C (as shown), as well as a PDMS sample prepared using spin-coating for comparison to flat material.

2.3.1.5. Coating Hydrophobicity

WCAs were measured to investigate the effect of changing the activation temperature on the coating hydrophobicity. For the lowest activation temperature applied (200°C), the obtained WCA was 99.4°, which is comparable to the WCAs obtained on flat PDMS (less than 100°).²⁹ This indicates that the deposited film obtained at this lower temperature is nearly flat, with no rough features formed. WCAs for the films deposited at higher activation temperatures show a significant increase, with average WCAs of 127.25°, 140.8° and 143.2° obtained for the PDMS coating made at a temperature of 280, 360, and 400°C respectively. **Figure 2.11** shows photographs of 5 μ L water droplets placed on the surface to measure the WCAs. This increase in WCAs indicates that increasing temperature enhances the surface roughness (as

discussed further in Section 2.3.1.6). For samples prepared at 400°C, the advancing and receding WCAs were 167° and 113.6° respectively. Water bouncing was also performed for this sample, and a single bounce was observed (**Figure 2.12**). While this suggests a WCA around 150°,^{30,31} the other hydrophobicity tests indicated that the sample is rather on the boundary of being superhydrophobic. The WCA recorded for the 400°C-activation temperature sample was found to be the maximum achievable using this technique. Increasing the temperature beyond this (the typical temperature tried was 450°C) was found to decrease the WCA (124.6°). Further discussion is in the following section.

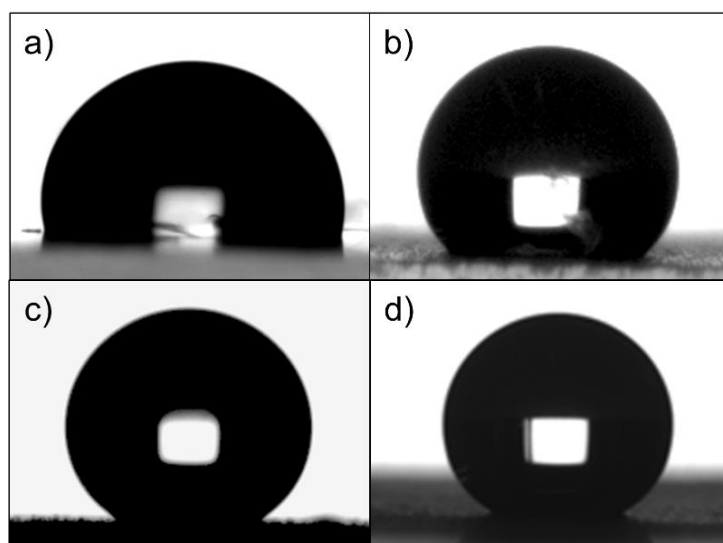


Figure 2.11: Photographs for 5 μL water droplets placed on the substrate to measure the WCAs. The substrates are PDMS-coated using ta-AACVD at different activation temperatures; a) 200, b) 280, c) 360 and d) 400°C.

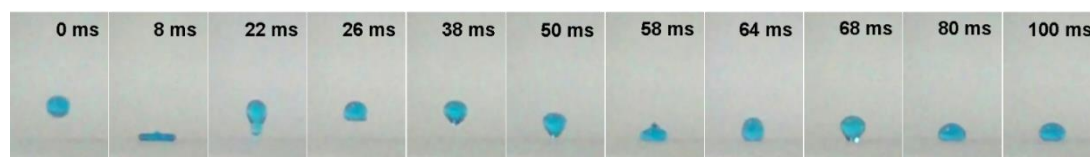


Figure 2.12: Photographs of an 8 μL water droplet (coloured with methylene blue) which were dropped from a height of 20 mm (tip to the surface) and left to bounce on a PDMS-coated glass slide (prepared at an activation temperature of 400°C).

2.3.1.6. Surface Imaging

The prepared samples were imaged using SEM to investigate the roughness of the obtained polymer films (**Figure 2.13**). Starting with the film deposited at an activation temperature of 200°C (**Figure 2.13a**), it was found that little roughness was formed and the surface is generally flat, and only wrinkles with small dimensions are present. To rationalise this, it is important to highlight the curing curve of PDMS (without a solvent). Whereby, at low temperatures the Sylgard elastomer starts at a very slow curing rate, taking around 24 hours to be fully cured at room temperature. This rate

could be increased by raising the temperature, such that the polymer would take less than an hour to be cured at temperatures above 150°C. Since the deposition temperature is very low (compared to the temperature required for fast polymer curing), the activation temperature needs to be high such that the polymer would be almost cured when it exits through the furnace outlet towards the substrate. Accordingly, a 200°C-activation temperature was not enough to cure the polymer in the short time spent in the hot reactor, so the deposition occurs in a molten state, which prevents the preservation of any features that could be formed. In addition, the solvent residuals could re-solvate the polymer, and this would make the surface flat. This agrees with the low WCA obtained.

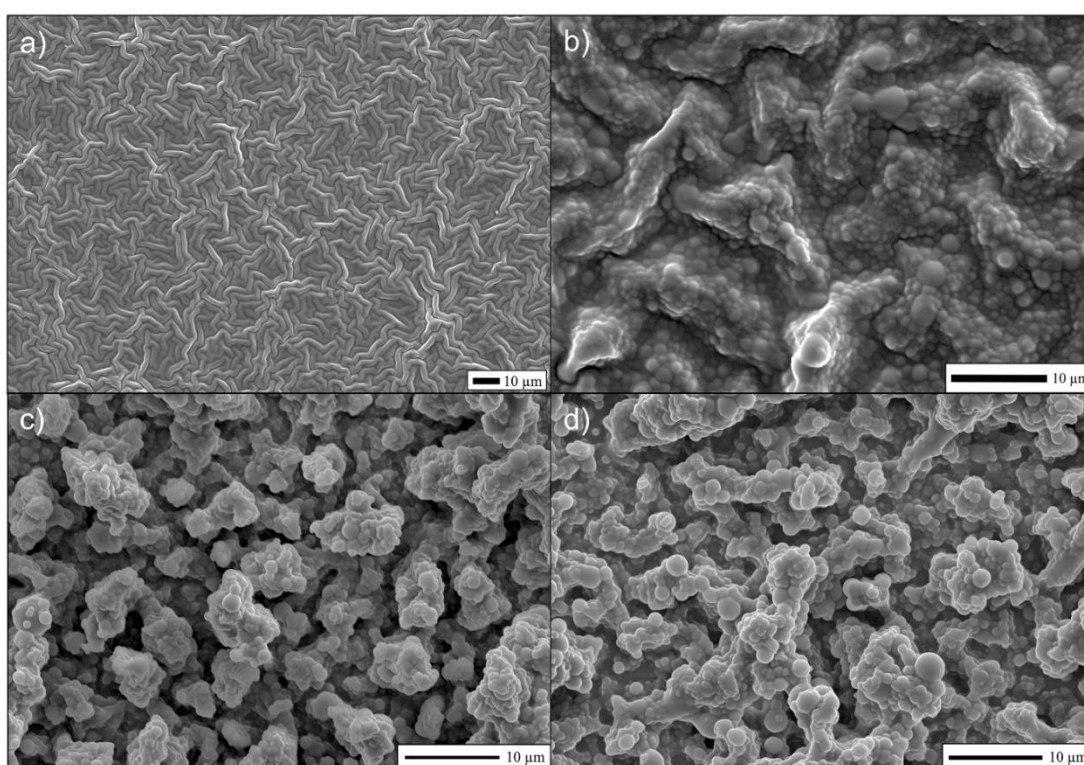


Figure 2.13: SEM images of PDMS deposited onto glass substrates using ta-AACVD at different activation temperatures; a) 200, b) 280, c) 360 and d) 400°C. Scale bars are included for each SEM image.

Increasing the temperature to 280°C (**Figure 2.13b**) allows for the formation of some spherical structures. This is due to the curing of a higher portion of the polymer, and the spherical structure is due to the small aerosol droplets which enter the furnace and be cured in this form. However, there are still some regions where a softened polymer could be found, which means that both polymer curing and solvent evaporation did not take place completely at this temperature. Both the increase in the WCA and the change in the light-scattering behaviour match with the SEM

images, which shows a marked rise in the surface roughness. Moving to a higher temperature (360°C, **Figure 2.13c**), the formation of rough features could be noticed, which led to the increase in the WCA. At 400°C (**Figure 2.13d**), further deposition of rough features occurs, which increases the WCA again. The SEM images of these two samples suggest a high roughness, producing a large amount of light scattering and resultantly low transparency.

Continuing the temperature increase did not produce enhanced coatings. **Figure 2.14** shows an SEM image of a PDMS film deposited at an activation temperature of 450°C. A lower amount of polymer is present, and a larger area of the substrate remained without coating. This could be explained by the faster curing occurring at this temperature that led to the deposition of a considerable amount of the polymer onto the furnace walls, instead of moving with the gas flow towards the furnace outlet. The WCA decreased as well (124.6° was obtained). This suggests that a too-high temperature could affect the film roughness and the water repellence negatively.

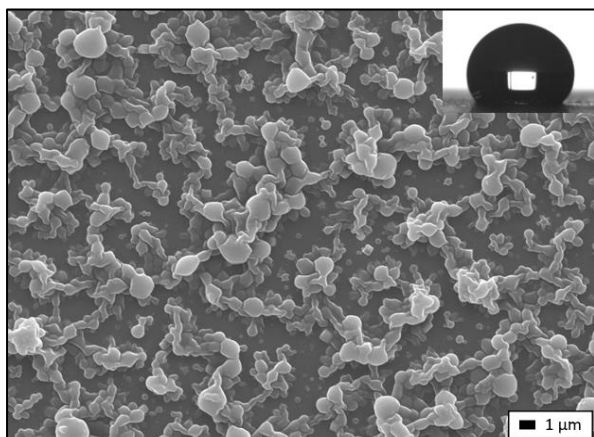


Figure 2.14: SEM image and a photograph used to measure the WCA of a polymer film deposited at an activation temperature of 450°C. Scale bar is included.

2.3.1.7. Other Factors Examined

Along with activation temperature, other factors have been tested/optimised:

- i) **Carrier gas flow rate:** a lower flow rate (0.6 L/min) was evaluated, and a relatively low WCA (~ 90°) coating was obtained. This suggests that the low flow rate allows the polymer to spend more time in the hot region, with most material depositing on the furnace walls. Leaving only a small amount of PDMS to deposit.
- ii) **Deposition time:** longer deposition times that also required larger amounts of the precursor solution were used. This was shown in all cases to decrease the WCA. This could be reasoned by the larger amount of polymer blocking the apparent air gaps (i.e. less roughness) and leaving less trapped air to support water droplets, therefore lowering WCAs.

iii) **Dilution:** preparing diluted precursor solutions was not observed to affect the WCAs. Depositions with the same amount of polymer incorporated in a greater amount of solvent (double the solvent amount was tried, i.e. half the concentration), and with no change in temperature or flow rate were attempted. The depositions took longer to be completed, however, a similar film structure and wetting properties were observed.

2.3.1.8. Temperature-Sensitive Substrates

After determining the optimum deposition conditions, a selection of temperature-sensitive substrates was tested to demonstrate the applicability of this technique to such surfaces. Examples include paper and cardboard, with their thermal instability at high temperatures and their ability to undergo combustion easily are ubiquitous. In addition, aluminium substrates were included, as for aluminium –and many other metals-, exposure to high temperatures could facilitate the formation of an oxide layer on the metal surface. A temperature as mild (compared to AACVD conditions for PDMS deposition) as 200°C could be enough to form a thick oxide layer.³² **Figure 2.15** shows SEM images for the PDMS films deposited on these substrates. The activation temperature applied for the deposition on all these substrates was 400°C. The roughness features formed on these substrates have a similar structure and features of micro-dimensions, which indicates the rough-films deposition is relatively independent of the substrate used and suggests a wider reproducibility with a possibility to coat most conceivable substrates. For these samples, WCAs showed similar results to those described earlier for the PDMS-coating on glass substrates at the same activation temperature. The typical values were 142° for paper, and 143° for both cardboard and aluminium.

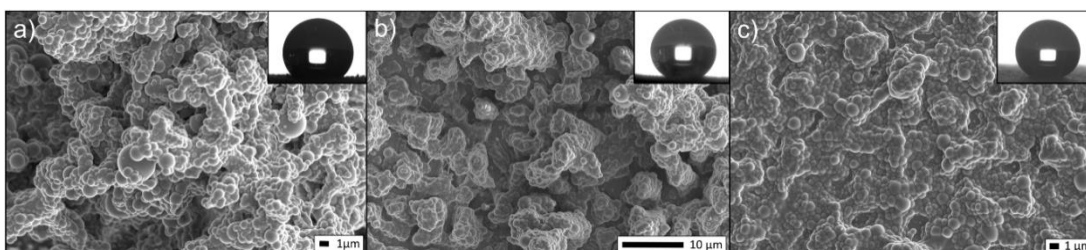


Figure 2.15: SEM images of PDMS films deposited on a) paper, b) cardboard and c) aluminium substrates. Photographs used to measure the WCAs are also included. Scale bars are shown for each image.

2.3.2. Deposition of Thermoplastic Polymers

Extending the application of the AACVD technique to the deposition of thermoplastic polymers has been previously attempted.¹⁰ Dyneon™ FC-2120 (a mixture of polyvinylidene fluoride and polyhexafluoropropylene, with no curing agent added) was used to coat glass substrates, by dip coating as well as AACVD. The flat, dip-coated Dyneon™ FC-2120 layer displayed a good hydrophobicity, with an average WCA of 99°. However, utilizing AACVD did not have a large impact on the measured WCA as expected, as the average CA only reached 104° and the highest recorded was 118°. This was not observed for the other thermosetting polymers that were tried (Sylgard 184 and NuSil Med-4850), where the average WCA for the dip-coated layer was 95°. However, this increased rapidly as AACVD was used at raised temperatures, reaching WCAs around 160° (at 330°C and 390°C for Sylgard 184 and NuSil Med-4850, respectively). This was attributed to the differences between thermoplastic/thermosetting polymers and how they react to heat application. As explained earlier in Section 2.1.1.1, thermoplastic polymers do not cure when the temperature is raised, but they soften and then melt. Hence the development of surface structure was hindered as no curing took place.

The working principle of the ta-AACVD technique with thermosetting polymers depends on the ability of the polymer to cure under high-temperature conditions, and the removal of solvent to avoid re-structuring/re-solvating of the cured polymer spheres. While both AACVD and ta-AACVD share the same principle, the room-temperature deposition featured in ta-AACVD can allow fast solidification of the droplets, which can contribute to the formation of a rough morphology. This section presents the application of ta-AACVD for thermoplastic polymers.

2.3.2.1. *Chemical compatibility*

ta-AACVD was applied with thermoplastic polymers to investigate the possibility of forming superhydrophobic rough surfaces. The hypothesis was that the hot region in ta-AACVD would allow the polymer to melt and the solvent to evaporate, but once the polymer is carried away from this region, the room temperature deposition would allow polymer solidification which will preserve the droplet shape while deposition occurs. The polymers tested were PVC, PEG and PScMS. Chloroform was kept as a solvent, and a range of temperatures was tried.

PVC was found not to be completely soluble in chloroform, which is not ideal for film deposition. The limitations on the choice of solvents hindered finding an alternative.

However, the deposition was observed to take place on the substrate. FT-IR spectra were collected for these coatings to investigate the chemical compatibility (**Figure 2.16**). The figure shows the spectrum of pure PVC powder, as well as spectra of PVC coatings deposited using ta-AACVD at different activation temperatures (100°C, 150°C and 200°C). The spectrum of PVC powder shows peaks at 2968 cm⁻¹ and 2910 cm⁻¹ for asymmetric and symmetric stretching of the C-H bond, respectively.³³ These peaks were a bit shifted in the other spectra (2959 cm⁻¹ and 2924 cm⁻¹) and an extra peak at 2872 cm⁻¹ appeared. The peak at 1427 cm⁻¹ in all spectra is assigned for C-H bending,³³ while an additional peak around 1460 cm⁻¹ appeared in the ta-AACVD-PVC coatings spectra. The peak at 1250 cm⁻¹ is for the bending of the C-H bond near Cl. Again, ta-AACVD-PVC coatings showed an additional peak around 1111-1122 cm⁻¹. This peak indicates the formation of CO₂, along with the strong peak at 1720 cm⁻¹ for C=O stretching, as well as the double peaks at 2361 cm⁻¹ and 2297-2328 cm⁻¹.³⁴ It was clear that the film material analysed was either a denatured PVC or a non-pure polymer (mixture with other contaminants).

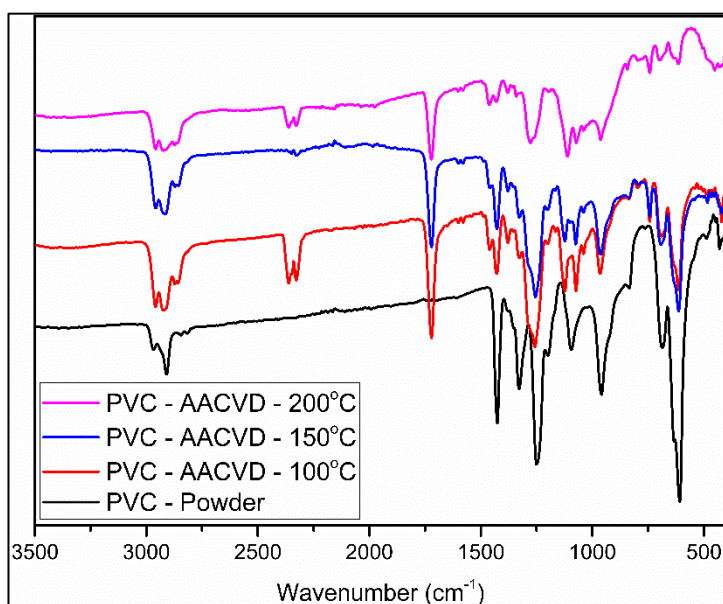


Figure 2.16: FT-IR spectra for powder PVC and PVC films deposited using ta-AACVD at 100°C, 150°C and 200°C.

This thermal degradation of PVC was not expected at the tested temperatures. As indicated from the TGA plot of PVC, the significant mass loss did not take place until 250°C (**Figure 2.17**). However, PVC is known for its heat sensitivity.³⁵ In addition, the TGA was conducted under an inert atmosphere, while in the ta-AACVD, although nitrogen is used to carry the aerosol, the polymer is still exposed to oxygenated air. It was then concluded that the application of PVC was hindered due to chemical compatibility issues.

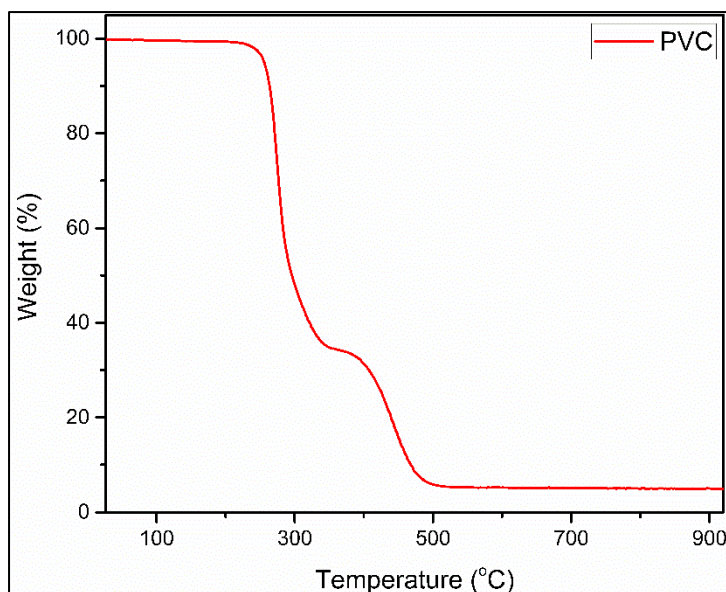


Figure 2.17: TGA plot for powder PVC, showing thermal degradation starting around 250°C.

In contrast to PVC, both PEG and PscMS were soluble in chloroform. PEG coatings seemed to maintain their chemical structure. **Figure 2.18** shows the FT-IR spectra of PEG powder and PEG coatings deposited using ta-AACVD at 60°C, 100°C, 150°C and 200°C. The spectra of the coatings did not show peak alteration from the polymer powder spectrum. The characteristic peaks for PEG were assigned as the following: C-O, C-C stretching and CH₂ rocking at 841 cm⁻¹, 1059 cm⁻¹, 1095 cm⁻¹ and 1146 cm⁻¹, CH₂ twisting at 960 cm⁻¹, 1240 cm⁻¹ and 1279 cm⁻¹, CH₂ wagging at 1360 cm⁻¹, CH₂ scissoring at 1466 cm⁻¹, and C-H stretching at 2879 cm⁻¹.³⁶ Similarly, FT-IR showed that the ta-AACVD of PscMS did not cause polymer degradation (**Figure 2.19**). The deposition was conducted at temperatures of 100°C, 200°C and 300°C. The characteristic peaks for PscMS were assigned as the following: C-H bending at 546 cm⁻¹, 696 cm⁻¹ and 758 cm⁻¹, C-C (aromatic and aliphatic) vibration at 1030 cm⁻¹ and 1076 cm⁻¹, CH₂ wagging at 1381 cm⁻¹, CH₂ scissoring at 1445 cm⁻¹, and C-H stretching at 2926 cm⁻¹.^{36,37}

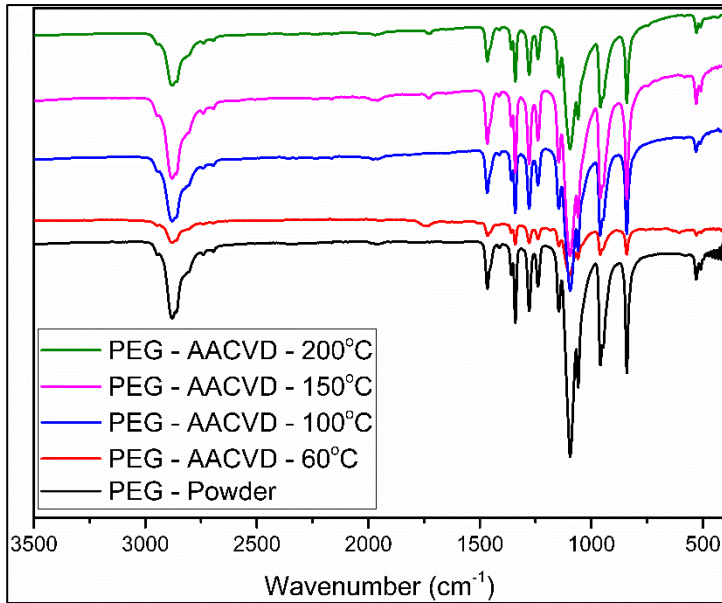


Figure 2.18: FT-IR spectra for powder PEG and PEG films deposited using ta-AACVD at 60°C, 100°C, 150°C and 200°C.

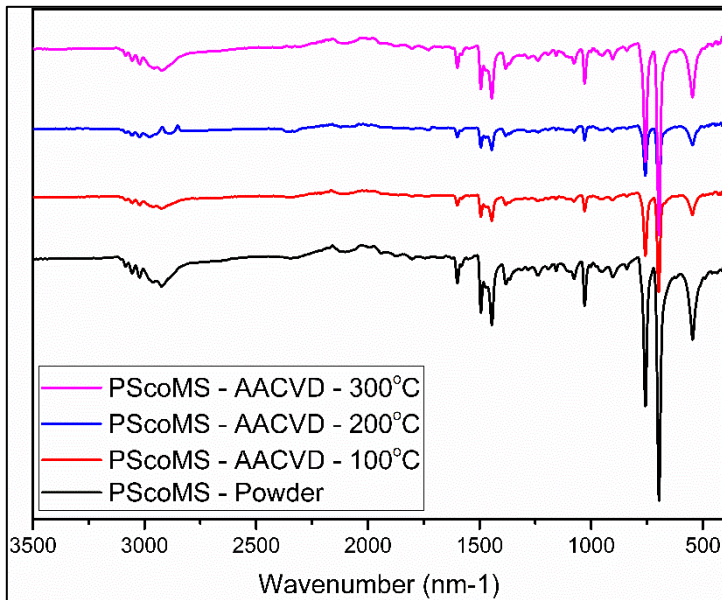
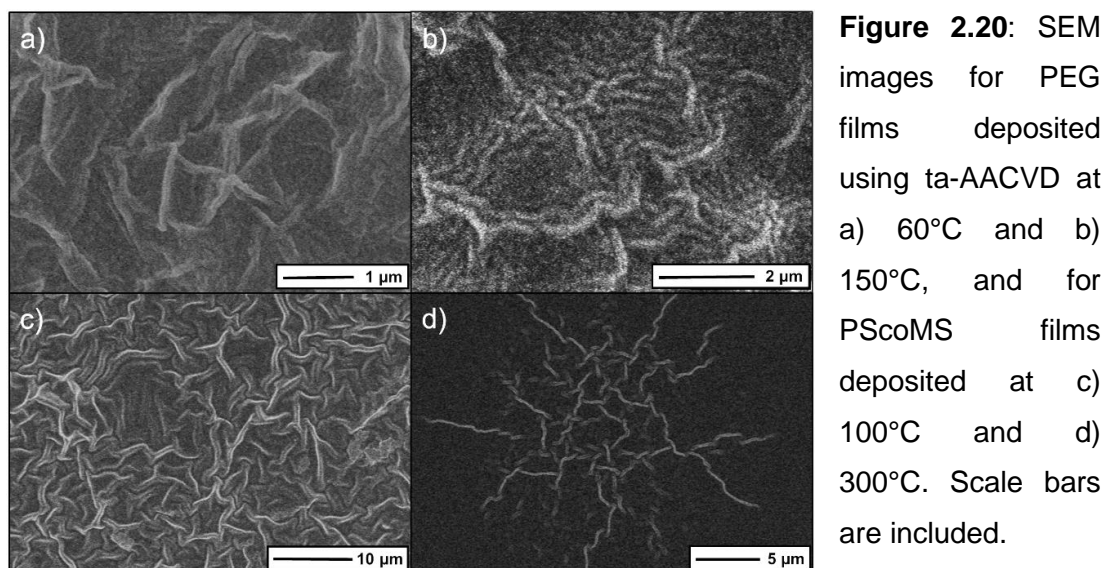


Figure 2.19: FT-IR spectra for powder PScMS and PScMS films deposited using ta-AACVD at 100°C, 200°C and 300°C.

2.3.2.2. Surface roughness

The prepared films were imaged using SEM to discover the polymer microstructure (**Figure 2.20**). It was found that a structure similar to what was obtained for the PDMS coating at 200°C was formed at all the tested temperatures and thermoplastic polymers used. The main feature presented in these images where the formation of polymer wrinkles, but no indication for sphere-like geometries that would increase the surface roughness. Lower activation temperatures (typically 60°C for PEG and 100°C for PScMS, **Figure 2.20**) resulted in the deposition of more polymer into the substrate, but this did not affect the film roughness of these films. Less polymer was deposited when the temperature was raised.



The obtained results suggested that the mentioned hypothesis regarding thermoplastic polymers deposition was not achieved using these conditions/methodologies, and the operating mechanism of ta-AACVD requires using a thermosetting polymer to generate a rough morphology.

2.4. Conclusions

AACVD has been reported to fabricate rough surface coatings from thermosetting polymers, which were shown to possess high water repellence due to their hydrophobic nature and the high degree of roughness.^{10–12,15} However, a limitation of utilizing this technique is the excessive heating required for coating deposition, which confines the choices of substrates. ta-AACVD is a modified version of AACVD, where the setup was re-designed such that the substrate is removed from the heated reactor. The activation of the polymer was achieved by passing the aerosol through a heated reactor by gas flow, where the polymer cures and the solvent evaporates, and then the polymer leaves the reactor and gets deposited on the desired substrate. Although the substrate temperatures did not change significantly, moving to higher activation temperatures was found to enhance the course nature of the microstructure, due to the greater extent of polymer curing. The result is an AACVD process that is highly applicable to a variety of substrates, including those that oxidise/decompose easily at high temperatures. Examples of this type of substrate were utilised to prove the concept and the results were similar to those obtained from samples deposited on glass substrates. Extension of this deposition technique into thermoplastic polymers was found ineffective in generating rough coatings, as the

polymers were melted by the heating action. The thermosetting nature was concluded to be necessary for the formation of structured coatings using this method.

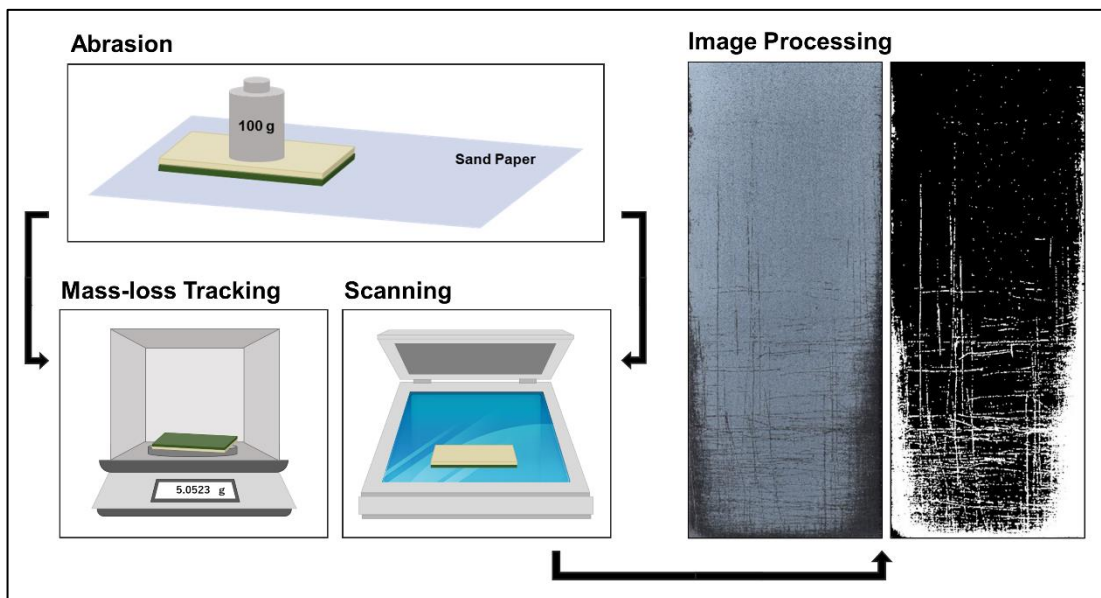
2.5. References

- 1 C. R. Crick, University College London, 2011.
- 2 R. Gordon, *J. Non. Cryst. Solids*, 1997, **218**, 81–91.
- 3 M. R. Zaghoul, *J. Appl. Phys.*, 2004, **95**, 3339.
- 4 M. Hecke and W. K. Schomburg, *J. Micromechanics Microengineering*, 2003, **14**, R1.
- 5 B. S. Hayes and J. C. Seferis, *Polym. Compos.*, 2001, **22**, 451–467.
- 6 V. Diesen, C. W. Dunnill, J. C. Bear, S. Firth, M. Jonsson and I. P. Parkin, *Chem. Vap. Depos.*, 2014, **20**, 91–97.
- 7 A. J. Gardecka, G. K. L. Goh, G. Sankar and I. P. Parkin, *J. Mater. Chem. A*, 2015, **3**, 17755–17762.
- 8 N. P. Chadwick, E. N. K. Glover, S. Sathasivam, S. N. Basahel, S. A. Althabaiti, A. O. Alyoubi, I. P. Parkin and C. J. Carmalt, *J. Mater. Chem. A*, 2015, **4**, 407–415.
- 9 Van Honschoten J W, E. M. T. N. R and E. M, *J. Colloid Interface Sci.*, 2009, **329**, 133–139.
- 10 C. R. Crick and I. P. Parkin, *Thin Solid Films*, 2010, **518**, 4328–4335.
- 11 C. R. Crick and I. P. Parkin, *J. Mater. Chem.*, 2009, **19**, 1074–1076.
- 12 C. R. Crick, J. A. Gibbins and I. P. Parkin, *J. Mater. Chem. A*, 2013, **1**, 5943–5948.
- 13 E. Ozkan, C. C. Crick, A. Taylor, E. Allan and I. P. Parkin, *Chem. Sci.*, 2016, **7**, 5126–5131.
- 14 C. R. Crick, J. C. Bear, P. Southern and I. P. Parkin, *J. Mater. Chem. A*, 2013, **1**, 4336–4344.
- 15 C. R. Crick and I. P. Parkin, *Thin Solid Films*, 2011, **519**, 2181–2186.
- 16 C. R. Crick, J. C. Bear, A. Kafi and I. P. Parkin, *Adv. Mater.*, 2012, **24**, 3505–3508.
- 17 Y. A. Mehanna, R. L. Upton and C. R. Crick, *J. Mater. Chem. A*, 2019, **7**, 7333–7337.
- 18 C. R. Crick, S. Ismail, J. Pratten and I. P. Parkin, *Thin Solid Films*, 2011, **519**, 3722–3727.
- 19 C. R. Crick and I. P. Parkin, *J. Mater. Chem.*, 2011, **21**, 14712–14716.
- 20 C. R. Crick and I. P. Parkin, *J. Mater. Chem.*, 2011, **21**, 9362–9366.
- 21 C. R. Crick, V. Clausen-Thue and I. P. Parkin, *J. Nanosci. Nanotechnol.*, 2011,

- 11, 8358–8362.
- 22 N. Vargaftik, B. Volkov and L. Voljak, *J. Phys. Chem. Ref. data*, 1983, **12**, 817–820.
- 23 R. K. Henderson, C. Jiménez-González, D. J. C. Constable, S. R. Alston, G. G. A. Inglis, G. Fisher, J. Sherwood, S. P. Binks and A. D. Curzons, *Green Chem*, 2011, **13**, 854–862.
- 24 D. R. Branch, A. L. S. S. Hian and L. D. Petz, *Tech. Note*, 1982, **42**, 46–53.
- 25 B. Wu, J. Lyu, C. Peng, D. Jiang, J. Yang, J. Yang, S. Xing and L. Sheng, *Chem. Eng. J.*, 2020, **387**, 124066.
- 26 C. Peng, Z. Chen and M. K. Tiwari, *Nat. Mater.* 2018 174, 2018, **17**, 355–360.
- 27 T. Zhu, Y. Cheng, J. Huang, J. Xiong, M. Ge, J. Mao, Z. Liu, X. Dong, Z. Chen and Y. Lai, *Chem. Eng. J.*, 2020, **399**, 125746.
- 28 Peng Wang, Mingji Chen, Huilong Han, Xiaoliang Fan, Qing Liu and Jinfeng Wang, *J. Mater. Chem. A*, 2016, **4**, 7869–7874.
- 29 B. He, J. Lee and N. A. Patankar, *Colloids Surfaces A Physicochem. Eng. Asp.*, 2004, **248**, 101–104.
- 30 C. R. Crick and I. P. Parkin, *Chem. Commun.*, 2011, **47**, 12059–12061.
- 31 C. R. Crick and I. P. Parkin, *J. Mater. Chem. A*, 2013, **1**, 799–804.
- 32 L. P. . Jeurgens, W. . Sloof, F. . Tichelaar and E. . Mittemeijer, *Thin Solid Films*, 2002, **418**, 89–101.
- 33 M. Pandey, G. M. Joshi, A. Mukherjee and P. Thomas, *Polym. Int.*, 2016, **65**, 1098–1106.
- 34 M. Sanati and A. Andersson, *J. Mol. Catal.*, 1993, **81**, 51–62.
- 35 Y. Kanade, How Thermal Degradation Of Pvc Occurs During Processing? | LinkedIn, <https://www.linkedin.com/pulse/how-thermal-degradation-pvc-occurs-during-processing-yashodhan-kanade/>, (accessed 11 February 2022).
- 36 N. S. Vrandečić, M. Erceg, M. Jakić and I. Klarić, *Thermochim. Acta*, 2010, **498**, 71–80.
- 37 Moulkheir Ayat, Mohamed Belbachir and Abdelkader Rahmouni, *Bull. Chem. React. Eng. Catal.* , 2016, **11**, 376–388.

Chapter 3:

Quantitative Imaging Analysis of Coating Abrasion



Publications:

Image analysis methodology for a quantitative evaluation of coating abrasion resistance. Y. A. Mehanna and C. R. Crick. *Applied Materials Today*, 2021, **25**, 101203(1-6).

Contributions:

MATLAB Code: Sourcing the base code and contributing to code development was carried out by Dr Osama Maklad (University of Greenwich).

3. Quantitative Imaging Analysis of Coating Abrasion

3.1. Introduction

While a considerable amount of research has been conducted to produce superhydrophobic surfaces using a broad spectrum of materials, fabrication methods, resultant properties, and wide-ranging targeted applications, the impact of these surfaces on everyday materials is currently limited.¹⁻³ While this is caused by many factors (Section 1.5), the low physical resilience of these surfaces stands as one of the main challenges against wider applicability.^{2,3} The main reason for this is the surface architecture consisting of micro and/or nanoscale features.^{4,5} Although these small-scale features provide surface roughness that is essential for super-repellent properties (in addition to an inherent chemical hydrophobicity), they are fundamentally weak and are therefore susceptible to breaking with minimal physical loads.^{3,6}

In response to this challenge, the fabrication of surfaces with improved resilience is needed (Chapter 4), as well as the development of Characterisation methods to assess coatings resilience and to evaluate their behaviour against physical loads. This section gives a brief overview of the current methods reported for the assessment of coating resilience.

3.1.1. Current Methods for Assessment of Coating Resilience

In general, testing the resilience of a coating involves two main steps: i) applying a physical load on the coating, and ii) subsequent analysis of how the surface changes in response to this load. There is a wide variety of reported methods for each step, which allows finding a suitable alternative for a different range of coatings/applications.

3.1.1.1. *Abrasion techniques*

The physical load applied can take various forms, and range in the scale of testing between nano, micro and macro-scale.^{1,3} Common examples involve tape peeling,^{7,8} sand abrasion,^{9,10} linear abraders (nanoindenter,¹¹⁻¹³ micro-abraders,^{14,15} etc.), pencil hardness,¹⁶⁻¹⁸ cross-cutting,^{19,20} sand impact,^{21,22} in addition to others (**Figure 3.1**). While nano/microscale tests are highly precise and capable of providing information on a range of mechanical properties of the coating, they involve using advanced equipment.¹⁴ In addition, results obtained from small-scale testing may be hard to

implement to understand how the coating will react to large-scale real-life challenges. The information extracted using these techniques does not directly indicate the general performance, and in most cases, it is very specific to the region of the material tested. Macroscale tests can give more insight into sample performance in real-life applications, however, there is a lack of consistency in many chosen methodologies throughout the literature, as many simulate physical challenges associated with a specific application.¹

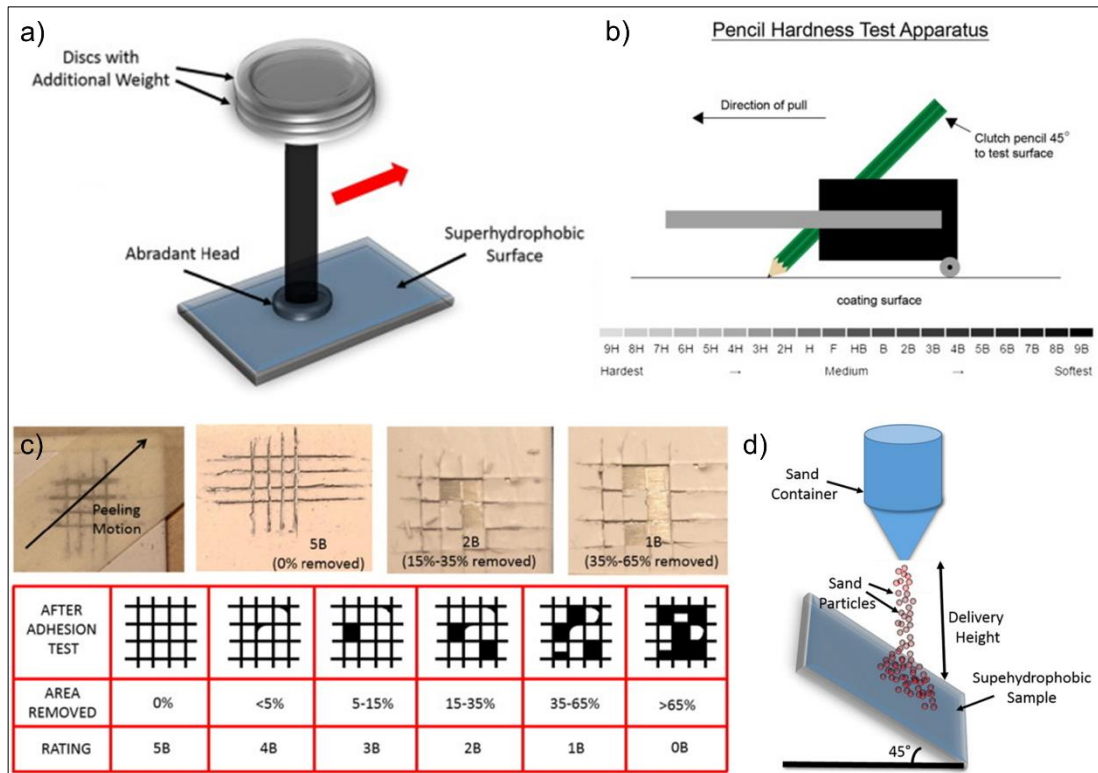


Figure 3.1: Examples of common abrasion methods. a) A linear abrader setup, where the abrading head (dimensions can vary depending on the desired scale of damage) moves across the surface. Different weights can be loaded to change the force applied on the surface. b) Pensile hardness is conducted by dragging a tilted pencil (with a quantified hardness) across the surface at a constant speed. The hardness scale is shown in the figure. The hardness of the surface is defined by the maximum pencil grade the surface tolerates without leaving a permanent mark. c) Cross-cut testing involves scratching the surface horizontally and vertically to make a square grid. In many cases, this can be followed by tape peeling. The percentage of areas removed is compared against a scale (shown in the figure). d) Sand impact is measured by releasing a known mass/size of sand particles from a fixed height on a 45°-tilted surface, followed by assessing the surface damage. Figure retrieved from ref.¹

3.1.1.2. *Post-abrasion assessment*

Along with the variation in methods used to apply a physical load, there is also a range of approaches adopted to analyse the coating damage afterwards. Many of these methods are considered to be complex, non-quantifiable, and/or lack reliability. Many reports examine the effect of abrasion on superhydrophobic properties, e.g. by measuring WCAs or other hydrophobicity measurements.^{9,23–25} While this approach is simple, there are many limitations to its implementation. Firstly, physical degradation may occur unevenly, which alters the WCA values accordingly, providing significant variance across the examined surface. This issue is intensified when serious degradation occurs, with some parts of the coating are completely removed, partially exposing the substrate material during measurement (further discussed in Section 3.3.4). In addition, the change to WCA is not only linked with the physical loss of roughness but also reflects changes in chemical degradation and air-retention ability. Hence using WCAs to conclude on surface resilience could be misleading, as it is an indirect measure. Another example of mentoring superhydrophobic properties is measuring the slip length.²⁶ Superhydrophobic surfaces entrap air as a result of their roughness, reducing the drag as water flows on these surfaces.^{26–28} The change in slip length (the ratio of slip-velocity to the shear rate at the surface) with shear rate could be traced and used to conclude on surface degradation.²⁶ Similar to WCAs, the change in slip length is linked also to the loss in air retention, which could happen by air displacement with water even if no physical degradation has occurred.³ Other reports relied on the high precision of nanoindenters to quantitatively measure the lateral force required for scratching a coating and get information on the coating hardness.^{29–31} As discussed earlier, these tests are very local and not always relatable to real-life performance.

Visualisation of the surface after physical degradation is one of the most straightforward approaches to tracking surface failure, as it does not involve monitoring other properties/effects. There is a range of surface visualisation techniques that have been implemented. Two-dimensional imaging using optical microscopy or SEM has been reported.^{14,32–34} While these can differentiate uneven coating removal patterns, they are considered to be generally qualitative. 3D imaging with optical confocal or atomic force microscopy (AFM) can achieve quantitative analysis, and provide a detailed presentation of roughness changes.^{25,35,36} However, along with the relative complexity of these methods, they also suffer from drawbacks with limited resolvable distances (in optical microscopy) and incomplete imaging of roughened surfaces (in AFM). Imaging techniques have a great potential for wider

applicability in post-degradation analysis, as they are relatively simple, informative and provide reliable indications of sample performance. Therefore, efforts to develop imaging-based methodologies and tailor them to meet the applicability requirements are highly important. However, current reports addressing this are limited. One example, reported by Nielsen *et al.* for anti-reflective coatings, combined the use of micro-abraders and the processing of optical microscope images to quantitatively track surface degradation.¹⁴ This work addressed many issues with current imaging techniques, by reducing complexity, introducing quantification and providing a methodology to assess micro-scale scratches. However, examples targeting macro-scale analysis are very rare in the literature. Also, current imaging techniques provide information on coating adhesion failure (including complete coating removal/deep scratches), but lacking insight on coating cohesion (i.e. superficial coating removal). As a result, there is further need for accessible methodologies that target quantitative macroscale analysis.

3.1.2. Chapter Aim

In this chapter, a straightforward imaging methodology is presented, which combines facile macroscale sandpaper abrasion with basic scanning and image processing to deliver quantified information on coating removal. In addition, this was combined with the monitoring of the coating mass-loss with abrasion cycles and used to differentiate between superficial coating removal (cohesion failure – coating-coating binding) and deep scratches (adhesive failure - coating-substrate binding). This method possesses great potential in the analysis of any coating that can be optically differentiated from the substrate, with any macroscale abrasion method causing visual damage. While this technique was applied here for superhydrophobic coatings, it demonstrated applicability across other fields.

Here, coatings prepared from polymer/nanoparticle composites (further details could be found in Section 4.1.3) and deposited using spray coating were utilised to develop the imaging technique. The chapter discusses the process of establishing the technique, where the selection of the analysis components was built based on the nature of the coatings and how fast they degrade. Then, the development of an image-processing tool is presented along with an investigation of its efficiency. Moreover, the results of mass-loss tracking were combined and a thorough discussion of the significance of these results is followed.

3.2. Experimental Methods

3.2.1. Materials

Sylgard-186 Silicone Elastomer (Two parts: PDMS and a silicon-based curing agent) was purchased from Ellsworth Adhesive Ltd. Low M_w PVC (48,000, product number 81388), silicon dioxide nanopowder (10-20 nm), and HMDS (reagent grade, $\geq 99\%$) were purchased from Sigma Aldrich. Hexane (HPLC grade), tetrahydrofuran (THF, $\geq 99.5\%$, laboratory reagent grade), and toluene ($\geq 99.8\%$) were purchased from Fisher Scientific Limited. Glass microscope slides purchased from ThermoScientific were used as the substrates. Adhesion promoter (CYN20 Stick 2 Industrial Grade General Purpose Superglue - cyanoacrylate based) was purchased from EverBuild. Sandpaper sheets (23 × 9 cm) were purchased from Miady.

3.2.2. Silica Hydrophobization

A solution of HMDS (1 mL) in toluene (100 mL) was added to a suspension of as received silicon dioxide nanopowder (SiO_2 , 10 g) in toluene (250 mL) and refluxed at 120°C for 24 hrs with magnetic stirring. The hydrophobized nanoparticles were centrifuged, washed with toluene (twice) and ethanol (twice) for purification, dried at 90°C overnight and stored dry under ambient conditions.

3.2.3. Coating Preparation

The determination of polymer/silica/solvent formulation with the appropriate mass ratios (M_{ratio}) was investigated (detailed in previous work).²³ Here we applied the ratios that were reported as most superhydrophobic. The PVC coating solution was prepared by dissolving PVC (0.1 g) in THF (30 mL) by stirring until fully dissolved (typically ~15 minutes). Hydrophobized silica nanoparticles (0.235 g, polymer/silica $M_{\text{ratio}} = 0.426$) were then added and the mixture was stirred for 4 hours to ensure complete polymer/nanoparticle mixing.

PDMS coating solutions were prepared by mixing both parts of the Sylgard 186 elastomer as recommended by the manufacturer (with a ratio of 10:1, total polymer mass = 0.5068 g), adding hexane (70 mL) and stirring until dissolved. Hydrophobized silica nanoparticles (0.2586 g) were added to 50 mL of the PDMS solution and stirred and room temperature for an hour (note: this stirring time was reduced compared to that used for PVC to prevent premature onset of thermosetting reaction). The remainder of the polymer solution was retained to use with the adhesive, as explained in the following section.

3.2.4. Coating Deposition

Spray-coating processes, illustrated in **Figure 3.2**, were carried out in line with previous reports using a compression pump and airbrush gun (made by Voilamart), at a pressure of 2 bar.^{9,23} The coating suspensions (Section 3.2.3) were sprayed onto glass substrates, with all spraying carried out approximately 4 cm away from the surface.

For PVC coatings, glass slides were pre-heated at 100°C for 30 min. Approximately 8 mL of the solution was sprayed per glass slide at the same temperature. Coated slides were left for a few seconds until fully dried (**Figure 3.2a**).

PDMS coatings involved a pre-coating step (spraying with an adhesive layer) to promote higher robustness. This was made by spreading 8 drops (~ 150 μ l) of adhesion promoter (CYN20) manually over the slide (using the edge of another microscope slide) and then placing it on a 50°C-adjusted hotplate to spray approximately 4-5 mL of PDMS/hexane solution. This was allowed to partially cure by heating the coated slide at the same temperature for 15 min (**Figure 3.2b**). The slides then were moved to a 120°C-adjusted hotplate to spray ~8 mL of the PDMS/silica solution. The coated slides were allowed to fully cure on the 120°C hotplates for 30 min (**Figure 3.2c**).

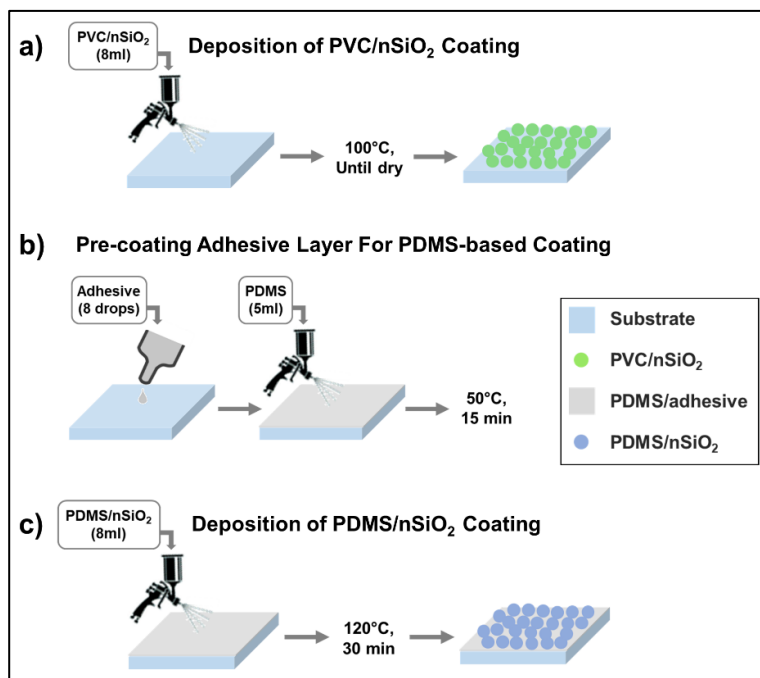


Figure 3.2: Schematic showing the coating deposition procedure for; (a) PVC/nSiO₂ coatings, (b) pre-coating adhesive layer for PDMS-based coatings, (c) PDMS/nSiO₂ coatings.

3.2.5. Resilience Assessment

All glass slides were weighed before and after coating, as well as after each abrasion cycle to track the mass loss during the abrasion process. The weight was measured twice (or until getting two readings with a maximum difference of ± 0.0004 g) and the average was taken. Sandpaper abrasion was carried out as previously reported.^{9,23} The coated glass slide was placed face-down onto sandpaper (grit no. 120) with a 100 g-weight placed on top of it. Both the glass slide and the weight were pushed for 10 cm, before being turned 90° and moved for a further 10 cm to complete one cycle (**Figure 3.3**).

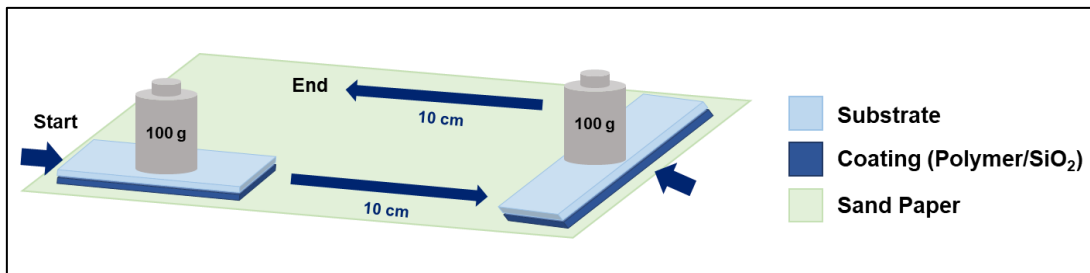


Figure 3.3: The abrasion cycle applied during degradation testing. The coated substrate was placed face-down onto sandpaper (grit no. 120) with a 100 g-weight placed on top of it. Both the substrate and the weight were pushed for 10 cm, turned 90° and moved for a further 10 cm to complete one cycle.

After each cycle, the slide was scanned using Epson Perfection V39 Scanner (resolution used: 600 dpi), using a black paper card as backing to ensure a dark background for high contrast in the scanned images (**Figure 3.4**). As the coatings used were white in colour and were deposited on a transparent substrate, this made the areas where the coating was removed appear black in the coloured images. The slide was also scanned before abrasion (at 0-cycle) for reference. All images were converted to binary using MATLAB to extract the percentage of remaining coating. This was done by applying a cutting threshold on the RGB values of the images (RGB stands for Red Green Blue, primary colours that form other synthetic colours. These are coded on 256 levels from 0 to 255, such that black is R=0, G=0, B=0 and white is R=255, G=255, B=255). Points that have an RGB value higher than this threshold (more white, with coating on) are replaced with a black pixel, and points with a value lower than the threshold are replaced with a white pixel (**Figure 3.5**). More details on the code development are discussed in Section 3.3.2.

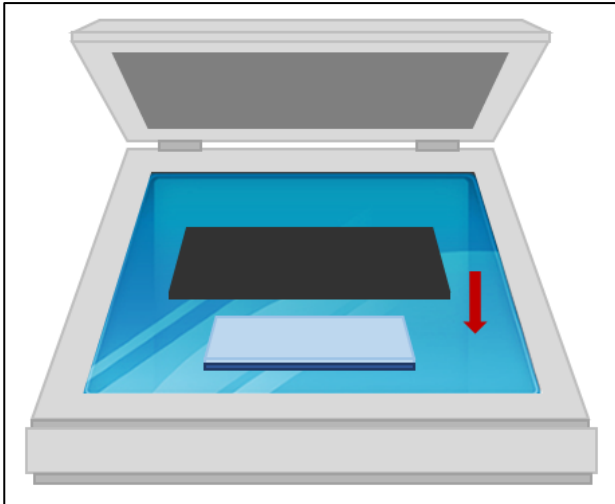


Figure 3.4: The scanning setup. The coated substrate was placed face-down with a black paper card on top of it to ensure a dark background for high contrast.

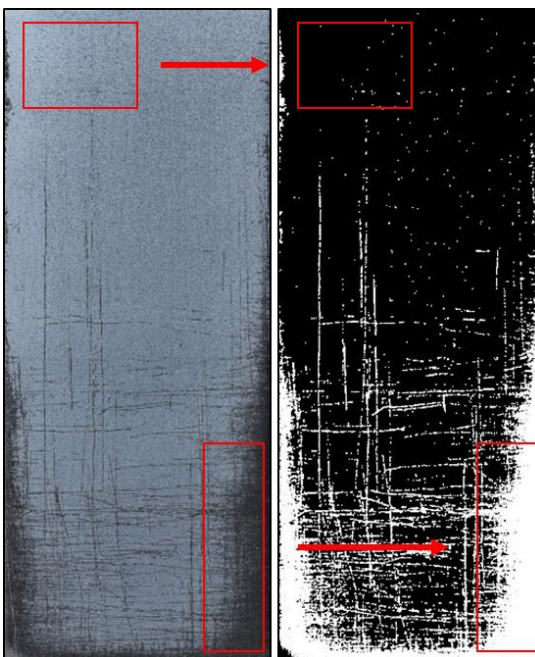


Figure 3.5: An example of a scanned image and its binary copy. Areas seen as white in the coloured image (with coating on) have an RGB value higher than the threshold and hence transformed to black pixels in the binary image. The opposite happens with areas seen as black in the coloured image (coating being removed and the black background being exposed).

3.3. Results and Discussion

3.3.1. Establishing the Technique

This section highlights the three main components of this technique: abrasion, imaging/image processing and mass detection, and elaborates on the chosen conditions for each component. This discussion aims to investigate the suitability of these conditions for the examined samples.

3.3.1.1. Abrasion conditions

The abrasion method used for the coatings reported was sandpaper abrasion, due to its straightforward procedure and its compatibility with the substrate/coatings systems (i.e. a suitable degree of hardness). This abrasion methodology was able to leave

apparent degradation scratches with each cycle, which allowed the tracking of the gradual degradation of the coatings. This process can be altered depending on the type of coating being tested and its resilience, by varying the force (applied weight) and/or the sandpaper grit. The conditions used can also be selected based on the type of challenges expected in a particular application field. For example, the 100 g weight and 120 grit sandpaper used are estimated to be comparable to forces experienced by the handling of everyday items (e.g. cell phones).

3.3.1.2. *Selecting imaging method*

Imaging the substrates was firstly done using a digital camera. This was not convenient due to the difficulty faced in maintaining a consistent light exposure for each image. The image brightness was noticed to be easily affected by minor changes in camera and/or substrate positioning, as well as the changes in the surrounding lighting. As a result, the post-processing of these images was not reliable, as it was highly influenced by this change in brightness. This means that, since the coatings used here were white and a black background was used, a dimmer image would have less white/black contrast, and hence some dim areas with no apparent damage could be confused with black regions where the coating has been removed. This will lead to a conclusion of a higher percentage of coating removal compared to a brighter image, even if the brighter image was actually more damaged (e.g. from a subsequent abrasion cycle). **Figure 3.6** shows images of a PDMS/SiO₂ coating (prepared by mixing different SiO₂ particle sizes – details indicated later in Chapter 4). It can be noticed that images for the (2nd, 3rd, 4th, 6th and 8th) cycle are less bright than the images for the (1st, 5th, 7th, 9th and 10th) cycle, and hence their binary images (the procedure for generating the binary images is detailed in Section 3.3.2) appear with more background noise and less percentage of coating remained. To overcome this problem, a scanner was used to image the substrates. This was shown to produce better images as it ensured a consistent light exposure, and hence the average brightness of the collected images would only differ as a result of the amount of coating on the substrate.

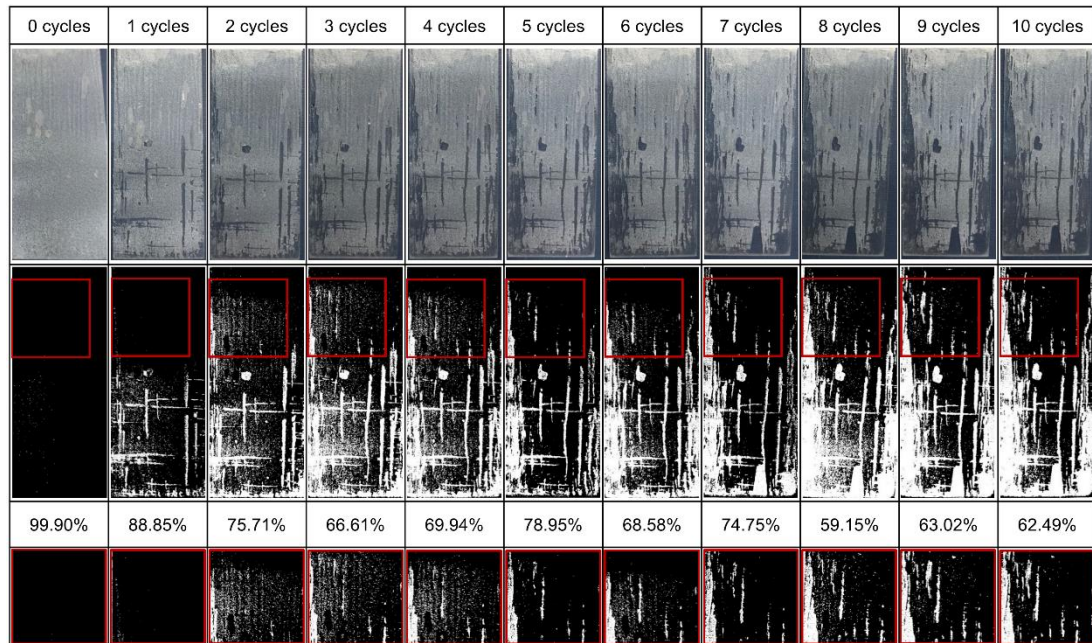


Figure 3.6: The images of a PDMS/SiO₂ coating after each abrasion cycle (taken by a conventional camera), and the produced binary images (applied threshold = 100). The percentage of black pixels (percentage of coating remaining) is indicated for each binary image. The last row shows magnified images for the top-left sample region highlighted by red squares in the binary images, demonstrating the inconsistency of the noise for each image.

3.3.1.3. Mass detection

The substrates were weighed before and after coating, and the difference was taken to obtain the coating weight. This was repeated after each abrasion cycle to detect the change in the coating weight with abrasion. The weighing was done using a high sensitivity benchtop balance, able to detect changes in weight up to 0.0001 g. The coated substrates usually had masses over 5 g, and the change in mass between each cycle (although can differ significantly) would mostly be ≥ 0.0010 g and was never seen to be less than 0.0005 g. As a result, the error in each measurement was considered low, particularly in combination with repeated reading for each cycle and repeated experiments for each coating type.

3.3.2. Developing the Code for Image Processing

3.3.2.1. Influence of threshold on the generated binary images

As explained in section 3.2.5, the binary-image generation occurs by transforming pixels in the coloured image with black/white dots. This is determined by the RGB value of each pixel and by the value of the selected threshold. The threshold value

directly affects the ratio of white/black pixels, and hence changes the appearance of the produced binary image, varying how much it related to the original coloured image. **Figure 3.7a** shows a PVC coating after 10 abrasion cycles, and different binary images produced using different thresholds. As expected, applying a too low threshold reduced the number of scratches that get detected and reflected in the binary image. On the contrary, thresholds that were too high could intensify the thickness/lengths of the scratches in a way that does not match with what is noticed visibly, and also increase the background noise (TH = 90; **Figure 3.7a**). **Figure 3.7b** shows the same concept by plotting the percentages of black pixels (percentages of coating remained) through the whole abrasion cycles tested, as calculated using different thresholds.

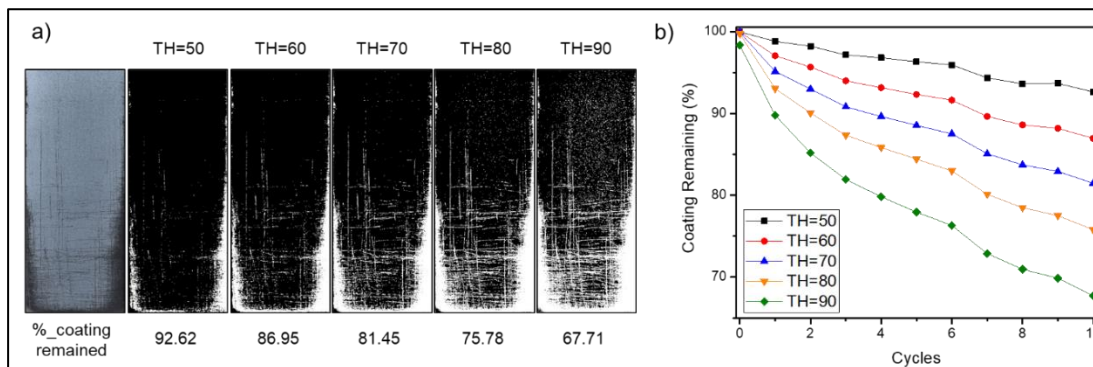


Figure 3.7: The effect of the threshold value on the ratio of white/black pixels on the produced binary images, illustrated by a) showing different threshold applications on the same image and b) a plot of the percentages of black pixels (percentages of coating remaining) vs. abrasion cycles.

3.3.2.2. Threshold-selection code conceptualization

Since the threshold selection can highly affect the generated binary images and hence influence the conclusions, it was important to automate the threshold selection to minimise bias in the choices made and to produce reliable data. After trialling approaches, the method of choice was tracking the average RGB value of the image and checking how it changes after each cycle. When the white coating (high average RGB value) is removed, more of the black background appears, and therefore, the average RGB value becomes lower. The decrease in the average RGB value for images can be used as an indication of material removal. This change could be represented as a plot of average RGB value vs. abrasion cycles. The slope of this plot depends on the amount of coating removed. Such that, when a lower amount of coating material is being removed with each cycle, a lower slope of average RGB values (vs. cycles) is apparent. This slope is referred to here as " $Slope_{RGB}$ ". As seen

in **Figure 3.7**, the threshold application transforms the image into a ratio of white/black pixels, with this ratio increasing with increasing the applied threshold. Again, this ratio could be represented as a plot of the percentage of black pixels (percentage of coating remained) vs. cycles. The slope of this plot is referred to here as “ $Slope_{Black}$ ”. The threshold selection code was optimised to make a choice based on the value of these two slopes and selects the threshold that produced a $Slope_{Black}$ matching with the $Slope_{RGB}$. As both are directly correlated to the appearance of the image and its colour distribution, this approach was selected as the most suitable manner of picking the applied threshold.

3.3.2.3. Threshold-selection code description

The code consists of three sections with three “for” loops. The first loop calculates the average RGB value for each image in the sample image set (from cycle_0 to cycle_10) and gets the slope of average RGB vs. cycles ($Slope_{RGB}$). The second loop starts with a threshold = 20, calculates the percentage of black pixels for each image using this threshold and gets the slope of the percentage of coating remaining vs. cycles ($Slope_{Black}$, with another variable, $Slope_{Black_old}$ initially have a value = 0). The loop ends with an if statement to check the absolute difference between $Slope_{RGB}$ and $Slope_{Black}$. If:

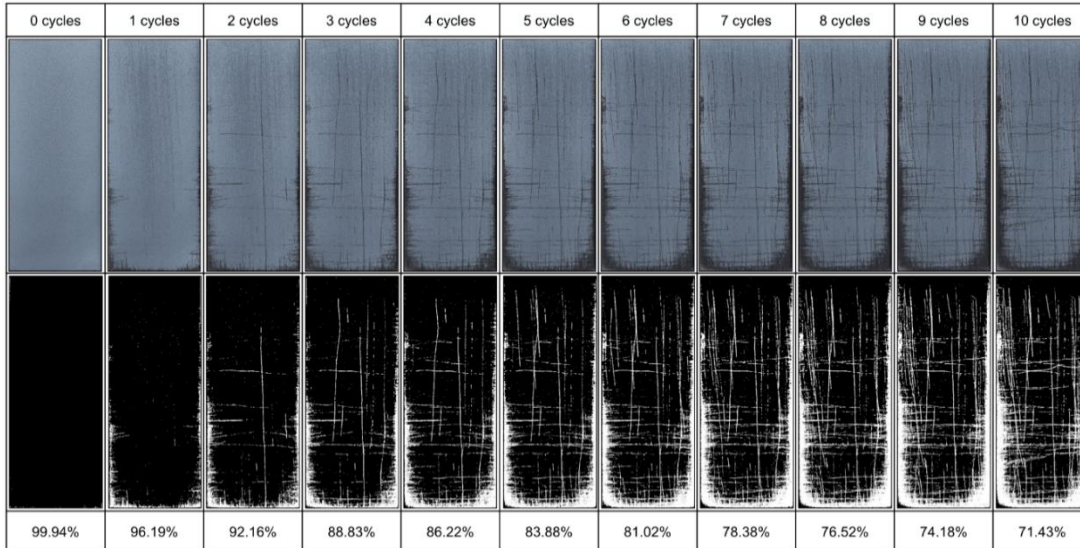
$$Abs(Slope_{RGB} - Slope_{Black}) \leq abs(Slope_{RGB} - Slope_{Black_old})$$

the value of $Slope_{Black}$ gets stored in $Slope_{Black_old}$ and the loop continues to test another threshold (the old threshold + 1). Once $abs(Slope_{RGB} - Slope_{Black})$ gets higher than $abs(Slope_{RGB} - Slope_{Black_old})$, i.e. the threshold is too high that its slope is steeper than $Slope_{RGB}$, the loop breaks and the code selects the previous threshold (the current threshold that broke the condition – 1). The final loop runs the images at the selected threshold to generate the binary images. The code utilised is found in Appendix 1.

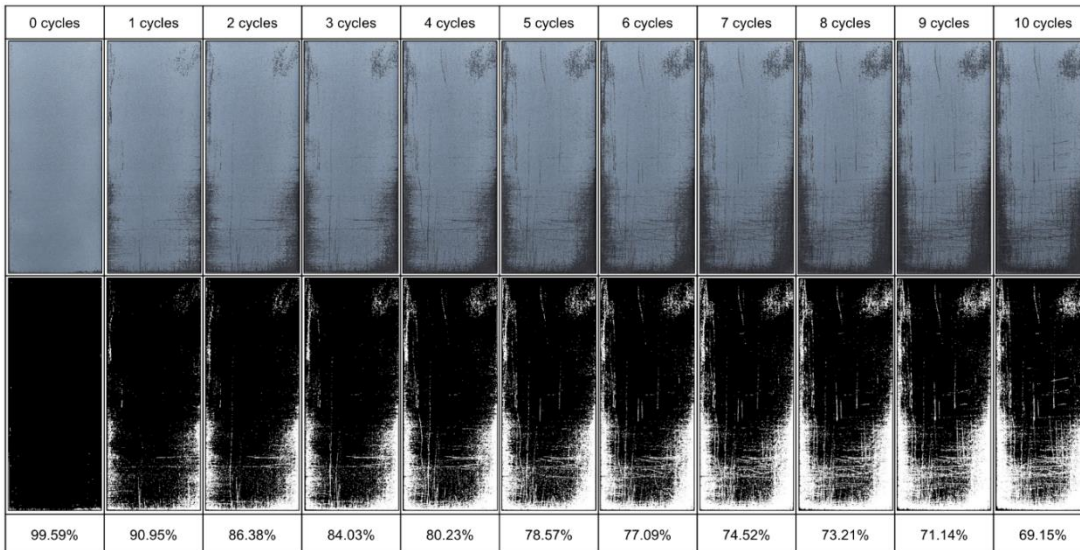
Figure 3.8 shows the processing of PVC and PDMS coatings, with three runs carried out for each coating type. For each run, the images taken for the ten abrasion cycles are shown, along with the binary images produced and the corresponding values for the percentage of coating remaining after each cycle. **Table 3.1** lists the average RGB values for these images and their slope, as well as the applied threshold for each sample run.

Figure 3.8: The full image sets for the sample runs of PVC (a-c) and PDMS (d-f) coatings, showing the coloured (upper), binary (lower) images, and the associated percentage of coating remained as predicted by image analysis.

a) PVC – Run No.1:



b) PVC – Run No.2

























c) PVC – Run No.3

0 cycles	1 cycles	2 cycles	3 cycles	4 cycles	5 cycles	6 cycles	7 cycles	8 cycles	9 cycles	10 cycles
99.86%	94.34%	91.86%	89.44%	88.20%	86.98%	85.80%	83.16%	81.70%	80.83%	79.19%























d) PDMS – Run No.1:

0 cycles	1 cycles	2 cycles	3 cycles	4 cycles	5 cycles	6 cycles	7 cycles	8 cycles	9 cycles	10 cycles
99.99%	97.81%	96.31%	94.09%	92.25%	89.85%	87.87%	85.69%	83.29%	80.68%	78.54%

e) PDMS – Run No.2:

0 cycles	1 cycles	2 cycles	3 cycles	4 cycles	5 cycles	6 cycles	7 cycles	8 cycles	9 cycles	10 cycles
										
										
99.99%	95.30%	93.60%	92.53%	91.47%	88.91%	87.60%	86.42%	85.74%	84.24%	84.41%

f) PDMS – Run No.3:

0 cycles	1 cycles	2 cycles	3 cycles	4 cycles	5 cycles	6 cycles	7 cycles	8 cycles	9 cycles	10 cycles
										
										
100.00%	94.51%	93.10%	90.10%	86.87%	84.80%	82.83%	78.93%	79.12%	79.13%	77.37%

Sample	Run	Curve	0	1	2	3	4	5	6	7	8	9	10	Slope
PVC	Run_1	RGB_average	134.58	128.28	122.90	119.25	116.46	114.50	111.90	109.68	108.21	106.57	104.56	-2.770
		%_coating remained (TH=64)	99.94	96.19	92.16	88.83	86.22	83.88	81.02	78.38	76.52	74.18	71.43	-2.760
	Run_2	RGB_average	144.90	137.06	132.40	129.70	125.74	124.14	122.49	120.19	118.81	117.04	115.52	-2.637
		%_coating remained (TH=63)	99.59	90.95	86.38	84.03	80.23	78.57	77.09	74.52	73.21	71.14	69.15	-2.665
	Run_3	RGB_average	144.90	141.91	139.07	136.54	135.06	133.35	131.96	129.72	128.30	127.46	126.15	-1.824
		%_coating remained (TH=74)	99.86	94.34	91.86	89.44	88.20	86.98	85.80	83.16	81.70	80.83	79.19	-1.844
PDMS	Run_1	RGB_average	126.95	122.83	120.97	118.40	116.55	114.36	112.43	110.56	108.33	106.19	104.02	-2.172
		%_coating remained (TH=53)	99.99	97.81	96.31	94.09	92.25	89.85	87.87	85.69	83.29	80.68	78.54	-2.146
	Run_2	RGB_average	139.22	136.65	134.85	133.02	132.05	129.60	128.08	126.87	126.02	124.75	124.44	-1.493
		%_coating remained (TH=44)	99.99	95.30	93.60	92.53	91.47	88.91	87.60	86.42	85.74	84.24	84.41	-1.471
	Run_3	RGB_average	147.17	143.85	141.87	138.70	135.80	133.80	131.53	128.17	127.82	126.91	125.20	-2.228
		%_coating remained (TH=49)	100.00	94.51	93.10	90.10	86.87	84.80	82.83	78.93	79.12	79.13	77.37	-2.209

Table 3.1: The full list of RGB values and %_coating remaining for the sample runs discussed, indicating how the slope of both curves matches, supporting the choice of the applied threshold for each sample run.

3.3.2.4. Evaluating the dependence on other variables

It is important to check the dependence of the change in RGB values on other possible factors. This would help anticipate the sources of errors and test their significance. An example is the dependence on the initial RGB value (before abrasion). Different coatings could differ in their initial RGB value. This occurs when the coating is less white, either because it is partially transparent (common with very thin films) or because the coating composition contains materials with a range of colour intensities. The possibility of an initial low RGB value driving the choice of lower threshold values has been investigated. Different abrasion/imaging runs of PVC and PDMS coatings have been made, and the RGB value of cycle_0 images was compared to the thresholds chosen by the code for each run (**Table 3.2**). It was noticed that, although PVC_Run_1 and PVC_Run_2 have initially different RGB values, the applied threshold was similar for both as the change of RGB values with abrasion cycles followed a similar trend. The same conclusion could be made about PVC_Run_2 and PVC_Run_3, where the initial RGB values matched yet different thresholds were applied. PDMS runs support this conclusion too, whereby the threshold choice is affected by how RGB values change throughout the abrasion experiment and not by the initial RGB value. This is indicated by PDMS_Run_1 having the lowest RGB value and the highest applied threshold compared to the other two PDMS runs.

Sample	PVC			PDMS		
Run	Run No.1	Run No.2	Run No.3	Run No.1	Run No.2	Run No.3
Average RGB value of (0_cycle) image	134.58	144.90	144.90	126.95	139.22	147.17
Applied threshold	64	63	74	53	44	49

Table 3.2: Comparing the average RGB value of the 0_cycle image with the threshold selected by the code for the sample runs discussed.

An additional factor is that the change in RGB value may not be solely related to the visibly noticed scratches, but also to superficial coating removal. As the top layers of the coating are removed through abrasion, the images become less white, even if complete removal has not taken place. To evaluate the significance of this, **Figure 3.9** shows two different parts of the same sample (PVC – 10_cycle), with one of them dominated by complete coating removal and the other undergoing mainly superficial loss. Comparing the average RGB value for these parts (noting the average RGB

value of the same regions before abrasion), it can be noticed that the difference caused by the deep scratches is much more significant.

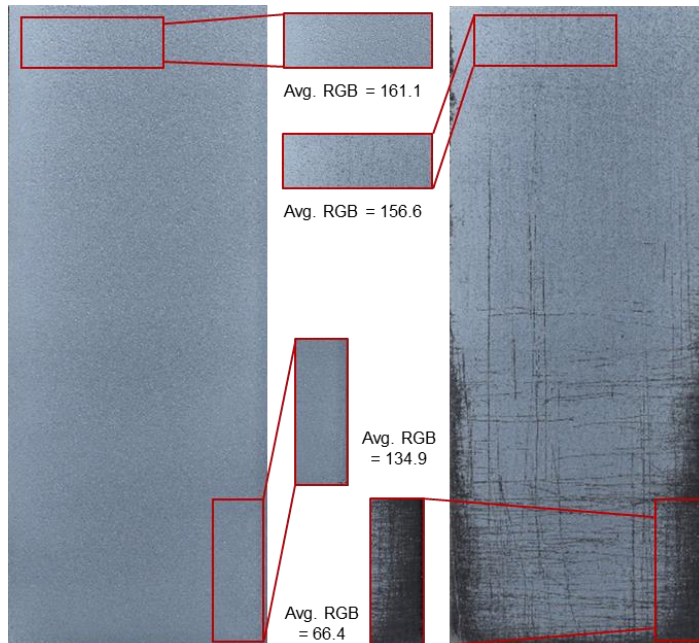


Figure 3.9: Calculating the RGB value from two different parts of a PVC coating after 10 abrasion cycles. One area is dominated by superficial coating removal and the other has deeper scratches.

3.3.3. Mass-loss Trend

To support the conclusions reached with image processing and to gain a greater level of understanding of coating degradation pathways, image processing was complemented with tracking the loss in the coating mass with each abrasion cycle. To obtain the coating mass, the substrate was weighed before the coating deposition and this was subtracted from the substrate weight obtained after the deposition. This process was repeated after each abrasion cycle to track how the coating mass changes with abrasion. These data were expressed and utilised in two ways:

- i) **As a percentage of the original coating weight:** which was obtained by dividing the coating mass after each abrasion cycle by the original coating mass. This quantity is referred to here as the percentage of coating remained by mass loss tracking (**Equation 3.1**).

$$Coating\ mass\ remained_{(after\ x\ cycles)}\ (%) = \frac{Coating\ mass\ (cycle\ x)}{Coating\ mass\ (cycle\ 0)} \times 100 \quad (3.1)$$

While this representation is informative in terms of how resilient the coating is, the information obtained can be maximised when comparing the percentages of coating remained both by image analysis and mass tracking. This will be discussed in section 3.3.3.1.

- ii) **By comparing the mass loss after each cycle:** this was obtained by subtracting the coating mass for every two consecutive cycles and normalised by dividing by the mass of the coating before abrasion. This quantity is referred to as the mass difference or the change in mass (**Equation 3.2**).

$$\begin{aligned} \text{Mass difference}_{(\text{cycle } x)} \\ = \frac{\text{Coating mass}_{(\text{cycle } x)} - \text{Coating mass}_{(\text{cycle } x-1)}}{\text{Coating mass}_{(\text{cycle } 0)}} \quad (3.2) \end{aligned}$$

This quantity indicates how fast the coating is degrading, which will be discussed in section 3.3.3.2.

3.3.3.1. Mass-tracking in comparison with image processing

By comparing the mass loss results with the values extracted by the image analysis, further conclusions can be drawn. This is because mass-loss data represents many types of failure, including both superficial coating removal and deep observable scratches, while image analysis primarily detects the latter. Therefore, the correlation between the projected amount of remaining coating by both mass-loss and image analysis may allow us to infer the mechanism of degradation. **Figure 3.10a** plots the percentage of coating remained (by mass tracking and image analysis) for PVC and PDMS coatings, and **Figure 3.10b** shows the scanned images/binary images for cycle_10 for each sample run for PVC and PDMS and indicates the percentage of coating remained after the final abrasion cycle. It could be observed that the percentage of the remaining coating after 10 abrasion cycles for PVC sample runs via mass-loss tracking (26%, 41% and 45%) was significantly different from those obtained by image analysis (71%, 69% and 79%, respectively). The image analysis values were consistently higher than the mass-loss measurements. This difference suggests that there is mass being lost that cannot be observed visually, suggesting superficial removal of the coating taking place. The tendency for a high level of superficial damage also implies that the cohesion of the coating components (polymer/nanoparticle) primarily contributes to the coating failure. Conversely, the percentage of remaining coating for the PDMS samples measured via mass-loss (88%, 85% and 80%), compared to that obtained by image analysis (78%, 84% and 77%, respectively), has provided similar values. This indicates that the failure principally occurs with the complete removal of coating material, further suggesting the failure originates from adhesion weaknesses.

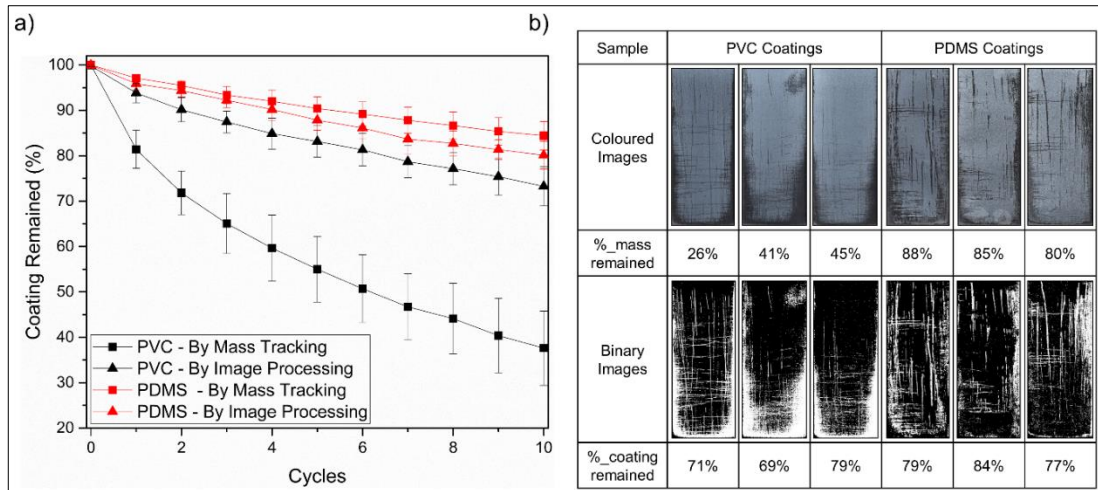


Figure 3.10: a) A plot of the percentages of remaining coating for PVC and PDMS coatings, as indicated by mass-loss tracking and as predicted by image analysis. b) Images (scanned and the equivalent binary) of PVC and PDMS coatings after 10 abrasion cycles, with percentages of coating remained indicated.

The higher percentages of mass-loss in comparison to those obtained by image analysis in PDMS coatings (noticed most with the 1st run with percentages at cycle_10 of 88% and 78% by mass tracking and image analysis, respectively) can be attributed to scratches that reveal the underlying substrate, but result in material that has curled up and remain attached to the surface instead of being completely removed (**Figure 3.11**). Degradation via this mechanism means this mass was still measured while not being detected by image analysis.



Figure 3.11: Scanned image of PDMS coating after 10 abrasion cycles. The image shows that for some parts of the coating, although has been removed leaving a scratch behind, they curled and remained hanging on the surface instead of being completely detached. This can be seen as brighter white dots on the image, like those highlighted with red circles.

Overall, the insight into cohesive/adhesive failure could not be made solely with optical imaging, which makes combining both imaging and mass-loss tracking highly advantageous.

3.3.3.2. Mass difference

Another way to utilise mass tracking data is to check the mass difference. While this can give a direct indication of how much coating was removed/remained, this can also be used to further explore the coating failure. **Figure 3.12** plots the mass difference for PVC and PDMS samples. This plot indicates how intensely failure tends to be initiated and how fast it drives further failure. For example, it can be noticed that the PVC coating undergoes a large mass loss during the first abrasion cycle, with the step between the zeroth and first cycle mass being double that between the first and second cycle. As abrasion continues, proportionally less coating is being removed during each cycle. This indicates that these PVC samples are highly affected by abrasion and show a rapid initial failure pattern. For the PDMS samples, not only a higher amount of coating remained after the abrasion was complete (as indicated in **Figure 3.10**), but the PDMS samples also showed a slower pattern of degradation. The mass difference between every two consecutive cycles is relatively consistent, suggesting that failure initiation and propagation occur at comparable rates.

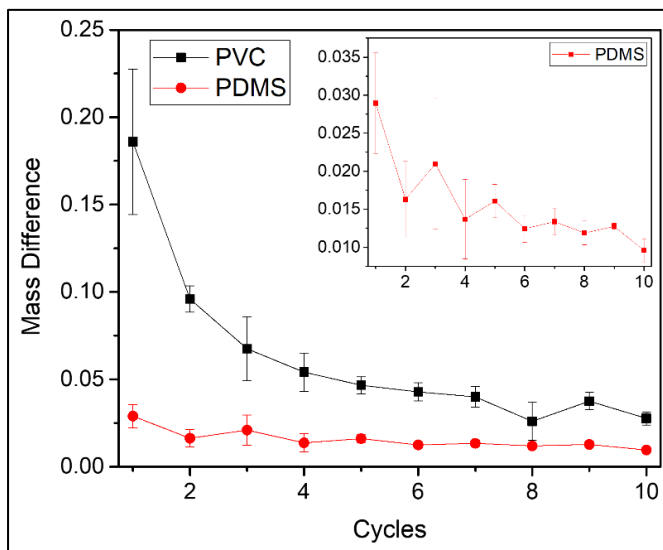


Figure 3.12: A plot of the difference in mass between every two consecutive cycles (normalised by dividing by the original coating mass) vs. abrasion cycles. This is shown for PVC and PDMS coatings. The inset plot shows PDMS coatings at a magnified scale.

This section highlights the tracking of the change in coating mass with abrasion and illustrates how this can help extract more information on coating degradation patterns. While the mass difference indicates how fast the degradation was initiated and propagated, comparing the percentages of coating remained by mass tracking and image analysis allows making conclusions on the adhesion/cohesion failure mechanisms.

3.3.4. Advantages, Limitations and Possible Adjustments to Different Sample Requirements

The presented methodology for degradation analysis has tremendous potential for wide adoption, due to its simplicity with respect to the information that could be extracted. As discussed in the introduction, relying on tracking the change in hydrophobicity (e.g. measuring WCAs) can be limited and, possibly, misleading. For hydrophobicity measurements to be reliable, the abrasion should be occurring evenly across the coating, which is difficult to ensure. As a demonstration, **Figure 3.13** shows WCA measurements taken for a PDMS coating and how it changes with abrasion cycles. For each cycle, 8 readings were taken on different areas of the coating using a 5 μL water droplet. Although the trend shows a decrease, it can be noted that the error in each cycle reading is getting higher, which is because of the uneven removal of the coating that makes hydrophobicity change dramatically across the coating. It is important to mention that, while some areas produced a visible scratch, the WCA sometimes occurred to be high due to the droplet being partially carried by surrounding coating, although using a different method (e.g. applying a water jet) showed water residuals in such areas.

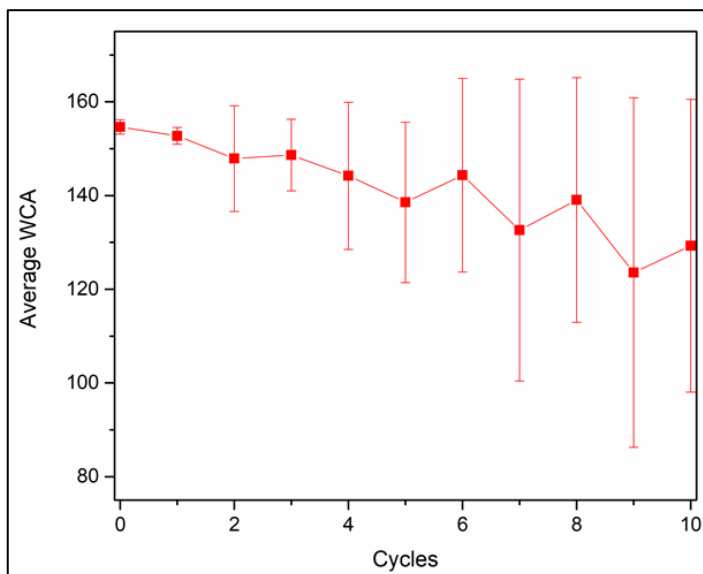


Figure 3.13: WCA measurements for a PDMS coating undergoing sand-paper abrasion. After each abrasion cycle (including cycle 0), 8 readings were taken using a 5 μL water droplet.

If coating imaging only is utilised, information on cohesion vs. adhesion failure is hard to gain without using a 3D imaging technique, e.g. confocal microscopy. While here, tracking changes in coating mass has substituted (to some extent) the need to investigate the third dimension. The primary benefit of the methodology is that it can be used to quantitatively compare different sets/formulations of the same coating (e.g. variation of coating starting materials and/or deposition conditions). The resultant effect that these differences have on coating resilience can easily be probed using

the suggested technique. Owing to the straightforward procedure, analysis of a relatively large variety/sets of samples is feasible on both time and cost aspects.

There are however some limitations to this method, which primarily emerge from the fact that all the changes in (i) sample colour, (ii) coating degradation and (iii) mass loss need to be detectable:

- i)** Firstly, the coatings need to be visually distinguishable from the underlying substrate. While the substrates used here were transparent, it is expected that it would be sufficient to have the substrate of a different colour than the coating, and the code can be easily altered to pick that colour shade. For example, in a system where a red substrate and a white coating are utilised, the removal of the coating would lower the green and blue values only in the average RGB, while the red values would remain high. In this case, the code can be modified to look for the change in the green and blue values only instead of the whole RGB values. However, in materials where both the coating and substrate are colourless (or have the same colour), visual detection will be challenging. This limitation with similarity of the colour of substrate/coating can be tackled by dyeing one of the components to make it distinguishable from the other one, although this may not be applicable in some formulations.
- ii)** In addition, the coating degradation should be observable using the abrasion techniques, such that they need to leave a visible mark on the coating, while not removing the coating too easily. This can be optimised using the reported method, by altering the mass (and therefore force) applied to the samples, or the grade of sandpaper used accordingly. While the generated scratches could possibly not be visible to the naked eye, they could be monitored using a more advanced imaging method, e.g. optical microscope.
- iii)** Finally, if the mass loss is relatively minor, this may be hard to detect with standard means (i.e. bench-top balance). This may add a layer of complexity as advanced/precise weighing techniques are needed.

Materials that do not meet these specifications will require more advanced techniques for investigation, i.e. 3D imaging, in place of this straightforward methodology. With its current design, this analysis method could be widely applicable, and adjustments can be considered if special requirements are needed.

3.4. Conclusions

The development of a quantitative assessment technique for measuring coating resilience was discussed in this chapter. The abrasion methodology was optimised for the samples selected for testing (PVC/SiO₂ and PDMS/SiO₂), followed by scanning and weighing the substrate after each abrasion cycle. The scanned images were processed based on the average RGB values and used to produce binary images with percentages of the coating remaining after each cycle. Coating remaining percentages were also deduced by tracking the loss in the coating mass. As the scanned images detect primarily deep scratches, while the coating mass reflects both deep and superficial coating removal, comparing these two data sets allowed for differentiating between each coating removal pattern and highlighted failure mechanisms initiated by cohesion and/or adhesion weaknesses. This was demonstrated for PVC samples, where the percentage of the coating remained (deduced from mass-loss tracking) after ten cycles was significantly lower than the percentage indicated by image processing, suggesting that cohesion failure is taking place for these samples. This methodology presents a straightforward and effective way of evaluating coating resilience. The imaging technique presented is expected to be applicable to any coating degradation process, provided the removal of material is optically distinguishable. This method provides quantitative insight into understanding coating degradation and, if adopted, would allow for the design and fabrication of ever stronger materials.

3.5. References

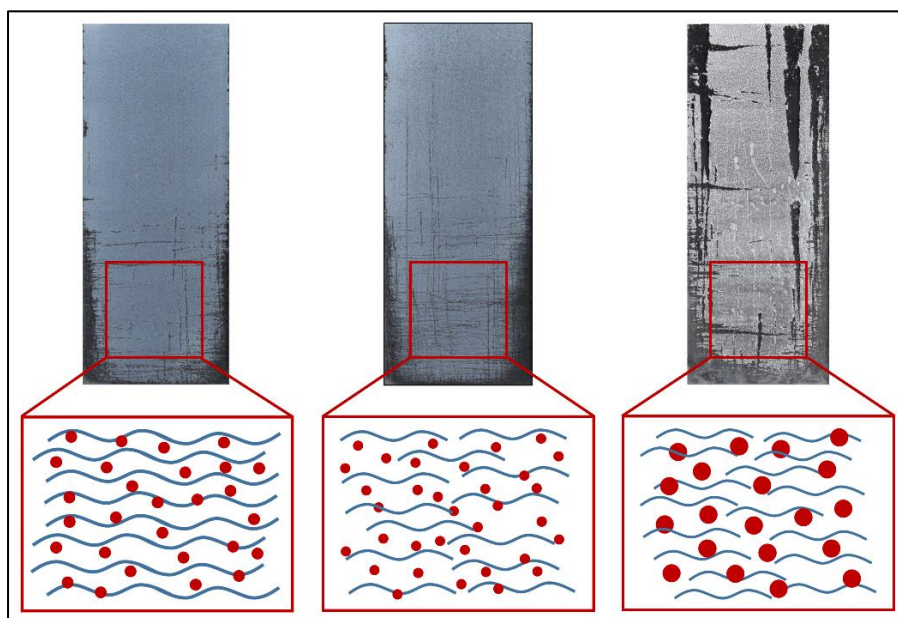
- 1 A. Milionis, E. Loth and I. S. Bayer, *Adv. Colloid Interface Sci.*, 2016, **229**, 57–79.
- 2 J. Zhang, J. Zhao, W. Qu, X. Li and Z. Wang, *J. Colloid Interface Sci.*, 2020, **580**, 211–222.
- 3 C. R. Crick, in *Superhydrophobic Surfaces-Fabrications to Practical Applications*, IntechOpen, 2018, pp. 11–38.
- 4 C. R. Crick and I. P. Parkin, *Chem. - A Eur. J.*, 2010, **16**, 3568–3588.
- 5 Y. A. Mehanna, R. L. Upton and C. R. Crick, *J. Mater. Chem. A*, 2019, **7**, 7333–7337.
- 6 A. Davis, Y. H. Yeong, A. Steele, E. Loth and I. S. Bayer, *AIChE J.*, 2014, **60**, 3025–3032.
- 7 A. Cholewinski, J. Trinidad, B. McDonald and B. Zhao, *Surf. Coatings Technol.*, 2014, **254**, 230–237.

- 8 A. Steele, I. Bayer and E. Loth, *J. Appl. Polym. Sci.*, 2012, **125**, 445–452.
- 9 Y. Lu, S. Sathasivam, J. Song, C. R. Crick, C. J. Carmalt and I. P. Parkin, *Science*, 2015, **347**, 1132–1135.
- 10 R. L. Upton, Z. Davies-Manifold, M. Marcello, K. Arnold and C. R. Crick, *Mol. Syst. Des. Eng.*, 2019, **5**, 477–483.
- 11 M. Liu, J. Wu and C. Gao, *J. Non. Cryst. Solids*, 2019, **526**, 119711.
- 12 E. M. Rossi, P. S. Phani, R. Guillemet, J. Cholet, D. Jussey, W. C. Oliver and M. Sebastiani, *J. Mater. Res.*, 2021, 1–14.
- 13 S. Zhou, X. Ding and L. Wu, *Prog. Org. Coatings*, 2013, **76**, 563–570.
- 14 K. H. Nielsen, S. Karlsson, R. Limbach and L. Wondraczek, *Sci. Rep.*, 2015, **5**, 1–10.
- 15 E. Moayedi and L. Wondraczek, *J. Non. Cryst. Solids*, 2017, **470**, 138–144.
- 16 M. Qu, S. Liu, J. He, J. Feng, Y. Yao, L. Hou, X. Ma and X. Liu, *RSC Adv.*, 2016, **6**, 79238–79244.
- 17 M. Xu, Y. Feng, Z. Li, X. Wang, C. Li, H. Jiang and Y. Chen, *J. Alloys Compd.*, 2019, **781**, 1175–1181.
- 18 R. V. Lakshmi, T. Bharathidasan and B. J. Basu, *Appl. Surf. Sci.*, 2011, **257**, 10421–10426.
- 19 C. J. Weng, C. H. Chang, C. W. Peng, S. W. Chen, J. M. Yeh, C. L. Hsu and Y. Wei, *Chem. Mater.*, 2011, **23**, 2075–2083.
- 20 D. Kumar, X. Wu, Q. Fu, J. W. C. Ho, P. D. Kanhere, L. Li and Z. Chen, *Appl. Surf. Sci.*, 2015, **344**, 205–212.
- 21 X. Deng, L. Mammen, Y. Zhao, P. Lellig, K. Müllen, C. Li, H. J. Butt and D. Vollmer, *Adv. Mater.*, 2011, **23**, 2962–2965.
- 22 L. Xu, D. Zhu, X. Lu and Q. Lu, *J. Mater. Chem. A*, 2015, **3**, 3801–3807.
- 23 R. L. Upton, Z. Davies-Manifold, M. Marcello, K. Arnold and C. R. Crick, *Mol. Syst. Des. Eng.*, 2020, **5**, 477–483.
- 24 R. L. Upton, C. R. Crick and C. R. Crick, *Mol. Syst. Des. Eng.*, 2020, **5**, 876–881.
- 25 A. Millionis, J. Languasco, E. Loth and I. S. Bayer, *Chem. Eng. J.*, 2015, **281**, 730–738.
- 26 H. Xu, C. R. Crick and R. J. Poole, *J. Mater. Chem. A*, 2018, **6**, 4458–4465.
- 27 Y. A. Mehanna, E. Sadler, R. L. Upton, A. G. Kempchinsky, Y. Lu and C. R. Crick, *Chem. Soc. Rev.*, 2021, **50**, 6612.
- 28 Z. Li, J. Marlena, D. Pranantyo, B. L. Nguyen and C. H. Yap, *J. Mater. Chem. A*, 2019, **7**, 16387–16396.
- 29 S. Sawamura, R. Limbach, H. Behrens and L. Wondraczek, *J. Non. Cryst. Solids*, 2018, **481**, 503–511.
- 30 R. Taurino, E. Fabbri, D. Pospiech, A. Synytska and M. Messori, *Prog. Org. Coatings*, 2014, **77**, 1635–1641.

- 31 G. N. B. M. de Macedo, S. Sawamura and L. Wondraczek, *J. Non. Cryst. Solids*, 2018, **492**, 94–101.
- 32 R. Hensel, A. Finn, R. Helbig, H. G. Braun, C. Neinhuis, W. J. Fischer and C. Werner, *Adv. Mater.*, 2014, **26**, 2029–2033.
- 33 Z. Geng and J. He, *J. Mater. Chem. A*, 2014, **2**, 16601–16607.
- 34 R. E. Ramírez-García, J. A. González-Rodríguez, M. Arroyo-Ortega, S. A. Pérez-García and L. Licea-Jiménez, *Int. J. Appl. Ceram. Technol.*, 2017, **14**, 39–49.
- 35 V. Mortazavi and M. M. Khonsari, *Wear*, 2017, **372–373**, 145–157.
- 36 L. Šimurka, R. Čtvrtlík, J. Tomašík, G. Bektaş, J. Svoboda and K. Bange, *Chem. Pap.*, 2018, **72**, 2143–2151.

Chapter 4:

Investigation of the Resilience of Polymer / Particle Composite Coatings



Publications:

Study on the Influence of Polymer/Particle Properties on the Resilience of Superhydrophobic Coatings. Y. A. Mehanna and C. R. Crick. *ACS Omega*, 2022, DOI: 10.1021/acsomega.2c01547.

Contributions:

Confocal Fluorescence Microscopy: Imaging was carried out by Dr. Marco Marcello (Liverpool Centre for Cell Imaging).

Mould Fabrication: Designing and 3D-printing was done by Dr. Osama Maklad (University of Greenwich).

4. Investigation of the Resilience of Polymer/Particle Composite Coatings

4.1. Introduction

The susceptibility of superhydrophobic surfaces to physical degradation, originating from their rough micro/nanoscale structure, stands as one of the main challenges to their applicability.^{1,2} Routes to fabricating robust superhydrophobic materials, and developing a general approach for doing so, are central challenges in this research area. This chapter sheds light on some approaches for fabricating resilient superhydrophobic coatings, as well as the obstacles limiting further progress in this area.

4.1.1. Approaches for Resilience

Many research reports have attempted to fabricate superhydrophobic coatings with high robustness. This could be achieved by controlling the coating components. A way of achieving this is by the incorporation of materials known for their high mechanical stability, examples include CNTs and carbon fibres.³⁻⁵ These materials can either be used as the main building block of the coating,⁵ as well as incorporated as additives.^{3,4} Another way is to utilise materials for which covalent linking can be introduced. Deng *et al.* utilised porous silica capsules to make a superhydrophobic coating, and incorporated CVD to chemically bind the silica to enhance its resilience.⁶ It was shown using sand impact and tape peeling tests that the CVD has significantly improved superhydrophobicity retainment compared to where the capsules are binding only by weak van der Waals interactions.

Another approach is to adjust the fabrication/deposition technique to achieve better resilience. This can lead to an improved coating/substrate adhesion but was also reported to increase cohesion forces between coating components. Electroplating was reported for superhydrophobic coating fabrication to provide strong substrate adhesion.⁷ An example is a Zn/Ni/Co composite coating which demonstrated enhanced robustness compared to other Zn/Ni composites deposited using different techniques. Wu *et al.* reported a fluorinated resin/Fe₃O₄ nanoparticles-based coating prepared by inverse infiltration, where a two-layer coating was prepared by spraying and curing of a base layer followed by spraying of the polymer/nanoparticle mixture.⁸ This allowed polymer infusion through both layers which strengthened the adhesion between nanoparticles. The coatings maintain superhydrophobicity through harsh abrasion conditions (260 cycles of sand-paper abrasion and 25 cycles of sand impact).⁸ Xu *et al.* reported a multi-step coating process, where nanoporous silica thin

film was grown on glass substrates to increase substrate adhesion, followed by dip-coating/heat-treatment/hydrophobic treatment to ensure roughness and hydrophobic nature. The film demonstrated robustness against sand impact, as well as improved performance in the pencil hardness test (compared to a silica thin film coating attached by van der Waals forces).⁹ A method reported to increase cohesion between coating components is to compress into superhydrophobic disks. While the high pressing pressure (reaching 40 MPa) resulted in a compact silica/polymer composite, the surface roughness was maintained. These disks could stand different mechanical challenges, including knife scratching, abrasion and hummer beating, although this was not quantitatively presented.¹⁰

Controlling the architecture of the surface can help generate more resilient surfaces. This was reported through the fabrication of dual-scale roughness where the larger, more resilient surface features form protective points against abrasion. Kondrashov *et al.* generated hierarchical micro-cones/nano-grass silicon surfaces using a dry etching process. Optimisation of the micro-cones density, apex angle and length, the surface was able to retain superhydrophobicity after 20 N shear load.¹¹ In another report, Huovinen *et al.* manufactured a variety of surface patterns by micro-structuring/moulding of polypropylene. By optimising the number/positions of the protective pillars, mechanical robustness against a 20-MPa compression and 120-kPa abrasive wear was achieved.¹²

4.1.2. Challenges Facing the Fabrication of Superhydrophobic coatings

While attempts for fabricating robust superhydrophobic coatings are numerous, systematic progress towards truly resilient materials is limited. This can be rationalised due to firstly the lack of consistent degradation analysis protocol that enables direct comparison between different coatings reported, and secondly the lack of understanding of the source of robustness and how it is related to (and affected by) the properties of the materials forming the coating.¹ Currently, many well-established abrasion methods have been utilised in the examination of coating resilience (Section 3.1.1), and they provide wide varieties to suit the examined surfaces. Despite the frequent adoption of these techniques, the specific protocol utilised can greatly vary between different reports, including the definition of an abrasion cycle and the load applied on the coating. This divergence makes deducing definitive conclusions, and planning routes in the development of resilient coatings extremely challenging.¹³ Furthermore, many of these reports include composite materials, which presents an additional layer of complexity when considering how

each component may influence and contribute to the robustness of the coating.¹⁴ This in-depth consideration is not normally reported, and in combination with the lack of consistency in analysis techniques, this hinders the progress of research efforts.

4.1.3. Superhydrophobic Polymer/Particle Composites (SPPCs)

The deposition of PDMS coatings *via* AACVD, reported by Crick *et al*, demonstrated great hydrophobicity and high roughness (Chapter 2).¹⁵⁻¹⁷ Meanwhile, the process is not optimum for scaling requirements, due to the long deposition time per unit area as well as the difficulty of implementing large substrates. Modifications to the coating formula/technique were introduced to overcome this issue, resulting in the development of SPNC formulations, which can be deposited using simple and scalable techniques, e.g. spray coating.¹⁴ The formulations consist of three main components: solvent, polymer and particles. The latter was introduced to account for surface roughness, as spraying polymer solutions usually produce flat coatings.¹⁸ In these formulations, the coating is hypothesized to form by the encapsulation of particles by the polymer. The thickness of the polymer is crucial to the hydrophobicity as well as the functional properties of the coating. A deficiency of the polymer results in a low physical resilience due to poor inter-particle cohesion as well as coating/substrate adhesion. On the other hand, excess of the polymer quantity diminishes the hydrophobicity, as the polymer fills the porosity provided by the arrangement of the particles (**Figure 4.1**). Therefore, the optimum polymer/particle M_{ratio} needs to be identified. Due to the flexibility these composites provide in terms of the chosen polymers/particles as well as the deposition technique, they were chosen in this study for investigating the coating resilience, as discussed in the following section.

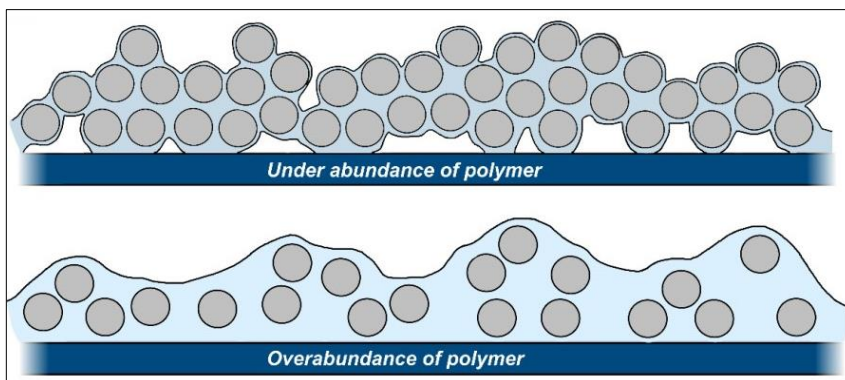


Figure 4.1: Schematic illustrating the polymer/particle encapsulation in SPPC coatings and showing the importance of

applying an appropriate amount of polymer to obtain resilient and rough coatings. Figure retrieved from ref.¹⁸

4.1.4. Chapter Aim

The purpose of the study conducted in this chapter is to utilise the quantitative scanning/weighting abrasion analysis methodology (described in Chapter 3) to evaluate the resilience of SPPC coatings and understand how the components' properties contribute to the resultant resilience. The effect of varying the properties of the composite formulation components has not been reported in the literature. The main factors examined here are the effect of (i) variation in the physical properties of the polymer (M_w , tensile strength (TS)) and (ii) changing the particles' size and size distribution.

To achieve this, three variants of PVC (with different M_w), along with three variants of PDMS (with different TS) were used to make SPPC formulations and the sprayed coatings were compared in terms of their resilience to sand-paper abrasion (Section 4.3.2). In addition, coatings were fabricated using micron-sized and nano-sized particles to investigate the effect of changing the particle size on the physical degradation behaviour (Section 4.3.3.2). Finally, micro/nano-sized particles were combined to check the effect of hierarchy introduction (Section 4.3.3.3).

4.2. Experimental Methods

4.2.1. Materials

PVC was purchased from Sigma Aldrich with M_w (as reported by the manufacturer) of 48,000, 90,000 and 233,000 Daltons, respectively (product number 81388, product number 81387, and product number 346764). These will be referred to as PVC-L, PVC-M and PVC-H for low, medium and high M_w , respectively). Likewise, PDMS was purchased in three different forms. Sylgard-186 Silicone Elastomer (a two-part thermosetting PDMS elastomer, catalysed with a platinum curing agent) was purchased from Ellsworth Adhesives Ltd. Two further silicone elastomers in the same product line (Sylgard-182 and Sylgard-184) were purchased from Dow. These elastomers differ (along with other properties) in their TS as reported by the manufacturer (for Sylgard 186 = 2.1 N/mm²), for Sylgard 184 = 6.7 N/mm²) and for Sylgard 182 = 7.6 N/mm²). These are referred to as PDMS(186), PDMS(184) and PDMS(182), respectively.

Silicon dioxide nanopowder (\emptyset - 10-20 nm) and HMDS (reagent grade, $\geq 99\%$) were purchased from Sigma Aldrich. Silicon dioxide powder (\emptyset ~1.5 microns, 99.9%) was purchased from Alfa Aesar. Hexane (HPLC grade), THF ($\geq 99.5\%$, laboratory reagent grade), and toluene ($\geq 99.8\%$) were purchased from Fisher Scientific Limited. Glass

microscope slides purchased from ThermoScientific were used as the substrates. An adhesion promoter (CYN20 Stick 2 Industrial Grade General Purpose Adhesive - cyanoacrylate based) was purchased from EverBuild. Sandpaper sheets (grit no. 120, dimensions; 23 × 9 cm) were purchased from Miady.

4.2.2. Silica Hydrophobization

The silica hydrophobization procedure and conditions were conducted similarly to the previously detailed description in Section 3.2.2. This was applicable for both nano-sized (referred to as $n\text{SiO}_2$) and micron-sized (referred to as μSiO_2) silicon dioxide powder.

4.2.3. Coating Preparation

The preparation of PVC/ $n\text{SiO}_2$ and PDMS/ $n\text{SiO}_2$ coatings was conducted similarly to the previously detailed description in Section 3.2.3.

μSiO_2 was utilised in combination with PDMS only, as superhydrophobic coatings could not be successfully formulated using PVC. Different M_{ratio} were tested, and the optimum ratio was found to be 0.3 (Section 4.3.3.1). Typically, 17 mL of the previously prepared PDMS stock solution was diluted with 73 mL of hexane to provide a similar silica concentration. Hydrophobized μSiO_2 (0.403 g) was added and stirred at room temperature for an hour.

A mixture of both $n\text{SiO}_2$ and μSiO_2 was also prepared. Typically, 30 mL of the PDMS stock solution was diluted with 20 mL of hexane, and then $n\text{SiO}_2$ (0.129 g) and μSiO_2 (0.121 g) were added and stirred at room temperature for an hour.

4.2.4. Coating Deposition

The spraying process for PVC/ $n\text{SiO}_2$ coatings, the pre-coating adhesive layer for PDMS-based coatings as well as PDMS/ $n\text{SiO}_2$ coatings, was conducted similarly to the previously detailed description in Section 3.2.4 (**Figure 3.2**).

The combination of different silica particle sizes was examined. For the two sizes included in this study, three combinations were made (**Figure 4.2a-c**): (i) a two-layer coating consisting of a PDMS/ μSiO_2 layer followed by a PDMS/ $n\text{SiO}_2$ layer (referred to as μ - n coating), (ii) a two-layer coating consisting of a PDMS/ $n\text{SiO}_2$ layer followed by a PDMS/ μSiO_2 layer (referred to as n - μ coating), and (iii) a single-layer coating: spraying a mixture of both $n\text{SiO}_2$ and μSiO_2 (as described in Section 2.3, referred to as n/μ mix). The first layer of the μ - n coating was prepared by spraying 16 mL of

PDMS/ μ SiO₂ solution, followed by curing at 120°C for 30 min. The second layer was prepared by spraying 8 mL of PDMS/nSiO₂ solution, followed by the same curing conditions (**Figure 4.2a**). For the n- μ coating, 8 mL of PDMS/nSiO₂ solution was sprayed, followed by spraying 8 mL PDMS/ μ SiO₂ layer. Each layer was allowed to cure similarly (**Figure 4.2b**). Finally, the n/ μ mix coating was made by spraying 16 mL of the mixture solution and curing as previously described (**Figure 4.2c**).

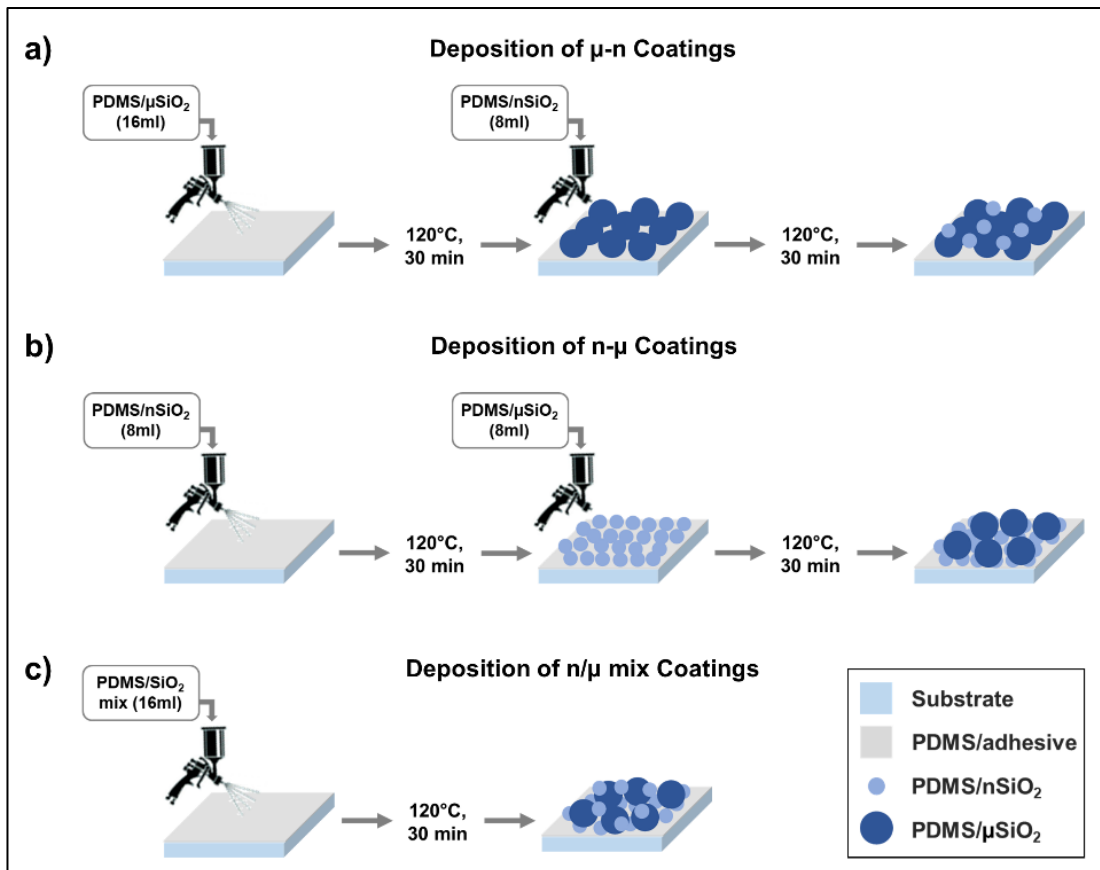


Figure 4.2: Schematic showing the coating deposition procedure for the following PDMS-based coatings; (a) μ -n coating, (b) n- μ coating, (c) n/ μ mix coating.

4.2.5. Resilience Assessment

The resilience assessment procedure and conditions were conducted similarly to the previously detailed description in Section 3.2.5.

4.2.6. Mechanical Testing

4.2.6.1. Films Preparation

PVC films were prepared as illustrated in **Figure 4.3**. 0.3 g of PVC was added to 30 mL of THF and stirred until dissolved. This solution was poured into a crystallisation dish ($\varnothing = 11.5$ cm), covered by aluminium foil (small holes were made to allow slow evaporation) and placed in a fume cupboard at RT. This was repeated every 4-6 hours for a total of five iterations, to increase the overall film thickness (total polymer mass and THF volume = 1.5 g and 150 mL, respectively). After complete evaporation (~ 48 hrs after the last solution was added), the film was removed from the dish and then cut into dog-bone shaped pieces. Typically, a dog-bone shaped metal cutter (dimensions indicated in the following section) was heated at 110°C, placed on a PVC film and put in a hot press (heated at the same temperature). The press was secured and a pressure of around 1.5 MPa was applied (indicated by a pressure gauge attached to the press). The film was quickly removed after 20 seconds and stored in ambient conditions until mechanical testing was carried out. Each film produced 5-6 dog-bone samples, which were all tested and the average of the closest 3 runs was obtained. Furthermore, 3 films were prepared for each polymer to make 3 testing rounds, hence the reported averages in Section 4.3.1.1 are for 9 runs. This was attempted for the three PVC variants utilised in this work.

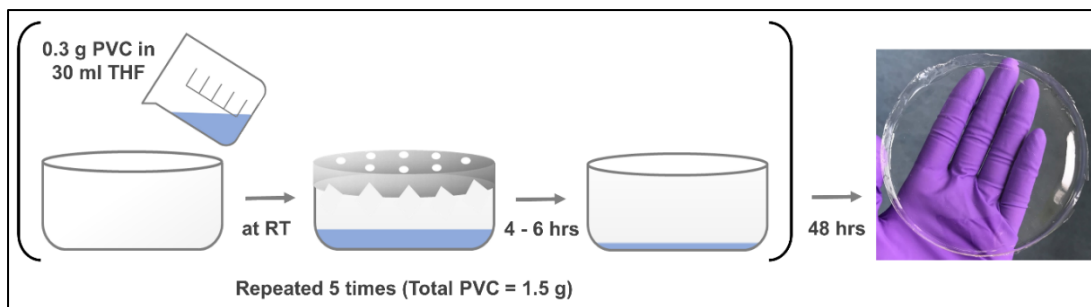


Figure 4.3: Method for preparing PVC films for mechanical testing. PVC powder was solvated in THF and left to dry in a crystallization dish ($\varnothing = 11.5$ cm) covered with aluminium foil at room temperature for 4-6 hrs. This was repeated five times (total PVC quantity = 1.5). The film was removed after complete solvent evaporation (48 hrs from the last solution added).

PDMS samples were prepared according to a previous report,¹⁹ and was conducted using PDMS(184) only. The two Sylgard 184 components (PDMS = 5 g, ratio 10:1 PDMS to curing agent) were magnetically stirred at 200 rpm for 30 min. The mixture was then moved into a vacuum desiccator for 30 min to remove air bubbles. The 3-

part mould consisted of two top and bottom aluminium sheets (covered with grease paper to facilitate sample removal) and a 3D-printed 100*40*2 mm piece of tough polylactic acid (PLA) in the middle with a dog-bone shaped hole (**Figure 4.4**, dimensions indicated in the following section). The PLA part was placed above the covered aluminium sheet and the polymer was poured inside the hole, and then covered with the other grease paper/aluminium sheet. The mould was then clamped and placed vertically for 30 min to ensure that any remaining bubbles will move upwards away from the testing region. The sample was cured at 120°C for 33 min and then removed from the mould once cooled down.

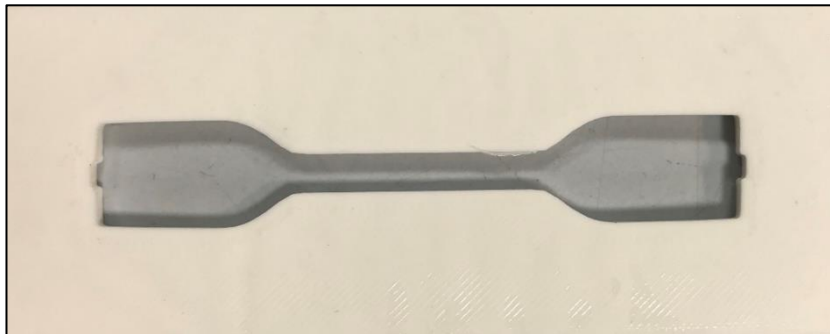


Figure 4.4: An image of the 3D-printed PLA mould used for PDMS samples.

4.2.6.2. Testing conditions

Tensile stress-strain curves of polymers were carried out using a universal testing Machine (SHIMADZU EZTest) with a crosshead rate (pulling speed) of 3 mm/min. The testing temperature was fixed at 25 °C using an air conditioner. Dog-bone samples were made into ISO 527-2/5A size (**Figure 4.5**). The PVC films thicknesses averaged 0.1 mm, where it was around 2 mm for PDMS samples.

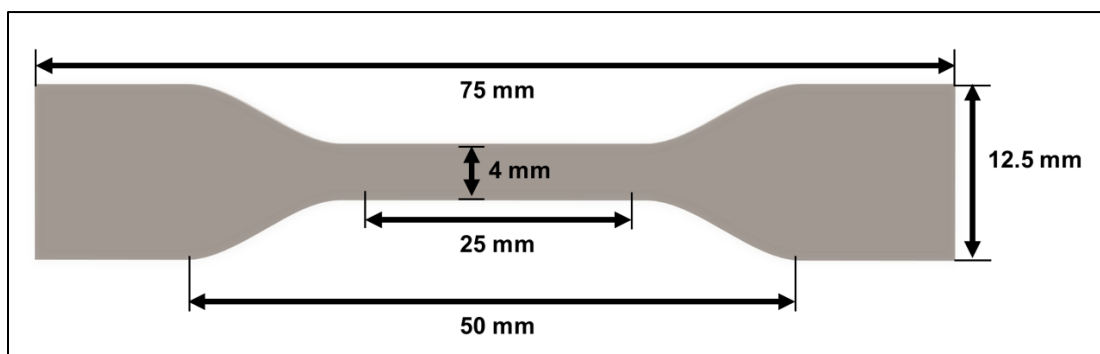


Figure 4.5: A sketch of the dog-bone metal cutter used for PVC films with dimensions highlighted.

4.2.7. Characterisation

4.2.7.1. *Confocal imaging conditions*

Confocal fluorescence microscopy was carried out using a Zeiss LSM 880 upright confocal microscope on a Zeiss Axio Examiner Z1 (Zeiss, Jena, Germany) with a 20x/1.0 Dic (water immersion) objective (Zeiss). Samples were excited using laser lines Diode (461 nm). Data was captured using ZEN software (Zeiss, Jena, Germany).

4.2.7.2. *Preparation of fluorescent coatings*

Fluorescent coatings were prepared in a similar procedure to that mentioned in Section 3.2.3. A stock solution of Nile Red dye in chloroform (1.96 mM, 10 mL) was prepared. Fluorescent PVC/nSiO₂ coatings were made by adding 120 µL of the dye solution to a premade solution of PVC (0.1 g) in THF (30 mL). This was allowed to stir for 30 min before adding the nSiO₂ (0.235 g), and the following stirring and spraying conditions were kept the same as the previously described PVC/nSiO₂ coatings (Section 3.2.3). Likewise, fluorescent PDMS/nSiO₂ coatings were made by solvating PDMS (0.5068 g, 10:1 of polymer:curing agent) in 70 mL of hexane, then adding 290 µL of the dye solution and was stirred for 30 min. nSiO₂ (0.2586 g) was added to 50 mL of the prepared solution and stirred for an hour, while the remaining solution was used for the adhesive layer, as described in Section 3.2.3. The coatings were abraded, and the scratches were imaged.

4.2.7.3. *Other Characterisation*

Drop Shape Analyser was used to measure WCAs, using a water droplet volume of 5µL. This was repeated five times for each coating and the average was calculated. SEM imaging was performed using a field emission microscope (JEOL, JSM-7001F) using an acceleration voltage of 3 kV.

4.3. Results and Discussion

4.3.1. Mechanical Properties of Polymers

The resilience of a coating involves different aspects, which influence how the coating behaves under abrasion. These include the coating-substrate adhesion, as well as the cohesive forces within the coating material. While the former is expected to be affected by different parameters, the latter is mainly dominated by the component properties, including their mechanical strength. Therefore, it is important to know the

mechanical properties of the polymers reported in this study before discussing the abrasion experiments.

4.3.1.1. PVC polymers

The physical resilience of the PVC polymers is not reported by the manufacturer. As elaborated in the previous section, three different types of PVC polymers were investigated, which differ in their M_w . It is expected that a higher M_w results in an increased polymer strength due to the higher degree of intermolecular interactions between the polymeric chains.²⁰ However, this has not been previously verified for these PVC polymers. Therefore, mechanical testing was conducted to obtain values for TS, strain at the breaking point, and elastic modulus (shown in **Figure 4.6**). It was observed that the repetitions from different runs showed a high degree of variation that provided a high degree of error to these measurements, particularly in the elastic modulus values. This was most likely due to variation in the films introduced during their preparation method, e.g. the speed of solvent evaporation caused by the air circulation. The elastic modulus is calculated from the slope of the linear portion (elastic deformation) of the stress-strain curve, which tended to be very short with the polymer samples deforming mostly inelastically. This type of deformation mechanism maximises the influence of any differences between the samples.^{21,22} For the strain values, this variation, although present, was less dramatic. It is noted that the maximum strain increases with increasing the M_w , which adheres to the previously stated expectations. Meanwhile, the most important to the study context is the TS values. It is observed that the values are relatively close to each other, especially when the error is taken into consideration. However, the average TS values are larger for higher M_w , which is generally expected for thermoplastic polymers,²⁰ while this variation is not particularly large (as seen in **Figure 4.6**).

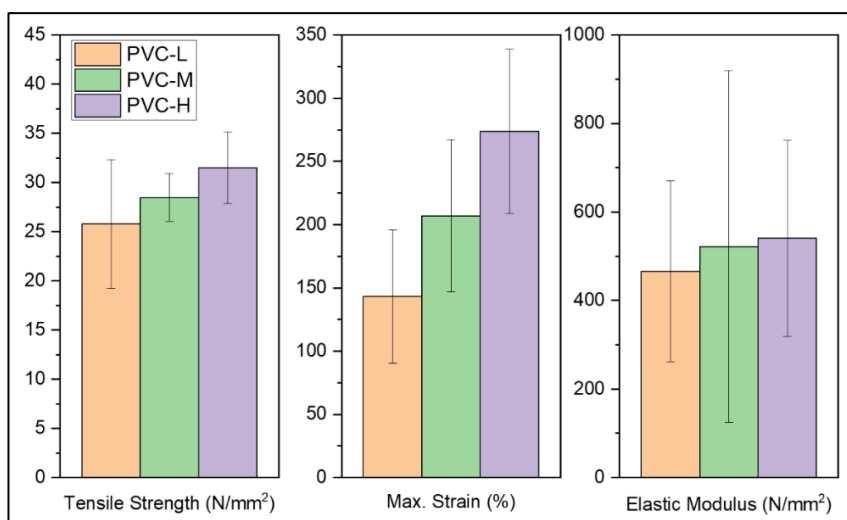


Figure 4.6: TS, maximum strain, and elastic modulus results for PVC polymers.

4.3.1.2. PDMS polymers

For PDMS polymers, the TS was provided by the supplier, however, these tests were carried out at a reported crosshead rate of 508 mm/min (details from supplier). This is a much higher rate than what was applied for the PVC films described above. To establish a reasonable comparison, predicting the TS at a lower crosshead rate was required. In general, higher strain rates, while decreasing the strain at which the sample breaks, increase the measured TS value.^{23,24} This is supported by another reported tensile test on Sylgard 184 at a different crosshead rate (5.13 N/mm² at 254 mm/min by Johnston et al. 2014).¹⁹ To confirm this, mechanical testing was conducted on a sample of Sylgard 184, and the TS was found to be around 1.7 N/mm². The main note to take here is that, for the polymers tested in this study, PVC polymers show higher TS compared to the PDMS polymers.

4.3.2. Influence of Polymer

For the coatings discussed in this section, the incorporated particles were kept the same (nSiO₂), along with all the coating preparation and deposition conditions (detailed in Sections 3.2.3 and 3.2.4), while only the polymer was changed. A detailed examination of the appropriate M_{ratio} of polymer/particle leading to the optimum polymer thickness was conducted previously for PDMS and PVC coatings with nSiO₂.¹⁴ While only one polymer variant was studied (PDMS(184) and PVC-M), utilizing the other variants was not found to require re-adjustment of the M_{ratio}, as illustrated in **Figure 4.7** by the high WCAs achieved for the other polymer variants. The figure shows other coatings made with silica variants, which will be discussed in Section 4.3.3.

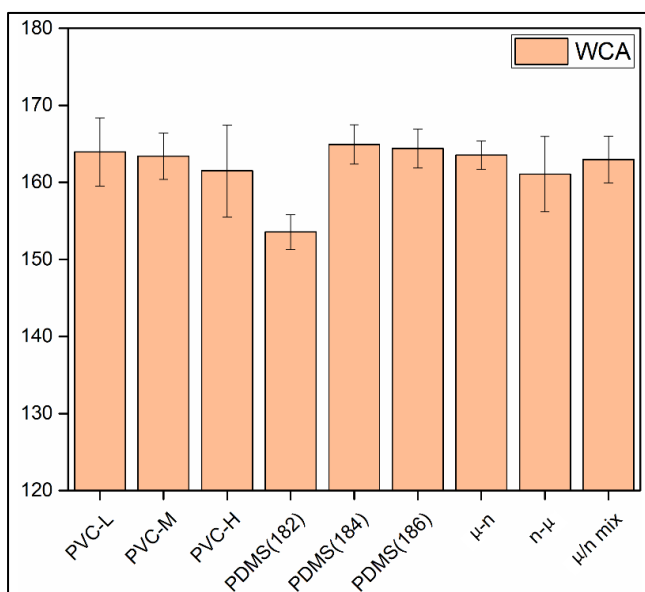


Figure 4.7: WCAs for the coatings tested in this study, made with PVC, PDMS or silica variants, showing their superhydrophobicity before abrasion.

As highlighted in the previous chapter, both image processing and mass-tracking were conducted for the abraded coatings. The mass-loss data was expressed in two different ways: (i) as a percentage of coating remained by mass tracking, and (ii) as a mass difference (between two consecutive cycles). The former identifies the amount of coating that persisted after abrasion cycles, while the latter indicates the relative rate/ease of the coating degradation.

PVC-L and PDMS(186) coatings have been utilised in the previous chapter to demonstrate the abrasion analysis technique and were discussed in detail. These coatings are discussed here again to compare their results with the coatings prepared using other polymer types.

4.3.2.1. PVC polymers

4.3.2.1.1. Coating performance

Figure 4.8 shows images from the abrasion experiments for PVC-L, PVC-M and PVC-H after 10 abrasion cycles, along with the corresponding binary images and the estimated percentage of coating that remained. The full image sets indicating all abrasion cycles are shown in **Figure 3.7a-c** (Section 3.3.2.3) for PVC-L, and in Appendix 2 (Figure A2.1a-f) for PVC-M and PVC-H.


















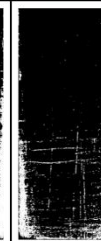
Sample	PVC-L			PVC-M			PVC-H		
	Run_1	Run_2	Run_3	Run_1	Run_2	Run_3	Run_1	Run_2	Run_3
Coloured Images									
Binary Images									
%_coating remained	71%	69%	79%	59%	80%	85%	75%	81%	90%

Figure 4.8: Images for the sample runs of PVC with different M_w after 10 abrasion cycles, showing the coloured (upper), binary (lower) images, and the associated percentage of coating remained as predicted by image analysis.

Plots of percentages of coating remained by image analysis/mass tracking as well as the mass difference for PVC coatings are shown in **Figure 4.9a-c**. Comparing the degradation results for these coatings, it can be noticed that PVC-H coatings tend to experience less damage as a result of abrasion. This is supported by image analysis (**Figure 4.9a**, percentage of coating remaining = 73%, 75% and 82% for PVC-L, PVC-M and PVC-H, respectively) as well as mass tracking results (**Figure 4.9b**, percentage of coating remaining = 38%, 42% and 56% for PVC-L, PVC-M and PVC-H). In addition, the mass difference with each abrasion cycle indicates a slower degradation process (i.e. lower mass loss between cycles) for PVC-H within the first few cycles (**Figure 4.9c**). This suggests that, while the three polymers tend to respond similarly as abrasion continues, the higher M_w (and, subsequently, higher TS) appears to minimise initial damage and delay the propagation of coating failure.

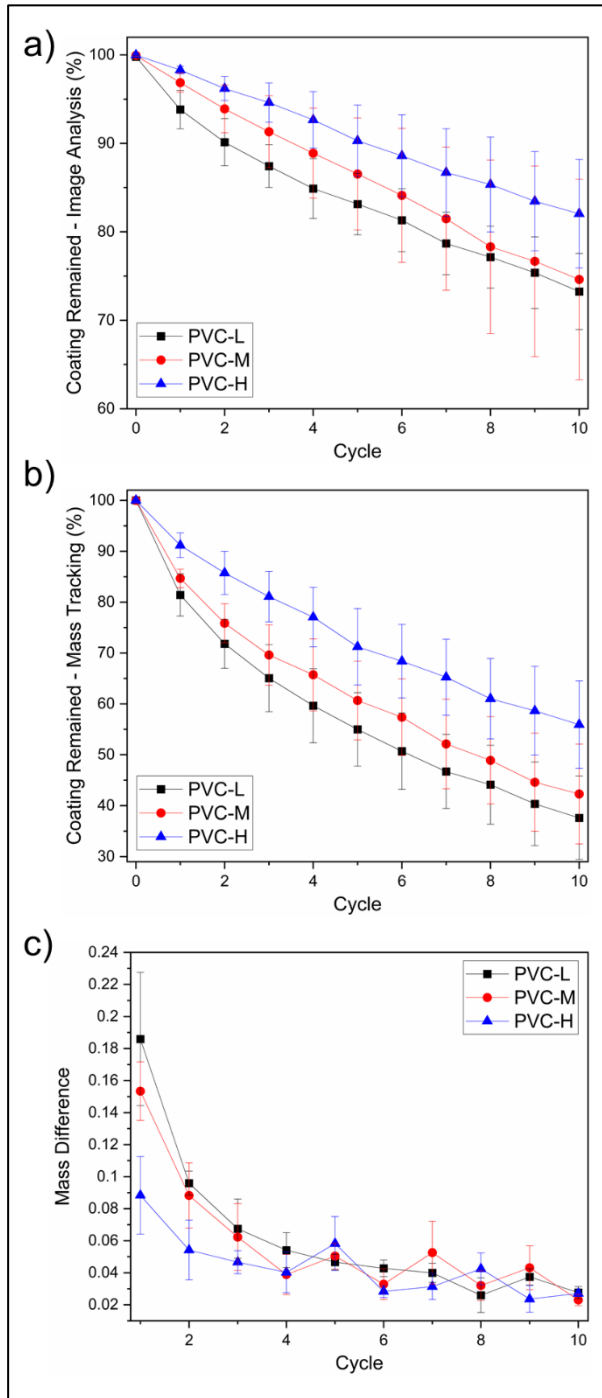


Figure 4.9: Plots for PVC sample runs resilience performance vs. abrasion cycles. (a) shows the percentage of coating remained as predicted by image analysis, (b) shows the percentage of coating remained as measured by mass tracking, and (c) shows the mass difference between every two consecutive cycles (normalised by dividing by the initial coating mass).

4.3.2.1.2. Adhesion/cohesion failure

Further information could be extracted by comparing the percentage of coating remaining by mass tracking to that obtained by image analysis. This is beneficial as it provides additional insight into possible degradation pathways, particularly adhesion vs. cohesion failures (Section 3.3.3.1). The combined imaging/mass-loss analysis results of the PVC samples after 10 abrasion cycles are shown in **Table 4.1**. A significant difference is observed in results achieved with the two approaches,

which suggests that superficial coating removal is taking place, as concluded for PVC coatings in the previous chapter. This superficial failure is also following a similar pattern to that noticed with the percentages of coatings remaining (both by mass loss and image analysis), as PVC-H appears to lose less coating mass as a result of this type of failure. This shows that the higher M_w polymer is also more resistant to cohesion failure.

Coating	PVC-L	PVC-M	PVC-H	PDMS(182)	PDMS(184)	PDMS(186)	μ -n	n- μ	n/ μ mix
Avg. % remained – by mass	37%	43%	56%	75%	75%	84%	59%	71%	65%
Avg. % remained – image analysis	73%	75%	82%	67%	71%	80%	55%	75%	56%
Difference	36%	32%	26%	-8%	-4%	-4%	-4%	4%	-9%

Table 4.1: Percentage of coating remained (obtained by mass tracking and image analysis) for the coatings discussed. The difference between both is also indicated.

To demonstrate the previous deduction in another way, images for the three PVC polymers were taken after 10 abrasion cycles. A square area was cropped (similar dimensions for all samples) from a region where no/very little scratches are visible (**Figure 4.10**). The average RGB was calculated for these low damage areas and compared to the average RGB value of the same region before abrasion (cycle 0). While changes in RGB values would not be noticeable until substantive change occurs, a decrease in RGB value still indicated a partial coating removal. As the figure shows, this decrease was minimal for the PVC-H coating. The above conclusions could be justified by the increased intermolecular forces for longer polymer chains, and hence, the higher force required to separate/remove these chains.

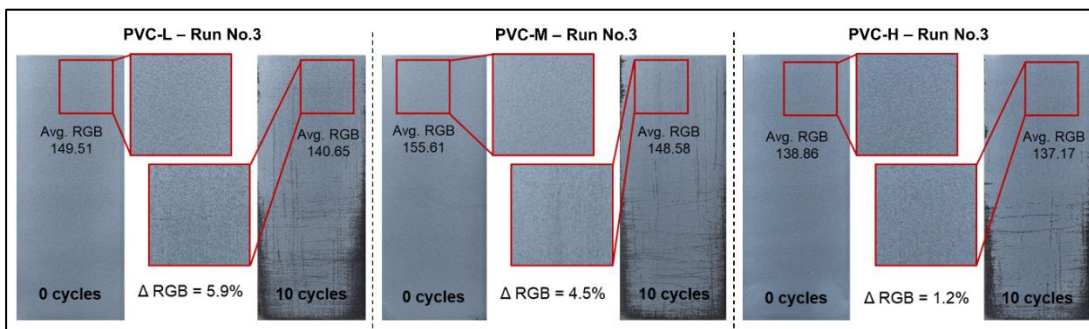


Figure 4.10: A comparison between superficial coating removal for PVC coatings. Regions with minimal visible scratches in the 10th cycle images were compared to those in 0th cycle images in terms of RGB change (Δ RGB).

Confocal fluorescence microscopy was carried on to investigate the nature of the scratches in PVC coatings. **Figure 4.11** shows a 3D mapping of 200 μ m*200 μ m

scratch areas on abraded coatings after 10 abrasion cycles. The coatings imaged were PVC-L (a, b), PVC-M (c, d) and PVC-H (e, f). The common observation in PVC scratch images is that the material removal does not affect the surrounding areas near the scratch, i.e. the coating height near the scratch is similar to the rest of the imaged area. This, again, indicates the low cohesion between the coating components in PVC coatings, as it is easily detached from the neighbouring materials and underwent complete removal.

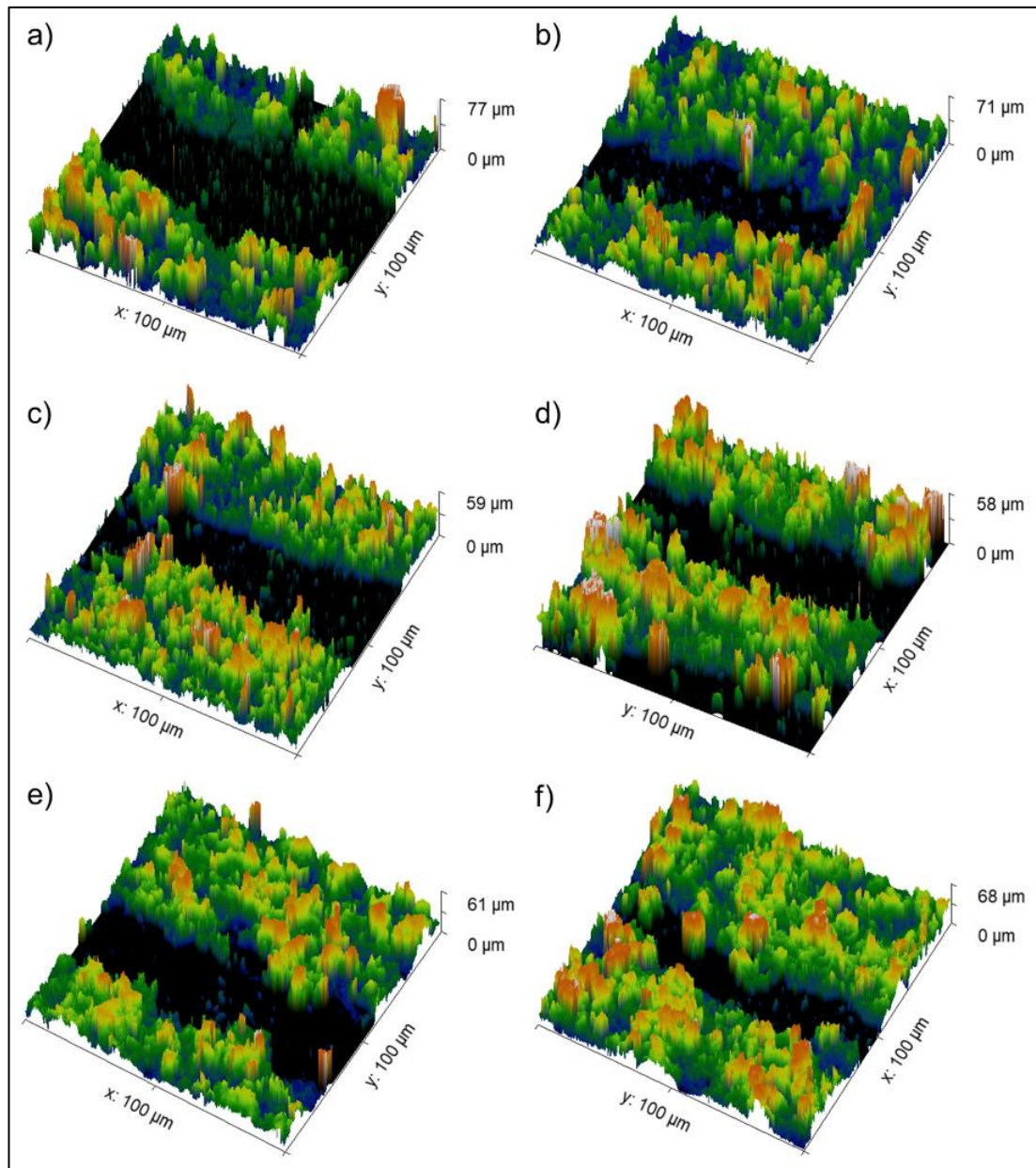


Figure 4.11: Confocal fluorescence images of scratches on abraded coatings of PVC-L (a-b), PVC-M (c-d) and PVC-H (e-f).

4.3.2.2. PDMS polymers

4.3.2.2.1. Correction for noise

Abrasion analysis was carried out similarly for PDMS coatings. However, due to the PDMS polymers generally producing a less white coating (i.e. with lower RGB values) in comparison with PVC polymers (particularly for PDMS(182) and PDMS(184) coatings), some noise was noticed with the initial cycles (before abrasion). The relatively darker coating colour originates from the higher transparency of PDMS and differences in morphology causing less light scattering. Ideally, the pre-abrasion images should provide a percentage value with no coating removed (i.e. 100% of the coating remaining). However, some of these initial images had lower percentages due to the noise present in the relatively darker starting material. This results in the percentages of the following cycles being slightly lower than expected. A correction was applied to account for this noise. This was made for sample runs with % coating for the 0th cycle image <99%, and was corrected to reach 99%. For instance, a sample run with a % coating for the 0th cycle image = 94% means that there is 5% noise being read and deducted for all the images in this set. Hence, a correction is made by adding 5% to the % coating values of the whole image set. This was judged to be reasonable, as this background noise could be tracked consistently in all images after abrasion and not just in the primary cycles. The values before/after correction are shown in **Figure 4.12**. The image sets are shown in Appendix 2 (Figure A2.2a-f, with the original percentages obtained by image analysis).

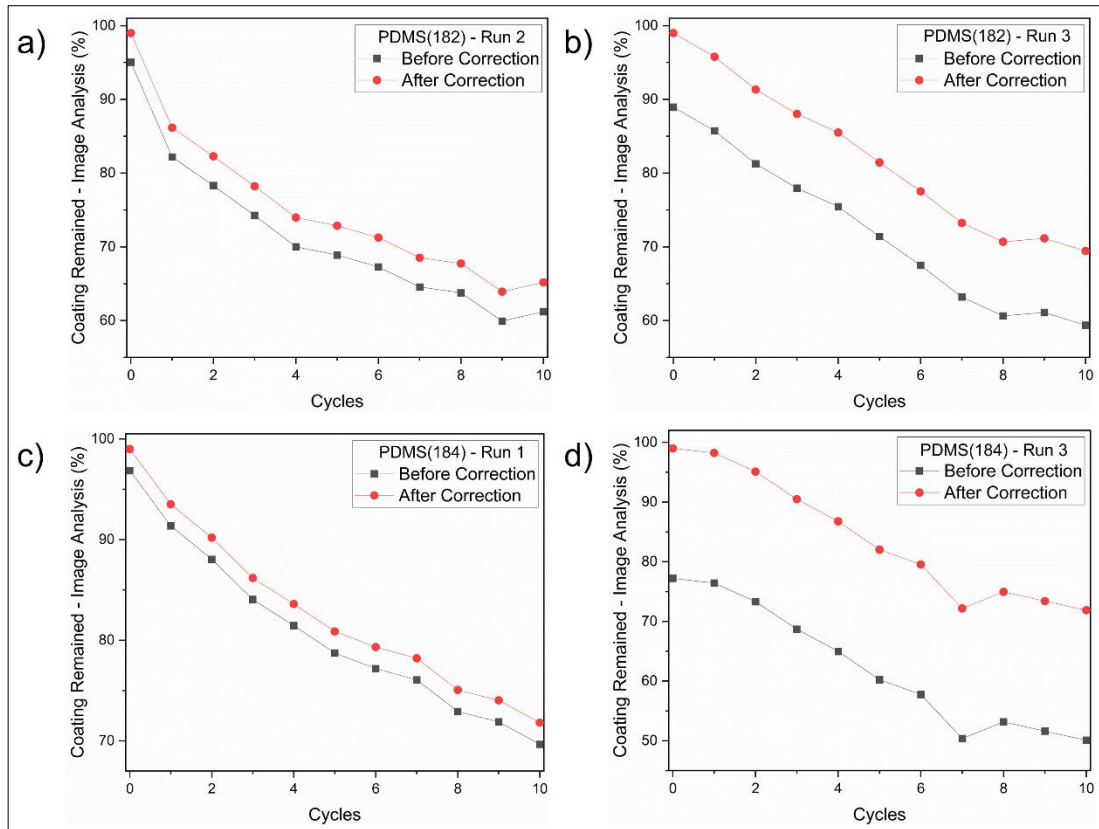


Figure 4.12: Image analysis values before and after correction for PDMS(182) (Run 2 (a) and Run 3 (b)) and PDMS(184) (Run 1 (c) and Run 3 (d)).

4.3.2.2.2. Coating performance

Figure 4.13 shows images from the abrasion experiments for PDMS(182), PDMS(184) and PDMS(186) coatings after 10 abrasion cycles, along with the corresponding binary images and the estimated percentage of coating that remained. The figure shows the values after correction for the percentage of coating remained for PDMS(182)_Run 2, 3 and PDMS(184)_Run 1, 3. The full image sets indicating all abrasion cycles are shown in **Figure 3.7d-f** (Section 3.3.2.3) for PDMS(186), and in Appendix 2 (Figure A2.2a-f) for PDMS(182) and PDMS(184).










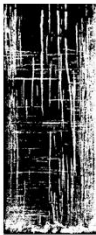







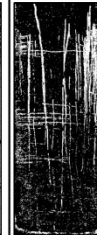
Sample	PDMS(182)			PDMS(184)			PDMS(186)		
	Run_1	Run_2	Run_3	Run_1	Run_2	Run_3	Run_1	Run_2	Run_3
Coloured Images									
Binary Images									
%_coating remained	68%	65%	69%	72%	69%	72%	79%	84%	77%

Figure 4.13: Images for the sample runs of PDMS with different TS after 10 abrasion cycles, showing the coloured (upper), binary (lower) images, and the associated percentage of coating remained as predicted by image analysis.

Regarding the performance of the PDMS polymers against abrasion (**Figure 4.14a-c**), it can be noticed that both PDMS(182) and PDMS(184) follow similar trends in coating degradation. Whereby, the percentage of coating remaining (as measured by mass tracking) was 75% for both coating compositions. This can be rationalised through the relatively small difference in their TS values. The similar mass differences for these polymers between abrasion cycles suggest that the degradation initiation and propagation mechanisms are comparable. However, PDMS(186), which has a significantly lower TS value, showed higher resistance to coating removal (total % of coating remaining = 84%), as well as a slower degradation pattern. Image analysis supported this conclusion as well, with percentages of coating remaining were found to be 67%, 71% and 80% for PDMS(182), PDMS(184) and PDMS(186), respectively.

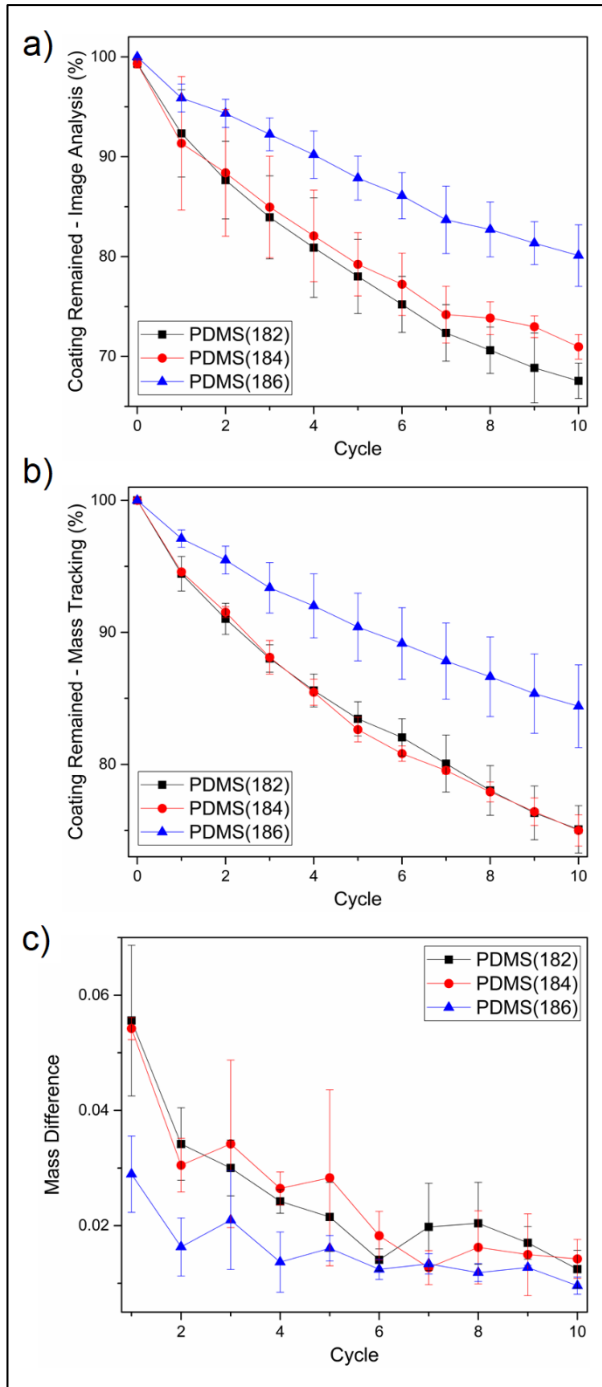


Figure 4.14: Plots for PDMS sample runs resilience performance vs. abrasion cycles. (a) shows the percentage of coating remained as predicted by image analysis, (b) shows the percentage of coating remained as measured by mass tracking, and (c) shows the mass difference between every two consecutive cycles (normalised by dividing by the initial coating mass).

4.3.2.2.3. Relating coating performance to polymer properties

It is noticed here that, unlike what was observed with PVC polymers, the abrasion resistance tended to increase with lower TS. To explain this, the differences between PVC and PDMS should be considered. PVC is a thermoplastic polymer, where the polymeric chains are only connected by weak intermolecular forces that do not fully restrict their relocation as a response to an outer stimulus, e.g. stress. It should also be noted that the major deformation mechanism for the PVC samples was inelastic in nature. While the bonding between these chains can, in general, enhance the

polymer performance, they can still break with moderate force. During the abrasion experiment, the sandpaper particles apply a certain amount of force that exceeds the binding force experienced by some of the polymer chains, leading them to deform inelastically, and causing the polymer to be removed from the coating. Higher binding forces (indicated, in this case, by the increased M_w and TS) lead to less polymer removal. In addition, the brittle nature of the polymer, given by its amorphous structure and relatively high glass transition temperature (T_g), supports the observed coating failure where the polymer tends to break with abrasion. In contrast, PDMS is a thermoset polymer where curing and covalent crosslinking result in a rigid network of polymer chains. Unlike thermoplastics, the degradation is expected to take place by removal of larger bulks of polymers rather than loose chains, due to the stronger covalent binding and the large proportion of elastic deformation prior to breaking. While a low abrasion force would be expected to not cause much damage to such rigid networks, damage can still occur using a high enough force. The extent of damage would be related to the extent of crosslinking, with higher crosslinking means more connected areas that, when degradation is initiated in a part of it, complete removal of the whole network is expected. If the difference in TS for the PDMS polymers is reflected in the increased extent of crosslinking, then this could explain the behaviour of PDMS(186). Another difference is that, unlike PVC, PDMS is a crystalline polymer with a T_g lower than room temperature, which suggests a more ductile nature and hence a different failure pattern. Although this justification explains the observed pattern in these polymer systems, it must be noted that the coatings explored here have a higher order of complexity than the mechanical testing of bulk polymers. The materials are nanocomposites, as such, their mechanical performance may vary from bulk measurements.

Another observation is that, while the TS for PDMS polymers is much lower compared to PVC polymers, the image analysis of coatings for both polymer types showed similarity in performance and even an enhancement in resistance in the PDMS polymers in terms of mass-loss tracking. This could be attributed again to the differences between them. Besides the relative degree of crosslinking in the PDMS/PVC polymers and the probable deviation of nanocomposites from the bulk polymer behaviour, there are differences in their failure mechanism as indicated by their stress-strain curves (**Figure 4.15**). For PVC, the test sample tended to record a maximum stress value shortly after the test starts, then the stress drops and the sample continues to elongate further (for 150%-250% of its original length) while the stress increases, until recording another maximum just after the sample breaks. For

PDMS, the strain increases steadily with the stress until reaching the breaking point. While a complete understanding of the implications of these differences in the coating resistance for abrasion is not complete, the main conclusion that could be extracted from this is that these differences invalidate direct comparisons between both types of polymers.

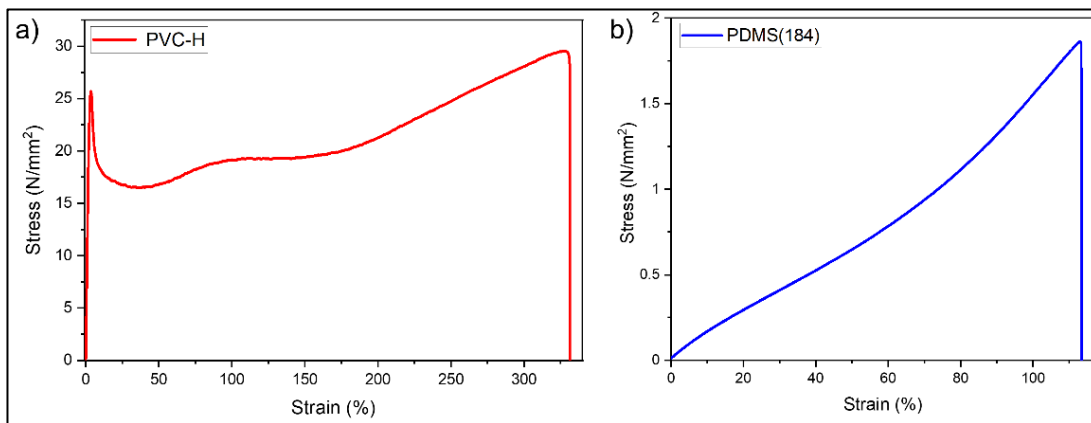


Figure 4.15: Stress-strain curve for a) PVC and b) PDMS.

4.3.2.2.4. Adhesion/cohesion failure

The final analysis to consider for PDMS results is the difference between mass loss and image analysis values (**Table 4.1**). Here, these values were more comparable in contrast to the case with PVC coatings, suggesting that coating-substrate adhesion failure is dominant for these coatings. As demonstrated in the previous chapter (Section 3.3.3.1.), the mass percentages were slightly higher than that obtained by image analysis for the PDMS coatings, resulting in a negative difference (-8% for PDMS(182), and -4% for both PDMS(184) and PDMS(186)). This was attributed to parts of the coating being detached from the substrate but not from the rest of the coating material, leaving small portions of the polymer. This is illustrated by the confocal images of scratches in a PDMS(186) coating (**Figure 4.16**). In comparison to the PVC scratches, it could be noticed that the scratch is surrounded by a pile of polymer that is higher in thickness compared to areas away from scratch boundaries. This suggests that the removed material during abrasion (or part of it) is being pushed into a different area rather than completely detached from the coating surface. This further supports that cohesion failure was not common, given that the abrasion force was, in some cases, enough to break the adhesion but not to completely overcome cohesion forces.

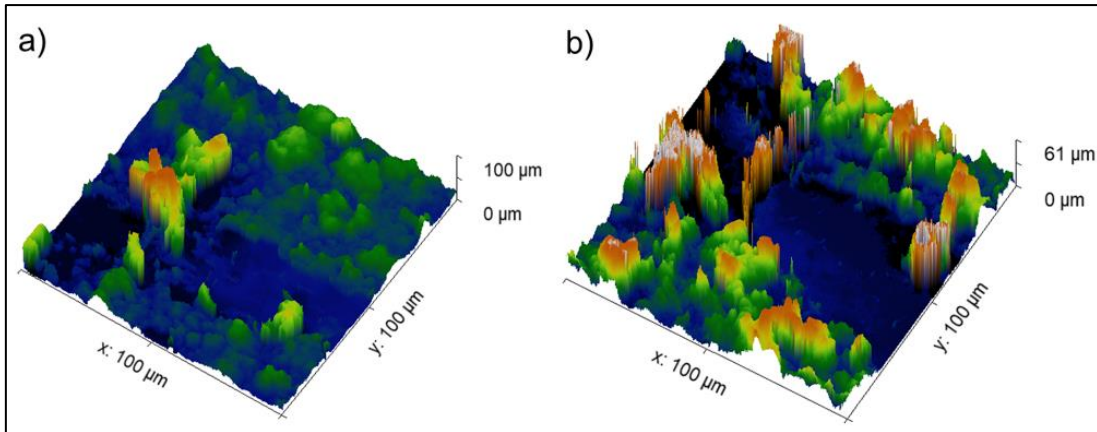


Figure 4.16: Confocal fluorescence images of two scratches on abraded coatings of PDMS(186) (a-b).

4.3.3. Influence of Particles

The effect of changing particles size and combining different particle sizes was investigated. Silica particles were incorporated in this study in two different sizes: $\varnothing \sim 15 \text{ nm}$ and $\varnothing \sim 1.5 \mu\text{m}$. In this part, the polymer used was PDMS(186) and was kept the same across all sample runs.

4.3.3.1. Determining optimum mass ratio for μSiO_2

As mentioned earlier, the optimum M_{ratio} for nSiO_2 -based coatings (with either PVC or PDMS) has been previously investigated. Increasing the size of the silica particles was found to change the optimum M_{ratio} , and hence a re-optimisation was conducted. **Figure 4.17a-d** shows how the polymer/silica encapsulation changes with increasing the M_{ratio} from 0.2 to 0.5. The lower ratios (0.2 and 0.3) allowed a thin coverage of the particles with residual polymer 'gluing' the particles together. Increasing the ratio to 0.4 increased the observed thickness of the polymer shell, which can reduce the roughness of the surface. This was reflected in the measured WCA (**Figure 4.17e**), as it decreased from 165° and 170° for $M_{\text{ratio}} = 0.2$ and 0.3 , respectively, to reach 137° for $M_{\text{ratio}} = 0.4$. Further increase of polymer quantity ($M_{\text{ratio}} = 0.5$) led to a mostly flat surface, with a WCA of 108° was recorded. The optimum M_{ratio} was concluded to be 0.3.

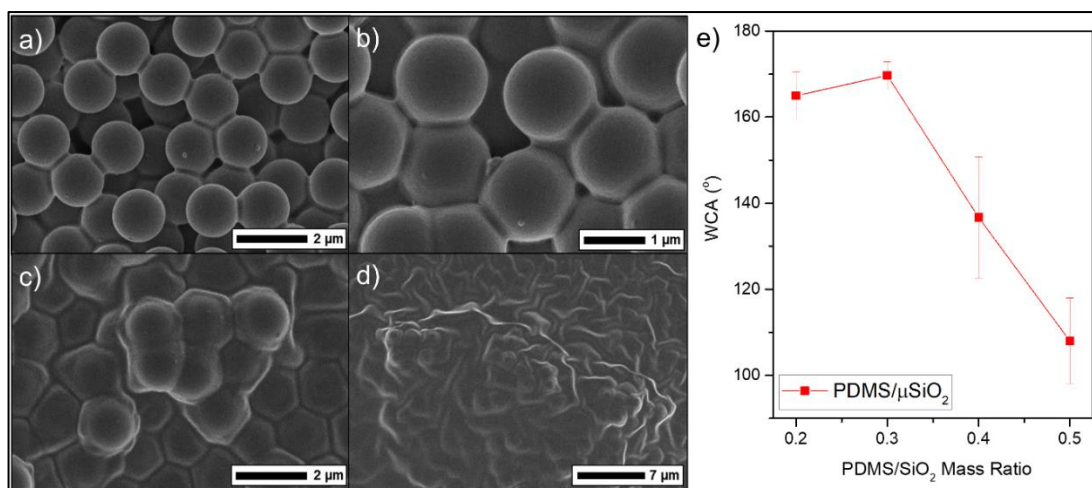


Figure 4.17: a-d) SEM images of PDMS/ μ SiO₂ coatings prepared using different polymer/silica M_{ratio} . The typical M_{ratio} shown are a) 0.2, b) 0.3, c) 0.4 and d) 0.5. Scale bars are shown for each image. e) Plot of the WCAs measured for these coatings.

4.3.3.2. Changing particle size

PDMS/nSiO₂ and PDMS/ μ SiO₂ coatings were prepared. Due to the difference in the optimum M_{ratio} between both particles, keeping both silica/polymer quantities similar across these coatings was not applicable. It was chosen to keep the polymer mass the same and change the silica quantity accordingly, as the polymer is expected to contribute largely to the coating robustness. The μ SiO₂ coating appeared to produce less coverage of the substrate, hence the coating volume was needed to be doubled to ensure complete coverage. The images from the abrasion experiment are shown in **Figure 4.18**. The main observation was that the particle size influences the size of scratches made on the coatings. While the scratches in nSiO₂ coatings tend to be narrow, μ SiO₂ coatings are prone to much wider scratches and material removal upon abrasion. If the coating is formed as aggregates of particles glued together by the polymer, and with the μ SiO₂ being 100-times larger in diameter, it is expected that these aggregates would cover bigger areas of the substrate. This causes the variation in consequences of the failure induced by the sandpaper, although this failure induction might occur similarly for both coatings.

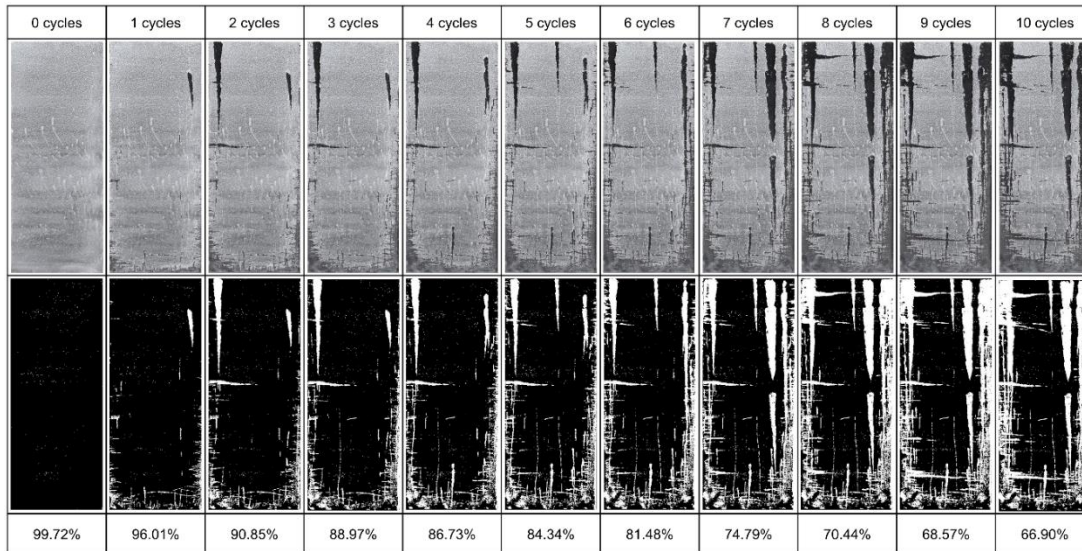


Figure 4.18: The image set for the sample run of μSiO_2 coating, showing the coloured (upper), binary (lower) images, and the associated percentage of coating remained as predicted by image analysis.

Comparing image analysis, mass tracking and mass difference results (**Figure 4.19**), it could be noticed that the amount of coating that remained after 10 abrasion cycles is lower (by image analysis: 67% vs. 80% for nSiO_2 coatings, by mass tracking: 63% vs. 84% for nSiO_2 coatings). The μSiO_2 coating tended to lose more mass with each cycle. Moreover, the mass difference did not follow a similar pattern as nSiO_2 coatings with the loss decreasing as the abrasion continues. These results suggest a similar conclusion as discussed above, with the nanoparticles being more resistant to coating removal due to the smaller aggregates removed with each abrasion cycle.

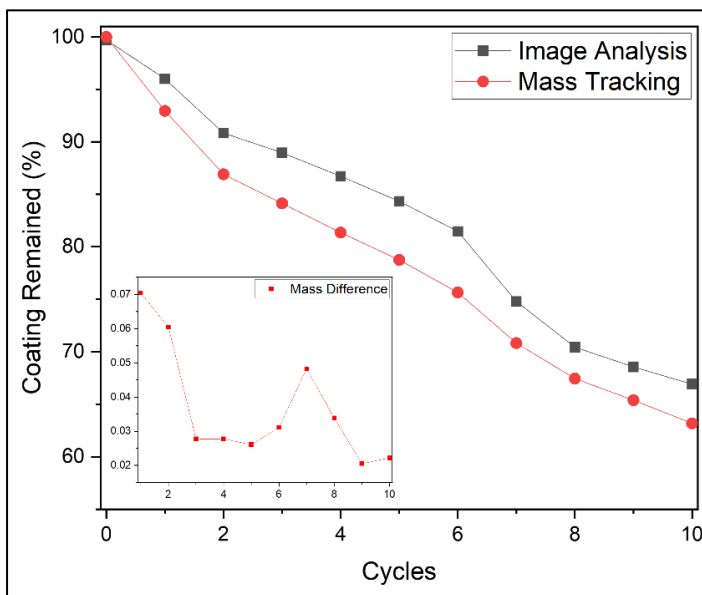


Figure 4.19: Plot for Image analysis, mass tracking and mass difference (inset) results of μSiO_2 coating.

4.3.3.3. Combining different particle sizes

Another factor examined was the effect of combining different particle sizes in the coating. This would induce structural hierarchy, which is widely reported to enhance superhydrophobicity, but its effect on the robustness is not as established. This inclusion was made in three different methods (as detailed in Section 4.2.4), either by spraying a layer of each particle size separately or by mixing both particles before the spraying process. The WCAs measured for these coatings confirmed their superhydrophobicity (**Figure 4.7**). **Figure 4.20** shows images from the abrasion experiments for μ -n coatings, n- μ coatings and μ /n mix coatings after 10 abrasion cycles, along with the corresponding binary images and the estimated percentage of coating that remained. The full image sets indicating all abrasion cycles are shown in Appendix 2 (Figure A2.3a-i).




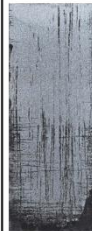



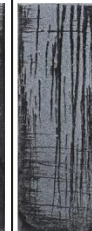




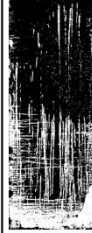





Sample	μ -n			n- μ			μ /n mix		
	Run_1	Run_2	Run_3	Run_1	Run_2	Run_3	Run_1	Run_2	Run_3
Coloured Images									
Binary Images									
%_coating remained	44%	55%	65%	67%	78%	80%	55%	49%	62%

Figure 4.20: Images for the sample runs of silica (with different sizes and deposition order) after 10 abrasion cycles, showing the coloured (upper), binary (lower) images, and the associated percentage of coating remained as predicted by image analysis.

Plots for coatings performance are shown in **Figure 4.21**. It was observed that the least resistant was the μ -n coatings. They showed the highest coating removal percentage, as well as a faster degradation pattern in the first abrasion cycles as indicated by the mass difference plot. This is expected in light of the behaviour of the PDMS/ μ SiO₂ coatings explained above. While here there was an additional layer of smaller particles deposited, it appeared that the low adhesion of the micron particles aggregates forming the base of the coating influenced the coating robustness. A

similar observation was noticed for the $n-\mu$ coatings, where the narrow, short scratches and less material removal resemble the abraded PDMS/ $n\text{SiO}_2$ coatings. While these combinations behaved predictably according to the base coating, however, comparing these coatings to each other (**Figure 4.21d-f**), the $n-\mu$ coatings appeared to show lower resilience. This suggests that the mixing of different particle sizes could introduce some irregularity that results in coatings more prone to failure.

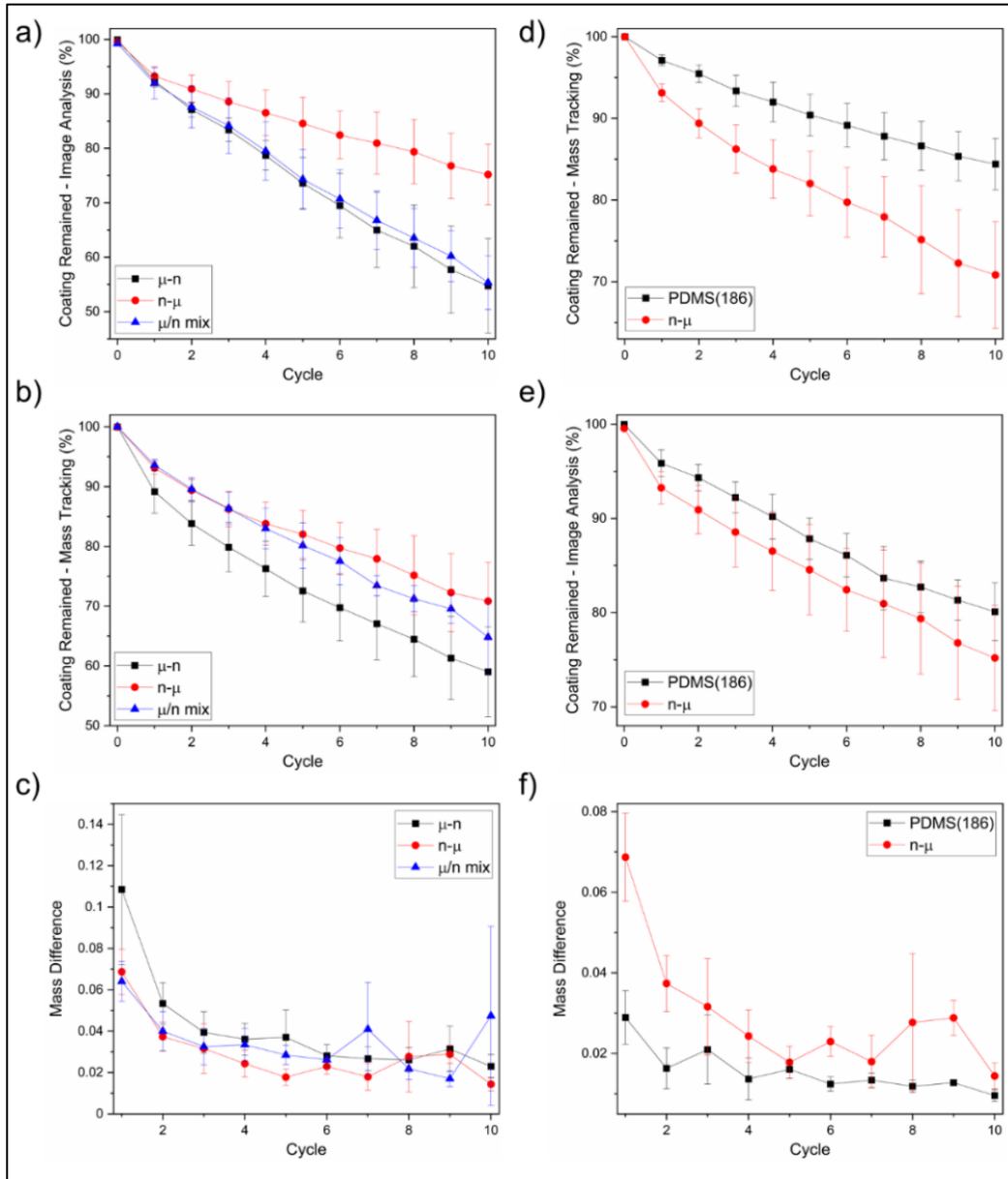


Figure 4.21: Plots for silica sample runs resilience performance vs. abrasion cycles (a-c), and a comparison between PDMS Sylgard 186 and $n-\mu$ resilience performance (d-f). (a, d) shows the percentage of coating remained as predicted by image analysis, (b, e) shows the percentage of coating remained as measured by mass tracking, and (c, f) shows the mass difference between every two consecutive cycles (normalised by dividing by the initial coating mass).

The lower substrate adhesion shown by the μSiO_2 can also explain how the n/ μ mix coatings showed better resistance compared to μ -n coatings, as the former would hypothetically have less of these particles at the base (caused by the particle mixing and the one-step spraying). Although this mixing would maximise the irregularity, making the coatings lose more mass towards the final abrasion cycles. This also agrees with the data shown in **Table 1**. While both (μ -n) and (n/ μ mix) coatings show the same trend of incomplete coating detachment and high mass remaining than expected by image analysis, this was reversed for the n- μ coatings. This, again, is probably due to the low adhesion of the μSiO_2 that occupies larger areas at the surface and can easily detach even if the n SiO_2 particles are not removed.

4.4. Conclusions

Resilience analysis of advanced materials and coatings is key in assessing their potential for real-world application. The methodology utilised here is demonstrated to provide insight into the fundamental resilience of various coating formulations and enable the identification of polymers and surface architectures that can provide maximised resistance to physical degradation. It was found that the resilience was maximised in PDMS coatings when PDMS(186) was incorporated while selecting higher M_w polymer for PVC coatings enhanced the performance. In addition, nano-sized silica performed better than the micron-sized particles, suggesting slower degradation patterns for coatings involving smaller particles. This resilience data were used to quantitatively compare different coatings, and due to the two measures used (image analysis and mass difference), an insight into respective degradation pathways can be gained. This is highlighted in the comparison between PDMS and PVC coatings, whereby PVC coatings provide a substantially higher difference between these two measures, with a higher degradation detected through sample weighing. In addition, the nature of scratches was investigated *via* confocal fluorescence microscopy, where PDMS coatings material showed a non-complete detachment from the surface once being removed *via* abrasion.

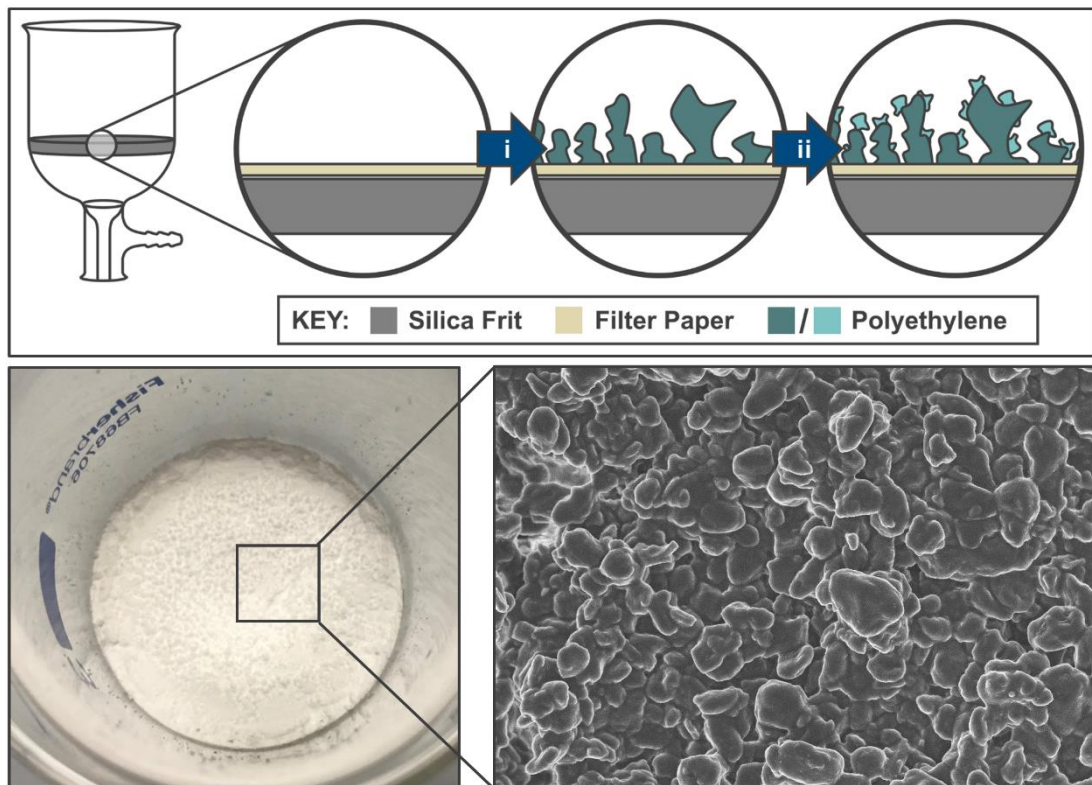
4.5. References

- 1 C. R. Crick, in *Superhydrophobic Surfaces-Fabrications to Practical Applications*, IntechOpen, 2018, pp. 11–38.
- 2 F. Guo, Q. Wen, Y. Peng and Z. Guo, *J. Colloid Interface Sci.*, 2017, **494**, 54–63.
- 3 R. L. Upton, A. Fedosyuk, J. B. Edel and C. R. Crick, *ACS Appl. Nano Mater.*,

- 2021, **4**, 10090–10102.
- 4 K. K. Jung, Y. Jung, C. J. Choi and J. S. Ko, *ACS Omega*, 2018, **3**, 12956–12966.
 - 5 P. Wang, T. Zhao, R. Bian, G. Wang and H. Liu, *ACS Nano*, 2017, **11**, 12385–12391.
 - 6 X. Deng, L. Mammen, Y. Zhao, P. Lellig, K. Müllen, C. Li, H. J. Butt and D. Vollmer, *Adv. Mater.*, 2011, **23**, 2962–2965.
 - 7 T. Xiang, Y. Han, Z. Guo, R. Wang, S. Zheng, S. Li, C. Li and X. Dai, *ACS Sustain. Chem. Eng.*, 2018, **6**, 5598–5606.
 - 8 B. Wu, X. Cui, H. Jiang, N. Wu, C. Peng, Z. Hu, X. Liang, Y. Yan, J. Huang and D. Li, *J. Colloid Interface Sci.*, 2021, **590**, 301–310.
 - 9 L. Xu, Z. Geng, J. He and G. Zhou, *ACS Appl. Mater. Interfaces*, 2014, **6**, 9029–9035.
 - 10 X. Zhang, D. Zhi, L. Sun, Y. Zhao, M. K. Tiwari, C. J. Carmalt, I. P. Parkin and Y. Lu, *J. Mater. Chem. A*, 2018, **6**, 357–362.
 - 11 V. Kondrashov and J. Rühle, *Langmuir*, 2014, **30**, 4342–4350.
 - 12 E. Huovinen, L. Takkunen, T. Korpela, M. Suvanto, T. T. Pakkanen and T. A. Pakkanen, *Langmuir*, 2014, **30**, 1435–1443.
 - 13 A. Millionis, E. Loth and I. S. Bayer, *Adv. Colloid Interface Sci.*, 2016, **229**, 57–79.
 - 14 R. L. Upton, Z. Davies-Manifold, M. Marcello, K. Arnold and C. R. Crick, *Mol. Syst. Des. Eng.*, 2020, **5**, 477–483.
 - 15 C. R. Crick, S. Ismail, J. Pratten and I. P. Parkin, *Thin Solid Films*, 2011, **519**, 3722–3727.
 - 16 C. R. Crick and I. P. Parkin, *J. Mater. Chem.*, 2009, **19**, 1074–1076.
 - 17 C. R. Crick and I. P. Parkin, *Thin Solid Films*, 2010, **518**, 4328–4335.
 - 18 R. L. Upton, University of Liverpool, 2021.
 - 19 I. D. Johnston, D. K. McCluskey, C. K. L. Tan and M. C. Tracey, *J. Micromechanics Microengineering*, 2014, **24**, 035017.
 - 20 K. Balani, V. Verma, A. Agarwal and R. Narayan, in *Biosurfaces: A Materials Science and Engineering Perspective*, John Wiley & Sons, Ltd, 1st edn., 2015, pp. 329–344.
 - 21 A. V. Belashov, Y. M. Beltukov, O. A. Moskalyuk and I. V. Semenova, *Polym. Test.*, 2021, **95**, 107132.
 - 22 T. De Larrard, J.-B. Colliat, F. Benboudjema, J.-M. Torrenti, G. Nahas, T. De Larrard, J. B. Colliat, F. Benboudjema, J. M. Torrenti and G. Nahas, *Nucl. Eng. Des.*, 2010, **240**, 166–184.
 - 23 Michael Sepe, The Strain Rate Effect | Plastics Technology, <https://www.ptonline.com/articles/the-strain-rate-effect>, (accessed 6 January 2022).
 - 24 S. Nemat-Nasser and H. Deng, *Acta Metall. Mater.*, 1994, **42**, 1013–1024.

Chapter 5:

Micronized Polyethylene Filters for Oil/Water Separation



Publications:

Heat-Treated Micronized Polyethylene Powder for Efficient Oil/Water Separating Filters. Y. A. Mehanna and C. R. Crick. *Materials*, 2020, **13**, 3160(1-12).

5. Micronized Polyethylene Filters for Oil/Water Separation

5.1. Introduction

With the increased demand for oil drilling, transporting and usage in many industries, the development of systems for oil/water separation became a crucial need to treat contaminated water as a result of leakages and/or inappropriate disposal (Section 1.4.4).^{1,2} The fabrication of filters with special wetting (super-hydrophilic/hydrophobic) has been widely adopted for this application while growing efforts are being devoted to the further development of applicable technologies.³⁻⁷ The optimal technical solution should combine a high separation efficiency with a straightforward fabrication procedure at a low cost.⁸ Meanwhile, the environmental compatibility of the prepared systems, as with many other applications, needs to be considered.^{8,9} An aspect of this is the development of systems where recycled materials can be incorporated. This chapter attempts to do this by utilizing micronized polymer powder to generate superhydrophobic filters. In this section, a brief discussion of the process of micronization and its relevance to the subject of polymer recycling, along with the treatment of powder materials, will be included.

5.1.1. Polymer Recycling and Micronization

Due to their distinguished properties and great diversity, the involvement of polymers has rapidly increased and extended to numerous applications.^{10,11} Driven by the demand to meet both the functionality and cost requirements for the targeted products, along with the potential difficulty of preparing a single-material design that satisfies all these requirements, multi-material designs have been introduced.^{12,13} Incorporating multi-material composites can be advantageous in reducing cost, improving performance and integrating complex functionality.¹¹ A common method that is widely adopted in industry for the manufacturing of multi-material products is co-injection moulding. In this technique, two different polymers can be simultaneously injected into the mould to form a core/shell hybrid structure.¹⁴ This technique is favourable over routes that involve post-assembly of single-material manufactured parts, due to the enhanced quality of products and the reduced manufacturing cost/time.^{15,16} However, multi-material composites are more difficult to recycle as they require separation steps, which raises huge environmental concerns.^{17,18}

Efforts for the development of recycling routes that do not require material separation have been invested, as this approach could be promising in reducing the cost of

recycling as well as extending the process to include more products.^{19,20} The most commonly reported for this target is micronization. Micronization is a process of reducing the particle size of the material,²¹ which can be achieved through different approaches. Examples include grinding, spray drying, and spiral jet milling, in addition to others.^{11,22} While the size of the generated particles using simple methods (i.e. grinding) can be around 0.4 mm, other methods are utilised when a smaller scale is required and can generate particles with a size around 10 μm .¹¹ The application of micronization in materials recycling has been reported for several material types. This was heavily considered in the field of construction. Examples include the manufacturing of mortar paste from recycled barite mineral,²³ recycled concrete made from micronized silica derived from rice husk,²⁴ and the production of bricks from micronized biomass waste.²⁵ Recycling of polymers through micronization was also reported for tire rubber, which is difficult to recycle through conventional techniques due to its thermosetting nature. Zhang *et al.* reported the preparation of a thermoplastic elastomer made through the incorporation of micronized rubber powder, which was found to be processable through injection, extrusion, etc.²⁶ Micronization of other thermoplastic polymers was also studied, examples include polyurethane²⁷ and polyamide.²⁸

5.1.2. Sintering

Sintering refers to the process of forming a solid coherent material from loose powder by the application of heat (and/or pressure) without complete melting of the powder (**Figure 5.1**). The conditions of sintering can influence the morphology of the generated material. This is mostly represented by its structural integrity as well as its porosity.²⁹ The latter, in turn, influences many of the mechanical, thermal and electrical properties of the formed solid material.³⁰

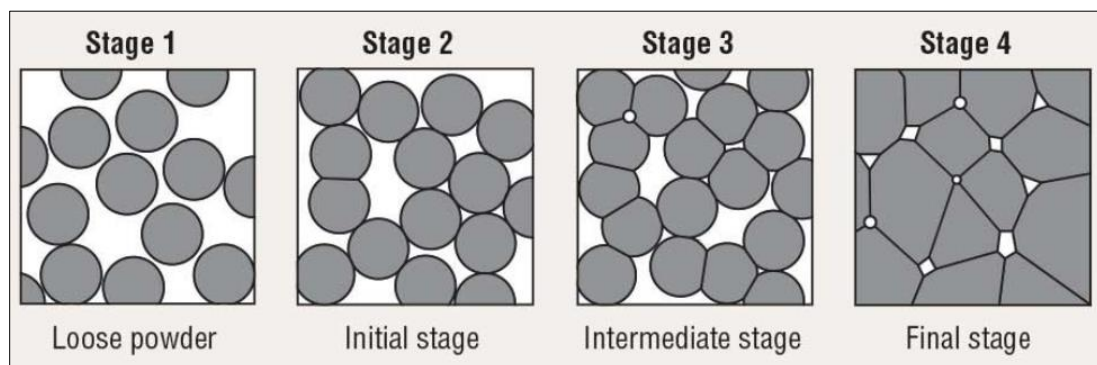


Figure 5.1: Sintering stages for converting loose powder (left) into a solid material (right). Figure retrieved from ref.³¹

This process is widely applied for the treatment of powder materials, and the fabrication of superhydrophobic filters is a common example where this technique is utilised. The porosity that is usually provided by this fabrication route allows the passage of hydrophobic solvents, which is key for effective separation.²⁹ Examples include the hydrophobic modification of sintered hydrophilic glass filters,^{29,32} as well as the sintering of hydrophobic powder materials.^{33,34} As with any superhydrophobic surface, surface roughness is essential for high water repellence. While this can be achieved by conventional surface roughening routes (roughening of the surface and/or deposition of rough materials), the porosity of the sintered material could be sufficient for this aim, providing its presence in the appropriate ratio, size and/or surface distribution.³⁴

5.1.3. Chapter Aim

The utilisation of micronized polymer powder to fabricate superhydrophobic filters is investigated here. Generally, superhydrophobic surfaces have features ranging from the nanoscale to a few microns.³⁵ Utilising this principle, a surface constructed from microparticles of a hydrophobic polymer would be sufficient to observe a superhydrophobic behaviour, as such particles being present on the surface would generate the required roughness. Micropowders of hydrophobic polymers have been reported for surface modification, which resulted in changing the wetting properties of the materials decorated with these particles.^{36,37}

As an example, polyethylene is a hydrophobic polymer, with a WCA of $\sim 100^\circ$ for a flat polymer layer deposited on a flat surface.³⁸ Owing to its compatibility with many systems, it has been reported numerously for the fabrication of superhydrophobic coatings.³⁹⁻⁴¹ The heat-treatment of polyethylene powder to produce a hydrophobic film has been reported previously.⁴² However, the high temperature applied resulted in a complete melting of the polymer, generating a flat, nonporous film that needs to be roughened and pricked to make it functional. Herein, the aim is to optimise the conditions of micropowder treatment to construct a readily-permeable, rough-surface filter system for oil/water separation. In doing this, it is important to ensure that the applied treatment is effective to bind the powder together without blocking possible pathways for liquid passage.

To achieve this, first the properties of the powder, in terms of its hydrophobicity, need to be investigated. After this, the treatment parameters (heating temperature, heating

time, use of solvent) will be optimised. Finally, the filter will be constructed accordingly and the separation efficiency of hydrophobic solvent/water mixtures will be tested.

5.2. Experimental Methods

5.2.1. Materials

Finely micronized polyethylene with different mean particle sizes (Three grades; 4.25-4.75, 5-7 and 7-9 μm , product codes are: MPP-620XXF, MPP-620VF and MPP-620F, respectively) were generously gifted by Kromachem Ltd. For simplicity, these particles will be referred to as S- μ , M- μ and L- μ for the small (4.25-4.75 μm), medium (5-7 μm) and large (7-9 μm) particles, respectively. Chloroform (analytical grade, $\geq 99.8\%$), toluene (analytical grade, $\geq 99.8\%$), dichloromethane (DCM, laboratory-grade, $\geq 99\%$) and hexane (HPLC grade, $\geq 95\%$) were purchased from Fisher Scientific. Methylene blue was purchased from Sigma Aldrich. Nile Red (9-(Diethylamino)-5Hbenzo[a]phenoxazin-5-one) was purchased from Tokyo Chemical Industry UK Ltd. Filter papers (\varnothing – 4.25 cm, grade 1, pore size 11 μm) were purchased from Whatman. Glass microscope slides (76 \times 26 mm) were purchased from ThermoScientific.

5.2.2. Filter Preparation

Polyethylene filters were fabricated using a dual-layer design prepared in two different steps (**Figure 5.2**). The first layer (i) used 3.2 g of polyethylene powder, which was added into a Buchner funnel (\varnothing – 5 cm) on top of a filter paper to prevent the powder from falling through the funnel. After roughly dispensing the powder in the paper, 10 mL of hexane were used to wet and more evenly distribute the powder across the surface using a Pasteur pipette. The funnel was then placed upright in a preheated oven at 140°C for 10 min when the polymer was lightly compacted (using the base of a glass beaker and while the powder is still hot) to help reduce cracking and form a uniform surface. To prevent the powder from sticking to the glass, the beaker was covered with a sheet of synthetic rubber. The funnel was left at the same temperature for another 5 min after compacting.

For the second layer (ii), 1 g of the same polyethylene powder was dispersed in 40 mL of hexane. The entire solution was evenly spray-coated on top of the first layer prepared previously. Spray-coating was carried out using a compression pump and airbrush gun (Voilamart), at a pressure of 2 bar. All spraying was carried out approximately 4 cm away from the surface. After spray coating was complete, another

10 mL of hexane was sprayed to ensure all powder has been placed uniformly and none is left at the spray nozzle. The funnel was returned to the oven at a lower temperature (114°C) for 10 min.

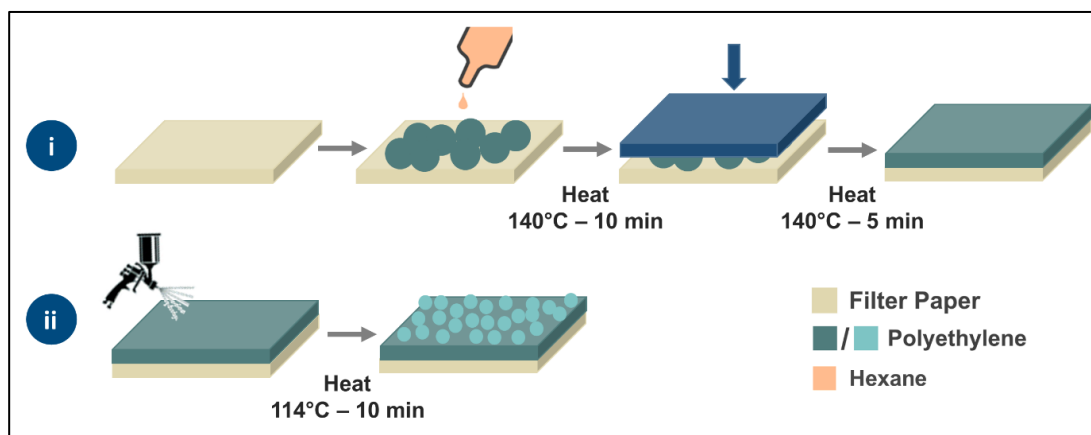


Figure 5.2: A schematic showing the fabrication method of the polyethylene micropowder filters. For the primary layer (i), the powder is placed on a filter paper, dispersed by hexane and heat-treated (140 °C), followed by compacting and further heating. The second layer (ii) of powder is deposited by spray coating a suspension of particles in hexane and is annealed at 114 °C.

Comprehensive materials analysis was hindered when the powder was formed inside the Buchner funnel. As a result, sample analysis of the filter surface was mimicked on glass microscope slides by using the conditions outlined above for the secondary layer. Microscope slides were utilised for sample imaging, WCA and tilt angle (TA) measurements. TA measurements were also conducted on the filters fabricated within the Buchner funnels and were compared to measurements taken using the slides.

5.2.3. Separation Efficiency Assessment

Separation efficiency was examined using hydrophobic solvents (chloroform, DCM, hexane and toluene) and water (**Figure 5.3**). For each test, 1 mL of each of the hydrophobic solvents was mixed with 1 mL of water. All hydrophobic solvents were coloured with Nile-Red dye and methylene blue was used to dye the water (a dye concentration of ≈ 7 mg/mL was used). This insured visualisation of the separation process, and an immediate indication of the purity of the solvent that passed through/collected on the filter. The separation efficiency was monitored by comparing the quantity of water applied to and then collected from the filter – this was determined using the difference in weight before and after separation. Between each test, the

filter was heated for a few seconds using a heat gun and dried with a tissue to ensure none of residual solvent/water is present. The reported efficiency percentage is the

average of five readings taken for the same filter and solvent.

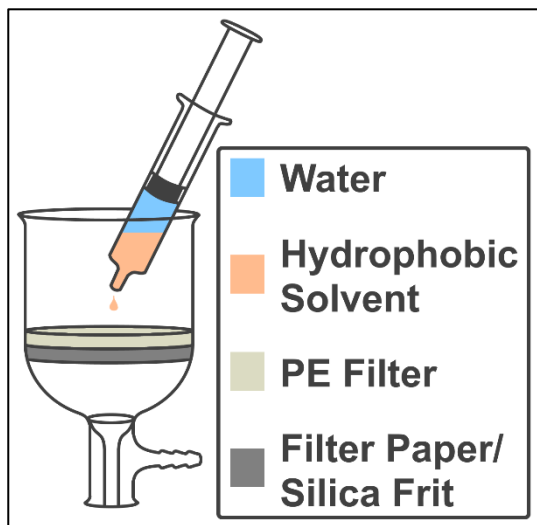


Figure 5.3: A schematic showing the separation efficiency measurement setup. Equal volumes (1 mL) of both water and hydrophobic solvent are poured onto the filter using a syringe. When the separation is completed, the syringe is used to collect the water above

the filter for weighing.

5.2.4. Characterisation

Kruss (DSA100E) Drop Shape Analyser was used to measure TAs, for both the polyethylene filters and the materials deposited onto glass microscope slides. These measurements were repeated at least ten times for each sample and the average was calculated.

For WCA measurements conducted on the filters (in the Buchner funnel) and coated glass slides, water droplet volumes of 20 μL and 5 μL were used respectively. For the filters, WCAs were measured by taking photographs of water droplets placed on top of the filters while in the Buchner funnel.

Water bouncing was done using the same glass funnels, and water droplets were dropped from a height of 20 mm (tip to the surface) using a micro-syringe fitted with a 27-gauge dispensing tip.⁴³ The water droplets from this tip were estimated at 8 μL in size and were left to detach under using their weight. Methylene blue was added to the water to aid visualisation, this was not observed to change the behaviour of the water droplets on the surface. The bouncing was filmed at 500 frames per second using a SONY RX10-IV camera.

SEM imaging was performed using a Hitachi S4800 microscope, operating at an acceleration voltage of 3-5 kV for polymer samples deposited on glass slides.

Samples were coated with a thin layer of chromium metal to ensure electrical conductivity and high-quality SEM images.

5.3. Results and Discussion

5.3.1. Powder Properties

The polyethylene micropowder was chosen as it is inherently hydrophobic, and also to the thermoplastic nature of polyethylene. All the powders were exceptionally hydrophobic as received (≈ 8 bounces using water bouncing test, corresponding to a WCA $\approx 165^\circ$ ⁴³, **Figure 5.4**). This was due to the combination of their hydrophobic chemistry and roughness on the correct length scales. However, the particles could not be used as received to form a consistent superhydrophobic surface, nor as a water-oil separation membrane, as the microparticles were mobile when impacted by liquids. To prevent this, heat treatment of the powders would be used to force the particles to agglomerate, forming a continuous membrane for separation that would be fixed in place. The thermoplastic nature of the polyethylene would be utilised to induce partial melting and bind the particles together at the edges of the micron-sized aggregates, without completely blocking the filter permeability. Hence forming a hydrophobic permeable material that would repel water and allow the passage of hydrophobic solvents.

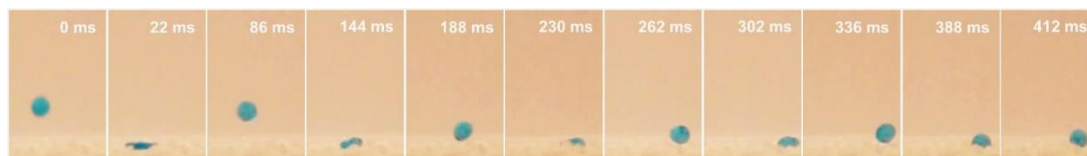


Figure 5.4: Photographs of a water droplet bouncing on polyethylene micropowder placed on a glass slide without any treatment.

Although the loose powder is characterised by a high hydrophobicity, this hydrophobicity could decrease dramatically with, for example, excessive heating (as low as 109° when heated at 160°C). Therefore, the choice of treatment conditions (i.e. the type/quantity of solvent used for particle dispersion, the temperature used, and exposure time) should be carefully considered as this has a large impact on the manufactured filter properties. This was thoroughly investigated in the following section to establish the optimal process for generating elevated hydrophobicity, and thus high oil-water separation efficiencies.

5.3.2. Treatment of Powder and Effect of Hydrophobicity

Heat-treatment of the filters without dispersal of the powder (using a solvent) proved incapable of generating a solid and uniform material. This resulted in a low powder cohesion, and in most cases, there was no (or little) physical change in the material form, regardless of how long the heat-treatment lasted. This was not observed when the powder was dispersed with a solvent before heat treatment, as after 15 minutes (at 140°C) the powder started to adhere together to form particle agglomerates. This suggested that using a solvent to disperse the powder enhanced the agglomeration process by evenly distributing the microparticles, which led to more consistent heating throughout the material and a more uniform (partial) melting behaviour resulting in a uniform filter.

5.3.2.1. Use of Solvent

Two types of solvent were examined for pre-treating the microparticles: hexane and toluene. These were chosen for their ability to disperse the particles without dissolving them. The main difference between these two solvents that would influence the filter properties is their boiling temperature (hexane: 68°C, toluene: 110°C), as a longer heat-exposure time is required with a higher boiling temperature to reach complete evaporation. Hexane was found to be more suitable, as its boiling temperature was low enough to ensure rapid evaporation, compared to toluene, which required a longer time to completely dry the filter. The filters formed using toluene resulted in a less hydrophobic base layer, and this was assumed to be caused by a flatter morphology. This was reflected in no bouncing of the water droplet. When hexane was used, a greater level of surface roughness was preserved, leading to a degree of superhydrophobicity, which was indicated by four water bounces (corresponding to a WCA around 155°).⁴³ The difference in bouncing behaviour is indicated in

Figure 5.5.

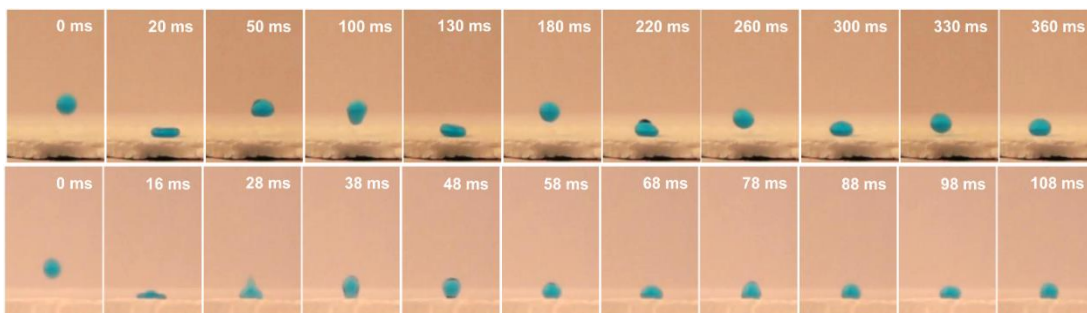


Figure 5.5: Photographs of a water droplet bouncing on the powder cured at 110°C, using hexane (top) and toluene (bottom) as a dispersing solvent.

The quantity of solvent used was also found to affect the surface roughness. Using a large quantity of hexane (≥ 4 mL/g) would lead to the same effect as using toluene as the powder would remain wetted for a long time and evaporation would be delayed. With too little solvent quantities (≤ 2 mL/g) this was found to limit the extent to which the heat treatment would generate a solid/uniform structure. To minimise the loss in hydrophobicity while maintaining a well-structured filter, the quantity of solvent that would be just enough to wet the whole powder was used. In addition, the solvent was poured slowly using a Pasteur pipette to ensure even distribution and to avoid putting too much solvent. Typically, for a 3.5 g of powder, 10 mL of hexane was enough to reach a good wetting.

5.3.2.2. Heat Treatment

The ideal temperature of heat treatment was explored, using the reported melting point for bulk polyethylene (114°C) as a foundation. Temperatures lower than this would not be sufficient for inter-particle binding. Meanwhile, when heated at a higher temperature, i.e. above 160°C, a large portion of the powder would melt completely after 10 min. This high-temperature treatment led to a non-porous, marginally hydrophobic material when cooled to room temperature. Therefore, three temperatures (114°C, 140°C and 160°C) were chosen for heat treatment of the powder, and the filters treated at these temperatures were compared to the un-treated powder in terms of the roughness of the filters and inter-particle binding using SEM (**Figure 5.6**).

For loose powder (**Figure 5.6a-c**), as expected, particle binding was not observed. Holding the polymer at its melting point (114°C) was found not enough to form a well-structured filter, as the structural integrity was poor and the filter could be easily broken with minimal force. Imaging these filters showed a moderate degree of cohesion and inter-connectivity (**Figure 5.6d-f**). In addition, retention of the roughness can be observed, where microscale features remain present. Moving to a higher temperature (140°C, **Figure 5.6g-i**), a large degree of particle agglomeration can be seen. Furthermore, small (~200 nm) wrinkles can be observed on the surface of the polymer particles, indicating a high degree of surface melting and resultant resolidification.⁴⁴ This higher level of surface melting is observed on the macroscale with a greater level of cohesion in the filter material. Operating at a higher temperature (160°C, **Figure 5.6j-l**) results in a complete melting of the polymer. This led to the loss of the initial morphology from the microparticles, resulting in a structure closer to a flat film.

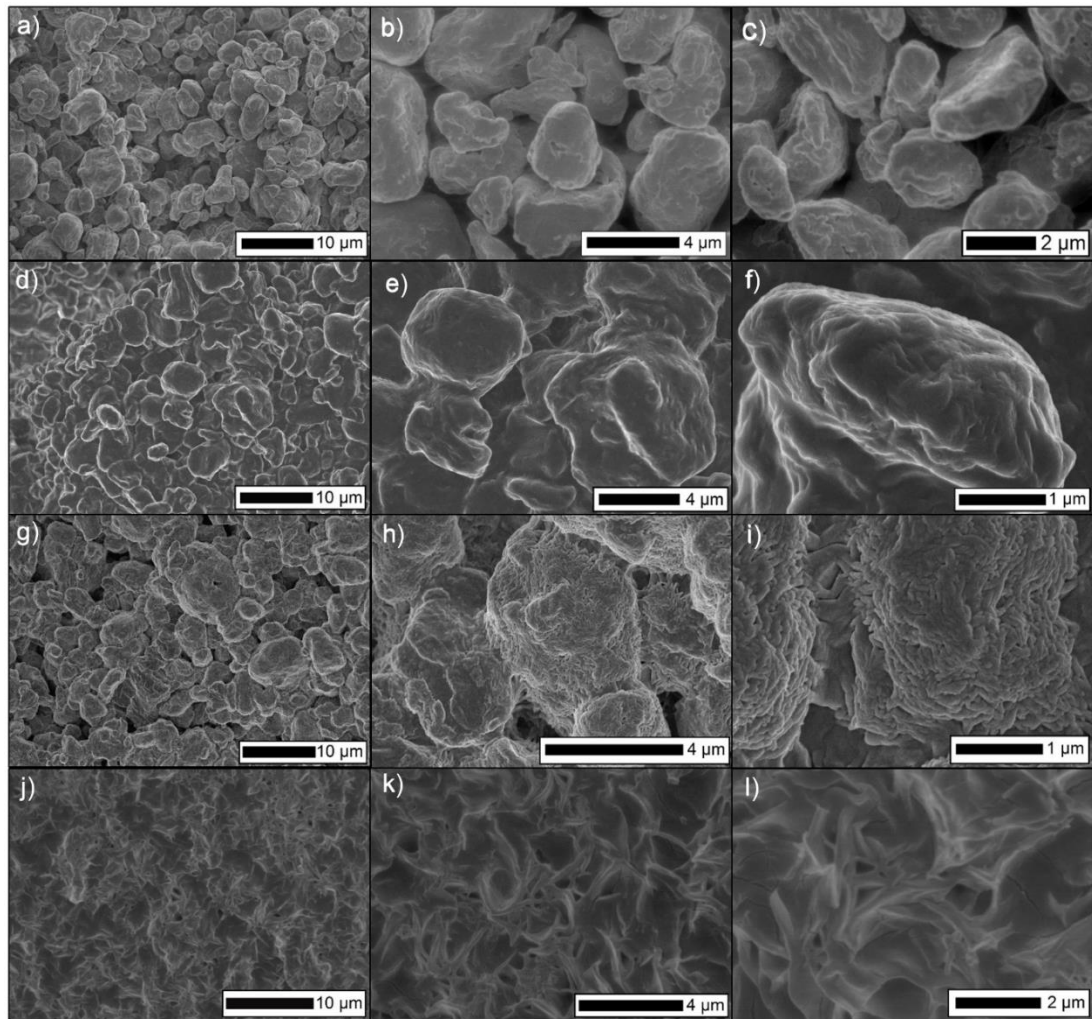


Figure 5.6: SEM images of S- μ powder without heat treatment (a–c) and under different heat treatments: at 114°C (d–f), 140°C (g–i), and 160 °C (j–l).

5.3.2.3. Hydrophobicity of the filters

Hydrophobicity was assessed for the prepared filters. As could be concluded from the degree of roughness preserved after the heat treatment in the previous discussion, the wetting behaviour of the filter was highly dependent on the heat treatment process. WCA measurements were not straightforward when the filter was mounted in the Buchner funnel, this was due to optical distortions caused by the thick glass Buchner funnel, in addition to the high surface roughness (macro/microscale) that made full visualization of water droplets challenging (**Figure 5.7a**). This difficulty stemmed from small polymer features hindering the observation of the gas/water and water/solid interfaces in the water droplet images. Therefore, wetting analysis of the filters was obtained through three key alternative measurements:

- (i) **Contact angle measurements:** taken for the spray-coated layers on glass microscope slides, heated at the same temperature. These were prepared to resemble the surface of the original filters, which is the major determinant of the measured WCA.
- (ii) **Tilt angle measurements:** for both the fabricated filters and coated glass slides.
- (iii) **Water bouncing:** measured for the fabricated filters.

Glass-coated substrates with sprayed S- μ powder were cured at two different temperatures (114°C and 140°C, **Figure 5.7b-c**). The measured WCAs were 155° and 137°, respectively. This indicates the loss of superhydrophobicity for the high-temperature treatment, which agrees with the reduction in roughness and the increased melting observed in the SEM images. Similar results were obtained using M- μ powder, as the CAs obtained were 156° and 135° for the powder heated at 114°C and 140°C, respectively (**Figure 5.7d-e**). The treatment at 160°C was found to significantly reduce the surface hydrophobicity (WCA = 113°, **Figure 5.7f**). Again, this matches with the flatness of the surface textures observed in the SEM images as a result of extended melting. For the largest particle size tested (L- μ powder) the particle dispersion was too large to be sprayed, and most of the polymer could not pass through the spray nozzle. As a result, a superhydrophobic surface was not achieved for this powder size.

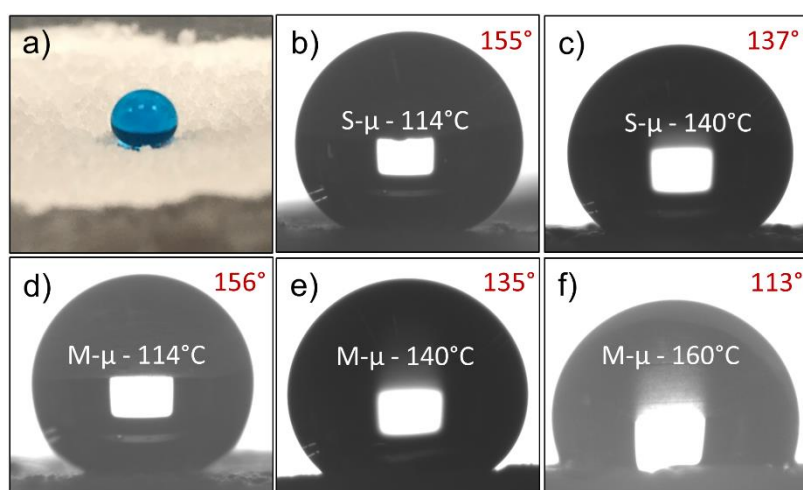


Figure 5.7: a) A 20- μ L water droplet on an S- μ filter mounted in a glass funnel where the dual-layer filter is placed. Besides light distortion through glass, some polymer features are

covering the liquid/air interface at the filter surface, making accurate measurements of CAs challenging. b-f) Images showing WCAs for the secondary layer sprayed on a glass slide. The powder sizes and heat-treatment temperatures are: S- μ powder heated at b) 114°C, c) 140°C, and M- μ powder heated at d) 114°C, e) 140°C and f) 160°C.

TAs were measured for both S- μ and M- μ powders. These were measured on the filters as well as the coated glass slides. TAs recorded on the filters (11° and 13° for the S- μ and M- μ filters, respectively) were found to be higher than the same measurements made on the coated glass slides (8° and 6°, respectively). The difference in the constructed filters and glass slide filters is hypothesized through the additional macro-roughness achieved in the filter samples that enabled greater pinning of water droplets. Overall, the S/M- μ filters were judged to have similar wetting behaviours.

Water bouncing was the final wetting characterisation measurement (**Figure 5.8**). The uneven surfaces made the measuring of WCAs and TAs challenging, and water bouncing provided a method to overcome this. The water bouncing measurements can indicate static wetting properties (akin to the WCAs), but also demonstrate the dynamic wetting/de-wetting behaviour relevant to oil-water separation applications. After a few bounces (≈ 5), the droplet travelled across the surface of the filter until it reached the un-coated glass part of the funnel, where it became adhered to the glass to reduce the contact with the rough filter surface (as observed in the last photo in **Figure 5.8**). The measurements shows clearly the water-repelling nature of the filter material, with water bouncing proving an estimated WCAs of the filter membranes around 160°. ⁴³

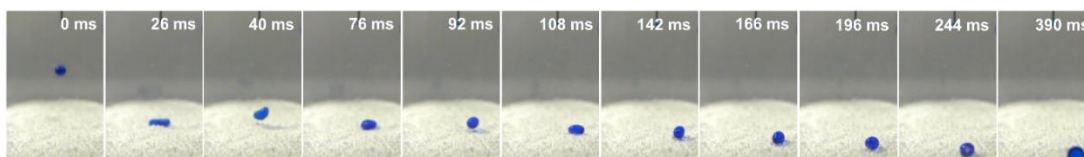


Figure 5.8: Photographs of a water droplet bouncing on a polyethylene filter. The final photo shows the strong adhesion of the water droplet to the uncoated glass part of the funnel.

5.3.2.4. Structure of the filter

The previous results of the hydrophobicity, permeability and structural integrity were used to deduce the best conditions for filter fabrication. To achieve a balance where hydrophobicity/permeability and structural integrity are acceptable, a temperature of 140°C was utilised. The formed filter was found to be relatively rigid, while still being permeable so the hydrophobic solvent can pass through. The highest measured WCA at this temperature (achieved with the S- μ particles) was found to be 142°. However, these were not yet superhydrophobic. To increase the WCAs for the filters, a lower temperature heat treatment was required, which would, on the other hand, produce

weak filters. To overcome these limitations, the filter was fabricated in a two-step process: a base layer heated at 140°C to provide rigidity and suitable permeability, and a second layer sprayed on top of the previous one heated at 114°C to maximise the hydrophobicity. In addition, the filter was fabricated inside a funnel to support the filter structure. A schematic of the filter structure is shown in **Figure 5.9**, and the detailed preparation method was illustrated earlier in Section 5.2.2.

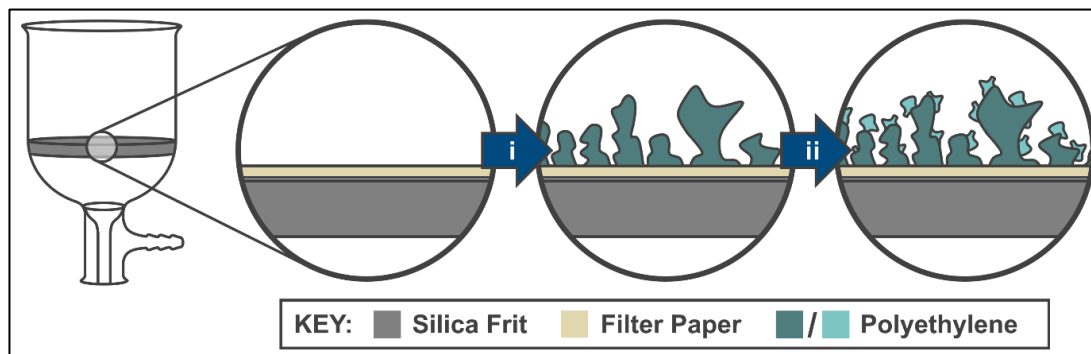


Figure 5.9: A schematic showing the composition of the polyethylene micropowder filters. The filter is constructed using a Buchner funnel/silica frit with filter paper placed on top. The first layer (i) uses a heat treatment temperature of 140 °C, which forms a uniform base for the second layer (ii). The second layer uses a lower heat treatment (114 °C) which preserves the high surface roughness.

5.3.3. Separation Efficiency

Separation efficiency experiments were carried out by applying water/solvent mixtures onto the filter material (**Figure 5.3**). Typically, 1.00 g (± 0.01) of water was weighed and transferred by a syringe, then around 1 mL of hydrophobic solvent (chloroform, DCM, hexane or toluene) was taken up into the same syringe. The entire syringe contents were emptied onto the filter all at once, at an approximate distance of 3 cm. After a few seconds, the water on the filter surface was collected *via* syringe and weighed. The separation efficiency percentage was calculated by dividing the mass of the water collected by the mass of the water poured onto the filter. An image of a chloroform/water mixture separated using an S- μ filter is shown in **Figure 5.10**.

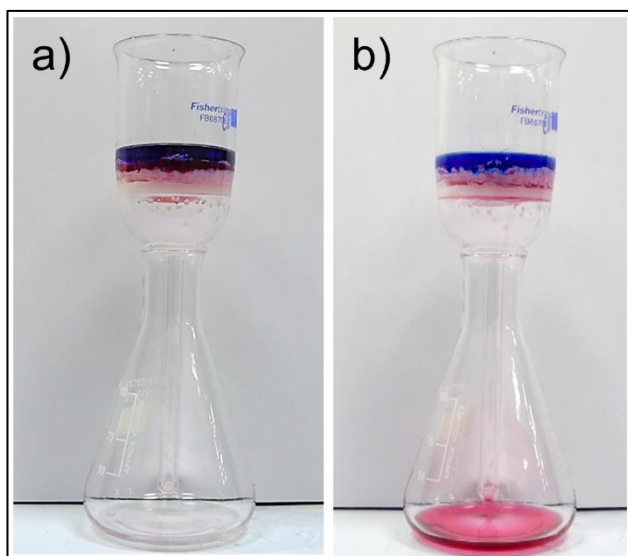


Figure 5.10: The chloroform/water mixture before (a) and after (b) separation using an S- μ filter.

The separation efficiency for all solvents and filters is shown in **Figure 5.11**. Generally, the separation was shown to be very efficient, with an average of 98.9% for all experimental runs. A maximum of 99.9% was recorded for the separation of water/chloroform mixture using the S- μ particle size, and a minimum of 98.1% was recorded for separating the same mixture using the M- μ particle size. As noted earlier, the spraying of L- μ particles was non-optimal, and hence the filters made using that size showed reduced WCAs. However, they tended to still perform well. This suggested that for these materials superhydrophobicity was not essential to achieving high separation efficiencies. For the smallest particle size used (S- μ), some readings were above 100%, this was expected to be due to experimental error in the measurement of the mass of recovered water. Extra mass generated from recovered oil was deemed to be less likely, as red colouration from the dyed oil was not observed. Overall, the filters are found to be well suited to oil-water separation. Although the L- μ filters highlighted that superhydrophobicity was not necessary for high separation efficiency, this is expected to be beneficial for any potential application. Particularly if recovery of the water is important, as superhydrophobicity would aid the removal of water from the filter surface.

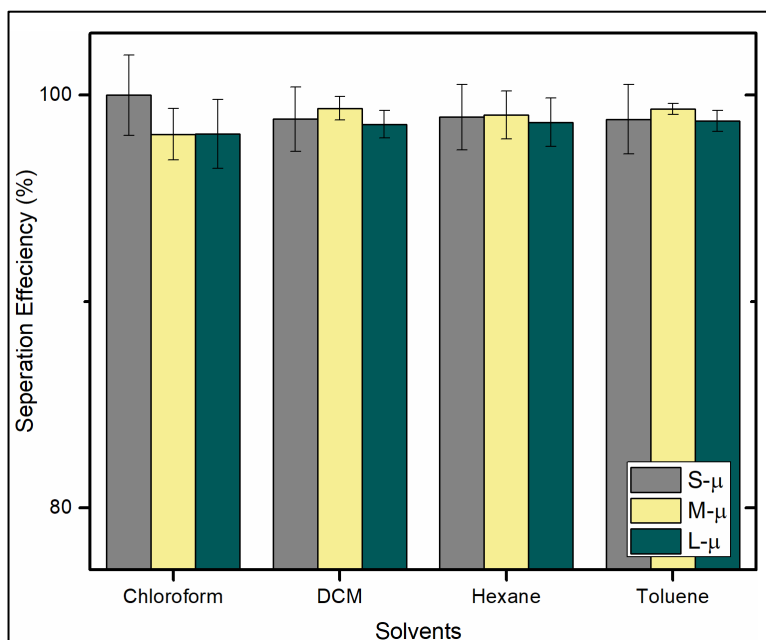


Figure 5.11: The separation efficiency results for different water/oil mixtures with filters made using different powder sizes.

5.4. Conclusions

The reported method utilises micronized polyethylene in the formulation of a dual-layer filter, generated by a straightforward heat-treatment process to form a solid filter with a rough surface. The fabrication conditions, including temperature and dispersion solvent type/quantity, were thoroughly investigated, along with different sizes of polyethylene microparticles. The two layers were used to combine both structure integration and high surface roughness. The filters show high hydrophobicity and efficient separation of different oil/water mixtures, which were as high as 99.9% for chloroform/water mixtures separated using a microparticle average size of 4.5 μm . This material design demonstrated here is aimed to offer an approachable and cost-effective method to achieve the efficient separation of oil/water mixtures. The filter fabrication approach demonstrates a high potential of versatility, and resultant utilisation in a real-world application, in both academic research and industry.

5.5. References

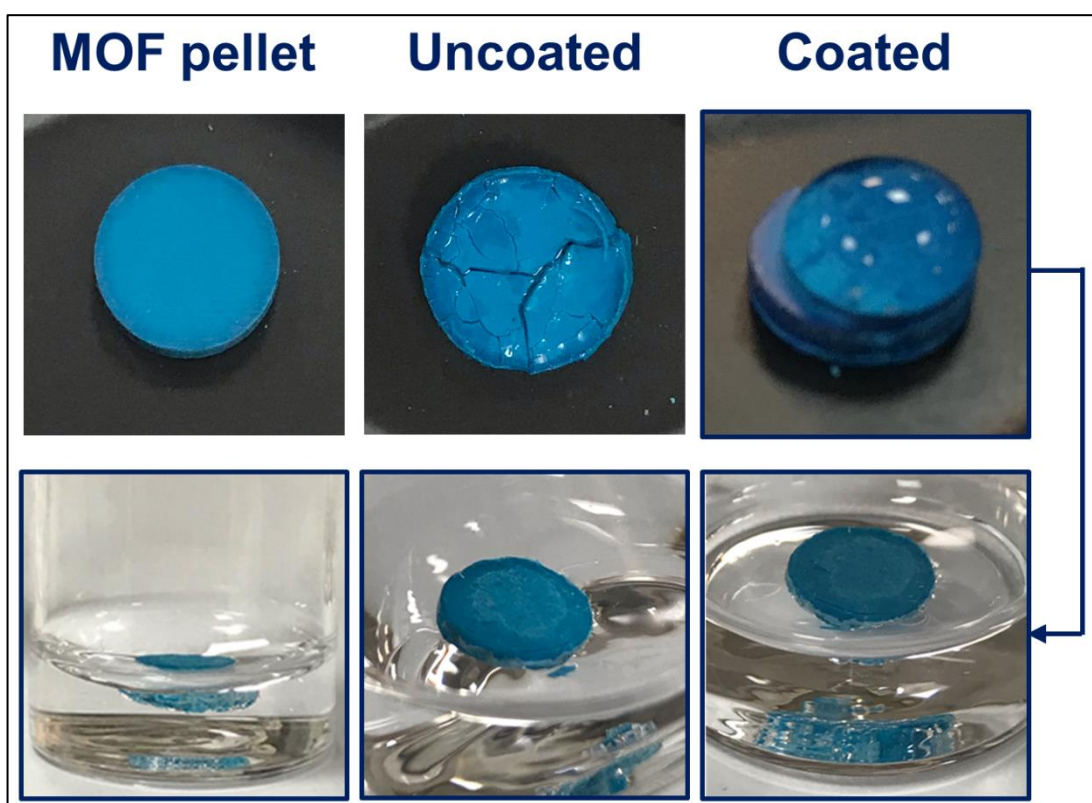
- 1 R. K. Gupta, G. J. Dunderdale, M. W. England and A. Hozumi, *J. Mater. Chem. A*, 2017, **5**, 16025–16058.
- 2 J. S. van Eenennaam, M. Rohal, P. A. Montagna, J. R. Radović, T. B. P. Oldenburg, I. C. Romero, A. T. J. Murk and E. M. Foekema, *Mar. Pollut. Bull.*, 2019, **141**, 164–175.
- 3 N. P. Ventikos, E. Vergetis, H. N. Psarftis and G. Triantafyllou, *J. Hazard. Mater.*, 2004, **107**, 51–58.

- 4 H. Li, M. Zheng, L. Ma, C. Zhu and S. Lu, *Mater. Res. Bull.*, 2013, **48**, 25–29.
- 5 D. D. Nguyen, N. H. Tai, S. B. Lee and W. S. Kuo, *Energy Environ. Sci.*, 2012, **5**, 7908–7912.
- 6 C. R. Crick, D. S. Bhachu and I. P. Parkin, *Sci. Technol. Adv. Mater.*, 2014, **15**, 065003.
- 7 J. Bong, T. Lim, K. Seo, C. A. Kwon, J. H. Park, S. K. Kwak and S. Ju, *Sci. Rep.*, 2015, **5**, 1–6.
- 8 G. Cao, W. Zhang, Z. Jia, F. Liu, H. Yang, Q. Yu, Y. Wang, X. Di, C. Wang and S. H. Ho, *ACS Appl. Mater. Interfaces*, 2017, **9**, 36368–36376.
- 9 Z. Yuan, Z. Ke, Y. Qiu, L. Zheng, Y. Yang, Q. Gu and C. Wang, *ACS Appl. Mater. Interfaces*, 2020, **12**, 46923–46932.
- 10 G. Julier, *The Culture of Design*, Sage, London, 3rd edn., 2013.
- 11 E. G. Ashton, W. Kindlein, R. Demori, L. H. A. Cândido and R. Mauler, *J. Clean. Prod.*, 2016, **116**, 268–278.
- 12 Y. Weimin and S. Thomas, Eds., *Advances in Polymer Processing: From Macro To Nano Scales*, Woodhead Publishing Limited, 1st edn., 2009.
- 13 H. Wagnier, F. X. Kromm, M. Danis and Y. Brechet, *Mater. Des.*, 2014, **56**, 44–49.
- 14 N. H. Kim and A. I. Isayev, *Polym. Eng. Sci.*, 2015, **55**, 88–106.
- 15 G. Boothroyd, P. Dewhurst and W. A. Knight, *Product Design for Manufacture and Assembly*, CRC Press, 3rd edn., 2010.
- 16 S. G. Advani and K.-T. Hsiao, Eds., *Manufacturing Techniques for Polymer Matrix Composites (PMCs)*, Woodhead Publishing, 1st edn., 2012.
- 17 E. Worrell and M. Reuter, Eds., *Handbook of Recycling: State-of-the-art for Practitioners, Analysts, and Scientists*, Elsevier Inc., 1st edn., 2014.
- 18 J. M. Allwood and J. M. Cullen, Eds., *Sustainable Materials: With Both Eyes Open*, The Use Less Group, 1st edn., 2018.
- 19 S. K. Najafi, E. Hamidinia and M. Tajvidi, *J. Appl. Polym. Sci.*, 2006, **100**, 3641–3645.
- 20 S. Bertin and J. J. Robin, *Eur. Polym. J.*, 2002, **38**, 2255–2264.
- 21 K. R. Vandana, Y. Prasanna Raju, V. Harini Chowdary, M. Sushma and N. Vijay Kumar, *Saudi Pharm. J.*, 2014, **22**, 283–289.
- 22 M. Vogt, K. Kunath and J. B. Dressman, *Eur. J. Pharm. Biopharm.*, 2008, **68**, 283–288.
- 23 J. Stark, J. Lee, C. Nguyen, A. Tehrani, S. Young and M. Swaco, in *American Association of Drilling Engineers*, Fluids Technical Conference and Exhibition, Houston-Texas, 2014.
- 24 R. Sutradhar and V. B. R. Suda, *Mater. Today Proc.*, 2020, **27**, 1331–1336.
- 25 J. A. De La Casa and E. Castro, *Constr. Build. Mater.*, 2014, **61**, 320–326.
- 26 S. L. Zhang, Z. X. Xin, Z. X. Zhang and J. K. Kim, *Waste Manag.*, 2009, **29**, 1480–1485.

- 27 A. Mao, R. Shmulsky, Q. Li and H. Wan, *BioResources*, 2014, **9**, 4253–4265.
- 28 US Pat., 10 208 205 B2, 2019.
- 29 E. Sadler and C. R. Crick, *Sustain. Mater. Technol.*, 2021, **29**, e00321(1-6).
- 30 F. Ternero, L. G. Rosa, P. Urban, J. M. Montes and F. G. Cuevas, *Met. 2021*, Vol. 11, Page 730, 2021, **11**, 730(1–21).
- 31 M. Saline, Sintering and Additive Manufacturing, <https://www.industrialheating.com/articles/94932-sintering-and-additive-manufacturing>, (accessed 25 March 2022).
- 32 H. Zheng, M. J. Lehtinen and G. Liu, *J. Environ. Chem. Eng.*, 2021, **9**, 106449(1–10).
- 33 W. Hou and Q. Wang, *J. Colloid Interface Sci.*, 2009, **333**, 400–403.
- 34 C. Jiang, W. Hou, Q. Wang and T. Wang, *Appl. Surf. Sci.*, 2011, **257**, 4821–4825.
- 35 H. Teisala, M. Tuominen, M. Aromaa, M. Stepien, J. M. Mäkelä, J. J. Saarinen, M. Toivakka and J. Kuusipalo, *Langmuir*, 2012, **28**, 3138–3145.
- 36 I. S. Bayer, F. Brandi, R. Cingolani and A. Athanassiou, *Colloid Polym. Sci.*, 2013, **291**, 367–373.
- 37 I. S. Bayer, A. J. Davis, E. Loth and A. Steele, *Mater. Today Commun.*, 2015, **3**, 57–68.
- 38 N. De Geyter, R. Morent and C. Leys, in *Surface and Interface Analysis*, John Wiley & Sons, Ltd, 2008, vol. 40, pp. 608–611.
- 39 R. L. Upton, Z. Davies-Manifold, M. Marcello, K. Arnold and C. R. Crick, *Mol. Syst. Des. Eng.*, 2020, **5**, 477–483.
- 40 Y. Cheng, B. Wu, X. Ma, S. Lu, W. Xu, S. Szunerits and R. Boukherroub, *J. Colloid Interface Sci.*, 2018, **525**, 76–85.
- 41 Y. Guan, C. Yu, J. Zhu, R. Yang, X. Li, D. Wei and X. Xu, *RSC Adv.*, 2018, **8**, 25150–25158.
- 42 T. Zhao, D. Zhang, C. Yu and L. Jiang, *ACS Appl. Mater. Interfaces*, 2016, **8**, 24186–24191.
- 43 C. R. Crick and I. P. Parkin, *Chem. Commun.*, 2011, **47**, 12059–12061.
- 44 Y. A. Mehanna, R. L. Upton and C. R. Crick, *J. Mater. Chem. A*, 2019, **7**, 7333–7337.

Chapter 6:

Water Protective Coatings for Metal-Organic Frameworks



6. Water Protective Coatings for Metal-Organic Frameworks

6.1. Introduction

The investigation of possible routes for the applicability of superhydrophobic coatings has been carried out extensively in numerous fields. Among these, surface protection against water stands as one of the main fields where superhydrophobic treatment is required. As mentioned earlier in Section 1.4.2, protection against water could be needed either because the exposure to water promotes material degradation, and/or when this exposure affects the functionality of the material. In this chapter, a class of water-sensitive material was chosen to apply the previously described PDMS-based coatings prepared *via* ta-AACVD (Chapter 2) to examine its applicability for water protection.

6.1.1. Metal-Organic Frameworks

Metal-organic frameworks (MOFs) are a class of hybrid organic-inorganic materials that have been greatly explored for various applications. They are generally consisting of metal ions linked by organic ligands through self-assembly, forming three-dimensional networks.^{1,2} These materials possess a high level of crystallinity and porosity, which led to their exceptional performance in many applications, like gas storage, gas separation, sensing, and catalysis.¹⁻⁶ Numerous MOFs have been developed using different combinations of metal ions and organic ligands, examples include the family of zeolitic imidazolate frameworks (ZIFs), MOF-5 and Hong Kong University of Science and Technology (HKUST-1, **Figure 6.1**).

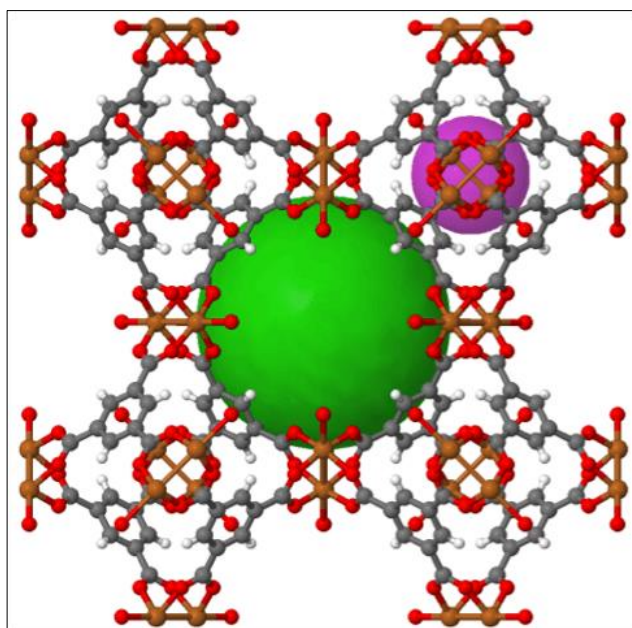


Figure 6.1: Illustration of the HKUST-1 MOF structure, showing the metal ions (Cu, brown), the organic linker (benzene-1,3,5-tricarboxylic acid, grey/white) and the binding sites (carboxylic groups, red). The green and purple spheres show the primary and secondary pore sizes, respectively. Figure retrieved from ref.⁷

Provided by their hybrid nature and the ability to manipulate the choice of building blocks to obtain certain properties, numerous examples of MOFs with different porosities and adsorption abilities have been reported.⁸ While this increases their potential for involvement in many systems, some factors limit their applicability, including their water stability which is considered to be the most detrimental factor for the structure of MOFs.⁹

6.1.1.1. *Issues with water stability*

While several MOFs were reported to exhibit water stability, most of the MOFs undergo structural degradation in presence of water or moisture, which limits their applicability in real-life reactions where it could become infeasible to get rid of moisture.^{10–14} This water sensitivity is caused by the water molecules attacking the bonds formed between metal ions and organic ligands. This can lead to ligand displacement, which occurs when some parts of the MOF get replaced with water molecules, or hydrolysis, which refers to the reaction of water molecules with ligands causing breakage of metal/ligand bonds.⁹ Therefore, it is important to consider the strength of the coordination metal/ligand bond, as this affects the MOF stability against water.⁸ Other factors can influence the water stability as well, including the steric hindrance and the hydrophobicity of the MOF surface.^{9,15} In general, protection against water could be beneficial not just to preserve the material structure, but also to increase its selectivity to hydrophobic reactants where materials are employed as catalysts for reactions happening in a water medium or where water is present as a side product.^{16–18}

6.1.1.2. *Methods for protection against water*

Hydrophobic treatment of MOFs has been attempted to enhance their tolerance to water.^{3–5} The reported routes can be categorised into two main approaches: i) direct synthesis of water-stable (hydrophobic) MOFs, and ii) post-synthesis modifications of water-sensitive MOFs.¹ For the first approach, fluorinated linkers have been involved as building blocks for hydrophobic MOFs.^{19,20} The second approach allows more freedom in choosing the treatment method. This includes similar routes to the hydrophobic linker utilization, while here the MOF synthesis takes place firstly followed by chemical attachment of hydrophobic groups.^{21–24} Alternatively, hydrophobic molecules can be encapsulated in the MOF porosity to provide the necessary protection. Examples include fluorinated compounds, polyoxometalates and CNTs.^{25–27} Other reports presented coating of MOF crystals with an organosilicon layer, as well as utilizing CVD to apply a polymer coating.^{1,28,29} In all these methods,

the generated MOFs demonstrated a hydrophobic/superhydrophobic nature, which reduced their interaction with water and helped maintain their structure. Meanwhile, the coating of MOFs was usually done to the individual crystals (**Figure 6.2a**), often conducted by placing MOF powder/crystals in a solution of the desired polymer. While this approach has proven effective in making MOFs more water-resistant, these coating methods raise questions regarding the accessibility of the MOFs beneath.

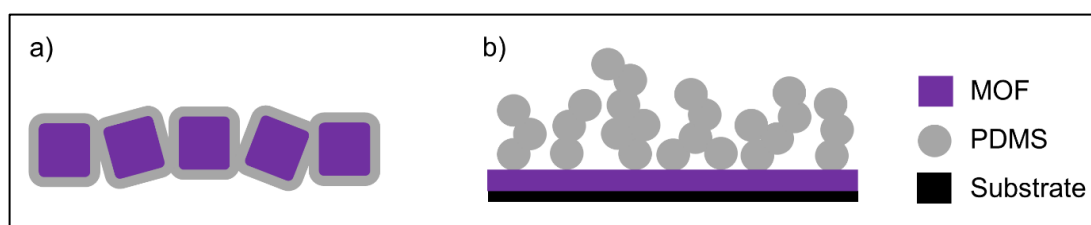


Figure 6.2: Schematic showing a) the coating of MOF crystals by a polymer layer and b) depositing a rough layer of a polymer on a film of MOFs.

6.1.2. Chapter Aim

The superhydrophobic materials fabricated *via* ta-AACVD (Chapter 2) provided high WCAs and the repulsion of dynamic water droplets. The inspiration for generating a near room-temperature process was to make the AACVD coating applicable to thermally sensitive substrates, which was demonstrated by deposition onto paper/cardboard. Moreover, this coating mechanism was noticed to render substrates hydrophobic while not completely blocking them, as parts of the substrate remain accessible (**Figure 2.12c-d**). Inspired by this system, having MOFs fixed into a substrate and then coating this substrate with a hydrophobic PDMS layer using ta-AACVD can achieve the required water resistance. Moreover, this would provide partial coverage of the superficial MOF surface, leading to less coating material per mass of MOFs (**Figure 6.2b**). This could potentially reduce the risk of pore-blockage and accessibility limitations.

For the targeted system, the MOFs need to be fixed into a substrate or packed in a solid form. This can be done by growing a thin film of MOFs on a glass substrate, compressing MOF powder into solid pellets and/or fixing it into a holder. The resultant form can then be coated by a rough PDMS layer using ta-AACVD. In this way, the MOF crystals would still be accessible by any hydrophobic material that would penetrate through the polymer layer, yet it is protected against water. The key feature in the presented system is maintaining both MOFs accessibility and activity while providing sufficient protection against water.

The aim of using MOFs here is two-fold; (i) to assess the effect (if any) of the polymer depositions *via* ta-AACVD, and (ii) to examine the functionality of the coating as a protective layer.

6.2. Experimental Methods

6.2.1. Materials

Hydrogen peroxide (H₂O₂, 35% w/w aq. Soln., stab.), zinc nitrate hexahydrate (Zn(NO₃)₂·6H₂O, 99%, metals basis), cobalt nitrate hexahydrate (Co(NO₃)₂·6H₂O, ACS, 98.0-102.0%), terephthalic acid (98+%), zinc acetate dihydrate (Zn(CH₃COO)₂·2H₂O, ACS, 98.0-101.0%) and benzene-1,3,5-tricarboxylic acid (98%) were purchased from Alfa Aesar. Sulfuric acid (H₂SO₄, Min 95% d = 1.83), methanol (MeOH, analytical reagent grade, >= 99.9%), N,N-dimethylformamide (DMF, laboratory reagent grade, >=99%), sodium hydroxide (NaOH, pellets, >=97%) and chloroform (analytical grade, ≥99.8%) were purchased from Fisher scientific. 2-methylimidazole (MeIM, 99%) and copper nitrate trihydrate (Cu(NO₃)₂·3H₂O, 99%) were purchased from Acros Organics. Triethylamine (≥ 99%) was purchased from Sigma Aldrich. SYLGARD® 184 Silicone Elastomer was purchased from Dow Chemical. Glass microscope slides were purchased from Thermochemical.

6.2.2. MOFs Synthesis

6.2.2.1. *Thin-film deposition of ZIF-8*

The glass substrates were cleaned using a piranha solution (H₂SO₄:H₂O₂, 60:40 (v/v)) for 5 min, after which the substrates were rinsed with distilled water and dried under nitrogen flow. Two solutions (Zn(NO₃)₂·6H₂O in MeOH (25 mM) and MeIM in MeOH (50 mM)) were prepared. 10 mL of each solution were mixed and stirred, and then the substrates were immersed in this solution for 30 min. The substrates were then dried under nitrogen flow.³⁰

6.2.2.2. *Synthesis of ZIF-8 powder*

A solution of Zn(NO₃)₂·6H₂O (2 mmol, 0.67 g) and MeIM (2 mmol, 0.167 g) in 50 mL of DMF was prepared and stirred vigorously until a clear solution was obtained. TEA (0.4 mL) and NaOH solution (10 M, 3.5 mL) were added and then the solution was heated at 140°C for 24 hrs. The solution was centrifuged, and the white powder was washed three times with DMF and placed in MeOH for 2 days (during which the

solvent was decanted and replenished four times). Finally, the solution was centrifuged and the product was allowed to dry at 90°C overnight.³¹

6.2.2.3. Synthesis of ZIF-67 powder

Co(NO₃)₂·6H₂O (2.33 g) and MeIM (2.63 g) were each dissolved in 100 mL of MeOH to form two solutions, which were then mixed and stirred thoroughly for 30 sec. The mixed solution was left at room temperature without stirring for 24 hrs. After that, the purple precipitates were collected by centrifugation, washed three times with MeOH and allowed to dry at 90°C overnight.¹

6.2.2.4. Synthesis of MOF-5 powder

Terephthalic acid (0.507 g) and triethylamine (0.85 mL) were dissolved in 40 mL of DMF. Zn(CH₃COO)₂·2H₂O (1.699 g) was dissolved in 50 mL DMF and was slowly added to the first solution. This was kept under magnetic stirring at room temperature for 2.5 hrs. The precipitate was collected by centrifugation, washed with DMF (twice) and chloroform (twice), and then allowed to dry at 90°C overnight.²⁹

6.2.2.5. Synthesis of HKUST-1 powder

Cu(NO₃)₂·3H₂O (1.82 g) and benzene-1,3,5-tricarboxylic acid (0.875 g) were each sonicated in 50 mL of MeOH. Once dissolved, the copper nitrate solution was added to the tricarboxylic acid solution, and the mixture was kept at room temperature for 2 hrs. The blue precipitate was collected by centrifugation, washed three times with MeOH and allowed to dry at 90°C overnight.¹

6.2.3. Compression into pellets

An 8-mm pellet die was used to compress MOF powder into pellets. Around 110-120 mg of MOF powder were weighed and transformed into the die. The die was then transferred into a manual hydraulic pellet press (Specac) and the load was adjusted (0.5, 1 or 3 tons). After 30 sec the press was released, and the pellet was collected. For the lowest load tried (40 kg), steel weights were placed above the pellet for the same duration.

6.2.4. Hydrophobic Treatment

For MOF pellets, ta-AACVD was conducted similarly to the process previously described for PDMS coatings in Sections 2.2.2 and 2.2.3, utilizing the same polymer/solvent quantities and excluding the pre-coating treatment done for glass

substrates. For MOF powder fixed into metal holders, PDMS solution was prepared by mixing both parts of the elastomer (with a ratio of 10:1, total polymer mass = 0.2172 g), adding hexane (30 mL) and stirring until dissolved. Hydrophobized silica nanoparticles (Sections 3.2.2 and 4.2.2, 0.155 g) were added to the solution and stirred at room temperature for an hour. The holder was moved to a 120°C-adjusted hotplate and the prepared solution was sprayed followed by curing at the same temperature for 30 min.

6.2.5. Water-Stability Testing

Water-Stability Testing was conducted using different forms of MOFs (powder, pellet or powder fixed into a metal holder) depending on the testing requirements. The duration of water exposure was varied (from 1 min to 3 days), and the exact duration applied for each sample discussed is mentioned in the results section.

For powder samples, around 0.2-0.3 g was placed in a 50-mL falcon tube and 15 mL of distilled water was added. After the desired exposure time has passed, the sample was centrifuged and dried at 80°C for 2 hrs. Stability against hexane and chloroform was conducted in the same procedure, as well as for PDMS/hexane solution (0.105 g PDMS/ 0.0105 g curing agent in 15 ml of hexane).

For fixed powder, around the same weight was transferred into the metal XRD sample holder and pressed using a glass slide to ensure the powder is well packed. The holder was then placed inside a 400-mL beaker and around 70 mL of distilled water was slowly poured. The holder was then moved and placed inside an oven at 80°C for 2 hrs.

For pellets, two water volumes were tested. The pellet was either put on a dish with a 10 µL drop placed on it or was moved into a vial with 2-mL distilled water. In both cases, the water was removed by a dropper and the pellet was briefly heated on a hot plate adjusted at 100°C for 30 min. The reduced time was due to the quick-drying observed for pellets in comparison to both loose and compact powder.

6.2.6. Characterisation

SEM imaging was performed on ZIF-8 thin films deposited on glass substrates using a field emission microscope (JEOL, JSM-7001F) at an acceleration voltage of 15 kV.

Powder X-ray diffraction (PXRD) was measured on a Panalytical X'Pert Pro diffractometer using Co K α_1 radiation ($\lambda = 1.7890 \text{ \AA}$) in Bragg–Brentano geometry and an X'Celerator detector, across 2θ values ranging from 5-50°.

Surface area measurements were conducted on a Micrometric 3-Flex 3500 Gas Sorption Analyser, at 77 K using nitrogen gas. The sample was degassed on the analysis port for 3 hrs at 150°C before measurement.

6.3. Results and Discussion

6.3.1. ZIF-8 thin-films

The aimed coating method was the earlier mentioned ta-AACVD (Chapter 2). The fixation of MOFs (which are usually synthesised in powder form) was needed to facilitate the coating process. Meanwhile, this was hypothesized to be beneficial, as it could allow easier insertion of the MOFs in this fixed form into the application setup. For this purpose, growing ZIF-8 thin films on glass was attempted. This was conducted by immersing glass substrates into a solution of ZIF-8 precursors, followed by drying the substrates under nitrogen flow. This was repeated depending on the required thickness of the ZIF-8 layer, which was examined using SEM imaging (**Figure 6.3**). In this figure, images of glass substrates after two (a-b), three (c-d), four (e- f) and five (g-h) immersions in ZIF-8 precursors solution are shown. It could be noticed that, while ZIF-8 formation took place in all the substrates, applying two immersions allowed the formation of isolated crystals, while with increasing the number of immersions, further growth was allowed, reaching five immersions where the substrate was completely covered. Although this method was simple and provided good control over the thickness of the MOFs layer, this was not completed, as the analysis of the MOFs in this form (i.e. XRD, surface area analysis, etc.) was restricted.

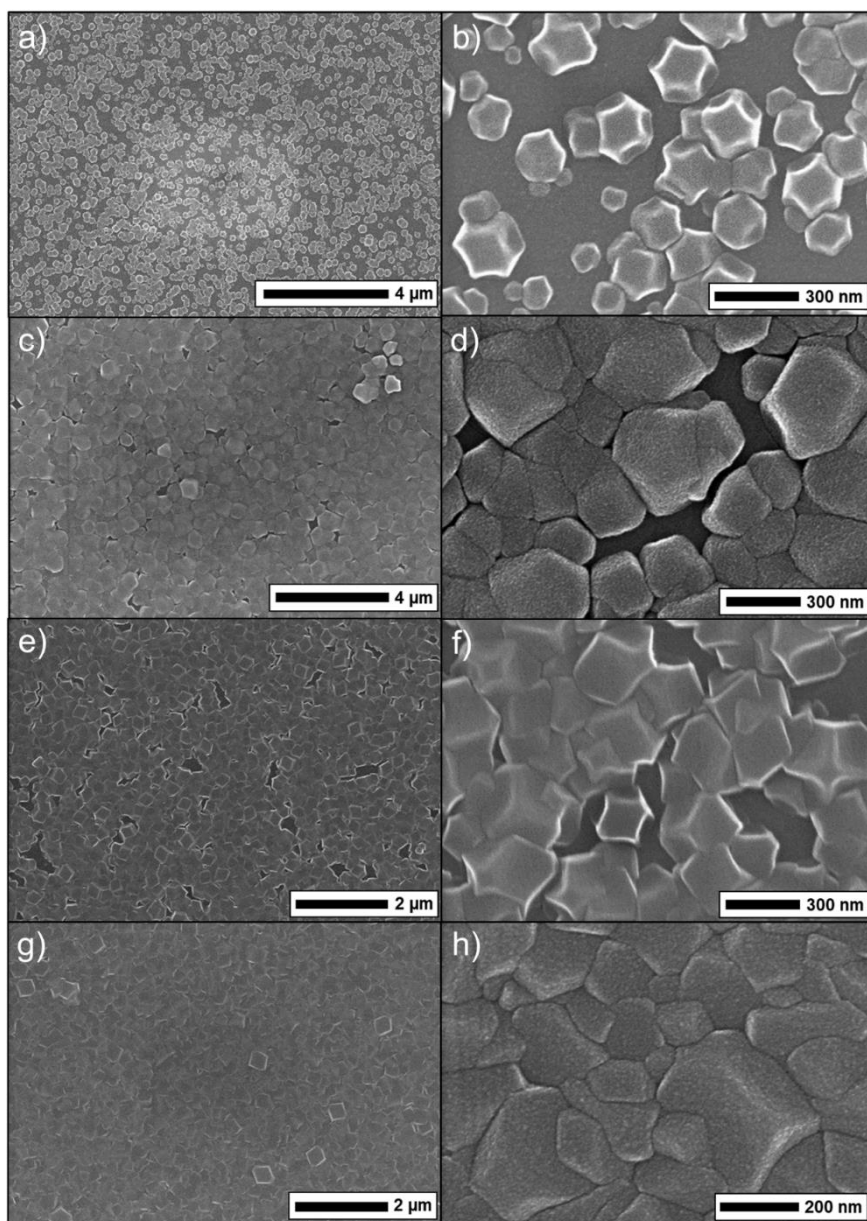


Figure 6.3: SEM images for ZIF-8 grown on glass substrates by repeated immersion of substrates in the MOF precursors' solution for a-b) 2, c-d) 3, e-f) 4 and g-h) 5 times. Scale bars are shown for each image.

6.3.2. MOFs pellets

Compression of MOFs powder into pellets was chosen as an alternative for growing MOF crystals into glass substrates. The chosen MOFs for these experiments were MOF-5, HKUST-1, ZIF-8 and ZIF-67, as they are known for their low water resistance.^{1,29} An important factor to consider during powder compression is the force applied. While higher forces ensure well-adhesion and facilitate pellet handling, this can affect the crystallinity of the MOFs. Therefore, an adjustment of applied force was required. **Figure 6.4** shows PXRD patterns of the powder MOFs as well as for pellets compressed using weights of 40 kg, 500 kg, 1 ton and 3 tons. In general, applying 40-kg weight was not sufficient for making rigid pellets, except for HKUST-1 where the pellet showed an acceptable extent of powder adhesion. Using a weight of 500-

kg resulted in reasonably structured pellets for MOF-5, HKUST-1 and ZIF-8. As indicated by the XRD patterns, this force did not result in altering the characteristic peaks of the MOFs. For MOF-5 and HKUST-1, this started to take place when the weight was increased to 3 tons, at which new different peaks emerged. For ZIF-8, changes in the pattern were noticed at the same applied force, although it resulted in the disappearance of main peaks. For ZIF-67, the pellets were very fragile until reaching 3-ton force, meanwhile, almost all the peaks have disappeared at this force. Therefore, ZIF-67 was excluded as the required force was detrimental to the MOF crystallinity.

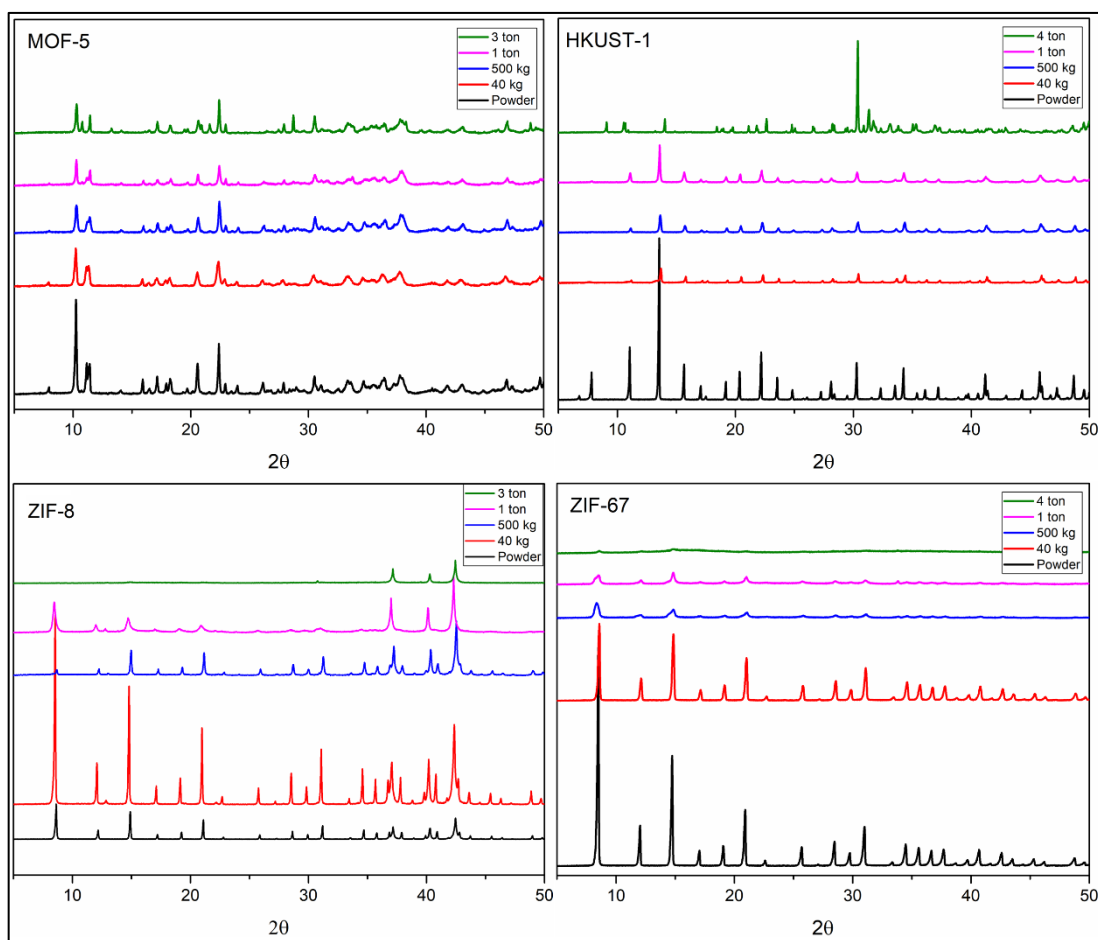


Figure 6.4: PXRD patterns for the MOFs powder, as well as the pellets prepared by compression of powder at varying forces (40 kg, 500 kg, 1 ton and 3 ton). The MOFs tested were MOF-5, HKUST-1, ZIF-8 and ZIF-67.

For the remaining discussion in this chapter, the examined pellets (unless otherwise mentioned) were prepared by compression under a load of 500 kg. As the pellet preparation conditions were optimised, the following step was to assess the water stability of the MOFs, examine the compatibility of the PDMS-coating and test the

efficiency of protection against water. These points are discussed in the following chapter.

6.3.3. Water stability

In determining the water stability of the MOF pellets, it is essential to ensure that the stability of the MOF is lower than the stability of the hydrophobic coating utilised. For PDMS coatings deposited via ta-AACVD, the WCA started to decrease after submersion of the coating for 3 days (followed by drying) to reach 144.4°, while a dramatic reduction was noticed for the measurement of the wet coating after 24 hrs (**Table 6.1**). Therefore, a MOF with longer stability against water will not be applicable for this coating method.

Submersion Time	12 hrs	1 D	2 D	3 D
With drying	-	148.2°	149.2°	144.4°
Without drying	146.2°	129.6°	-	-

Table 6.1: WCAs measured on wet/dried PDMS coating deposited on glass via ta-AACVD after submersion in water for a varied time.

A pellet of ZIF-8, MOF-5 and HKUST-1 was placed in 2-ml water for 3 days, followed by a drying step. It was noticed that the pellet could not preserve its structure, as the ZIF-8 and MOF-5 pellets were broken into powder while the HKUST-1 pellet significantly swelled (**Figure 6.5a**). After drying, they were crushed back into powder to enable XRD analysis. When comparing their XRD pattern against the un-wetted pellets, the patterns for ZIF-8 and MOF-5 pellets after immersion in water did not seem to change (**Figure 6.5b-c**). This is longer water stability than reported in the literature for the powder MOFs (1-2 days),^{29,32} which can be attributed to the compact structure providing better water stability. Hence, these two MOFs were excluded. Meanwhile, the HKUST-1 pellet was degraded, with peaks associated with HKUST-1 almost disappeared and new sharp diffraction peaks appeared, suggesting the MOF decomposition has taken place (**Figure 6.5d**).

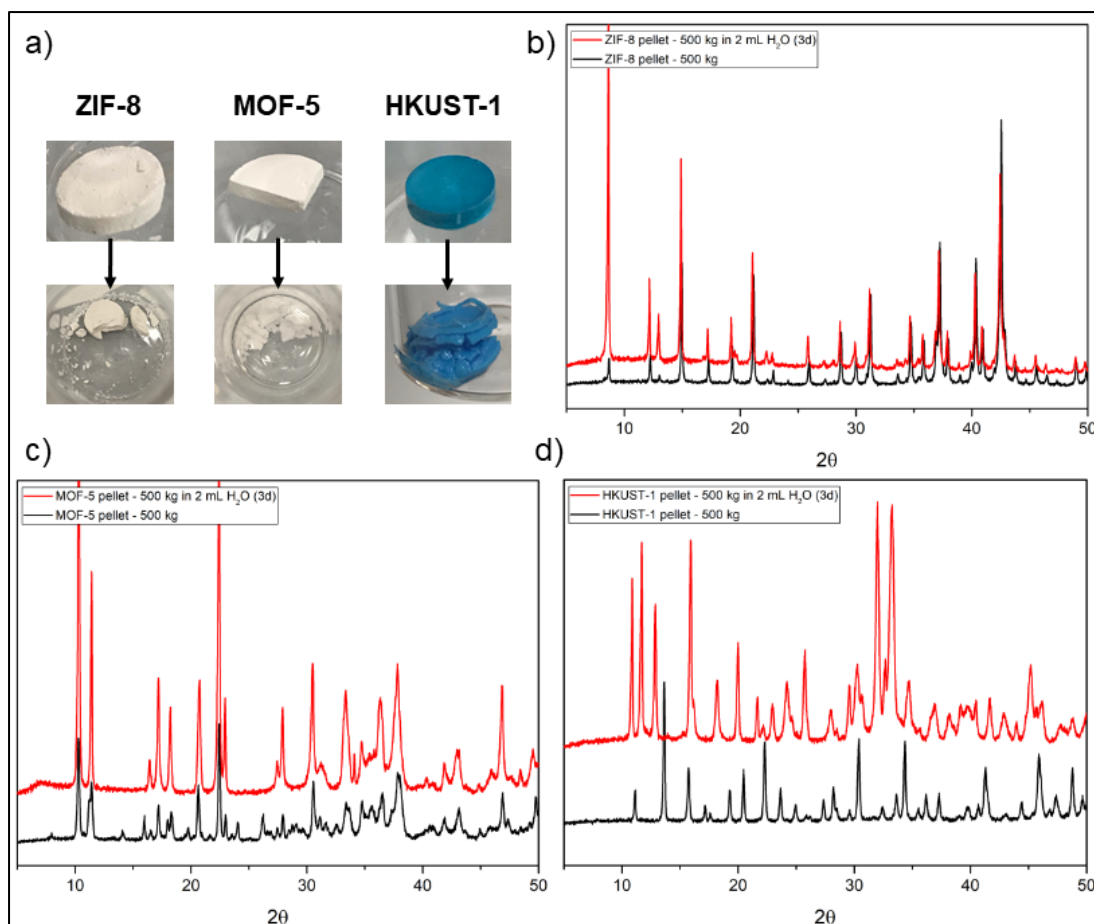


Figure 6.5: a) photographs of ZIF-8, MOF-5 and HKUST-1 pellets before and after submersion in water, showing the physical deformation of the pellets. b-d) PXRD patterns for the b) ZIF-8, c) MOF-5 and HKUST-1 pellets before and after water submersion, showing the effect of water exposure on the crystallinity of the MOFs.

A more gradual examination of HKUST-1 degradation after water exposure was conducted, starting with the powder form (illustrated in **Figure 6.6**). Upon immersing in water for 1 hour, the main peaks associated with HKUST-1 either shift from their position or split into two new peaks, indicating the decomposition of HKUST-1 has started. With increasing the exposure period to 2 hours, it could be noticed that more peaks have been developed and the formation of new phases (via the protonation of benzene-1,3,5-tricarboxylic acid ligands and/or the formation of Cu(II) hydroxide) was extended, the characteristic peaks of HKUST-1 disappeared.¹ Increasing the time did not change the pattern further, which suggests that the 1-hr exposure formed a sort of 'intermediate form' which was further developed when allowed in water for a longer time.

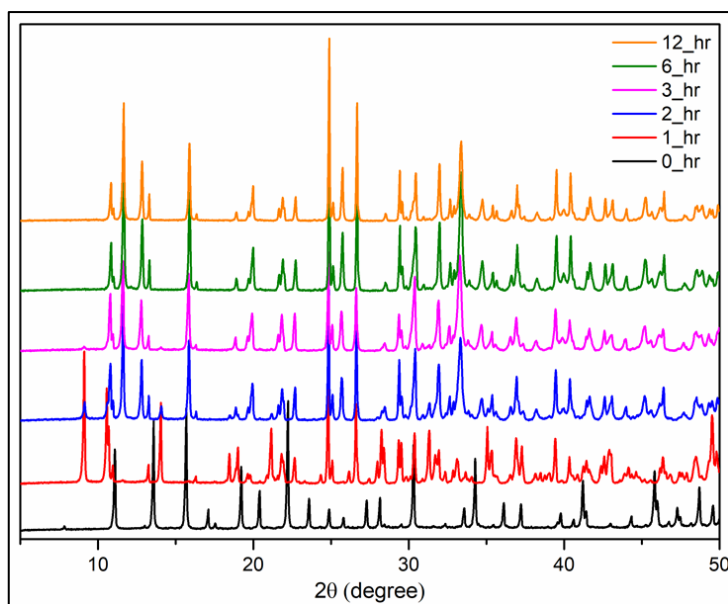


Figure 6.6: PXR D patterns for the HKUST-1 powder before and after water submersion (for 1, 2, 3, 6 and 12 hrs), showing the effect of water exposure on the crystallinity of the MOFs.

In addition, the powder was placed in chloroform and hexane (the two solvents usually used with PDMS) as well as a solution of PDMS/hexane to check if either the solvent or the polymer will cause any degradation to the MOF, which was not observed as the patterns did not change (**Figure 6.7**). Meanwhile, the sole act of placing the MOF powder in the PDMS solution did not delay the degradation of the MOF, as the XRD pattern of that powder after 1-hr water exposure was similar to that for the untreated powder after the same exposure time, which was shown in **Figure 6.6**.

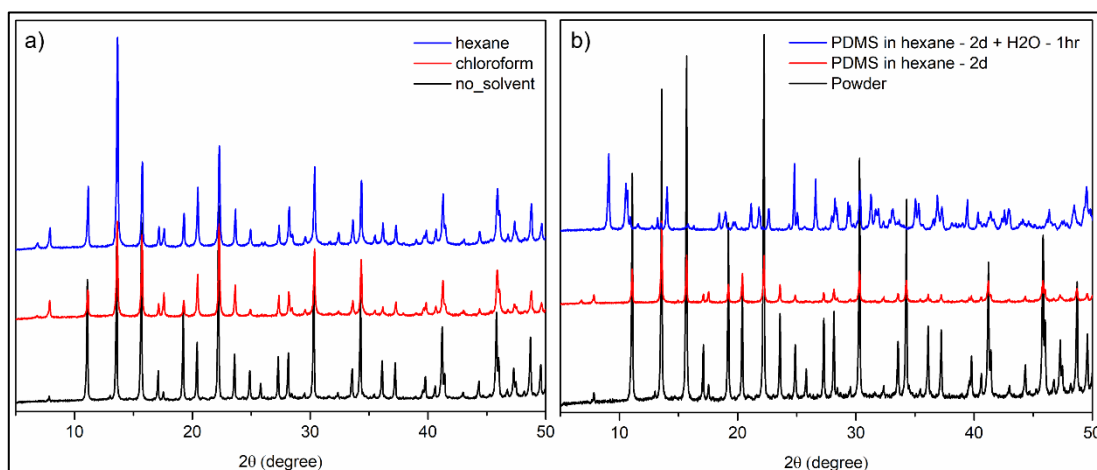


Figure 6.7: PXR D patterns for HKUST-1 powder a) submerged in chloroform/hexane and b) in a PDMS/hexane solution, before and after water submersion (for 1 hr).

After establishing the behaviour of the powder form of HKUST-1, pellets were assessed guided by the previously discussed results. HKUST-1 pellet was coated with PDMS using ta-AACVD, which resulted in darker pellet colour (associated with this MOF for the absence/reduction of moisture interaction). Meanwhile, the pellet resisted wetting by a 10- μ L droplet placed on its top for a day, while the uncoated

pellet was wetted and cracked (**Figure 6.8**). The XRD pattern for the uncoated pellet, while did not show peaks replacement, a minor broadening of some peaks was noticed. The XRD was not collected for the coated pellet before water exposure, although the pattern obtained from the water-exposed coated pellet showed good agreement with that for the un-wetted pellet. The main conclusion deduced from this is that the ta-AACVD coating did not affect the crystallinity of the MOF.

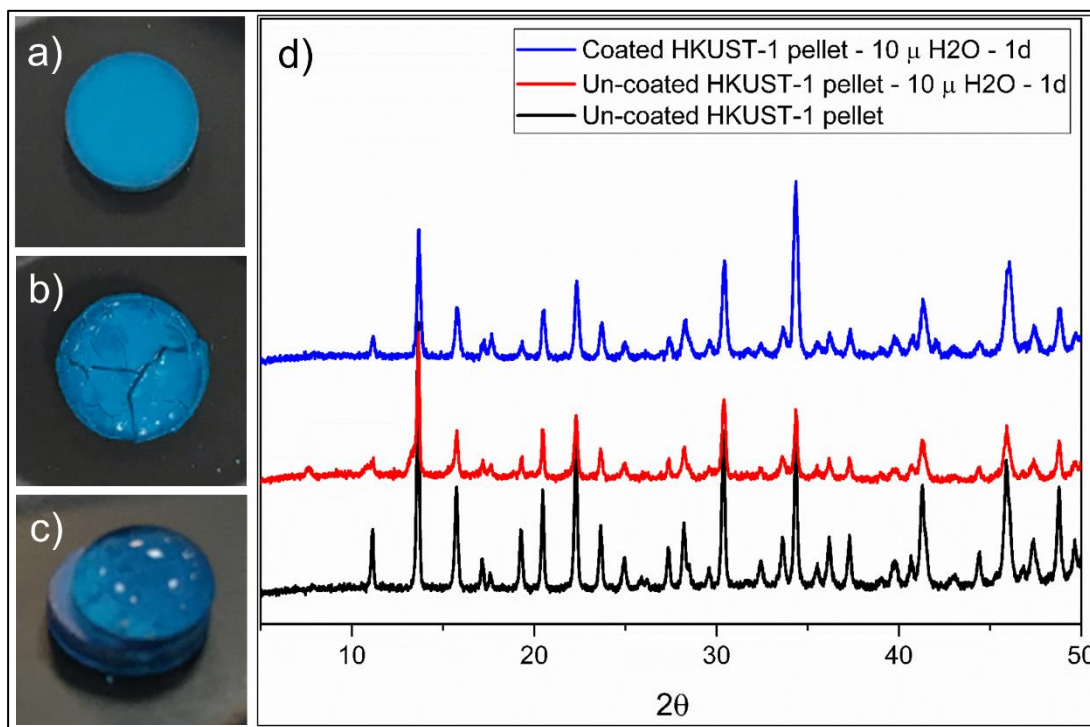


Figure 6.8: Images showing HKUST-1 pellets: a) un-wetted, b) after placing a 10- μ L droplet for a day and c) after the same treatment for a PDMS-coated pellet using ta-AACVD. d) PXRD patterns for these pellets.

The wetting of the pellets was conducted using a larger water volume, typically by placing pellets in a vial with 2-mL water for the desired time. Both XRD and surface area analysis was conducted for the pellets, and the results are shown in **Figure 6.9a-b** for the periods tried (30 min, 60 min, 12 hr, 1 d and 3 d). It was observed that the short exposure periods (30 and 60 min) resulted in minor deformation, represented in peaks broadening and slight loss of surface area in comparison to the unwetted pellets. Meanwhile, the deformation after longer exposure periods was more intense, as it was detrimental to the MOF crystallinity and porosity. Similar to what was conducted in the previous experiment with the reduced water volume, a PDMS-coated pellet was placed in water for a day. The choice of this period specifically was guided by a previous literature example as it was suitable for the un-treated MOF to show degradation while the treatment can still be effective.¹ Again, the coating

allowed repulsion of water, which was noticed here by the pellet floating instead of sinking for the un-coated ones (**Figure 6.9c**). However, the increased water volume renders the coating insufficient to protect the MOF beneath, indicated by the altered XRD pattern as well as the significantly-reduced surface area.

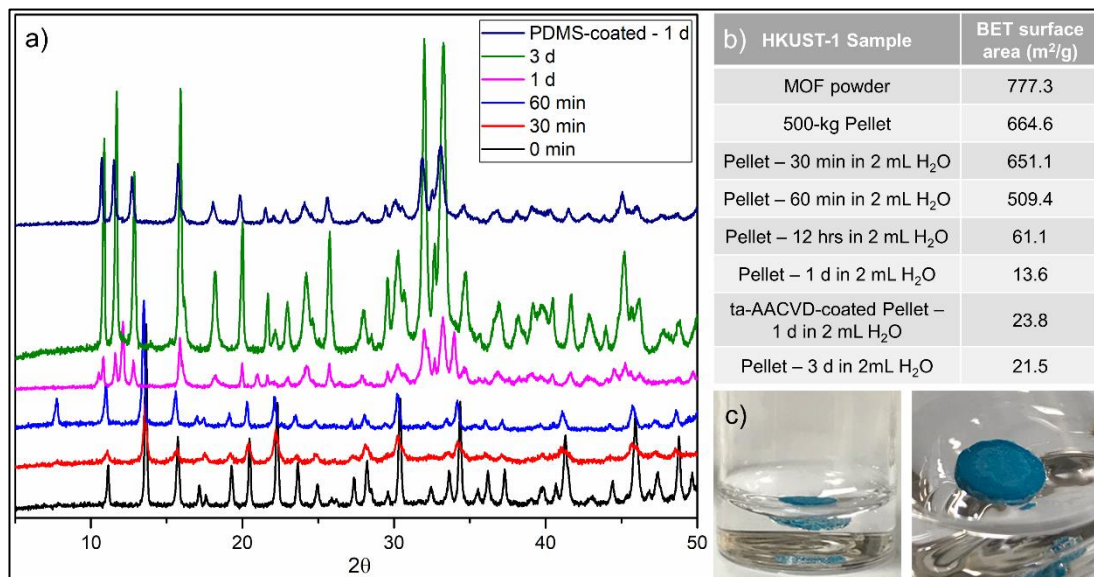


Figure 6.9: a) PXRD patterns for an un-wetted HKUST-1 pellet, in addition to after being placed in 2-mL of water for 30 min, 60 min, 1 d and 3 d. The pattern for PDMS-coated pellet via ta-AACVD exposed to water for a day is also indicated. b) BET surface area measurements for HKUST-1 powder, unwetted 500-kg pellet, pellets placed in 2-mL of water for 30 min, 60 min, 12 hrs, 1 d, 3 d as well as the PDMS-coated pellet placed in water for 1 d. c) the PDMS-coated pellet floating on water.

The protection of the coating was of lower efficiency than expected, and hence a more gradual analysis was required. Meanwhile, the process of the ta-AACVD coating was found to be time-consuming. As illustrated in Chapter 4, the spray-coated SPPCs provide a modified approach to scale up the AACVD coating process while generating rough structures, thus it was chosen as an alternative for the remaining experiments. As spraying pellets was found to be impractical, due to the small size and the lightweight making it difficult to conduct the spraying properly, the powder was fixed alternatively by compacting into a metal holder. The holder was placed in water (Section 6.2.5) for varied periods, starting from 5 min and increasing to reach an hour (**Figure 6.10a**). It was observed that the XRD patterns started to show a change in the $20\text{--}23^\circ$ region, where a few additional peaks appeared and the main peak around 22° broadened. No further change was detected until reaching 1 hr exposure, where the 22° -peak underwent further broadening and splitting, which could indicate new-phase formation.

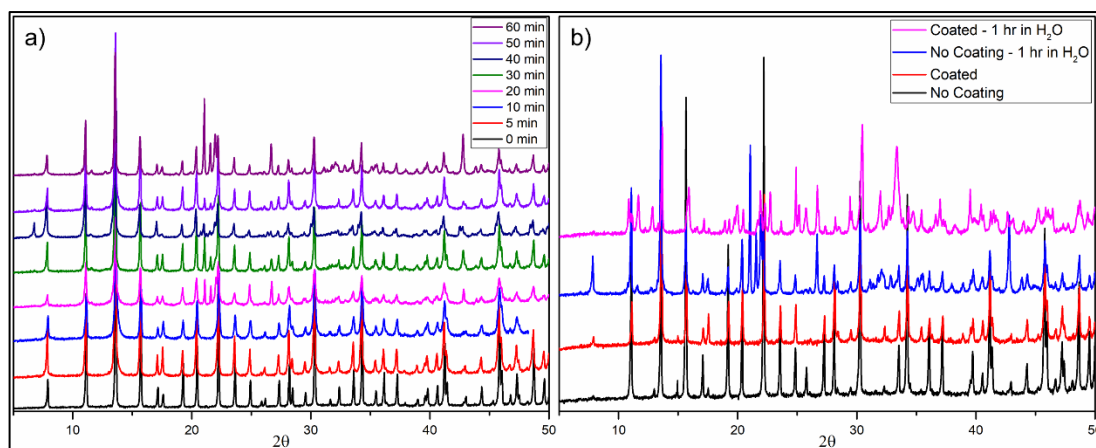


Figure 6.10: PXRD patterns for HKUST-1 powder fixed into metal holders, a) tested for different wetting periods and compared against the un-wetted powder, and b) compared with coated powder with PDMS/SiO₂ both before and after an hour of submersion underwater.

The SPPC-coated fixed-powder was then placed in water for the same time (1 hr) and the XRD pattern was compared (**Figure 6.10b**). The main remark here was the intensified change in the MOF crystallinity. This appeared only after the wetting took place, while the un-wetted, coated powder did not show any signs of deformation. This result is against the hypothesized hydrophobicity of the coating that should reduce the MOF-water contact and improve stability, or, if insufficient for this purpose, allow degradation of the MOF as expected when not coated, but not promoting it. An attempt to explain this can be the potential incompatibility of the coating with the MOF, leading to disruption of the regular phase formation/deformation mechanisms. This could be initiated through surface defects, where either the coating is not completely covering the MOF or the MOF compacted powder had some surface protrusions/cavities more prone to removal and, hence, exposing the surface beneath. Regardless, this coating material and/or technique was proven inadequate for the targeted application.

6.4. Conclusions

MOFs are widely known for their instability against water, which has encouraged research on their superhydrophobic treatment. The encapsulation treatment of the MOF powder was reported, although the utilization of different MOF forms (grown into substrates, compressed into pellets, etc.) can potentially facilitate their insertion into the application setup. Herein, the coating of fixed HKUST-1 MOF was attempted. The wetting behaviour has been established and the compatibility of the PDMS coating components was investigated. Furthermore, the coated samples were tested for

water resistance and compared to the behaviour without treatment. It was noticed that the coating has failed to provide the required protection against water, which could suggest that the encapsulation treatment is necessary for demonstrating reasonable stability. Meanwhile, the coating showed signs of incompatibility with HKUST-1, which could intensify the degradation. Future work is needed to investigate the possibility of applying similar coating approaches and conclude on its capability of providing effective MOF protection, and evaluate the potential, if any, possible advantages over regular encapsulation techniques.

6.5. References

- 1 X. Qian, F. Sun, J. Sun, H. Wu, F. Xiao, X. Wu and G. Zhu, *Nanoscale*, 2017, **9**, 2003–2008.
- 2 N. C. Burtch, H. Jasuja and K. S. Walton, *Chem. Rev.*, 2014, **114**, 10575–10612.
- 3 J. Liu, P. K. Thallapally, B. P. McGrail, D. R. Brown and J. Liu, *Chem Soc Rev*, 2012, **41**, 2308–2322.
- 4 K. K. Tanabe and S. M. Cohen, *Chem Soc Rev*, 2011, **40**, 498–519.
- 5 S. Ma and H.-C. Zhou, *Chem. Commun.*, 2010, **46**, 44–53.
- 6 Y. Wang, Z. Hu, T. Kundu, Y. Cheng, J. Dong, Y. Qian, L. Zhai and D. Zhao, *ACS Sustain. Chem. Eng.*, 2018, **6**, 11904–11912.
- 7 Chemtube3d.com, HKUST-1 Metal Organic Framework, <https://www.chemtube3d.com/mof-hkust-1-2/>, (accessed 30 March 2022).
- 8 N. C. Burtch, H. Jasuja and K. S. Walton, *Chem. Rev.*, 2014, **114**, 10575–10612.
- 9 B. Liu, K. Vikrant, K. H. Kim, V. Kumar and S. K. Kailasa, *Environ. Sci. Nano*, 2020, **7**, 1319–1347.
- 10 Y. Sun, Q. Sun, H. Huang, B. Aguila, Z. Niu, J. A. Perman and S. Ma, *J. Mater. Chem. A*, 2017, **5**, 18770–18776.
- 11 L. Li, Q. Yang, S. Chen, X. Hou, B. Liu, J. Lua and H.-L. Jiang^a, *Chem. Commun.*, 2017, **53**, 10026–10029.
- 12 J. Ying, A. Herbst, Y.-X. Xiao, H. Wei, G. Tian, Z. Li, X.-Y. Yang, B.-L. Su and C. Janiak, *Inorg. Chem.*, 2018, **57**, 899–902.
- 13 T. Zhang, B. Zou, M. Shao, X. Chen, S. Zhang, L. Li, Q. Du, H. Li, Y. Hu, J. Weng, W. Xiong, B. Zheng, W. Zhang and F. Huo, *A Eur. J.*, 2017, **23**, 7663–7666.
- 14 G. Huang, Q. Yang, Q. Xu, S. Yu and H. Jiang, *Angew. Chem. Int. Ed.*, 2016, **55**, 7379–7383.
- 15 C. Wang, X. Liu, N. Keser Demir, J. P. Chen and K. Li, *Chem. Soc. Rev.*, 2016,

- 45**, 5107–5134.
- 16 C. Yu, P. Zhang, J. Wang and L. Jiang, *Adv. Mater.*, 2017, **29**, 1703053(1–13).
 - 17 Z. Lu, W. Xu, J. Ma, Y. Li, X. Sun and L. Jiang, *Adv. Mater.*, 2016, **28**, 7155–7161.
 - 18 Y. Gao, N. Yang, S. Lu, T. You and P. Yin, *J. Mater. Chem. C*, 2019, **7**, 9926–9932.
 - 19 T.-H. Chen, I. Popov, O. Zenasni, O. Daugulis and O. S. Miljanic, *Chem. Commun*, 2013, **49**, 6848.
 - 20 S. Mukherjee, A. M. Kansara, D. Saha, R. Gonnade, D. Mullangi, B. Manna, A. V. Desai, S. H. Thorat, P. S. Singh, A. Mukherjee and S. K. Ghosh, *Chem. – A Eur. J.*, 2016, **22**, 10937–10943.
 - 21 L. Li, Q. Yang, S. Chen, X. Hou, B. Liu, J. Lu and H. L. Jiang, *Chem. Commun.*, 2017, **53**, 10026–10029.
 - 22 Y. Sun, Q. Sun, H. Huang, B. Aguila, Z. Niu, J. A. Perman and S. Ma, *J. Mater. Chem. A*, 2017, **5**, 18770–18776.
 - 23 Y. Wang, Z. Hu, T. Kundu, Y. Cheng, J. Dong, Y. Qian, L. Zhai and D. Zhao, *ACS Sustain. Chem. Eng.*, 2018, **6**, 11904–11912.
 - 24 Y. Dai, S. Liu and N. Zheng, *J. Am. Chem. Soc.*, 2014, **136**, 5583–5586.
 - 25 J. B. Decoste, G. W. Peterson, M. W. Smith, C. A. Stone and C. R. Willis, *J. Am. Chem. Soc.*, 2012, **134**, 1486–1489.
 - 26 D. Mustafa, E. Breynaert, S. R. Bajpe, J. A. Martens and C. E. A. Kirschhock, *Chem. Commun.*, 2011, **47**, 8037–8039.
 - 27 S. J. Yang, J. Y. Choi, H. K. Chae, J. H. Cho, K. S. Nahm and C. R. Park, *Chem. Mater.*, 2009, **21**, 1893–1897.
 - 28 G. Huang, Q. Yang, Q. Xu, S. H. Yu and H. L. Jiang, *Angew. Chemie - Int. Ed.*, 2016, **55**, 7379–7383.
 - 29 W. Zhang, Y. Hu, J. Ge, H. L. Jiang and S. H. Yu, *J. Am. Chem. Soc.*, 2014, **136**, 16978–16981.
 - 30 M. J. Park and J. S. Lee, *RSC Adv.*, 2017, **7**, 21045–21049.
 - 31 H. Y. Cho, J. Kim, S. N. Kim and W. S. Ahn, *Microporous Mesoporous Mater.*, 2013, **169**, 180–184.
 - 32 H. Zhang, M. Zhao and Y. S. Lin, *Microporous Mesoporous Mater.*, 2019, **279**, 201–210.

Chapter 7:

Conclusions

7. Conclusions

7.1. Discussion Outline

The research conducted and discussed in this thesis, while looking into different aspects of superhydrophobic surfaces and their development, could be viewed as aiming to promote the applicability of these surfaces and increase their involvement in real-life products. This has taken different approaches in each chapter and was achieved by: the inclusion of heat-sensitive substrates in a heat-dependant coating technique (Chapter 2), the introduction of a simple analysis methodology for resilience assessment (Chapter 3), the investigation of resilience-enhancement of polymer/particle composite coatings (Chapter 4), the inclusion of recycled waste polymers in the fabrication of superhydrophobic filters (Chapter 5), and the examination of the applicability of superhydrophobic coatings in protecting water-sensitive materials (Chapter 6).

In this short chapter, a summary of the main conclusions from each chapter is highlighted, along with a discussion of possible future work to be conducted if further improvement is considered.

7.2. Conclusions and Future Work

7.2.1. Chapter 2: Room-Temperature Deposition of Rough Coatings

In this chapter, the main focus was on the AACVD technique, which was previously reported for the deposition of superhydrophobic thermosetting polymer coatings at elevated temperatures.¹⁻³ The aim was to improve the technique such that the inclusion of heat-sensitive substrates can be achieved. To accomplish this, several deposition parameters were re-adjusted to move the deposition from the hot region of the CVD reactor to the outside of the reactor. Examples of these parameters include activation temperature, gas flow, deposition time, and polymer solution concentration. While the substrates were kept at room temperature, heat treatment of the polymer was needed at specific temperatures to evaporate the carrying solvent and partially cure the polymer before deposition. Typically, an activation temperature of 400°C was found to be optimum in providing suitable curing of the polymer without affecting the deposition. The deposition was conducted on glass substrates and then extended to paper, cardboard, and aluminium surfaces to show the applicability of the modified technique with heat-sensitive materials. The polymer utilised in these deposition experiments was PDMS, a thermosetting polymer, but the examination of

some thermoplastic polymers was also conducted to check if the technique principle applies to these polymers. However, it was observed that the soft nature of the heated thermoplastic polymer prevented the formation of rough morphologies. Hence, it was concluded that the curing ability (activated by heating) of the polymer is necessary for the formation of structured coatings using this method.

Meanwhile, the technique possesses some limitations. These could be related to common issues with CVD methods in general. For example, these methods are considered to be time-consuming. This issue is signified in ta-AACVD, where the coating of a circular area with a diameter of ~ 2 cm generally takes an hour. This is due to the relatively large reactor utilised that makes the slow aerosol flow spend a longer time to reach the substrate. Decreasing the diameter/length of the reactor, however, would produce a pre-mature deposition (anticipated from the discussion in Sections 2.3.1.1 and 2.3.1.7), and compensating for this with elevated temperature would remain limited to the polymer operating temperature range.

In addition, some disadvantages are more associated specifically with the addressed modification of the AACVD technique. For example, the restriction of the coated area using AACVD, similarly to the case of using conventional CVD, is limited by the size of the hot reactor. This means that enlargement of the reactor, given that all other deposition parameters are adjusted, can make deposition into relatively large areas possible. However, the area coated by ta-AACVD is smaller, as it is limited by the size of the gas outlet. Increasing the size of the outlet, however, can be associated with increased loss of polymer droplets.

A potential improvement that could be investigated to overcome these two issues is altering the design of the system to maximise the coating area and also reduce the coating time. This could be achieved by utilizing the reactor with several inlets/outlets. The increased lintels can allow the incorporation of more aerosol generators simultaneously, producing more polymer aerosol to take advantage of the large reactor utilised. Similarly, the multiple outlets can coat different areas in parallel.

Another issue is the hydrophobicity of the generated coatings. The highest recorded WCA for these coatings was 143.2° , which is not considered to be superhydrophobic. This was not observed for the coatings generated by AACVD using the same polymer, which exceeded 160° in some cases.^{1,4} This could be attributed to the slight differences in the relative size distribution of deposited polymer spheres between both techniques (refer to Figure 2.4 and Figure 2.12). In coatings generated by ta-AACVD,

the spheres were more uniform in size, different from those generated by AACVD where some smaller-scale ones can be noticed. This can result in an advanced structural hierarchy. The absence of this in ta-AACVS coatings can be due to the delayed deposition occurring outside of the reactor, as fast-curing small spheres will most likely not reach the substrate. Possible routes to add a component of multi-scale roughness can be achieved by incorporating nanoparticles in the polymer solution,⁵ or utilizing a different aerosol-generator that reduces the particle size to the nanoscale (Section 2.3.1.1).

7.2.2. Chapter 3: Quantifiable Resilience Assessment

Addressing the resilience assessment of the coatings against abrasion was the aim of Chapter 3, which was attempted through the introduction of a straightforward image analysis/mass-loss tracking technique. Typically, the technique combines i) facile sandpaper abrasion, ii) basic scanning and subsequent image processing, along with iii) monitoring of the coating mass-loss with abrasion cycles. The result was quantified information on coating removal, with the ability to differentiate between superficial coating removal and deep scratches (cohesive vs adhesive failure). The method demonstrated great potential in resilience analysis, which was further illustrated in Chapter 4.

A detailed discussion of the advantages of this technique, along with limitations of analysing certain surfaces and possible routes to adapt the technique to these surfaces has been done in Section 3.3.4. Mainly, each of the three main components of the technique requires certain standards on the analysed surfaces, which make the technique (in its reported form) limited to coatings that i) have visible degradation, ii) are distinguished from the underlying substrate, and iii) have a detectable mass loss. Suggested adjustments to the technique to suit other coatings that do not fit these requirements were also presented.

However, another limitation can be expected in the image-analysis method. The processing of the scanned coatings is done utilizing a MATLAB code that utilises the average RGB value of each image and how they change with the abrasion cycles to select a suitable RGB-value threshold to produce binary images (Section 3.3.2). However, this was shown, in some cases, to possibly detect noise resulting from the possible inconsistency of the coating colour (could result from defected deposition, Section 4.3.2.2.1). While a primitive correction was done (in Section 4.3.2.2.1) to account for the produced noise, this could be considered an area for the potential

development of the code. A suggestion to approach this is to introduce an auto-correction function in the code. This function would take the 0_cycle binary image, look for any noise been calculated (percentage of coating < 100%), and then determine the location of the noise pixels and cancel them. This should be combined with comparing the location of these pixels in the other binary images from subsequent abrasion cycles to make the correction consistent across all images. The advantage of inserting this function (rather than calculating the noise percentage primitively from the generated binary images) is that the binary image generation can be repeated after cancelling noise pixels, which will eliminate the possibility of the selection of the applied threshold, determined by the change in RGB values, being influenced by this noise.

7.2.3. Chapter 4: Resilience Enhancement of Composite Coatings

This chapter looks into SPNC coatings⁶ and aims to investigate the relation between the properties of the composite components (polymer/particles) and the observed resilience. The previously described resilience assessment technique was heavily applied to the prepared coatings for analysis of their degradation. The introduced variables were: i) changes in the polymer properties (M_w , TS) and ii) changes in the particles (particle size, size distribution). Typically, two main coating formulations were prepared, involving a thermoplastic (PVC) and a thermosetting (PDMS) polymer with silica particles. To test the effect of the polymer, PVC was incorporated in three different M_w , while the PDMS variants differed in their TS. Linking the change in M_w with a mechanical property was attempted for the PVC variants. To test the effect of the particles, silica was incorporated with PDMS in two different sizes, one of which is within the nanoscale while the other is in the microscale. Also, combinations of these two sizes were attempted with different deposition orders. All these formulations were imaged and analysed to compare their performance against sand-paper abrasion.

The drawn conclusions demonstrated an interesting difference between PVC and PDMS coatings. While it was hypothesized that a higher TS would be associated with improved resilience, this was only true for the PVC coatings, as the PDMS showed the opposite trend. While an attempt to link these observations to their distinguished nature (a thermoplastic vs a thermosetting polymer), further investigations of the origin of this behaviour are very important to complement this study and strengthen its outcomes. This can be achieved by trying other thermoplastic and thermosetting polymers to check whether these conclusions will be reinforced. In addition, the

explanation that was drawn in Section 4.3.2.2.3, regarding the increased extent of polymer cross-linking in thermosetting polymers leading to an increased area removal due to larger areas being strongly connected, could potentially be tested. This can be done by varying the abrasive force (by changing the sand-paper grade and/or the applied weight) and tracking how the coating would be affected. If this hypothesis is true, it is expected to notice that starting with the low abrasion forces range, minimal to no difference in the caused damage will be observed. This pattern will continue until reaching a certain threshold force that would lead to a significant loss of the polymer mass. This is distinguished from the thermoplastic polymer-based coatings, as the chains are weakly linked and can show a gradual degradation pattern with increasing the abrasion force (Section 4.3.2.2.3).

Regarding the properties of the particles, it was observed that nanoscale particles showed better resilience, which was justified by the small scale of the particles reduced the size of the generated scratches upon abrasion. Mixing different particle sizes in the same coating did not show potential for resilience improvement. This was an interesting finding, as it is widely established that the hierarchical structure provides improved superhydrophobicity,^{7,8} although the influence on the robustness is not widely discussed. A possible area of improvement here is to try to vary the difference between the two sizes incorporated and investigate if this can improve the adhesion between the particles and, hence, lead to better robustness.

7.2.4. Chapter 5: Oil-water Separation Filters

In this chapter, micronized polyethylene powder has been utilised for the fabrication of oil/water separation filters. Designing a functional system from micronized polymer provides an environmental advantage, as it allows the incorporation of recycled polymers. The conditions of powder treatment, including heating temperature and solvent type/quantity, were adjusted to obtain a permeable filter with maximised hydrophobicity and appropriate structural integrity. The fabricated filters consisted of a dual-layer formulation, each prepared using different treatment conditions, to achieve the targeted properties. The filters demonstrated high hydrophobicity and efficient separation of different oil/water mixtures, which were as high as 99.9% for chloroform/water mixtures separated using micronized powder of an average size of 4.5 μm .

The research utilised simple principles and was targeting a facile and cost-effective fabrication of oil/water separation filters, which was achieved in the presented research. Meanwhile, there are some areas of development that can be considered

in future studies to increase the applicability of these filters. For example, the incorporation of polymer powder in different designs/devices to enhance its suitability for broader separation requirements, detailed consideration of the design cost to further improve its economical compatibility, and investigation of separation scenarios where water is denser than oil (water gets poured first into the filter).

7.2.5. Chapter 6: Protecting MOFs

As surface protection is an important application of superhydrophobic coatings, the coating of water-sensitive MOFs has been studied in this chapter. This area attracts many research interests, resulting in different reports for MOF powder coating, commonly through encapsulation treatment. Meanwhile, the utilization of MOF in fixed forms (grown into substrates, compressed into pellets, etc.) can be beneficial in facilitating their insertion into the application setup. The coating of HKUST-1 MOF with a PDMS layer (through both ta-AACVD and SPPC coating) was attempted, along with investigating its water stability as well as compatibility with coating materials. The conclusion reached from this research was the incompatibility of the coating design with the required level of protection, as the structural degradation showed no signs of being prevented or retarded when compared to the uncoating MOF.

Several issues were present in this study in its current form, which prevented further development of the obtained results. This included the inconsistency of the generated XRD patterns across different MOF forms/treatment methods. This was demonstrated by the varying peak/noise ratios that were not necessarily linked (proportionally) with the level of degradation of the MOF. This is rationalised with the pre-analysis preparations potentially introducing differences in the crystallinity of the sample, especially at the surface of the pellet/powder that is being compressed for fixation. Another inconsistency issue appeared in the changes in signs of degradation, being sometimes presented by broadening and shortening of the main peaks, while at other times resulting in the appearance/disappearance of peaks in varying locations. This could be justified if the change in the MOF form can influence its degradation pathway, as a different range of forms has been prepared and, on many occasions, compared with each other.

Meanwhile, the coating approaches attempted, while did not show potential for successful protection, the reason behind their low performance still needs to be investigated. This can be achieved by investigating the extent of water penetration into these coatings, and how this can be affected by altering the water pressure (depth) and exposure time. Following this, the coating tolerance to water can be

compared to that of the MOF, and then a conclusion on the coating suitability can be made. The main point to consider is whether these coating approaches can be efficient in providing the same protection obtained by encapsulation techniques. Unlike the latter, coating the bulk surface of the fixed MOF means less coating per surface area of the material. Although this reduced the risks of functionality blockage, it may lead to insufficient coverage. A way to answer this question is to choose a coating method that can be consistently applied to both the loose powder and the fixed bulk and compare their behaviour in response to water exposure.

7.3. References

- 1 C. R. Crick and I. P. Parkin, *J. Mater. Chem.*, 2009, **19**, 1074–1076.
- 2 C. R. Crick and I. P. Parkin, *Thin Solid Films*, 2011, **519**, 2181–2186.
- 3 C. R. Crick and I. P. Parkin, *J. Mater. Chem.*, 2011, **21**, 14712–14716.
- 4 C. R. Crick and I. P. Parkin, *Thin Solid Films*, 2010, **518**, 4328–4335.
- 5 C. R. Crick, J. C. Bear, P. Southern and I. P. Parkin, *J. Mater. Chem. A*, 2013, **1**, 4336–4344.
- 6 R. L. Upton, Z. Davies-Manifold, M. Marcello, K. Arnold and C. R. Crick, *Mol. Syst. Des. Eng.*, 2020, **5**, 477–483.
- 7 N. Gao, Y. Y. Yan, X. Y. Chen and D. J. Mee, *Mater. Lett.*, 2011, **65**, 2902–2905.
- 8 W. Li and A. Amirfazli, *Soft Matter*, 2008, **4**, 462–466.

Appendix

Appendix 1: Threshold selection code

```

clc
close all
clear all

%Calling the images files
cd ('M:\Documents\SHARPs project\Images\Sand Paper Abrasion');
Image = {
'cycle_0.jpg','cycle_1.jpg','cycle_2.jpg','cycle_3.jpg','cycle_4.jpg','cycle_5.jpg','cycle_6.jpg','cy
cle_7.jpg','cycle_8.jpg','cycle_9.jpg','cycle_10.jpg'};

%Initial parameters
slope_black_old = 0;
p1=0;
x = [0:1:10];

%1st loop - calculates Avg-RGB values for all images
for j=1:length(Image)

    I = imread(Image{j});
    red = I(:, :, 1); green = I(:, :, 2); blue = I(:, :, 3);

    Ravg = mean2(red);
    Gavg = mean2(green);
    Bavg = mean2(blue);
    RGB_average(j) = round((Ravg+Gavg+Bavg)/3,2);
end

% Slope of the RGB values
a = polyfit(x, RGB_average, 1);
slope_RGB = a(1);

%2nd loop - starts with a threshold=20 and moving by 1 increment to optimise the threshold
value

for Threshold=20:1:100

%loop - applies the threshold on all images to generate binary images
    for j=1:length(Image)

        I = imread(Image{j});
        red = I(:, :, 1); green = I(:, :, 2); blue = I(:, :, 3);

        out = red < Threshold & red > p1 | green < Threshold & green > p1 | blue < Threshold &
blue > p1;
        out2=bwmorph(out,'dilate',1);

        %Calculate the percentage of black pixels (PB)
        PB(j) = (nnz(~out2) / numel(out2))*100;

    end

% Slope of PB
b = polyfit(x, PB, 1);
slope_black = b(1);

%if statement - compares slope of %_black_pixels with slope of RGB values

```

```
if (abs(slope_RGB - slope_black) <= abs(slope_RGB - slope_black_old))
    slope_black_old = slope_black;
else
    break
end
end

slope_RGB
slope_black_old
Threshold_final=Threshold-1

folder = 'M:\Documents\SHARPs project\Images\Sand Paper Abrasion\2021-10-06\Binary
Images\186_1.5u-3_p2=';

%3rd loop - uses the selected threshold and saves the binary images generated
for j=1:length(Image)

    I = imread(Image{j});
    red = I(:, :, 1); green = I(:, :, 2); blue = I(:, :, 3);

    out = red < Threshold_final & red > p1 | green < Threshold_final & green > p1 | blue <
Threshold_final & blue > p1;
    out2=bwmorph(out,'dilate',1);
    PB(j) = (nnz(~out2) / numel(out2))*100;

    pngFileName = Image{j};
    fullFileName = fullfile(folder, pngFileName);
    imwrite(out2, fullFileName);
end
```

Appendix 2: Full image sets for scanning experiments

Figure A2.1: The full image sets for the sample runs of PVC with different M_w , showing the coloured (upper), binary (lower) images, and the associated percentage of coating remained as predicted by image analysis. (a-c) PVC-M runs, (d-f) PVC-H runs. PVC-L runs were shown in **Figure 3.7a-c** (Section 3.3.2.3).

a) PVC-M – Run No.1:

0 cycles	1 cycles	2 cycles	3 cycles	4 cycles	5 cycles	6 cycles	7 cycles	8 cycles	9 cycles	10 cycles
99.99%	95.61%	90.41%	85.93%	82.04%	78.04%	73.69%	70.15%	64.55%	61.54%	58.79%

b) PVC-M – Run No.2:

0 cycles	1 cycles	2 cycles	3 cycles	4 cycles	5 cycles	6 cycles	7 cycles	8 cycles	9 cycles	10 cycles
99.86%	96.76%	94.33%	92.25%	90.39%	88.38%	87.23%	85.78%	83.83%	82.49%	80.38%

c) PVC-M – Run No.3:

0 cycles	1 cycles	2 cycles	3 cycles	4 cycles	5 cycles	6 cycles	7 cycles	8 cycles	9 cycles	10 cycles
99.94%	98.23%	96.95%	95.77%	94.24%	93.19%	91.45%	88.51%	86.55%	85.95%	84.68%

d) PVC-H – Run No.1:

0 cycles	1 cycles	2 cycles	3 cycles	4 cycles	5 cycles	6 cycles	7 cycles	8 cycles	9 cycles	10 cycles
100.00%	98.01%	94.58%	91.90%	88.78%	85.45%	83.09%	80.93%	78.95%	76.79%	74.88%

e) PVC-H – Run No.2:









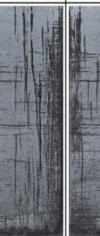






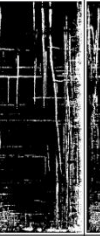
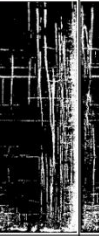
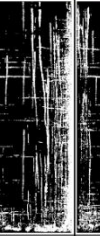


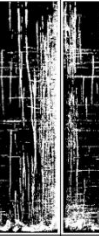

0 cycles	1 cycles	2 cycles	3 cycles	4 cycles	5 cycles	6 cycles	7 cycles	8 cycles	9 cycles	10 cycles
99.98%	97.96%	96.13%	94.58%	92.58%	90.13%	88.25%	86.14%	84.99%	83.08%	81.40%

f) PVC-H – Run No.3:














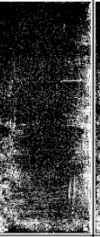
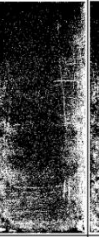

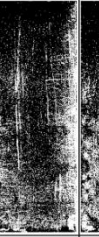


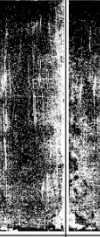
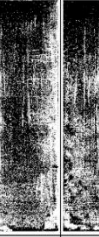

0 cycles	1 cycles	2 cycles	3 cycles	4 cycles	5 cycles	6 cycles	7 cycles	8 cycles	9 cycles	10 cycles
99.96%	98.91%	97.90%	97.36%	96.62%	95.31%	94.44%	93.04%	92.10%	90.51%	89.86%

Figure A2.2: The full image sets for the sample runs of PDMS with different TS, showing the coloured (upper), binary (lower) images, and the associated percentage of coating remained as predicted by image analysis. (a-c) PDMS (182) runs, (d-f) PDMS(184) runs. PDMS(186) runs were shown in **Figure 3.7d-f** (Section 3.3.2.3).

a) PDMS (182) – Run No.1:

0 cycles	1 cycles	2 cycles	3 cycles	4 cycles	5 cycles	6 cycles	7 cycles	8 cycles	9 cycles	10 cycles
										
										
99.97%	95.07%	89.37%	85.54%	83.20%	79.75%	76.82%	75.29%	73.44%	71.48%	68.07%

b) PDMS (182) – Run No.2:

0 cycles	1 cycles	2 cycles	3 cycles	4 cycles	5 cycles	6 cycles	7 cycles	8 cycles	9 cycles	10 cycles
										
										
95.02%	82.19%	78.30%	74.25%	70.01%	68.89%	67.28%	64.55%	63.77%	59.94%	61.20%
















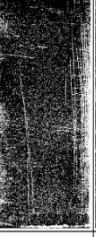

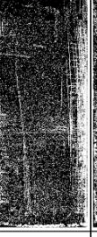
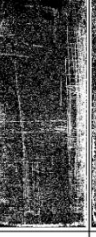

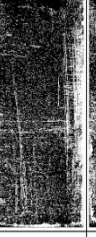

c) PDMS (182) – Run No.3:

0 cycles	1 cycles	2 cycles	3 cycles	4 cycles	5 cycles	6 cycles	7 cycles	8 cycles	9 cycles	10 cycles
88.94%	85.73%	81.27%	77.96%	75.45%	71.39%	67.48%	63.18%	60.63%	61.10%	59.37%

d) PDMS (184) – Run No.1:

0 cycles	1 cycles	2 cycles	3 cycles	4 cycles	5 cycles	6 cycles	7 cycles	8 cycles	9 cycles	10 cycles
96.86%	91.36%	88.05%	84.05%	81.45%	78.72%	77.18%	76.06%	72.91%	71.89%	69.66%

e) PDMS (184) – Run No.2:

0 cycles	1 cycles	2 cycles	3 cycles	4 cycles	5 cycles	6 cycles	7 cycles	8 cycles	9 cycles	10 cycles
										
										
99.96%	82.28%	79.87%	78.21%	75.86%	74.79%	72.81%	72.20%	71.52%	71.48%	69.22%

f) PDMS (184) – Run No.3:



































































0 cycles	1 cycles	2 cycles	3 cycles	4 cycles	5 cycles	6 cycles	7 cycles	8 cycles	9 cycles	10 cycles
										
										
77.20%	76.44%	73.30%	68.69%	64.97%	60.22%	57.75%	50.38%	53.16%	51.61%	50.08%

Figure A2.3: The full image sets for the sample runs of silica with different sizes and deposition order, showing the coloured (upper), binary (lower) images, and the associated percentage of coating remained as predicted by image analysis. (a-c) μ -n runs, (d-f) n- μ runs, (g-i) μ /n mix runs.

a) μ -n – Run No.1:

0 cycles	1 cycles	2 cycles	3 cycles	4 cycles	5 cycles	6 cycles	7 cycles	8 cycles	9 cycles	10 cycles
										
										
99.88%	91.63%	85.29%	80.43%	75.05%	67.30%	61.50%	56.06%	51.97%	47.50%	44.12%

b) μ -n – Run No.2:

0 cycles	1 cycles	2 cycles	3 cycles	4 cycles	5 cycles	6 cycles	7 cycles	8 cycles	9 cycles	10 cycles
										
										
99.98%	93.94%	88.57%	84.45%	79.47%	74.86%	71.26%	65.95%	63.86%	58.58%	54.81%

c) μ -n – Run No.3:

0 cycles	1 cycles	2 cycles	3 cycles	4 cycles	5 cycles	6 cycles	7 cycles	8 cycles	9 cycles	10 cycles
99.95%	91.60%	87.44%	85.35%	81.55%	78.65%	75.70%	72.92%	70.20%	67.08%	65.35%

d) n- μ – Run No.1:

0 cycles	1 cycles	2 cycles	3 cycles	4 cycles	5 cycles	6 cycles	7 cycles	8 cycles	9 cycles	10 cycles
99.84%	91.10%	87.32%	83.29%	80.67%	77.83%	76.32%	72.88%	71.08%	68.36%	67.37%























e) n- μ – Run No.2:

0 cycles	1 cycles	2 cycles	3 cycles	4 cycles	5 cycles	6 cycles	7 cycles	8 cycles	9 cycles	10 cycles
99.35%	95.36%	92.50%	91.23%	90.10%	88.62%	86.47%	85.03%	82.88%	80.12%	78.17%























f) n- μ – Run No.3:

0 cycles	1 cycles	2 cycles	3 cycles	4 cycles	5 cycles	6 cycles	7 cycles	8 cycles	9 cycles	10 cycles
99.51%	93.31%	92.92%	91.16%	88.84%	87.23%	84.53%	84.95%	84.17%	81.90%	80.05%








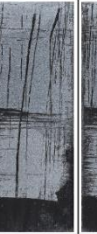
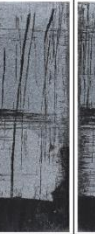
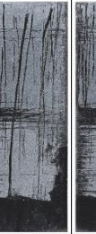












g) μ/n mix – Run No.1:

0 cycles	1 cycles	2 cycles	3 cycles	4 cycles	5 cycles	6 cycles	7 cycles	8 cycles	9 cycles	10 cycles
										
										
99.52%	91.58%	86.79%	84.24%	80.80%	76.69%	72.42%	71.85%	67.49%	62.45%	55.01%

h) μ/n mix – Run No.2:

0 cycles	1 cycles	2 cycles	3 cycles	4 cycles	5 cycles	6 cycles	7 cycles	8 cycles	9 cycles	10 cycles
										
										
98.76%	88.66%	83.38%	77.85%	72.42%	66.73%	63.48%	59.31%	55.90%	53.70%	49.49%

i) μ/n mix – Run No.3:

0 cycles	1 cycles	2 cycles	3 cycles	4 cycles	5 cycles	6 cycles	7 cycles	8 cycles	9 cycles	10 cycles
										
										
99.47%	95.59%	92.72%	90.38%	85.32%	79.49%	76.22%	69.17%	67.19%	64.50%	61.52%